UNIVERSITÀ DEGLI STUDI FIRENZE

Ph.D. COURSE IN SCIENCE FOR THE CONSERVATION OF CULTURAL HERITAGE

CYCLE XXVIII

Ph.D. COORDINATOR
Prof. Baglioni Piero

OPTICAL SPECTROSCOPIES: APPLICATION TO THE STUDY OF PAINT MODELS

CHIM/02

Ph.D. Candidate
Carlesi Serena

Tutor
Dr. Becucci Maurizio

Co-tutors
Dr. Ricci Marilena
Dr. Picollo Marcello

Ph.D. Coordinator
Prof. Baglioni Piero

Years 2012/2015

Tables of Contents

Abbreviations

ATR: Attenuated Total Reflection
CCD: Charge-Coupled Device
DA: Diels-Alder Reactions
dp: Data-Points
EE: Excitation-Emission Spectra
EES: Excitation-Emission Spectroscopy
FT-Raman: Fourier Transform Raman Spectroscopy
FT-IR: Fourier Transform Infrared Spectroscopy
FT-NIR: Fourier Transform Near Infrared Spectroscopy
GC-MS: Gas Chromatography Mass Spectroscopy
H-NMR: Proton Nuclear Magnetic Resonance
HPLC-ESI-QTOF High-Performance Liquid Chromatography Coupled with Electrospray Ionization and Quadrupole Time-of- Flight Mass Spectrometry
K-M: Kubelka-Munk Function
LOO: Leave One Out Cross Validation
Mid-IR: Medium Infrared Spectroscopy/Spectral Range
NIPALS: Non-Linear Iterative Partial Least Squares Algorithm
NIR: Near Infrared Spectroscopy/Spectral Range
PCA: Principal Component Analysis
PC: Principal Component
PCs: Principal Components
PLS: Partial Least Squares Regression
SVD: Singular Value Decomposition
UV-Vis: Ultraviolet Visible Spectroscopy/Spectral Range
2D-Fluorescence: 2 Dimensional Spectroscopy

Introduction

Knowledge of the materials present in artworks is crucial to ensure appropriate conservation procedures and to gain insight into their historical evolution. This knowledge is especially important when dealing with paintings, because they are complex systems, composed of various supports, preparation layers and painting materials, such as pigments and binders.

While the identification of pigments in paintings is today a relatively straightforward process in most cases, the identification of binding media remains a challenge [**1**]. The fact that organic materials are often added in scant quantity, in contrast with the presence of the high amounts of inorganic materials, as pigments and dryers, may hinder their reliable identification [**2**]. Furthermore, organic materials are less stable and may deteriorate faster than inorganic components so that they often only remain at trace levels in centuries-old paintings, thus making their identification even more difficult. Consequently, the chosen analytical techniques should provide high sensitivity and specific information, in order to avoid ambiguities or misinterpretations. To satisfy this requirement, the most prudent option is to apply more than one method, whether it is possible, to gather complementary information.

Analytical techniques such as separation methods (gas chromatography, capillary electrophoresis and liquid chromatography), mass spectroscopy and hyphenated techniques are well-suited for the analysis of organic compounds [**3-4**], even if their relatively large sample consumption, the time consuming, the complex sample preparation and the multi-parameter operating conditions imply obvious problems for the analyses of samples with historical interest.

Since the last decades many efforts have been devoted at developing non-invasive and non-destructive analytical tools and methodologies able to provide in-depth characterization of the artwork constituent materials, without any contact with the surface of the object, thus preserving its integrity. Vibrational and electronic spectroscopic methods (i.e. UV-Vis, fluorescence, infrared, reflectance and Raman [**5-7**]) have the potentiality to overcome the aforementioned issues, thanks to their non-destructiveness and effectiveness already shown for the study of the cultural heritage field. Besides, they do not need any sample pre-treatment, the time of analysis is very short, and they allow very small areas of the surface of the artwork to be studied. Nevertheless, data analysis performing one-by-one (or peak-by-peak) comparison of sample spectra with those of the standard materials, especially in the case of natural binding media, can be a tedious time consuming methodology not always effective. Moreover, while spectroscopic analysis makes relatively straightforward the differentiation between the various organic materials classes, like the proteinaceous and the fat-based ones, the differentiation of the

same class organic compounds, for example different kinds of glues or oils, continues to be quite challenging.
So, over the last few years, high attention has been paid by scientists to manage the whole information obtained from the collected data by different spectroscopic techniques, by means of chemometric analysis assistance [**8-10**]. In order to extract the maximum information concerning composition and to detect slight disparities between the spectroscopic data, it has been demonstrated that the combining of non-destructive analytical techniques with statistical methods is highly useful, such as multivariate chemometric tools. One of the most important chemometric analyses applied in the field of cultural heritage is represented by Principal Component Analysis (PCA) [**10**]. The main benefit of PCA is its capability to reduce dimensionality of the original data-set by representing them in terms of new and independent coordinates, the principal components (PCs), which contain more interpretable and representative information of the under investigation system. The PCs are hierarchically ordered and describe the largest variance of the original data set [**11**].
The application of PCA to large spectral data set can be therefore exploited to extract the meaningful information for the spectra classification, but it is not always sufficient to identify different compounds, especially those belonging to the same organic class. In order to increase the differentiation capability and the extraction of information, over the last few years, PCA has been applied on combined spectra [**12-13**].
Recently, FT-Raman and fibre-optic reflectance spectra, originating from the same samples, were combined for the identification of binder materials, bound pigments and pigment-binder interactions by considering some different lead-based paints [**12**]. Pallipurath *et al.* [**12**] assessed the quality of PCA was greatly improved by using combined spectra, giving a more accurate classification for the differentiation of proteinaceous and polysaccharide-based media in paint mixtures. Bueno *et al.* [**13**] used the Raman and FT-IR techniques combination into a single data set to improve the statistical differentiation of gunshot residues (GRS). The combined data, obtained from the same analyte, enhanced any potential statistical separation between the two non-equivalent GRS samples.
In both studies the sensitivity and the specificity were improved by combining the obtained data, using two complementary analytical methods over the separated tested techniques.

My PhD work is aimed at developing new methodologies based on the combination of traditional spectroscopic techniques with multivariate analysis tools to analyse artistic organic compounds.

This thesis explores the possibility to exhaustively characterize traditional neat binding media and complex systems, such as oil-paint models, applying PCA to combined first derivative Fourier Transform Near Infrared (FT-NIR) and Raman spectra. The combination of these two vibrational spectroscopic methods provides complementary information and, due to the different physical processes involved, also the possibility to obtain a much deeper insight into the structure, the binding properties of these compounds and an in-depth analysis of their interaction with pigments due to the ageing process. Furthermore, in order to point out significant differences between these systems, an appropriate data manipulation, based on the application of the first derivative algorithm, has been individuated. Consequently, small spectral differences in the original FT-NIR and Raman spectra, have been better underlined, making possible to enhance the differentiation and the sensitivity of the proposed methodology.
The materials analysed in this work have been selected on the basis of their chemical composition, as well as their use and availability, and they do not represent an exhaustive selection of oils, glues, gums and proteinaceous materials, but rather general classes of materials used in a painting. Studied materials include drying oils (linseed, walnut, poppy seed oil and stand-oil purchased from ordinary international stores), protein-based binding media (egg yolk, whole egg, egg white, casein, rabbit skin glue, fish glue and strong glue) and natural gums (Arabic gum and Tragacanth gum). As regards the oil-paint models, they have been prepared by mixing linseed oil, which was used in the Middle Ages, and poppy-seed oil, which has been utilized especially for artists' purposes since the 17th century [**14**], with a series of pigments used in art, both since antiquity (like lead white, azurite, Afghanistan lazurite) and in contemporary art (such as phthalocyanine blue, zinc oxide and synthetic ultramarine blue).

Additionally, in order to better understand the chemical composition of different binding media, together with their modifications with ageing, 2D-fluorescence maps have been further acquired from each of them. Within the context of the analysis of paintings, fluorescence spectroscopy represents an important tool, since it can provide indications and guide to further analytical investigations based on proper complementary techniques.
A preliminary study was performed to evaluate limits and potentialities of the combination of this spectroscopic technique with PCA with the aim of distinguishing and characterizing different traditional binding media. This latter study was performed at the laboratories of IELS-FORTH (Institute of Electronic Structure and Laser– Foundation for Research and Technology) at Heraklion (Crete).

The aforementioned considerations led to organize all the discussed topics into three main parts:

- ***Part I*** is focused on a brief description of the selected materials and spectroscopic techniques. An in-depth analysis of the analytical methodologies individuated to treat the different typologies of spectral data is discussed;
- ***Part II*** describes the results obtained by the application of the methodology based on the PCA to combined first derivative FT-NIR and Raman spectra, preliminary individuated.
  This section is divided into four different chapters.
  The *first chapter* is focused on the study of all the neat binding media after a natural ageing of 3 months. The main purpose is the evaluation of the potentialities of this methodology in order to characterize and distinguish these analysed binders.
  The *second chapter* shows the results and regards the application of the proposed approach to the study and the characterization of different typologies of "fresh" drying oils (3-months-aged), purchased from different international stores, in order to evaluate its sensitivity within the same organic class.
  The *third chapter* is dedicated to the use of this methodology for the analysis of oil-paint models after an ageing of 9 months, with the aim to evaluate the capability to exhaustively characterize more complex systems.
  The *fourth chapter* regards the ageing of neat linseed oil and the corresponding oil-paint models prepared with lead and zinc white pigments. The characterization of two 10-year old mock-ups prepared with linseed oil and lead and zinc white pigments is also discussed (these latter could be regarded as "real samples" from a contemporary painting). In this chapter, the proposed methodology is exploited to individuate probable ageing trends for the two white-oil models taken into account.
- ***Part III*** describes the results obtained by the application of 2D-fluorescence spectroscopy and its combination with PCA to analyse traditional neat binding media.

References

[1] B. Stuart, Analytical techniques in materials conservation, John Wiley and Sons Ltd., UK, Chichester, 2007.

[2] I. Bonaduce, M. Cito, M.P. Colombini, The development of a gas chromatographic-mass spectrometric analytical procedure for the determination of lipids, proteins and resins in the same paint micro-sample avoiding interferences from inorganic media, J. Chromatogr. A 2009, 1216, pp 5931-5939.

[3] I. Bonaduce, V. Castelvetro, M.P. Colombini, A. Lluveras-Tenorio, M. Raihane, M. Ibnoussina, A. Boujamid. Characterization of the Organic Materials Used in the Painting of the Vaulted Ceiling at the Saadian Tomb of Mulay Ahmed Al-Mansour (Marrakech), J. Cult. Herit. 2014, 15(3), pp 300-307.

[4] M.P. Colombini, F. Modugno. ''Organic Materials in Art and Archaeology'', in M.P. Colombini, F. Modugno (eds.), Organic Mass Spectrometry in Art and Archaeology, John Wiley and Sons, UK, Chichester, 2009, pp. 6-9.

[5] M. Picollo, M. Bacci, A. Casini, F. Lotti, S. Porcinai, B. Radicati, L. Stefani "Fiber Optics Reflectance Spectroscopy: a non-destructive technique for the analysis of works of art" Optical Sensors and Microsystems: New concepts, Materials, Technologies, edited by Martellucci et al., Kluwer Academic / Plenum Publishers, New York, 2000

[6] P. Vandenabeele, B. Wehling, L. Moens, H. Edwards, M. De Reu, G. Van Hooydonk, Analysis with Micro-Raman Spectroscopy of Natural Organic Binding Media and Varnishes Used in Art, Anal. Chim. Acta. 2000, 407(1-2), pp 261-274.

[7] A. Nevin, D. Anglos, S. Cather and A. Burnstock, The influence of visible light and inorganic pigments on fluorescence excitation emission spectra of egg-, casein-and collagen-based painting media, Appl. Phys. A 2008, 92, pp 69-76

[8] K. Castro, A. Sarmiento, M. Maguregui, I. Martı´nez-Arkarazo, N. Etxebarria, M. Angulo, M. Urrutikoetxea Barrutia, J.M. Gonza´ lezCembellı´n, J.M. Madariaga, Multianalytical Approach to the Analysis of English Polychromed Alabaster Sculptures: μRaman, μEDXRF, and FTIR Spectroscopies, Anal. Bioanal. Chem. 2008, 392(4), pp 755-763.

[9] C. Lofrumento, M. Ricci, L. Bachechi, D. De Feo, E.M. Castellucci, The First Spectroscopic Analysis of Ethiopian Prehistoric Rock Painting, J. Raman Spectrosc. 2012. 43,(6), pp 809-816.

[10] A. Nevin, I. Osticioli, D. Anglos, A. Burnostck, S. Cather, E. Castellucci, Raman Spectra of Proteinaceous Materials Used in Paintings: A Multivariate Analytical Approach for Classification and identification, Anal. Chem. 2007, 79, pp 6143-6151.

[11] M. Otto, Chemometrics: statistics and computer application in analytical chemistry; WILEY-VCH, Weinheim, New York, Chichester, Brisbane, Singapore, Toronto, 1999.

[12] A. Pallipurath, J.Skelton, P. Ricciardi, S. Buclow, S. Elliot, Multivariate analysis of combined Raman and fibre-optic reflectance spectra for the identification of binder materials in simulated medieval paints, J. Raman Spectrosc. 2013, 44, pp 866-874.

[13] J. Bueno, I.K. Lednev, Advanced statistical analysis and discrimination of gunshot residue implementing combined Raman and FT-IR data, Anal. Methods 2013, 5, pp 6292-6296.

[14] R.J. Gettens, H. Kühn, W.T. Chase, Lead White, in A. Roy (Ed.), Artists pigments: a handbook of their history and characteristics, vol. 2, Oxford University Press, New York, 1993, pp. 67-81.

PART I

Materials and Methods

Abstract

The first part of this thesis is focused on a brief description of selected materials and methods.

This PhD work analyses standards of drying oils, vegetable gums and proteinaceous media. In addition, linseed/poppy-seed oils have been blended with both traditional and more recent pigments.
A summary of performed investigation techniques is reported, focusing on how these analytical methods work and what kind of information can be gained. An introduction on Principal Component Analysis (PCA) as a tool in data interpretation and comparison is also shown.
Finally, new analytical approaches, developed in this research and based on the applying of PCA to traditional spectroscopic techniques, are illustrated.

1.1 Binding media

The materials used as binding media are all *film-forming* substances. A binding medium exists to hold the pigment to a surface [**1-2**].
The formation of a film involves the conversion of a liquid phase, in which the film-forming material may be present in solution or as an emulsion or be in the molten state, into a solid system. Depending on the nature of the compounds involved, the formation of the solid system may be result of a physical change or a chemical reaction, or a combination of both.
These materials can be used not only as binding media, but also as adhesives, stabilizers, protectives, varnishes and glues.

The natural film-forming materials are so numerous and so different that it is essential to group them into large categories.

Biochemists put forward the following classification [**3**]:

I. Lipidic media
II. Polysaccharide media
III. Proteinaceous media
IV. Terpenes or resinous materials

Sometimes, artists have used a mixture of different types of media, which often further consist of a mixture of compounds [**2**].
In this paragraph is reported a brief outline solely concerning the chemical properties and main applications of the binding media selected for this study (more precisely, classes I-III).

1.1.1 Lipidic media

Lipidic media can be sub-divided in two main groups, namely, *waxes* and *drying oils*. The former are usually solids, the latter liquid, at room temperature [**4**].
In this work, only drying oils have been analysed.
Oils are classified as *drying oils* when they undergo oxidation and crosslinking reactions to form solid films after exposure to light and oxygen [**4**]. Chemically, oils are defined as mixtures of mixed triglycerides, which are esters of the trihydric alcohol glycerol with a range of possible long chain fatty acids. The doubly unsaturated linoleic acid and the triply unsaturated linolenic acid are the compounds principally responsible for the drying properties of drying oils (**Fig. 1**). Also, various types of phenols and tocopherols (vitamin E) are present as a minor component of vegetable oils and they serve as natural antioxidants [**4**]. Additionally, oils contain less than 1 % of "non-saponifiables" compounds, very complex mixtures of triterpene alcohols, methyl sterols and sterols [**4**].

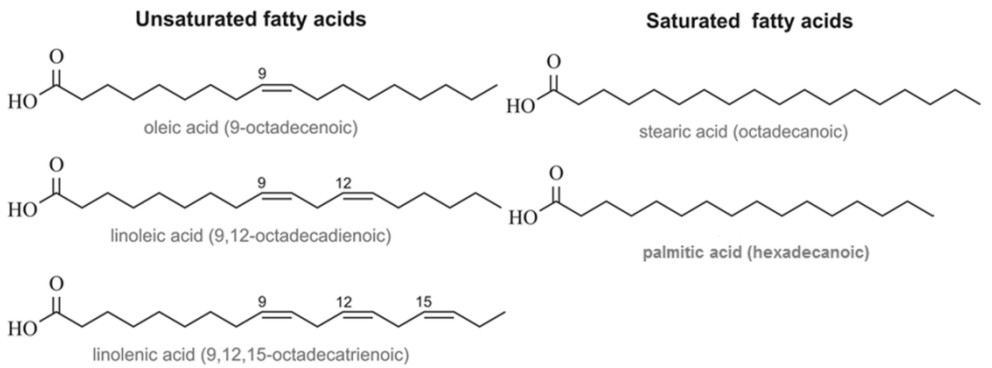

Fig. 1 The most important fatty acids present in the chemical composition of drying oils.

The most important drying oils used in European easel paintings are **linseed**, **poppy-seed** and **walnut** oils [**4**]. Linseed oil is originated from the seeds of the flax plant (*Linum usitutissimum*). Poppy seed oil is obtained by squeezing the seeds of the opium poppy (*Papaver somniferum*). Walnut oil is extracted from the walnuts of the walnut tree (*Juglans regia*).
Among these drying oils, differences of composition are largely quantitative rather than qualitative, as can be seen in **Table 1**, where their fatty acid composition is reported. In it, the headings, "18:0", "18:1", etc. indicate "chain lengths: number of double bonds".
Additionally, composition of an oil is not perfectly constant. It can vary for a number of reasons, among them: variety of plant, nature of the soil, and season of harvesting or variation in weather conditions.

In this work, also **stand-oil** has been analysed. Drying oils can be processed in various ways to produce materials in which the linking together of the triglycerides is already partially effected before the oil is put to use. The product is naturally more viscous than the raw oils. One of the main pre-polymerized drying oil is represented by the stand-oil. This particular drying oil is generated by heating linseed oil to near 300 °C for a few days in the absence of air. Under these conditions the polyunsaturated fatty esters convert to conjugated dienes which undergo Diels-Alder reactions (DA) and radical additions [**4-5**].

Table 1 Typical fatty acid composition (%) of the drying media studied [**6**].

Drying oil	Palmitic Acid C16:0	Stearic Acid C18:0	Oleic Acid C18:1	Linoleic Acid C18:2	Linolenic Acid C18:3
Linseed	7-8	3.4-4.6	18.5-22.6	14.2-17.2	52-55
Poppy-seed	10-14	2.5-3.2	16-24	56-70	0.4-0.6
Walnut	6.4-7.5	1.3-2.0	14-20	57-62	10-15

Linseed oil highlights the better performance as painting medium, compared with poppy-seed and walnut oils, mainly thanks to its faster drying, due to the higher concentration of linolenic acid, as can be seen in **Table 1**. In spite of this great advantage, linseed oil has a high tendency to turn yellow, especially when kept in the dark. It is known that oils with a high linolenic acid content are particularly prone to undergo this. By contrast, poppy-seed and walnut oils, although characterized by a slow drying process, show a slow yellowing tendency [**7**]. As regards stand-oil, it dries more slowly than raw oils and with the uptake of much less oxygen. Moreover, the predominance of carbon-carbon links over carbon-oxygen links in the resulting polymer is probably responsible for the more durable qualities of the film formed. Other advantages of this oil are a slow tendency to yellow (a reduction in linolenic acid content) and smaller volume changes (resulting in less wrinkling).

The mechanisms that play a role in the ageing of these drying oils are complex. Some of the reactions which take place during the drying process lead not to cross-linking, but to bond breaking and the formation of low molecular weight degradation products [**4**]. Metals, light, heat and enzymes can accelerate these reactions. Furthermore, the presence of environmental humidity and particular pigments such as lead and zinc white (basic pigments) often leads to the triglyceride hydrolysis process. The hydrolysis reaction frees fatty acids from their esters, capable of migrating and/or reacting [**8**]. The most important consequence is the *saponification* process which leads to the formation of metal

carboxylates/metal soaps. Generally, the saponification causes a darkening and a brittling of the painting [**9**].
The time when these drying oils were first used in painting is quite unknown. Linseed oil was known to the Ancient Egyptians, but there is no evidence that the oil was ever used by them for painting. Equally, although walnut and poppy-seed oils were known in the Greece and Rome of classical times, there is no mention of their use in painting. However, linseed oil was used in Europe from the thirteenth century at least and its use became more general in the sixteenth century. As regards poppy-seed oil it was used as a painting binder since the seventeenth century, whereas walnut oil was extensively used during the Renaissance [**4, 7**].

1.1.2 Polysaccharide media

Polysaccharides are polymeric carbohydrate molecules composed of long chains of monosaccharide units bound together by glyosidic linkages and on hydrolysis give the constituent *monosaccharides* or *oligosaccharides.* Monosaccharides (also called *sugars*) are the most basic units of carbohydrates and cannot be further hydrolysed to simpler compounds. [**4**].
In art field, the most important polysaccharides are represented by *plant gums.* These are water-soluble or water-dispersible materials of high molecular weight, exuded from trees/plants. The chemistry of gums is quite complex, since several sugars and acids can be present in their chemical composition, as can be seen in **Table 2**.
For this study, **Arabic gum** and **Tragacanth gum** have been selected.
Arabic gum is the product of a number of Acacia species of which *Acacia Senegal* is the most important. Its chemical structure is very complex. Natural factors influence its molecular weight, which varies between 250.000 and 1.000.000 g mol^{-1}. About 70% of its weight is made up of branched hetero-polysaccharides, the remaining weight being due to a glycoprotein (i.e. a protein linked to a carbohydrate). D-galactose, L-arabinose, L-rhamnose and D-glucoronic acid are the main constituents of the polysaccharide fraction, determining the hydrophilic character of this part. Since Arabic gum incorporates glucuronic acid it is acidic and exists as a salt with calcium, magnesium and potassium cations (Arabic acid). Arabic gum is completely water-soluble (in twice its volume) [**2, 7**].
Tragacanth gum is, instead, obtained from species of *Astragalus*. Its molecular weight is greater than that of Arabic gum, namely 840.000 g mol^{-1}, and it is characterized by macromolecules with an elongated shape. It is not wholly soluble in water and produces a viscous fluid (gel formation). This natural polymer consists of a mixture of water-soluble (*tragacanthin*) and water-

sweallable (*bassorin*) polysaccharide fractions. The water soluble *tragacanthin* constitutes around 30-40% of the gum. L-arabinose, D-galactose, L-fructose, L-rhamnose, D-xylose and D-galacturonic acid represent the main constituents [**2, 7**].

In addition, chemical analysis revealed the possible presence in both gums of residues of tryptophan and phenolic compounds [**10**].

Degradation of these gums can be induced by heating, acids and UV radiation. However, both gums are characterized by an enough stable behaviour [**4, 11-12**].

Arabic gum was extensively used in ancient Egypt and has been an article of commerce for thousands of years. Its high solubility makes it extremely suitable as medium for "watercolours". It has been also important as adhesive for postage stamps and envelopes. Tragacanth gum is another material known since classical times, even if it has been used much less than Arabic gum. Its capability to form a gel makes it suitable for painting on linen and for the manufacturing of pastel crayons [**2, 4, 7**].

Table 2 Sugar and uronic acid components of some gums [**4**].

Gum	Arabinose	Rhamnose	Galactose	Glucose	Mannose	Xylose	Fucose	Glucoronic acid	Galacturonic acid
Arabic	++	+	++					+	+
Tragacanth	+		+			+	+		+
Cherry	++		+		+	+		+	
Guar			+		++				
Carob					++	+			
Tamarind	+		+	+					
Karaya		+	+						++
Ghatti	++		+		+	+		+	

+indicates that the sugar is present; ++indicates a major component

1.1.3 Proteinaceous media

Proteins are macromolecules made up of one or more unbranched chains of amino acids which are joined together by peptide bonds between the carboxyl and amino groups of adjacent *amino acid* residues. Several amino acids are commonly found in animal and vegetable proteins. The number and the type of amino acids and their sequence determine the surface charge of the protein, its molecular configuration and its unique chemical and physical properties. The function of a protein is dependent on its three-dimensional structure. A number of agents can disrupt this structure, thus denaturing it, for example changes in pH, temperature, salt concentration and the presence of reducing substances. Both vegetable and animal proteins are encountered in art field [**13**].
Proteinaceous media are not generally pure materials, but rather contain mixtures of different proteins as well as fatty acid ester (e.g. egg yolk), various vitamins, and impurities related to preparation, ageing and deterioration processes [**2**].
The main common proteinaceous media are **egg-based** (egg white and egg yolk), **collagen-based** (rabbit skin glue, strong glue and fish glue) and **derivatives from milk** (casein).

The amino acid compositions of different proteinaceous binders are reported in **Table 3** [**4**].
As regards egg-based media, the composition of eggs, in terms of broad chemical groupings is shown in **Table 4** [**4**].
The lipids are made up of *triglycerides* (65 %), *phospholipids* (29 %) and *cholesterol* (5.2 %).
The cholesterol is thus present to the extent of some 0.5 % of whole egg and of 1.5% in egg yolk. This is a large amount compared with the content of any one sterol in vegetable oil [**4**].
The nature of phospholipids must briefly explain. They are in effect triglycerides in which one of the fatty acid ester groups is substituted by a phosphatide group, that is to say an ester with *phosphoric acid*. As phosphoric acid is tribasic, it may be further combined with various compounds. When so esterified with the strong nitrogenous base choline, the resulting compound is one of the group of compounds called *lecithins* [**4**].
The fatty acid composition of hens' eggs is, instead, reported in **Table 5**.

Table 3 Amino acid composition of proteinaceous media (results converted to weight percent of total) [**4**].

	Gelatin	Egg White	Egg yolk	Casein
Glycine	24.7	3.6	3.5	1.7
Alanine	10.1	6.3	5.6	2.7
Valine	2.2	8.3	6.4	7.2
Leucine	3.7	10.3	9.2	9
Isoleucine	1.2	6.2	5.1	6
Proline	13	4.5	4.5	13.2
Phenylalanine	1.6	5.2	3.9	5.1
Tyrosine	0	1.4	2.8	5.5
Serine	4	5.8	9.1	4
Threonine	2.2	3.7	5.6	2.7
½ Cystine	0	1.9	1.9	0
Methionine	1.4	1.2	2.3	2.3
Arginine	8.2	6.8	5.5	4
Histidine	1.5	2.4	2.4	3.6
Lysine	4.1	8	5.7	6.7
Aspartic Acid	5	10.5	11.5	6.1
Glutamic Acid	9.7	13.9	15	20.2
Hydroxyproline	7.4	0	0	0

Table 4 Composition of hens' eggs (%) [**4**].

	Egg white	Egg yolk	Whole egg
Water	88	49	75
Solids	12	51	25
Protein	10	16.5	12
Lipids	-	33	11
Carbohydrate	1	1	1
Inorganic	0.6	1.7	1

Table 5 Fatty acid composition of triglycerides present in hens' eggs [**4**].

	Palmitic Acid C16:0	Stearic Acid C18:0	Oleic Acid C18:1	Linoleic Acid C18:2	Linolenic Acid C18:3	Palmitoleic Acid C20:1
Hens' eggs	27	9	44	13.5	0.5	5

As regards the proteins which occur in eggs the general term used to indicate them is *albumins*. The albumins are readily soluble in water and belong to a class of globular proteins. These are held in a tight ball conformation by internal hydrogen-bonds. These proteins quickly denature, under the effects of heat and certain reagents. So, the internal hydrogen bonds rupture and the

molecular structure opens up and adopts an open chain-like structure, losing the overall hydrophilicity. Egg white and egg yolk qualitatively show no difference in terms of the amino acids present [**2, 4**].
The actual composition of eggs in terms of individual proteins is quite complex. Egg white contains a glycoprotein (i.e. a protein linked to a carbohydrate), *ovalbumin*, as the principal protein (about 65 %). Among the other proteins are mucin (2%), which is rich in carbohydrates, *globulins* (6%), *lysozyme* (3%), *conalbumin* (9 to 17%) and *ovomucoid* (9 to 14%). *Lysozyme* is the only non-glycoprotein contained in egg white [**2, 4**].
Regarding the proteins of egg yolk, which are associated with phosphorus-containing lipids, these include α-, β-, γ- *livetins, phosvitin* (a composite protein) and α- and β-lipovitellins, lipoproteins containing phospholipids.
Furthermore, the yellow colour of egg yolk is due to the presence of *carotene pigments* [**2, 4**].
The film obtained from egg white is very brittle, and for this reason it is necessary to add a plasticizer such as glycerol. In spite of its numerous shortcomings, brittleness and insolubility after ageing, egg white has been used as binding medium [**14**], as a retouching medium [**15**] and as varnish [**14**].
Egg yolk is a very old painting medium and is still highly appreciated nowadays. It solidifies quickly and presents a pleasant flexibility, but it remains soft for long time and does not resist mechanical abrasion [**16**].
Collagen-based media, usually named *glues,* are natural polymers derived from *collagen* – the major structural protein constituent of skins, connective tissue, cartilage and bones. These glues may exhibit varied physical, chemical and mechanical properties, depending on their origin and method of preparation.
Collagen consists of long protein molecules composed of naturally occurring amino acids that are linked in a specific sequence by covalent peptide bonds. Its molecular weight is about. Due to the spatial conformation of some amino acid groups (notably *glycine*, *proline* and *hydroxyproline*) and the many ionisable and polar functional groups in the protein chain, the individual chains form triple-stranded helical coils that are generally believed to be internally stabilised by hydrogen-bonding [**17**].
A lot of types of glues exist. As the name suggests, **rabbit skin glues** should be produced purely from rabbit skins; whereas the swim bladders of various species are the source for **fish glues**. **Strong-glue** is produced, using bovine skins and those of smaller mammals (consequently the impurities content can be major). However, the exact composition of collagen-derived glues and their overall performance may be difficult to judge, as manufacturers tend to keep their recipes secret [**17**].
Collagen is insoluble in cold water and is transformed into soluble *gelatin* by denaturation, a process of critical importance for the performance of the

resulting glue. This is achieved by hot water extraction (hydrolytic breakdown). Pre-treatment (either acidic or basic) is necessary for most skin and bone collagen (e.g. rabbit skin and strong glues), but is not required for the extraction of fish glue from fish bladders, which contain less cross-linkage within the collagen. The process of denaturation is necessary for collagen to convert to gelatin, which can be used as a glue [**2, 17**].

Animal glues, such as rabbit skin glue/strong glue, show molecules of widely different molecular weights (20.000 to 250.000 g mol^{-1} [**13**]). By contrast, fish glues are reported to be of lower structural stability than those from animal sources, owing to a lower proportion of amino acids present (hydroxyproline and proline residues). Its molecular weight in comparison with those of the other animal glues is minor (average molecular weight, 30.000 to 60.000 g·mol^{-1} [**13**]). The molecular weight of a glue largely accounts for its properties. Generally, high molecular weight glues have greater cohesive strength in the gelled state, and greater toughness and flexibility in the fully dried state [**17**].

Rabbit skin glue/strong glue are generally much more strongly coloured (amber to brown) and less transparent than fish glues, because of their higher impurities content [**17**].

Animal glues, such as rabbit skin glue/strong glues, since time immemorial found wide application as strong adhesives for wood and fabric, and as adhesives in the preparation of grounds on easel paintings. The solution of animal glues has powerful adhesive properties on hardening. By contrast, fish glues do not form a gel and its films are sensitive to moisture and are not very tough. Fish glue was used in painting media, coatings and grounds, in the gilding of illuminated manuscripts, and in pastel fixatives, from the time of ancient Egypt to twenty-century France [**2, 4**].

Casein is a phosphoprotein and the major constituent of milk. It can easily be filtered after precipitation by acidifying and heating of the skimmed milk. Casein contains a mixture of proteins (*α-*, *β-* and *γ- caseins*) that are characterized by containing phosphorous (0.8%). It results to be almost insoluble in water at its isoelectric point, pH 4.6. So, in order to dissolve this binder, its pH must be adjusted to the range of 9-13 by adding a base (usually ammonia or sodium hydroxide), so as to form a caseinate salt [**2**].

When the water is removed by evaporation and diffusion into the substrate, the gel dries into a film that is hard and brittle [**18**]. The flexibility can be improved by adding some glycerol, glucose, agar-agar or dimethyl phthalate. Casein can be used on canvas panels, illustration boards, paper, wood and Masonite. Casein paint was used since ancient Egyptian times as a form of distemper paint and is still used today. It is often used also as a protective colloid in emulsions and as a carpenter's glue and completing frescoes [**19**].

Proteins are rather stable to oxidation and undergo little chemical change under normal conditions of temperature and humidity. Moisture is their enemy, not only because this can by itself effect slow hydrolysis of the peptide linkages and so reduce average molecular weight, but also because it permits fungi and bacteria to flourish. These secrete proteolytic enzymes which break the protein down so that the amino acids can be digested by the organism. Also, reactions of proteins with oxidizing lipids and carbohydrates can take place (e.g. Maillard reactions). The formation of oxalate salts on paint surfaces has also been observed, suggesting some kind of photooxidation. The reduced solubility of proteins in ancient samples is related to denaturation and cross-linking processes during ageing: cations may act as catalysers for the protein oxidation, thus enhancing this phenomenon [**4, 13**].

1.2 Pigments

For this study four blue pigments (azurite, Afghanistan ultramarine, synthetic ultramarine and phthalocyanine blue) and two white pigments (lead white and zinc white) have been selected on the basis of both their chemical and mineralogical properties and their widespread use in easel paintings throughout history. In this paragraph, a brief outline about their historical appearance and chemical/physical properties is reported. Possible disadvantages for their application are also described.

1.2.1 Azurite

Azurite pigment is made by grinding to a powder the natural mineral azurite which is a copper basic carbonate, $(CuCO_3)_2{\cdot}Cu(OH)_2$ [**20**].
It was used as paint pigment as early as the Fourth Dynasty in Egypt. On the other hand, in Europe, it was widespreadly used during all the Middle Ages and the Renaissance. The terminal date for the use of natural azurite in Europe is the eighteenth century, when "Prussian blue" was discovered and started to displace azurite from the European palette. Furthermore, there are evidences that it was the most important blue pigment used in the Far East [**20**].
Depending on the degree of fineness to which is ground, azurite shows a wide range of blues. This pigment is characterized by a good lightfast.
Despite being a carbonate, and hence sensitive to acids, azurite has a good permanence when used in oil and tempera binders. It can be also used in mural paintings, even if it often turns to green due to the alteration process into malachite ($CuCO_3{\cdot}Cu(OH)_2$), owing to its sensitivity to the humidity. This last is a weathering process which involves the replacement of the carbon dioxide

units with water, changing the hydroxide ratio of the carbonate: hydroxide ratio of azurite from 1:1 to the 1:2 ratio of malachite [**20**].

1.2.2 Afghanistan ultramarine blue

The natural ultramarine blue pigment is obtained by *lapis lazuli*, which is a complex rock mixture. Fundamentally, it is a mineralized limestone containing grains of the blue cubic mineral called lazurite, which is the essential constituent of this pigment. The mineral lazurite is a complex sodium calcium aluminium silicate sulphate, $(Na,Ca)_8[(S,Cl,SO_4,OH)_2/(Al_6Si_6O_{24})]$. Additionally, two isomorphous minerals of the sodium-aluminium-silicate group, hauynite and sodalite – the former containing a sulphate group and the latter, chloride - may also be present. Other silicate minerals, such as diopside, forsterite, muscovite, and wollastonite, are likely ingredients of lapis lazuli, while invariably present are calcite (crystalline calcium carbonate) and pyrites (iron sulphide) [**21**].

The early occurrence of natural ultramarine used as pigment is in sixth- and seventh-century wall paintings in cave temples in Afghanistan, not far from the most famous source of lapis lazuli. In Europe, the pigment found its extensive use in the fourteenth to mid-fifteenth centuries. The high cost of the imported raw material and the long process of extraction combined to make good-quality, made natural ultramarine pigment expensive as gold. With the introduction of the synthetic form, at beginning of the nineteenth century, natural ultramarine blue started to disappear from the artists' palette [**21**].

The natural ultramarine blue has high stability to light and its tinting strength, although not comparable with, for example, modern phthalocyanine blue, is quite good – much better than that of other early blue pigments such as azurite or smalt. It can be used in mural paintings and in aqueous media such as Arabic gum or egg tempera. Usually, in oil-media it is used mixed with a white pigment to produce a brilliant opaque blue [**21**].

Natural ultramarine is very readily decomposed and decoloured by the contact with acids, which attack it, forming hydrogen sulphide. Dilute mineral acids such as HCl, HNO_3 or H_2SO_4, rapidly destroy the blue colour, whereas. acetic acid (vinegar) attacks the pigment rather slowly [**21**].

1.2.3 Synthetic ultramarine blue

Artificial ultramarine is a synthetic pigment characterized by a similar composition to that of natural ultramarine, approximately ($Na_8Al_6Si_6O_{24}S_4$) [**21**].

In 1828 it was synthesized by J.B. Guimet. Considering the high price of natural ultramarine blue, it was rapidly adopted by the artists after its invention. Moreover, synthetic ultramarine blue appears to have been a common component of the impressionist and post-impressionist palette. Today, it is still used [**21**].
The chemical properties of artificial ultramarine blue are very similar to those observed for natural one, even if it is darker and less blue. Also, the synthetic pigment has the tendency to be attacked by acids, but more readily than its natural counterpart. Consequently, it results to be more sensitive to acetic acid (vinegar). It is used in tempera (but without vinegar) and largely used in oil, despite a high percentage of oil needed. In respect with natural ultramarine blue, in mural painting it cannot be used, owing to its fast tendency to decolour [**21**].

1.2.4 Phthalocyanine blue

Phthalocyanine blue is a synthetic blue pigment belonging to the group of phthalocyanine dyes. It is a complex of copper with phthalocyanine ($C_{32}H_{16}N_8Cu$/copper phthalocyanine, CuPc) [**22-23**].
The first time that phthalocyanine blue was synthesized was in the 1927, when two chemists produced a deep blue material while trying to make dicyanobenzene from copper cyanide and dibromobenzene [**24**].
During the twentieth century different copper phthalocyanine blue polymorphs have been synthetized. They correspond to the stabilized and unstabilized α-, β- and ε-polymorphic modifications. The Colour Index generic name used for the copper phthalocyanine blue pigments is Pigment Blue 15 (PB15). More specifically, PB15:0 is used for the unstabilised α-CuPc, PB15:1 for the non-crystallising α-CuPc, PB15:3 for the unstabilised β-CuPc, PB15:4 for the non-flocculating β-CuPc and PB15:6 for the unstabilised ε-CuPc. All these polymorphic modifications are used in artists' paints, even if the more common is represented by PB15:3 [**24-25**].
Phthalocyanine blue pigments are characterized by high lightfastness, hiding power, tinting strength and resistance to the effects of alkalies and acids. They are commonly used in oil and acrylic binders [**24**].

1.2.5 Lead white

Lead white pigment is an artificial basic lead carbonate, $(PbCO_3)_2 \cdot Pb(OH)_2$, which naturally occurs as the mineral Hydrocerrussite [**26-27**].
It was used since antiquity as early as 400 B.C. and it was the only white pigment used in European easel painting until the nineteenth century, when its

poisonous lead content restricted its manufacture and sale as an artist's pigment along the beginning of a more extended zinc oxide production. In the twentieth century it has been extensively replaced by titanium dioxide [**26-27**].
Lead white is characterized by a good hiding power and lightfast. It can be used in aqueous media such as egg yolk and whole egg (egg tempera), Arabic gum (watercolour), animal glue and in oil binders. Although a carbonate, and hence reactive to acids, lead white has a remarkable record for permanence.
Moreover, this pigment has the capability to decrease the drying time of drying oils and to give better polymerized film [**28**].
Nevertheless, several papers have demonstrated that lead white in oil-paintings can lead to formation of lead-carboxylates, promoting the triglyceride hydrolysis process [**29-33**].
Furthermore, traces of hydrogen sulphide, present in the air or into hydrogen sulphide pigments, cause the blackening of its surface. This is a consequence of the chemical reaction of lead carbonate to black lead sulphide [**26-27**].

1.2.6 Zinc White

Zinc white pigment is a synthetic white which chemically corresponds to zinc(II)-oxide (ZnO) [**34**].
Despite, zinc oxide in the form of a fine white powder has been known since antiquity, its use as pigment appears from the end of the eighteenth century. Nevertheless, zinc white was not used extensively as an artist's pigment prior to the second quarter of the nineteenth century when more economical procedures for its production were discovered [**34**]. By 1850 zinc white was produced on an industrial scale both in Europe and in the United States. Thus, it is only in relatively recent history that we should expect to find zinc white used significatively as a pigment for commercial paints and artists' colours. Today, it continues to be available [**34**].
Zinc white produces a cool clear white and the paints prepared with it, tend to preserve their original whiteness during ageing, not only in watercolours, but also in oil paints. It has the advantages of being non-toxic, of not darkening in the presence of sulphur gases or hydrogen sulphide pigments and of havening a less tendency to yellowing. Zinc white is compatible with all inorganic pigments and it shows excellent ultraviolet-absorbing qualities which are used for light-scattering purposes [**35**].
It is characterized by a minor hiding power in oil than lead white. Moreover, zinc white is known to be hygroscopic, meaning that it can absorb water when exposed to air and may become "sticky" [**36**].
Researchers, over in the last few years, have found that zinc white can rapidly form a hard and brittle oil-film. Finally, also zinc white pigment tends to react

with drying oils, forming metal carboxylates, since it has a high reactivity with certain fatty acids, such as stearic acid [**37-39**].

1.3 Preparation of paint models

Four representative typologies of drying oils were chosen for this study: linseed oil, walnut oil, poppy-seed oil, and stand-oil (originated from linseed oil). All these drying oils were obtained from different manufacturers. The list of oils, providers and the associated names is presented in **Table 6**.
As regards proteinaceous binders, seven types of samples were selected (rabbit skin glue, strong glue, fish glue, egg white, egg yolk, whole egg and casein). Regarding vegetable gums, Arabic and Tragacanth gums were chosen. All these binding media were provided by Zecchi (Florence, Italy), except for hen eggs that were bought in a local market.
Each drying oil was individually applied as film on four microscope glass slides as supplied and left to dry on a shelf. By contrast, proteinaceous and polysaccharide binding media were prepared according to recipes from original treatises and artists' accounts [**40**]. Rabbit skin glue, strong glue and fish glue were swollen and dissolved in a warm water bath in demineralized water to give a solution of 5% (w/w). Egg white was beaten to form stiff peaks and left for 24 h; foam was skimmed and removed and a solution of 50% (w/w) clear egg white in demineralized water was prepared. Egg yolk was extracted from egg by piercing the yolk and allowing the liquid to drip from the encasing film; the yolk was diluted in demineralized water to give a 50% (w/w) emulsion. Whole egg was prepared by mixing one part of egg white solution and two parts on egg yolk emulsion along with one part of vinegar. Casein was swollen in water for 24 h to give a 1.5% (w/w) solution; dilute ammonia solution was added until the swollen gel dissolved and excess ammonia was left to evaporate. Arabic gum was dissolved in warm demineralized water with a ratio of 1 to 2, heating in a double-boiler; the mixture was left to soak 48 h for a full absorption and finally, the obtained solution was strained through two layers of cheesecloth into a clean jar. Tragacanth gum, with a ratio of 1 to 30, was added to demineralized water and left to swell in a mucilaginous suspension. Then, this suspension was strain in a similar way to that previously described for Arabic gum.
All these organic binders were individually applied as film on four microscope glass slides and left to dry on a shelf (T: ~ 20°C; RH: ~50-55%; light: solar light through a window). Hence, a total of sixty-eight model samples for neat binders was prepared.
The list of neat binding media together with their denomination is reported in **Table 6**.

Going to focus on the oil-paint models, azurite, Afghanistan ultramarine, synthetic ultramarine and phthalocyanine blue pigments were purchased from Zecchi (Florence, Italy), while the rest of pigments were supplied by Sigma-Aldrich (Milano, Italy).

Table 6 List of analysed neat binding media, with their manufacturer and identification symbols.

Neat binder	Producer/Manufacturer	Symbol
Drying oils		
Linseed Oil	Zecchi	**LOZ**
Linseed Oil	Maimeri	**LOM**
Linseed Oil	Ferrario	**LOF**
Poppy-seed Oil	Zecchi	**POZ**
Poppy-seed Oil	Talens	**POT**
Walnut Oil	Zecchi	**WOZ**
Walnut Oil	Ferrario	**WOF**
Stand-Oil	Zecchi	**SOLZ**
Proteinaceous binders		
Rabbit Skin Glue	Zecchi	**RG**
Strong Glue	Zecchi	**SG**
Fish Glue	Zecchi	**FG**
Egg White	Local market	**EW**
Egg Yolk	Local market	**EY**
Whole Egg	Local market	**WE**
Casein	Zecchi	**C**
Polysaccharide media		
Arabic Gum	Zecchi	**AG**
Tragacanth Gum	Zecchi	**TG**

Twelve oil-paint models were prepared according to the recipes reported in original treaties [**40**], by mixing these pigments with linseed oil (L) and poppy-seed oil (P) from Zecchi (Florence, Italy), on the smooth surface of a panel glass. The list of samples together with their denomination is reported in **Table 7**. The powdered pigments were initially crushed in an agate mortar in order to obtain a homogenously-fine particle grain size without lumps. The exact concentration of the pigment with respect to drying oil was not determined *a priori*; instead for each case, a mixture of similar consistency was used to prepare the paint models, so that they could be applied with a fine brush as a single thick layer onto microscope glass slides and left to dry on a bench top (**Fig. 2**). Four sets of oil-paint models were prepared, obtaining a total of forty-eight samples. The paint films had rough non-homogeneous surfaces as would be expected in real samples

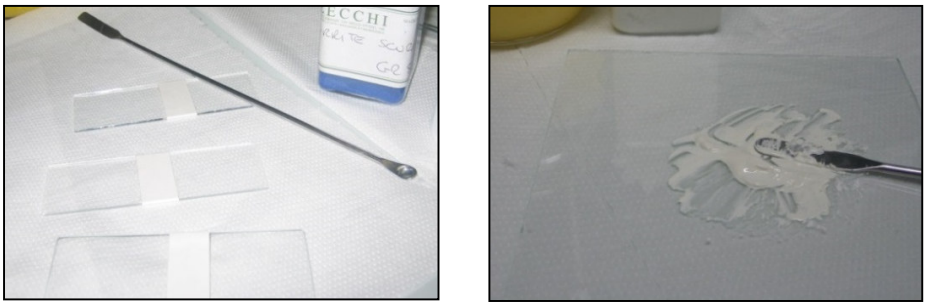

Fig. 2 Preparation of oil-model paints.

Table 7 Oil mixtures and their corresponding identification symbols.

Pigment	Producer/ Manufacturer	Drying Oil	Symbol
Lead White (**LW**), $2PbCO_3*Pb(OH)_2$	Sigma-Aldrich	+ linseed oil(**L**)	**LWL**
		+ poppy-seed oil (**P**)	**LWP**
Zinc White (**ZW**), ZnO	Sigma-Aldrich	+ linseed oil (**L**)	**ZWL**
		+ poppy-seed oil (**P**)	**ZWP**
Phthalocyanine Blue (**PB**), $C_{32}H_{16}N_8Cu$/copper phthalocyanine	Zecchi	+ linseed oil (**L**)	**PBL**
		+ poppy-seed oil (**P**)	**PBP**
Azurite (**A**), $Cu_3(CO_3)_2(OH)_2$	Zecchi	+ linseed oil (**L**)	**AL**
		+ poppy-seed oil (**P**)	**AP**
Synthetic Ultramarine Blue (**SU**), $Na_{8\text{-}10}Al_6Si_6O_{24}S_{2\text{-}4}$	Zecchi	+ linseed oil (**L**)	**SUL**
		+ poppy-seed oil (**P**)	**SUP**
Afghanistan Ultramarine Blue (**AU**), $(Na,Ca)_8[(S,Cl,SO_4,OH)_2/(Al_6Si_6O_{24})]$	Zecchi	+ linseed oil (**L**)	**AUL**
		+ poppy-seed oil (**P**)	**AUP**

1.4 SPECTROSCOPIC TECHNIQUES: Fourier Transform Near Infrared (FT-NIR) and micro-Raman spectroscopy

1.4.1 Basic principles of vibrational spectroscopy

In order to describe limits and advantages of the different vibrational spectroscopies (Raman, Mid-IR and NIR), a comparative overview is given in this chapter.

Although the three techniques are very different in several aspects, their basic physical origin is the same: signals in the Mid-IR, NIR and Raman spectra of chemical compounds can be observed as a consequence of molecular vibrations. However, while Raman spectroscopy is a scattering technique, Mid-IR and NIR spectroscopies are based on the absorption of radiation (**Fig. 3**) [**41**].

1.4.1.1 The absorption techniques of Mid-IR and NIR spectroscopy

1.4.1.1.1 The harmonic oscillator

In order to treat the methods based on the phenomenon of absorption, a harmonic diatomic oscillator model where the vibrating masses m_1 and m_2 (**Fig. 4**) lead to changes of the internuclear distance (<10%) will be considered. In this case, Hooke's law holds and the potential energy, V, can be represented by [**42**]:

$$V = \frac{1}{2}k(r - r_e)^2 = \frac{1}{2}kq^2$$

where k is the force constant of the bond, r is the internuclear distance during the vibration, r_e is the equilibrium internuclear distance, and $q=(r-r_e)$ is the displacement coordinate. The potential energy curve of such oscillator is parabolic in shape and symmetrical about the equilibrium bond length r_e. This model leads to the vibrational frequency ν_0:

$$\nu_0 = \frac{1}{2\pi}\sqrt{\frac{k}{m}}$$

where the reduced mass m is given by:

$$m = \frac{m_1 m_2}{m_1 + m_2}$$

From the previous equations, it becomes obvious that the vibrational frequencies are very sensitive to the structure of the investigated compound, and this is the basis for the widespread application of infrared spectroscopy for structure elucidation.
A quantum mechanical treatment by the Shrödinger equation shows that the vibrational energy has only certain discrete values that are given by [**42**]:

$$E_n = h\nu_0\left(n + \frac{1}{2}\right)$$

where h is Planck's constant, ν_0 is the vibrational frequency defined above and n is the vibrational quantum number that can only have integer values 0, 1, 2, 3,… and so on.

If the energy levels are expressed in wavenumber units (cm^{-1}), they are given by [**43**]:

$$G_n = \frac{E_n}{hc} = \bar{\nu}_0 \left(n + \frac{1}{2}\right)$$

where c is the speed of light and $\bar{\nu}_0$ is the wavenumber corresponding to the frequency

$$\bar{\nu}_0 = \frac{1}{2\pi c}\sqrt{\frac{k}{m}}$$

Interaction of infrared radiation with a vibrating molecule, however, is only possible if the electric vector of the radiation oscillates with the same frequency as the molecular dipole moment, μ. Thus, a vibration is infrared active only if the molecular dipole moment is modulated by the vibration [**44**] and

$$\frac{\delta\mu}{\delta q} \neq 0$$

where q is the vibrational coordinate. The requirement of a dipole moment change during the vibration makes Mid-IR spectroscopy specifically sensitive to polar functionalities (**Fig. 4**).
For the harmonic oscillator model the energy levels are equidistant and transitions are only allowed between neighbouring energy levels with

$$\Delta n = \pm 1$$

According to the Boltzmann distribution, most molecules at room temperature populate the ground level ***n=0***, and consequently the so-called fundamental vibrational transitions, i.e. allowed transitions between ***n=0*** and ***n=1*** dominate the vibrational absorption spectrum (**Fig. 3**). The potential of Mid-IR spectroscopy as a structure elucidation tool is based on the occurrence of the majority of absorption bands of chemical compounds corresponding to fundamental vibrations in this wavenumber region (4000 to 200 cm^{-1}).

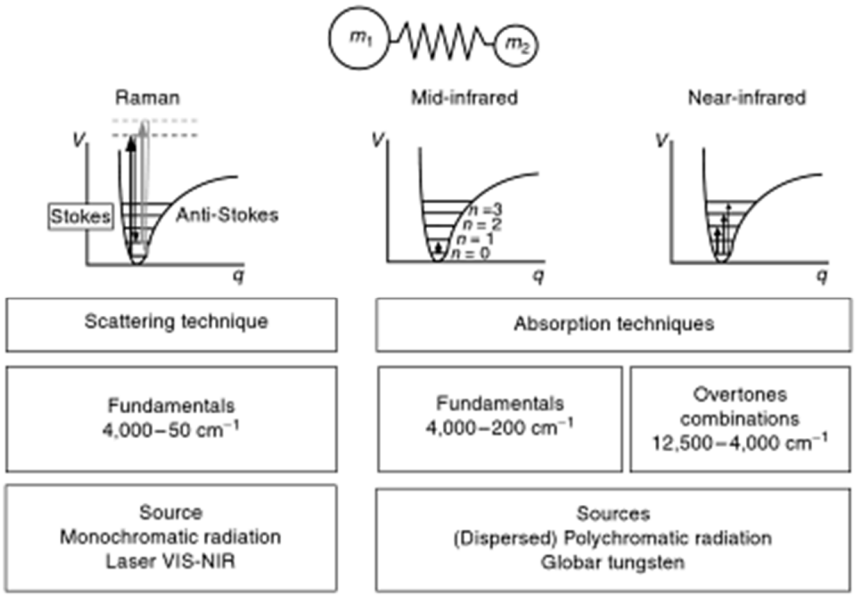

Fig. 3 The principles of Raman, Mid-IR and NIR spectroscopies [**41**].

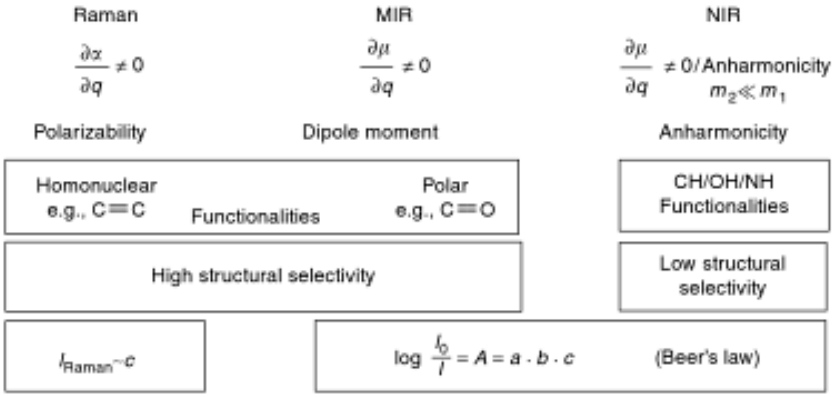

Fig. 4 Specific characteristics of Raman, Mid-IR and NIR spectroscopies (***I*₀**, incident radiation; ***I***, transmitted radiation; ***A***, absorbance; ***a***, absorptivity; ***b***, sample thickness; ***c***, sample concentration) [**41**].

1.4.1.1.2 The anharmonic oscillator

However, the model of the harmonic oscillator cannot be retained at larger amplitudes of vibration owing to:

- Repulsive forces between the vibrating atoms;
- The possibility of dissociation when the vibrating bond is strongly extended.

Accordingly, the energy levels predicted for an anharmonic oscillator are modified according to the following approximate expression [**42-43, 45**]:

$$G_n = \frac{E_n}{hc} = \bar{\nu}_0\left(n + \frac{1}{2}\right) - \chi\bar{\nu}_0\left(n + \frac{1}{2}\right)^2$$

where χ is the anharmonicity constant.
Unlike the harmonic oscillator, energy levels are not equidistant and the strict selection rule is expanded to include transitions over more than one energy level (even if still fundamental transitions carry most of the intensity in the vibrational spectrum). Furthermore, the potential energy curve can be represented by an asymmetric Morse function [**42-44**], as shown in **Fig. 3**. Generally, a nonlinear molecule contains N atoms has $3N-6$ vibrational degrees of freedom, while a linear has only $3N-5$ [**43, 46**]. The number of vibrational degrees of freedom represents the number of fundamental vibrational frequencies of the molecule or the number of different "normal modes" of vibration. For a given molecule, a normal mode of vibration corresponds to internal atomic motions in which all atoms move in phase with the same frequency, but with different amplitudes. Fundamental transitions are allowed and, additionally other transitions corresponding to

$$\Delta n = \pm 2, \pm 3, \ldots$$

are now also allowed and are called first, second, and so on, overtones.
Apart from overtones, combinations of different vibrational transitions (sum and difference "tone") may also be observed. However, the probability of these transitions decreases significantly with their order, and generally the absorption bands corresponding to overtone or combination vibrations have much lower intensity than their fundamental analogs. Contrary to the Mid-IR, the NIR region contains almost exclusively absorption bands that can be assigned to overtone and combination vibrations. Unfortunately, the overlap of these overtone and combination bands strongly decreases the specificity of NIR spectroscopy (especially for interpretation purposes) and that was one of the main reasons for the little attention given to this technique by spectroscopists for a long time.
However, the availability of chemometric evaluation procedures for qualitative discrimination and quantitative determination has eventually led to the breakthrough of the NIR technique [**41**].

1.4.1.1.3 The calculation of overtones and anharmonicities

The wavenumber position of the fundamental vibration or an overtone (***n=2, 3, ...***) of the anharmonic oscillator can be given by [**45**]:

$$\bar{\nu}_n = G_n - G_{0=}\,\bar{\nu}_0 n - \chi\bar{\nu}_0 n\,(n+1)$$

is not directly accessible and from the absorption spectra only the wavenumbers $\bar{\nu}_1, \bar{\nu}_2, \ldots$ may be obtained. Therefore, we substitute $\bar{\nu}_0$ by:

$$\bar{\nu}_0 = \frac{\bar{\nu}_1}{1-2\chi}$$

and can derive

$$\bar{\nu}_n = \frac{\bar{\nu}_1 n - \bar{\nu}_1 \chi n(n+1)}{1-2\chi}$$

for ***n=2, 3, 4, ...***

Thus, if the wavenumber position $\bar{\nu}_1$ of the fundamental vibration and the anharmonicity constant χ are known, the wavenumber positions of the overtones can be calculated. Alternatively, χ can be calculated if, for example, $\bar{\nu}_1$ and $\bar{\nu}_2$ are known.

The intensities of overtone absorption bands depend on the anharmonicity, and it has been shown [**45**] that vibrations with low anharmonicity constants also have low overtone intensities. ***X-H*** stretching vibrations, for example, have the largest anharmonicity constants and therefore dominate the spectra in the NIR region. **Table 8** summarizes the anharmonicity constants of the vibrations of some characteristic functionalities.

Table 8 Anharmonicity constant χ for selected vibrations [**45**].

χν(CH)	~1.9 x 10^{-2}
χν(CD)	~1.5 x 10^{-2}
χν(CF)	~4 x 10^{-3}
χν(CCl)	~6 x 10^{-3}
χν(C=O)	~6.5 x 10^{-3}

1.4.1.1.4 Fermi Resonance, Darling-Dennison Resonance and the Local Mode Concept

Apart from overtone and combination vibrations, some other characteristic effects may contribute to the appearance of signals in a vibrational spectrum [**43**].

A resonance that leads to a perturbation of the energy levels can occur if two vibrational levels belong to the same symmetry species and have similar energy. Such an accidental degeneracy of, for example, an overtone or a combination band that has the same symmetry and nearly the same frequency as that of a fundamental vibration is called Fermi resonance [**41**]. This resonance leads to two relatively strong absorption bands that are observed at somewhat higher and lower frequencies than the expected unperturbed frequency positions. When this perturbation takes place, the weaker absorption in the spectrum "steals" intensity from the stronger one. Typical examples of Fermi resonance have been analysed for the Raman as well for the NIR spectra of CO_2, [**43**], but this phenomenon has also been reported for numerous other compounds [**43-44**].

A resonance that is of importance in the NIR spectra of water has been discussed by Darling and Dennison [**41**], but can also occur in other molecules containing symmetrically equivalent X-H bonds. Thus, of the three normal modes of water – $\boldsymbol{\nu_2}$ bending vibration (1595 cm^{-1}), $\boldsymbol{\nu_3}$ anti-symmetric stretching (3756 cm^{-1}), and $\boldsymbol{\nu_1}$ symmetric stretching (3657 cm^{-1}) – the two stretching vibrations absorb at similar wavenumber positions, but belong to different symmetry species and therefore cannot interact directly. However, energy levels of these vibrations associated with specific vibrational quantum numbers $\boldsymbol{n_1}$, $\boldsymbol{n_2}$ and $\boldsymbol{n_3}$, [**43**] can interact if they belong to identical symmetry species and have similar energies. These interactions then lead to several pairs of NIR absorption bands with appreciable intensities.

Finally, a few comments shall be made on the concept of local modes as compared to normal modes [**43**]. The main idea of the local mode model is to treat a molecule as if it was made up of a set of equivalent diatomic oscillators, and the reason for the local mode behaviour at high energy (> 8000 cm^{-1}) may be understood qualitatively as follows. As the stretching vibrations are excited to high energy levels, the anharmonicity term $\boldsymbol{\chi\bar{\nu}_0}$ tends, in certain cases, to overrule the effect of interbond coupling and the vibrations become uncoupled vibrations and occur as "local modes".

The absorption bands in the spectrum can thus be interpreted as if they originated from an anharmonic diatomic molecule. This is the reason why NIR spectra are often said to become simpler at higher energy. Experimentally, it is found that the inversion from normal to local mode character occurs for high energy transitions corresponding to $\boldsymbol{\Delta n \geq 3}$.

1.4.1.2 The scattering technique of Raman spectroscopy

Scanning Mid-IR and NIR spectrometers operate with a polychromatic source for the individual frequency range (**Fig. 3**) from which the sample absorbs

specific frequencies, corresponding to its molecular vibrational transitions (mostly fundamental vibrations for the Mid-IR and overtone or combination vibrations for the NIR). In Raman spectrometers the sample is irradiated with monochromatic laser light whose frequency may vary from the Vis to the NIR region. This radiation excites the molecule to a virtual energy state that is far above the vibrational energy levels of this anharmonic oscillator for a Vis-laser and in the range of high overtones for an NIR-laser excitation (**Fig. 3** and **Fig. 5**). From the virtual (non-stationary) energy level, the molecule may return to the ground state by elastic scattering, thereby emitting light (the so-called Rayleigh line) that has the same frequency as the excitation line and does not contain information in terms of the molecular vibration (this case is not shown in **Fig. 3** and **Fig. 5**). If it returns to the first excited vibrational level by inelastic scattering, the emitted Raman line (called Stokes line) (**Fig. 3**) has a lower frequency (wavenumber), and the difference to the excitation line corresponds to the energy of the fundamental vibrational transition. In the case of anti-Stokes line, where the starting level is the first excited vibrational state and the molecule returns to the ground state by inelastic scattering (**Fig. 3**), the emitted Raman line is of higher frequency (here too, the frequency difference to the excitation line corresponds to the fundamental vibrational transition). Anti-Stokes lines have lower intensity compared to the corresponding Stokes lines, due to the lower population of the excited states (law of Boltzmann). Commonly, the Stokes lines are used for practical Raman spectroscopy.
One of the limiting factors for the application of the Raman technique, however, becomes evident by comparing the intensity of the laser source and scattered radiation [**44, 47-48**].

$$I_{Raman} \approx 10^{-4}\, I_{Rayleigh} \approx 10^{-8}\, I_{source}$$

From these figures it can readily be derived that a sensitive detection of the Raman line alongside an efficient elimination of the Rayleigh line are experimental prerequisites for the successful application of Raman spectroscopy. As shown in **Fig. 3**, Raman and Mid-IR spectroscopy cover approximately the same wavenumber region in terms of vibrational spectrum, with the Raman technique extending further into the low frequency region (down to about 50 cm^{-1}) owing to the different instrumental limitations (primarily because of the Mid-IR detector cut-off in the low frequency spectral range). In some cases, this additional frequency range is valuable, since it often contains absorptions of lattice modes of molecular crystals that may be very characteristic for a specific polymorph.

An important relation for the comparison of Vis vs. NIR-Raman spectroscopy, is the dependence of the scattered Raman intensity I_{Raman} on the fourth power of the excitation frequency ν_{exc}

$$I_{Raman} \approx \nu^4_{exc}$$

The impact of this law with reference to the application of either Vis- or NIR-Raman spectroscopy for an individual problem will be outlined below.
A similar condition as for Mid-IR spectroscopy holds for the Raman effect: a molecular vibration can only be observed in the Raman spectrum if there is a modulation of the molecular polarizability α by the vibrational motion [**44, 47-48**]:

$$\frac{\delta\alpha}{\delta q} \neq 0$$

Hence, Raman spectroscopy is primarily sensitive to vibrations of homonuclear bonds (**Fig. 4**). From the selection rules, it becomes obvious that Mid-IR and Raman spectroscopy are complementary techniques and the application of both methods can be very helpful for the efficient elucidation of a molecular structure.

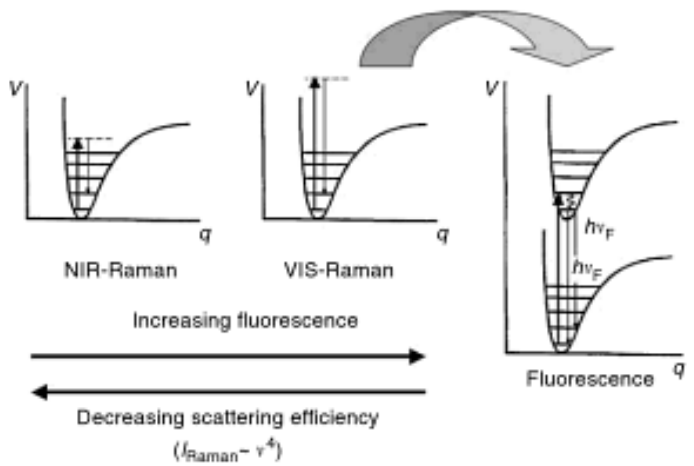

Fig. 5 Fluorescence and scattering efficiency in NIR- and Vis-Raman spectroscopy [**41**].

In Raman spectroscopy two different excitations can be used:
1) excitation by a Vis-laser (in the range from 400 to 800 nm) combined with monochromatization of the scattered radiation by a diffraction grating and

simultaneous detection of the dispersed radiation by extremely sensitive detectors.
2) NIR-laser excitation and measurement in a Fourier-Transform (FT)-spectrometer.
A possible limiting factor for Raman scattering experiments is given by the possible excitation of electronic transitions by the excitation radiation. If this happens then light emission from molecules in the electronic excited state (fluorescence) can superimpose to Raman scattering. Usually fluorescence (if present) is much stronger than Raman scattering and, if it is the case, the Raman spectroscopy experiment can be very difficult.
In **Fig. 5** the trends of the main limiting factors – fluorescence and low scattering efficiency – have been outlined with reference to the two excitation mechanisms. Thus, both alternatives establish only compromises and the choice of the applied technique depends on the individual problem.
If a molecule is irradiated with visible radiation, it may be excited to an energy level of the next higher electronic state. Return to the ground state or an excited vibrational level of the original electronic state can easily proceed via fluorescence as shown in **Fig. 5**. Thus, for a large proportion of samples, irradiation with visible light causes strong fluorescence by additives or impurities (or by the sample itself), which will superimpose and in many cases completely cover the Raman spectrum of the sample. The use of NIR-laser excitation provides a number of advantages on a Raman system. Both fluorescence and self-absorption are very much reduced in the Raman signal, and, owing to the lower energy of the excitation radiation, thermal degradation is also less of a problem. However, these advantages are partly neutralized by the disadvantages of using a low-frequency laser as the source (small scattering efficiency) (**Fig. 5**). Thus, a shift of the excitation line from the Vis region (e.g., Ar^+-ion laser, 488 nm) to the NIR region (e.g., Nd-YAG laser, 1064 nm) reduces the scattering intensity. However, NIR-Raman spectroscopy is performed on FT-spectrometers, and the sensitivity loss can be compensated by accumulation of multiple scans. As a valuable compromise to suppress fluorescence and at the same time retain an acceptable scattering efficiency, excitation with a diode laser at 785 nm is increasingly used.

1.4.1.3 A comparison of the qualitative and quantitative aspects of Raman, Mid-IR and NIR spectroscopy

The different excitation conditions of Raman, Mid-IR and NIR spectroscopy (**Fig. 4**) lead to extremely different signal intensities of these techniques for the same vibration of a specific molecular functionality.

NIR spectroscopy covers the wavenumber range adjacent to the Mid-IR and extends up to the Vis region (4000 to 12500 cm^{-1}). NIR absorptions are based on overtone and combination vibrations of the investigated molecule, and owing to their lower transition probabilities, the intensities usually decrease by a factor of 10 to 100 for each step from the fundamental to the next overtone (**Fig. 6**) [**43, 45**]. Thus, the intensities of absorption bands successively decrease in the direction from the Mid-IR to the visible region, thereby allowing an adjustment of the sample thickness (from millimetres up to centimetres), depending on the rank of the overtone.
This is a characteristic difference to Mid-IR and Raman spectra, where the signal intensities of the fundamental vibrations vary irregularly over the whole frequency range and depend exclusively on the excitation conditions of the individual molecular vibrations. As pointed out above, these different excitation conditions lead to the complementarity of the Raman and Mid-IR technique as structural elucidation tools, because Raman spectroscopy predominately focuses on vibrations of homonuclear functionalities (e.g., C=C, C-C, S-S), whereas the most intense Mid-IR absorptions can be traced back to polar groups (e.g., C-F, Si-O, C=O and C-O-C).

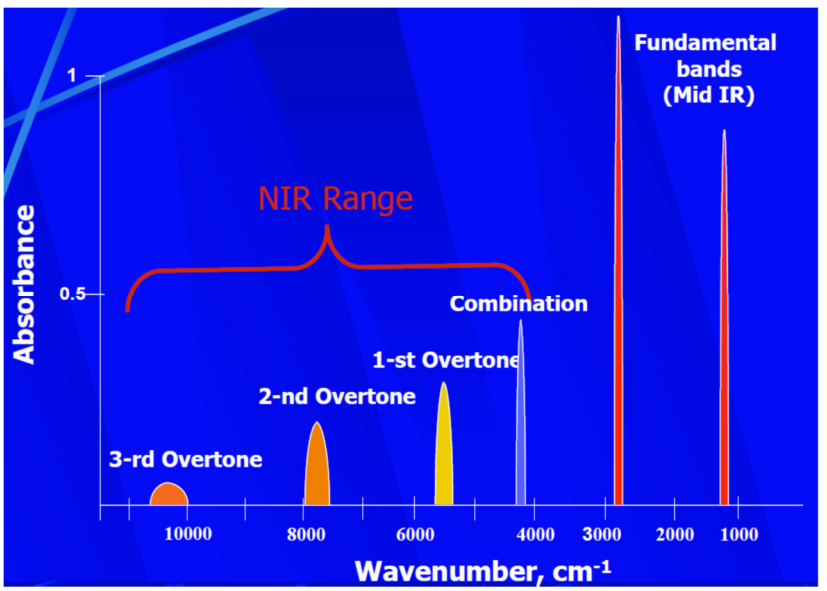

Fig. 6 Combination and overtone regions in a NIR range with reported the relative intensities for corresponding absorptions bands in comparison with those of Mid-IR spectral region [**49**].

NIR spectroscopy, on the other hand, requires – in addition to the dipole moment change – a large mechanical anharmonicity of the vibrating atoms (**Fig. 4**) [**43, 45**]. This becomes evident from the analysis of the NIR spectra of a large variety of compounds, where the overtone and combination bands of CH, OH

and NH functionalities dominate the spectrum, whereas the corresponding overtones of the most intense Mid-IR fundamental absorptions are rarely represented. One reason for this phenomenon is certainly the fact that most of the X-H fundamentals absorb at wavenumber >2000 cm^{-1} so that their first overtones already appear in the NIR frequency range.

The polar groups leading to the most intense fundamental absorptions in the Mid-IR (e.g., ν(C-F), ν(C=O), ν(Si-O)) on the other hand absorb at wavenumber <2000 cm^{-1}, so that their first (and sometimes higher) overtones still occur in the Mid-IR region. Owing to the intensity loss for each step from the fundamental to the next overtone, the absorption intensities of these vibrations have become negligible by the time they should occur in the NIR range. The best example in this respect is the ν(C-F) absorption band at about 1200 cm^{-1} (e.g., of poly[tetrafluorethylene]), which is one of the most intense absorption bands in the Mid-IR owing to the large dipole moment of the C-F bond.

However, because of the small anharmonicity constant (**Table 1**), the first and the second overtones that are expected at about 2400 and 3600 cm^{-1}, respectively, have already strongly reduced intensity, and no further overtone vibrations of this functionality can be observed in the NIR region. In fact, poly(tetrafluorethylene) is used as a nonadsorbing standard material for the NIR region.

Anharmonicity plays also an important role in the evaluation of the fundamental and overtone vibration intensities of functionalities with a high hydrogen-bonding tendency such as ν(O-H) and ν(N-H). **Fig. 7a** shows the Mid-IR spectrum of the ν(N-H) region of a polyamide 11 (PA11) film of about 30 μm thickness at room temperature. Under these conditions, the majority of the N-H groups (~99%) occur in the associated, hydrogen-bonded form. This is directly reflected in the very low intensity of the $\nu(N\text{-}H)_{free}$ absorption at 3450 cm^{-1} relative to the dominating $\nu(N\text{-}H)_{asset}$ absorption at 3300 cm^{-1}.

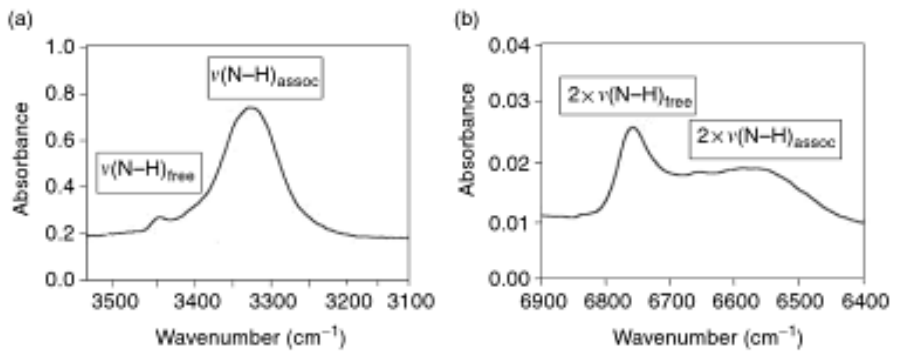

Fig. 7 a) Mid-IR spectrum of polyamide 11 film in ν(N-H) fundamental absorption region and b) NIR spectrum in 2 x ν(N-H) overtone absorption region [**41**].

If the same polymer is investigated at room temperature with a film thickness of about 750 µm in the NIR region, the spectrum shown in **Fig. 7b** is obtained. Here, the intensity ratio of the 2 x ν(N-H)$_{free}$ (6760 cm^{-1}) relative to the broad 2 x ν(N-H)$_{assoc}$ absorption at about 6510 cm^{-1} is reversed, although the state of order of the polymeric material has not been changed. The explanation for this effect is that, owing to its larger anharmonicity, the intensity of the ν(N-H)$_{free}$ overtone absorption is strongly enhanced relative to the corresponding overtone vibration of the associated N-H groups [**41**]. Hydrogen bonding is equivalent to increasing the mass of the vibrating H-atom, thereby leading to a reduction of mechanical anharmonicity of the ν(N-H)$_{assoc}$ vibration and a decrease of its absorption intensity.

The superposition of many different overtone and combination bands in the NIR region causes a very low structural selectivity for NIR spectra compared to the Raman and Mid-IR analogs where many fundamentals can usually be observed in isolated positions. Nevertheless, NIR spectra should also be assigned in as much detail as possible with reference to their molecular origin: this allows a more effective application for research purposes and combination with chemometric evaluation procedures. For the assignment of overtones and combination bands in the NIR to their corresponding fundamentals in the Mid-IR, it is recommended that the wavenumber notation be used instead of the widespread wavelength (nm or µm) scale [**43, 45**].

As far as the quantitative evaluation of vibrational spectra, Mid-IR and NIR spectroscopy follow Beer's law, whereas the Raman intensity $\boldsymbol{I_{Raman}}$ is usually directly proportional to the concentration of the active compounds (**Fig. 4**).

An important issue for the implementation of a technique as an industrial routine tool is the sample preparation required for this technique. In this respect, Raman and NIR spectroscopy have considerable advantages over Mid-IR spectroscopy. The formers experiments can be performed without a specific sample preparation while the last one usually requires individual sample preparation steps before data acquisition. Only the technique of attenuated total reflection (ATR) circumvents time-consuming sampling procedures for Mid-IR spectroscopy [**41**].

1.4.2 Experimental and instrumentation setup

1.4.2.1 FT-NIR spectroscopy

Diffuse reflectance is one of the various possibilities for employing the NIR spectral region (**Fig. 8**).

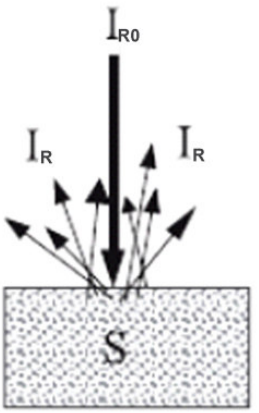

Fig. 8 A schematic representation of diffuse reflectance mode of measurement used in NIR reflectance spectroscopy (I_{R0} is the incident radiation, while I_R is the scattered radiation from the sample) [**50**].

The reflectance ***R*** is obtained by:

$$R=I_R/I_{R0}$$

where $\mathbf{I_R}$ is the intensity of radiation reflected by the sample and I_{R0} the same quantity reflected by a non-absorbing material over the whole spectral range of measurement (**Fig. 8**). The measurement of I_{R0} requires the collection of the scattered radiation by a perfectly reflecting reference (100% in all wavelengths).

A rigorous treatment of the signal obtained in diffuse reflectance measurement of an opaque and solid material was established by Kubelka-Munk theory [**51**] and its modifications [**52**]. This mathematical treatment replaces Beer's law, which is valid only for transparent homogenous materials.

The basic assumptions of the Kubelka-Munk theory are that radiation that interacts with matter could be scattered or absorbed. When a layer of the absorbing and scattering material is so thick that no radiation penetrates through the layer, the relationship given by Kubelka-Munk (K-M) for each wavelength is the following (*K-M function* $\boldsymbol{F(R_\infty)}$).

$$\boldsymbol{F(R_\infty)=\frac{(1-R_\infty)^2}{2R_\infty}=\frac{K}{S}} \text{ and } \boldsymbol{R_\infty=1+\left(\frac{K}{S}\right)-\sqrt{\frac{K^2}{S^2}-1}}$$

where $\boldsymbol{R_\infty}$ is the reflectance for a material with infinite thickness, $\boldsymbol{K}$ is the absorption coefficient and $\boldsymbol{S}$ is the scattering coefficient.

The simple Kubelka-Munk theory can be applied to materials that are completely opaque; when a pigmented material is transparent, other forms of the Kubelka-Munk theory must be used that take into account the colour of the background. In the aforementioned equation it is possible to see that changing just one of the coefficients causes the reflectance of the sample to increase or decrease (**Fig. 8**), so if $\boldsymbol{K}$ increases, $\boldsymbol{R}$ decreases and vice versa, if $\boldsymbol{S}$ increases, $\boldsymbol{R}$ increases as well [**53-54**].
In 1962 Duncan [**55**] demonstrated that the absorption-scattering ratio of a system made as a mixture of pigments $\boldsymbol{m}$ is given by the additivity of the individual contributions of absorption and scattering from each pigment present at each wavelength [**56**] (*K-M function for a mixture* $\boldsymbol{F(R_\infty)_m}$):

$$\boldsymbol{F(R_\infty)_m = \left[\frac{(1-R_\infty)^2}{2R_\infty}\right]_m = \left(\frac{K}{S}\right)_m = \frac{C_1K_1 + C_2K_2 + \cdots + C_nK_n}{C_1S_1 + C_2S_2 + \cdots + C_nS_n}}$$

$\boldsymbol{C}$ indicates the relative fraction concentration for each pigment ($\boldsymbol{n}$), the subscript number indicates the single pigment present in the mixture and $\boldsymbol{K}$ and $\boldsymbol{S}$ are the coefficients for unit concentration. This formula is widely used in pigment and varnish industrial manufacturing in order to predict the colour of a mixture. This means that the reflectance spectrum measured on a painting layer depends on the number of pigments and their concentration in the point analysed.

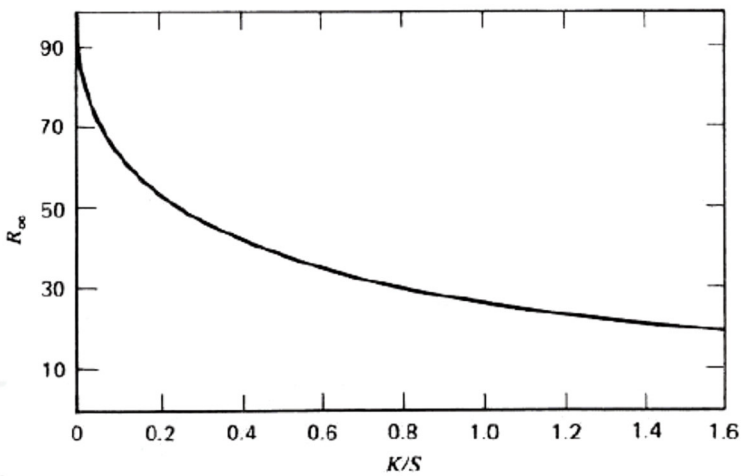

Fig. 9 Theoretical plot showing inverse relationship between reflectivity R and the ratio K/S [**54**].

Despite all this, Kubelka-Munk equation is rarely used and is substituted by the more practical, although non-linear, equation such as the following [**50**].

$$F(C) = \mathbf{Log}\frac{1}{R}$$

The relationship does not depart from Kubelka-Munk prediction and, for small changes in the reflectance R, can be assumed to present a linear behaviour with the concentration C of the analyte.

A NIR spectrophotometer can be assembled with optical components used for UV-Visible instruments. This fact imparts a lower cost to the NIR instrument [**50**].

Spectrophotometers based on the use of interferometers and Fourier transform (FT-NIR spectrometers) to recover the intensities of individual wavelengths in the NIR region are, undoubtedly, the instruments combining most of the best characteristics in terms of wavelength precision and accuracy, high signal to-noise ratio and scan speed [**50**].

For this study, reflection FT-NIR was carried out with the portable Bruker ALPHA FTIR spectrometer equipped with the novel external reflection module which kindly was provided for testing by Bruker Optics (Ettlingen, Germany). The reflection module (**Fig. 10**) focuses the beam via mirrors to the sample/object resulting in a beam diameter of about 3 mm. The reflected part is collected also by mirrors and directed to a DTGS detector. The background was acquired using a gold mirror as reference sample.

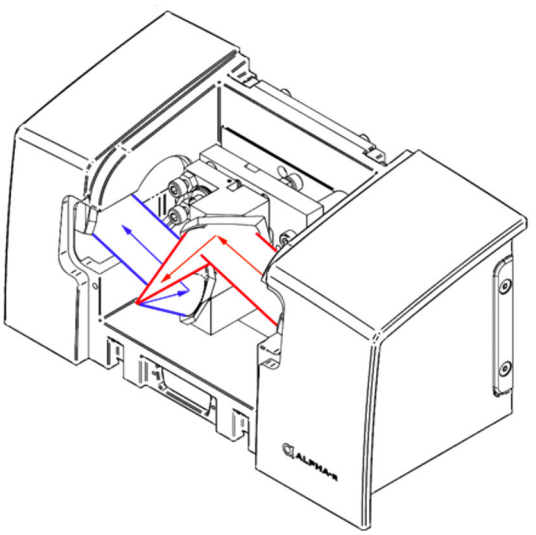

Fig. 10 Optical path of the external reflection module. Angle of incidence is equal to the angle of reflection (45°) [**57**].

1.4.2.2 Micro-Raman spectroscopy

A wide variety of expressions for Raman intensity as a function of experimental variables exists. A convenient approach is to separate the sample and laser variables from the collection and detection variables [**58**].
The following equation expresses the scattered intensity from an opaque matter, $\boldsymbol{I_{scatt}}$, in terms of the laser power density $\boldsymbol{P_D}$ (in *photons x s^{-1} x cm^{-2}*), the differential Raman cross-section, $\left(\frac{\boldsymbol{d\alpha}}{\boldsymbol{d\Omega}}\right)$ (in *cm^2 x molecule^{-1} x sr^{-1}*) and number density of scatterers $\boldsymbol{D}$ (in *molecules x cm^{-3}*) [**58**].

$$\boldsymbol{I_{scatt} = P_D\ x\ \left(\frac{d\alpha}{d\Omega}\right) x\ D}$$

Once an equation relating the scattering intensity is in hand, we can turn to the collection and detection of scattered light. A collection function may be defined which states the fraction of total scattered light that is collected, analysed, and detected by the spectrometer. The following equation states the observed Raman signal, $\boldsymbol{S}$, as a function of a variety of experimental variables [**58**].

$$\boldsymbol{S = I_{scatt}\ x\ A_D\ x\ \Omega\ x\ T\ x\ Q\ x\ t}$$
$$\boldsymbol{S = P_D\ x\ \left(\frac{d\alpha}{d\Omega}\right) x\ D\ x\ A_D\ x\ \Omega\ x\ T\ x\ Q\ x\ t}$$

where $\boldsymbol{S}$ is the observed signal (in *photoelectrons*), $\boldsymbol{t}$ is the observation time (in *seconds*), $\boldsymbol{A_D}$ is the sample area monitored by the spectrometer (in *cm^2*), $\boldsymbol{\Omega}$ is the collection solid angle of the spectrometer, at the sample (in *sr*), $\boldsymbol{T}$ is the transmission of the spectrometer and collection optics (*unit-less*), and $\boldsymbol{Q}$ is the quantum efficiency of the detector, (in *e-* per *photon*) [**58**].
So, it is reasonable to assume that to increase the signal $\boldsymbol{S}$, we can modulate the laser power ($\boldsymbol{P_D}$), the sample area monitored ($\boldsymbol{A_D}$), the collection solid angle ($\boldsymbol{\Omega}$) and the collection time ($\boldsymbol{t}$); whereas $\boldsymbol{T}$, $\boldsymbol{Q}$ and $\frac{\boldsymbol{d\alpha}}{\boldsymbol{d\Omega}}$ are related to the spectrometer, to the characteristics of detector and to intrinsic properties of molecules [**58**].
Micro-Raman spectrometers typically consist of four fundamental parts: a laser excitation source, an optical microscope, a diffraction grating or interferometer, and a photon detector (**Fig.12**).
Therefore, in the case of micro-Raman spectroscopy, the intensity of the collected Raman signal, $\boldsymbol{S}$, considerably increases, thanks to a better laser focusing ($\boldsymbol{P_D}$) and a bigger collection solid angle ($\boldsymbol{\Omega}$) due to the coupling of an optical microscope, even if the parameter $\boldsymbol{D}$ decreases [**58**].
The excitation beam, shown as a dashed line in **Fig. 11**, is directed to the microscope by beam steering optics. The microscope permits samples to be

examined visually at high magnification and then allows specific areas as small as 1 μm in diameter to be analysed selectively. The reflected, Rayleigh, and Raman photons are back collected through the same microscope objective and then directed to the spectrometer. The 180° geometry of the collection optics allows samples of any size or shape to be examined in situ and non-destructively so long as they can be placed on the microscope stage and under the microscope objective [**59**].

The reflected and Rayleigh scattered photons represent a major source of interference in Raman spectroscopy, as described above. They must be removed so as not to saturate the detector or overwhelm the comparatively weak Raman signal. This can be done either by using a narrow-band holographic Notch filter that is specific to the laser photon energy (and therefore the reflected and Rayleigh scattered photons as well), as shown in **Fig. 11**. Once the reflected and Rayleigh scattered light have been removed, the remaining Raman photons are either sorted spatially by a diffraction grating and detected by a CCD camera in a dispersive Raman spectrometer (see **Fig. 11**) or sorted interferometrically and detected by a photoconductive detector in an FT-Raman instrument.

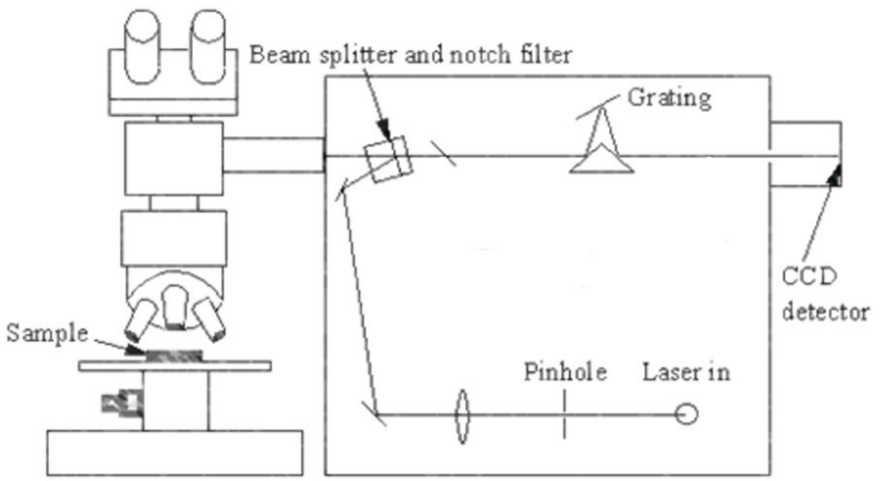

Fig 11 Schematic of research-grade dispersive Raman microscope [**59**].

For this study, the Raman spectra were collected using a Renishaw 2000 micro-Raman spectrometer equipped with a 785 nm diode laser.

1.5 SPECTROSCOPIC TECHNIQUES: 2D-Fluorescence spectroscopy

1.5.1 Principles of fluorescence spectroscopy

Fluorescence and phosphorescence are photon emission processes that occur during molecular relaxation from electronic excited states. These photonic processes involve transitions between electronic and vibrational states of polyatomic fluorescent molecules called *fluorophores*. The Jablonski diagram (**Fig. 12**) offers a convenient representation of the excited state structure and the relevant transitions. Electronic states are typically separated by energies on the order of 10000 cm^{-1}. Each electronic state is split into multiple sublevels representing the vibrational modes of the molecule. The energies of the vibrational levels are separated by about 100 cm^{-1}. Photons with energies in the ultraviolet to the blue-green region of the spectrum are needed to allow an electronic transition. Further, since the energy gap between the excited and ground electronic states is significantly larger than the thermal energy, thermodynamics predicts that molecule predominately reside in the electronic ground state (Boltzmann distribution) [**60-61**].

The electronic excited states of a polyatomic molecule can be further classified based on their *multiplicity*. The indistinguishability of electrons and the Pauli exclusion principle require the electronic wave functions to have either symmetric or asymmetric spin states. The symmetric wave functions, also called *the triplet states*, have three forms, multiplicity of three. The antisymmetric wave functions, also called *the singlet states*, have one form, multiplicity of one [**60-61**].

Optical transition couples states with the same multiplicity. So, this transition excites the molecules from the lowest vibrational level of the electronic ground state to an accessible vibrational level in an electronic excited state. Since the ground electronic state is a singlet state, the destination electronic state is also a singlet [**60-61**].

After excitation, the molecule is quickly relaxed to the lowest vibrational level of the excited electronic state. This rapid vibrational relaxation process occurs on the time scale of femtoseconds to picoseconds. This relaxation process is responsible for the Stoke shift. The Stoke shift describes the observation that fluorescence photons are longer in wavelength than the excitation radiation.

The fluorophore remains in the lowest vibrational level of the excited electronic state for a period on the order of nanoseconds, the *fluorescence lifetime*. Fluorescence emission occurs as the fluorophore decay from the singlet electronic excited states to an allowable vibrational level in the electronic ground state [**60-61**].

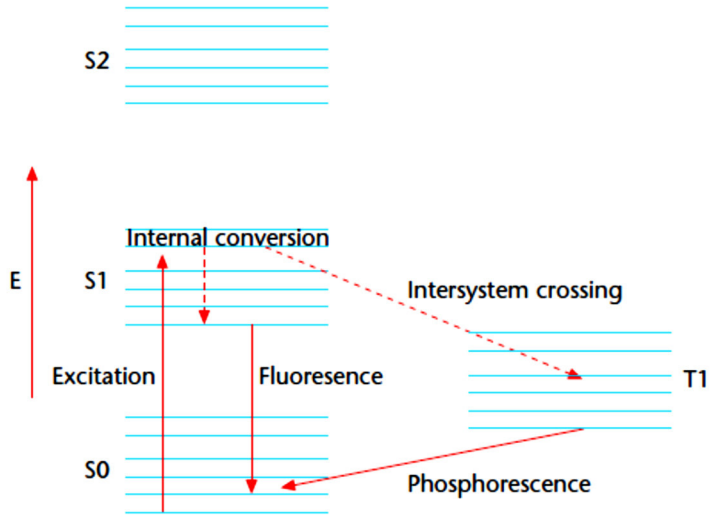

Fig. 12 The Jablonski diagram of fluorophore excitation, radiative decay and non-radiative decay pathways. E denotes the energy scale; S0 is the ground singlet electronic state; S1 and S2 are the successively higher energy excited singlet electronic states. T1 is the lowest energy triplet state [**60**].

The fluorescence absorption and emission spectra reflect the vibrational level structures in the ground and the excited electronic states, respectively. The Frank–Condon principle states the fact that the vibrational levels are not significantly altered during electronic transitions. The similarity of the vibrational level structures in the ground and excited electronic states often results in the absorption and emission spectra having mirrored features [**60-61**].

Molecules in the excited electronic states can also relax by non-radiative processes, where excitation energy is not converted into photons but are dissipated by thermal processes, such as vibrational relaxation and collisional quenching [**60-61**].

In general, the non-radiative decay (***k***) processes can be classified as:

$$k=k_{ic}+k_{ec}+k_{is}$$

where k_{ic} is the rate of *internal conversion*, k_{ec} is the rate of *external conversion*, and k_{is} is the rate of *intersystem crossing* [**60-61**].

Internal conversion is a process where the electronic energy is converted to the vibrational energy of the fluorophore itself. Since vibrational processes are driven by thermal processes, the internal conversion rate typically increases with temperature, which accounts for the commonly observed decrease in fluorescence intensity with rising temperature [**60-61**].

External conversion describes the process where the fluorophore loses electronic energy to its environment, through collision with other solutes.
Intersystem crossing is another process where fluorescence signal is reduced and phosphorescence is generated. Spin-orbit coupling is a quantum mechanical process that is responsible for intersystem crossing. Intersystem crossing describes the relaxation of the molecule from a singlet excited state to a lower energy, triplet excitation state. Since spin-orbit coupling is a weak effect, the intersystem crossing rate is low. The relaxation from the triplet state to the singlet ground state requires another change of multiplicity. Hence, the decay from the triplet states also has a very low rate [**60-61**].
The typical phosphorescence lifetime is on the order of microseconds to seconds. Phosphorescence has larger Stoke shift than fluorescence, owing to the triple state having lower energy [**60-61**].

1.5.2 Experimental and instrumentation setup

The component parts necessary within a typical fluorescence spectrometer (Spectrofluorimeter) are a sample holder, incident photon source (typically a xenon lamp), monochromators used for selecting particular incident wavelengths, focussing optics, photon-collecting detector (single, or preferably multiple channel) and finally a control software unit (**Fig. 13**). An emission monochromator or cut-off filters are also usually used. The detector is usually set at 90 degrees to the light source [**60**].
A fluorescence *emission spectrum* is recorded when the excitation wavelength of light is held constant and the emission beam is scanned as a function of wavelength. An *excitation spectrum* is the opposite, whereby the emission light is held at a constant wavelength, and the excitation light is scanned as a function of wavelength. The excitation spectrum usually resembles the absorbance spectrum in shape [**60**].
The majority of fluorescence assays are carried out in solution, the final measurement being made upon the sample contained in a cuvette or in a flow-cell. The cuvette is placed normal to the incident beam. The resulting fluorescence is given off equally in all directions, and may be collected from either the front surface of the cell, at right angles to the incident beam. On the other hand, for solid sample the most common geometry used is the front-face illumination (**Fig. 13**). This last is performed using the sample oriented at 30 to 60 degrees relative to the incident beam. An angle of 45 degrees should be discouraged. A large amount of light is reflected directly into the emission monochromator, increasing the chance that stray light will interfere with the measurements. This procedure has two advantages. First, less reflected light enters the emission monochromator. Second, the incident light is distributed

over a larger surface area, decreasing the sensitivity of the measurement to the precise placement of the cuvette within its holder. One disadvantage of this orientation is a decreased sensitivity because a larger fraction of the incident light is reflected off the surface of the cuvette/sample [**60**].

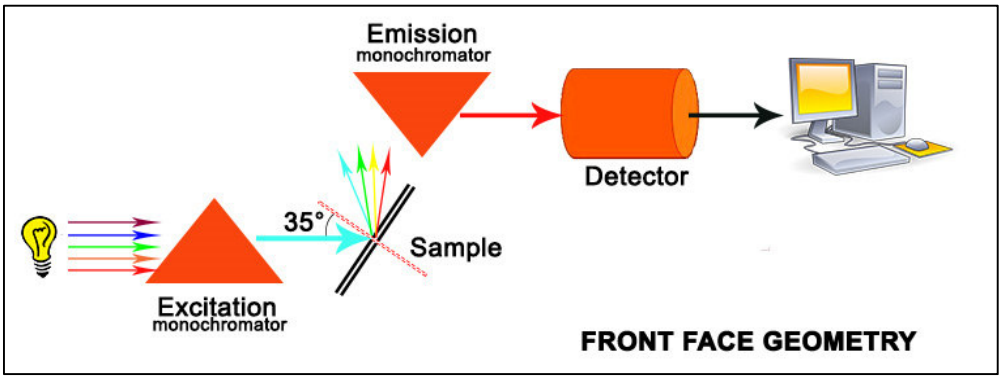

Fig. 13 A schematic description of a spectrofluorimeter with front-face illumination.

The 2D-fluorescence spectroscopy (also called Excitation-Emission Spectroscopy, EES) builds a two-dimensional emission intensity profile by scanning the emission spectrum at incremental steps of excitation wavelength, called EE spectrum. EE spectra can be particularly powerful because they map the presence of different fluorophores and have been exploited in the analysis of foods and binding media. Practically, EE spectra require long acquisition times, and the determination of the relationship between different spectra that contain multiple fluorophores is not necessarily straightforward [**62**].
In this study, a scanning spectrofluorimeter with excitation provided by a xenon arc lamp (Jobin-Yvon/Horiba Fluoromax-P) was used.

1.6 Multivariate statistical analysis

Several researches in the field of Cultural Heritage conservation require multivariate statistical analysis to optimise the use of the collected data. The main objective is to evaluate and compare artistic materials composition, the state of conservation, the chemical-physical changes over time, the results of conservation treatments and so on. Art materials and especially works of art have two particular characteristics which have to be taken into account in any statistical analysis. They are internally heterogeneous and individually distinct in composition, form and history [**63**]. This extreme variability has to be considered in the employ of statistical procedures, in particular with multivariate statistical analysis [**64**].
Chemometrics is the science which uses mathematics and statistics knowledge to explore a complex system and extract information from experimental data. It

is a highly interfacial discipline, using methods frequently used in *core* data-analytic disciplines such as multivariate statistics, applied mathematics, and computer science, in order to address problems in different fields [**65**].
Among several chemometric techniques, Principal Component Analysis, PCA, is here described.

1.6.1 Principal Component Analysis (PCA)

The starting point is an X-matrix with *n* objects and *p* variables, often called "data matrix". The objects can be observations, samples, experiments etc., while the variables typically are the different "measurements" on the samples. The important issue is that the *p* variables collectively characterize each, and all, of the *n* objects. The purpose of all multivariate data analysis is to decompose the data in order to detect, and model, the "hidden phenomena" (**Fig. 14A**); or better to define the set of natural coordinates for these variables that better show the similitudes and differences between the various samples. The concept of variance is very important. It is fundamental assumption in multivariate data analysis that the underlying "directions with maximum variance" are more or less directly related to these "hidden phenomena" [**66**].
This data matrix, with its *p* variable columns and *n* objects rows, can be represented in a Cartesian (orthogonal) coordinate system of dimension *p*. The *p*-dimensional coordinate system is called the *variable space*, meaning the space spanned by the *p* variables (**Fig. 14A**). Each *n* object can be "represented/plotted" as a point in this variable space. When all the X-values for all objects are plotted in the variable space, the result is a swarm of points in this *p*-dimensional space. In this swam of point there will be always a trend that will be so prominent that in some sense might be called a "hidden linear association" among the original variables. This revealing of the underlying covariance structure is really the backbone of PCA [**66**].
The objective of PCA is to substitute the representation of these objects, from the initial representation in the form of *p* original variables, into the new Principal Component coordinate space (**Fig. 14B**). The new coordinates are ordered according to their capability to explain variance written in the dataset. In fact, we do not simply wish to change the coordinate system; we also want the advantage of dropping the noisy, higher-order PC-directions. Thus PCA performs a *dual objective*: a transformation into a more relevant coordinate system (which lies directly in the centre of the data swarm of points), and a dimensionality reduction (using only the first principal components which reflect the structure in the data) [**66**].
Summarising, PCA represents a mathematical procedure which transforms a number of possibly correlated variables into a number of uncorrelated

variables called *principal components* (PCs). PCs are related to the original variables by an orthogonal transformation. This transformation is defined in such a way that the first principal component has variance as high as possible and each succeeding component in turn has the highest possible variance under the constraint that it be orthogonal to the preceding components [**67**].

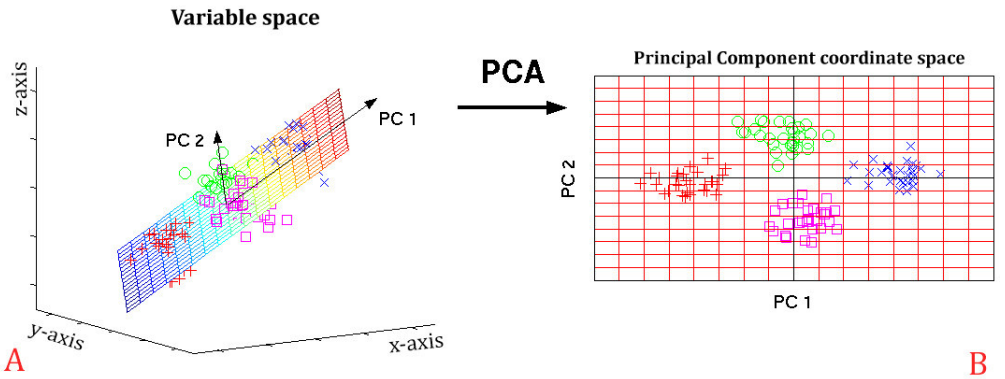

Fig. 14 Data plotted as a swarm of points in the variable space, revealing a hidden trend (A); their projection onto the coordinate space defined by the first two PCs (B) [**68**].

Once the principal components identified, the weights of each variable are defined in a loadings matrix. This creates the *loading plots*, bi-or mono-dimensional graphs in which it is possible to see how variables are distributed on the PC. *Score plots* are, however, graphs where the object's position is represented by the coordinates on the PC-space [**66**].
More precisely, score plots can be viewed as particularly 2-D "windows" into PC-space (**Fig. 15A**), where one observes how the objects are related to one another. The PC-space may certainly not always be fully visualized in just one 2-D plot, in which case two, or more score plots is all we need. Score plots are used for outlier identification, identification of trends, identification of groups, exploration of replicate similarities and more. When interpreted together with loadings, the influence of the original variables can also be deduced [**66**].
On the other hand, loading plots, can be viewed as the bridge between the variable space and the PC-space (**Fig. 15B**). These loadings are equally valuable for interpretation in their own right, but especially when compared with their corresponding score plots. The loading plot provides a projection view of the inter-variable relationships (variable similarities). The loading plot shows how much each variable contributes to each PC [**66**].

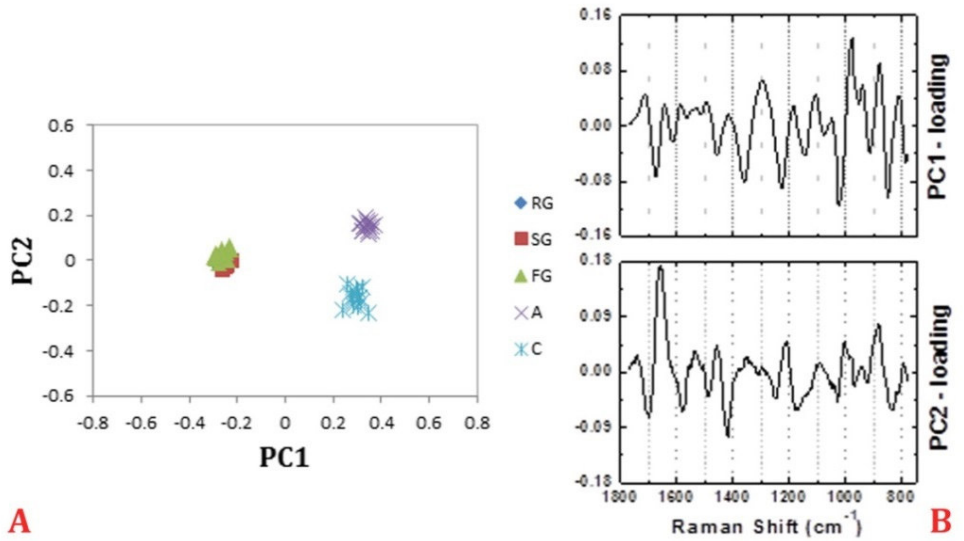

Fig. 15 Example of "score plot" along with "loading plots" of the corresponding PCs.

The mathematical idea of PCA is to approximate the original matrix **X** by a product of two small matrices –the score and loading matrices- according to (**Fig. 16**):

$$\boldsymbol{X} = \boldsymbol{U}\boldsymbol{V}^{\mathbf{T}}$$

where $\boldsymbol{X}$ is the original data matrix, consisting of n rows (objects) and p columns (variables); $\boldsymbol{U}$ is the scores matrix with n rows and k columns (number of principal components); $\boldsymbol{V}$ is the loading matrix with k columns and p rows; and T is the transpose of matrix [**67**].

In other words, the projection of $\boldsymbol{X}$ down on to a k-dimensional *subspace* by means of the projection matrix $\boldsymbol{V}^{\mathbf{T}}$ gives the object coordinates in this plane, $\boldsymbol{U}$. The columns in $\boldsymbol{U}$ are the score vectors and the rows in $\boldsymbol{P}$ are called loading vectors. Both vectors are orthogonal, i.e., $\boldsymbol{p}_i^T\boldsymbol{p}_j = \mathbf{0}$ and $\boldsymbol{u}_i^T\boldsymbol{u}_j = \mathbf{0}$, for $\boldsymbol{i} \neq \boldsymbol{j}$ [**67**].

The principal components are determined on the basis of the maximum variance criterion. Each subsequent principal component describes a maximum of variance, that is not modelled by the former components. According to this, most of variance of the data is contained in the first principal component. In the second component there is more information than in the third, etc. Finally, as many principal components are computed as are needed to explain a pre-set percentage of the variance.

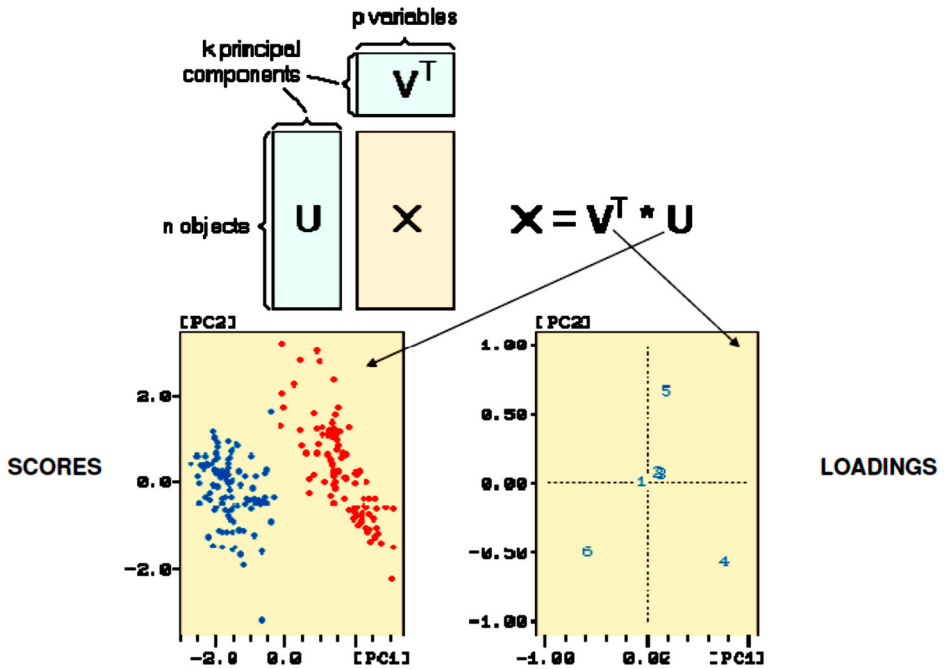

Fig. 16 The original matrix **X** represented as a product of two small matrices: the score and loading ones [**69**].

The PCs can be considered as projections of the original data matrix, **X**, on the scores, ***U***. For this, previous equation must be converted to the scores on the left side by [**67**]:

$$\boldsymbol{U = XV}$$

The new coordinates are linear combinations of the original variables. For example, the elements of the first principal component are read as [**67**]:

$$u_{11} = x_{11}v_{11} + x_{12}v_{21} + \cdots + x_{1p}v_{p1}$$
$$u_{21} = x_{21}v_{21} + x_{22}v_{21} + \cdots + x_{2p}v_{p1}$$
$$\cdots$$
$$u_{n1} = x_{n1}v_{11} + x_{n2}v_{21} + \cdots + x_{np}v_{p1}$$

1.6.2 Data analysis

Pre-processing of data set is essential for relevant and valid modelling results. The correct type of pre-treatment is generally given by the type of problem. Nevertheless, it is crucial to precise that a wrong pre-processing may give rise to misinterpretations.

For this PhD work, micro-Raman and FT-NIR spectral data-sets were processed using the Principal Component Analysis (PCA) method, by means of The Unscrambler® X version 10.3 software (CAMO).

The micro-Raman and FT-NIR datasets were pre-processed separately. Different causes can indeed lead to random noise in Raman and FT-NIR spectra, thus making more difficult the identification of spectral bands, particularly in computational analyses, as in the present work. Different basic smoothing methods were tested, before selecting the best compromise to avoid a loss of important information. In order to discern variability in the original spectra, first derivative was performed on the spectral data matrices before extracting the principal components (PCs).

A NIR spectral data set normally undergoes some types of pre-treatments before being used for qualitative or quantitative purposes. These data pre-treatments are mainly used to overcome different problems (i.e. some baseline-affecting phenomena, as those associated with scattered radiation by a solid sample which is measured by reflectance, or broad and overlapped combination and overtone bands [**50**]). First and second derivatives of the original NIR spectra have been used by different authors [**50, 70**]. For this study, the selected pre-treatment was limited to the first derivative, in order to keep some easier connection to the original data. In addition, even if most of the chemometric work on Raman experiments is performed directly on raw data, some previous uses of first derivative micro-Raman spectra with chemometric purposes can be found [**71-72**]. Thus, the same kind of first derivative pre-treatment for both set of data, in order to have a common procedure all along this work, was applied.

Firstly, spikes occurring in micro-Raman spectra, such as random signals from cosmic rays, were removed. Then, micro-Raman spectra were subjected to baseline subtraction, average reduction of variables (factor two) and first derivative calculation.

The baseline subtraction corrects the baseline of samples, removing constant or linear background or very broad band spectral features (e.g. those due to fluorescence or scattering) which do not belong to the Raman spectrum itself. Removal the background is, so, useful to acquire consistent spectra. This operation would be done automatically by the first derivative treatment: working, indeed, on a narrow window of data, these features would be effectively removed by this calculation. Nevertheless, sometimes random factors (e.g. light scattering from ill oriented surfaces) could lead to anomalous signals.

The transformation of average reduction enables to obtain a new spectral data step of 2 cm^{-1}.

The first-derivative transformation was made by the application of the Savitzky-Golay algorithm [**73**]. The derivative algorithm applied in this study permits a simultaneous smoothing of spectra (15 data points) which reduces the noise produced from derivative transformation.
FT-NIR spectra, instead, were subjected to the Savitzky-Golay algorithm (15 data points for neat binding media and for oil-paint models) without any other pre-processing.
In order to account for variations in intensity due to the experimental set-up in both FT-NIR and micro-Raman spectra, the spectra were vector normalized as described by Vandenabeele and Moens [**74**]. This approach ensures that spectra with different absolute peak heights, but whose features are similar, will be adjusted to appear similar. This also prevents the PCA from using absolute peak heights to differentiate the samples, which could lead to erroneous classifications [**75**].
After pre-processing, the total pre-processed FT-NIR and Raman spectra were loaded into a data matrix and combined to obtain new spectra, generating a new set of "combined first derivative near infrared and Raman" spectra, 16 for each typology of binder/oil-paint model/sample.
The Uncertainty Test was always performed to estimate the significance of variables. Then, PCA was performed by using the Non Linear Iterative Partial Least Squares (NIPALS) algorithm. Also, it was performed applying a mean-centering onto data column wise. Each model was always validated by Leave One Out (LOO) cross-validation and by a projection of evaluated sets of spectral data acquired by the same samples (4 spectra for each type of sample).
A schematic summary of the flowchart employed to process the acquired FT-NIR and micro-Raman spectra is reported in **Fig. 17**.

The present work reports data acquired with different instruments on various spectral ranges, thus the information contents for each data point are not fully equivalent (i.e. spectral dispersion and resolution are different) and it is not trivial to compensate for this physical problem. In support to the obtained results, the following remark is reported: a visual inspection of the PCs highlighted signals with almost the same spectral width, thus the combination of different numbers of data points and spectral resolution was effectively well balanced (a wrong combination of number of variables in the two experiments would have resulted in peaks with much different width in the two data segments).

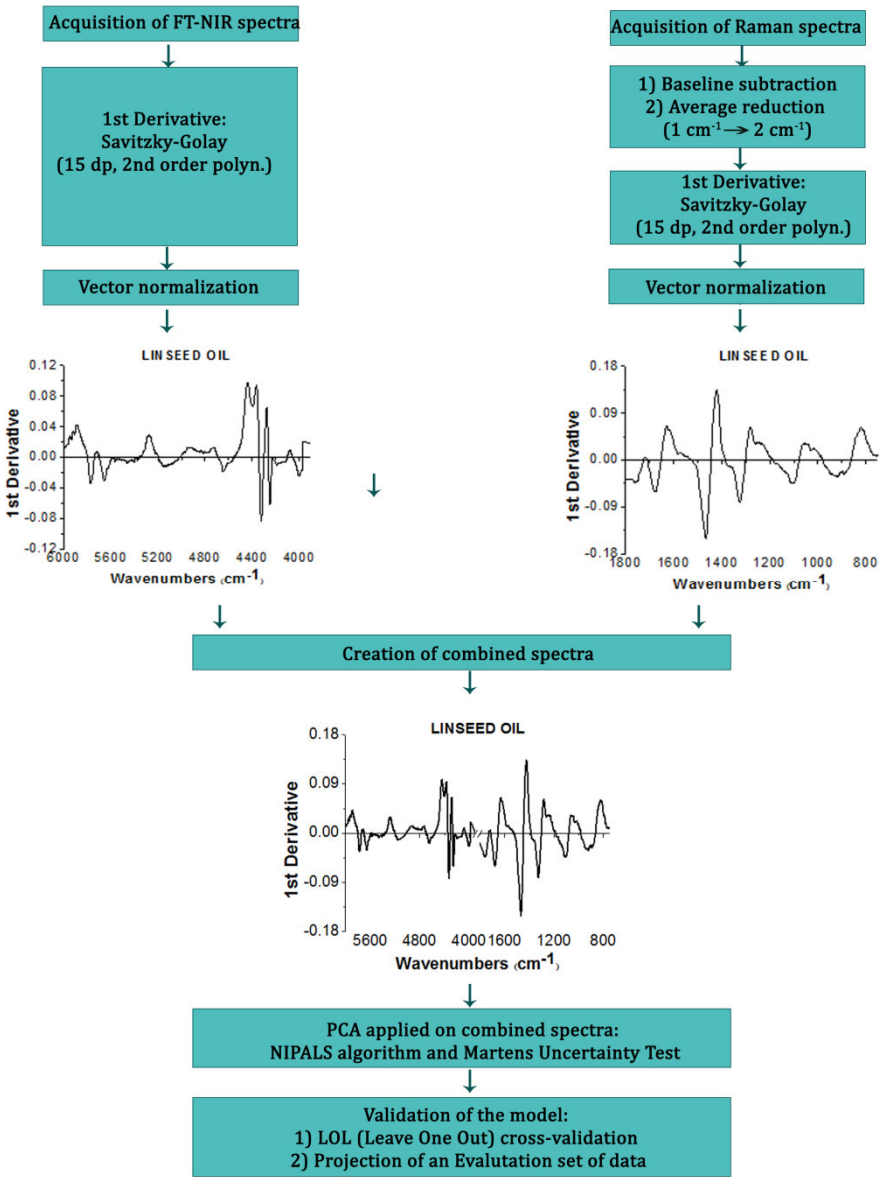

Fig 17 Working flowchart used in this work to process all FT-NIR and micro-Raman data ("dp" means "data-points").

As regards the analysis of excitation-emission (EE) maps, these were processed using the Principal Component Analysis (PCA) tool of the Matlab® software version R2012b (MathWorks Inc., USA). PCA was performed by using the Singular Value Decomposition (SVD) algorithm.
In order to evaluate each cell of the starting matrices, a code, written always in Matlab, allowed the transformation of each map into one vector, carrying the total information.
Each resulting/final loading plot is shown as a proper matrix with the same parameters of the starting analysed matrices. A colour scale aids discrimination among positive and negative contributions.
A schematic summary of the flowchart used to process the acquired EE maps is reported in **Fig. 18**.

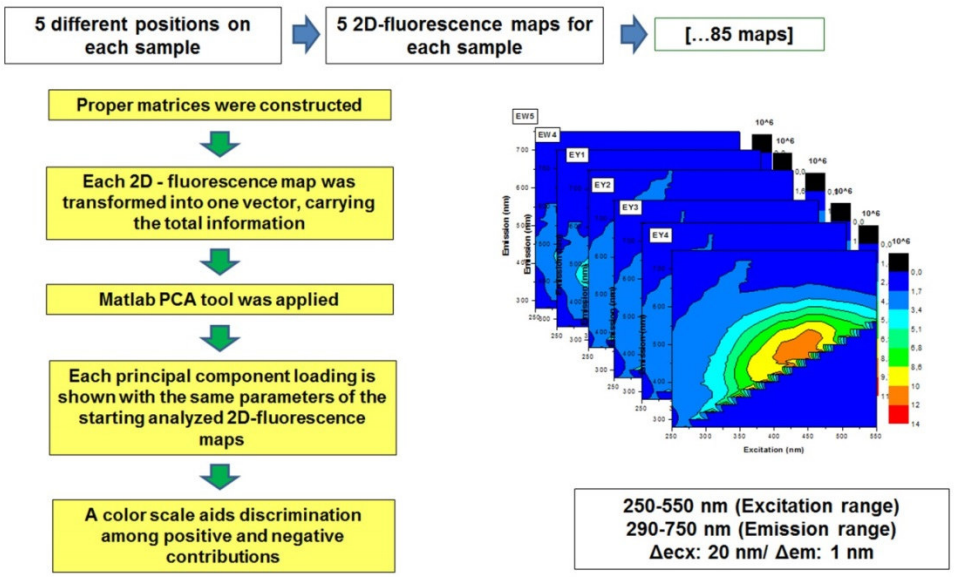

Fig. 18 Working flowchart used in this work to process all 2D-fluorescence maps of neat binding media.

References

[1] P. Grandou, P. Pastour (eds.), Peintures et vernis, Hermann, Paris, 1966.

[2] L. Masschelein-Kleiner, Ancient Binding Media, Varnishes and Adhesives, ICCROM, Rome, Italy, 1995.

[3] H. Pariselle, Chemie organique spéciale et industrielle, Masson, Paris, 1955.

[4] J.S. Mills, R. White, The organic chemistry of museum objects, 2nd ed., Arts and archaeology, Butterworth-Heinmann Ltd., Oxford, 1994.

[5] O. Zovi, L. Lecamp, C. Loutelier-Bourhis, C.M. Lange, C. Bunel, Stand Reaction of Linseed Oil, Eur. J. Lipid Sci. Technol. 2011, 113(5), pp 616-626.

[6] E. Manzano, L.R. Rodriguez-Simón, N. Navas, R. Checa-Moreno, M. Romera, L.F. Capitan-Vallvey, Study of the GC–MS determination of the palmitic–stearic acid ratio for the characterization of drying oil in painting: La Encarnación by Alonso Cano as a case study, Talanta 84 (2011) 1148-1154.

[7] P. Vandenabeele, B. Wehling, L. Moens, H. Edwards, M. De Reu, G. Van Hooydonk. Analysis with Micro-Raman Spectroscopy of Natural Organic Binding Media and Varnishes Used in Art, Anal. Chim. Acta. 2000, 407(1-2), pp 261-274.

[8] C.S. Tumosa, M.F. Meckleburg, Oil Paints: The chemistry of drying oils and the potential for solvent disruption, in: Marion F. Mecklenburg, A. Elena Charola, Robert J. Koestler (Ed.), New Insights into the Cleaning of Paintings, Smithsonian Institution Scholarly Press, Washington, 2013, pp 51-58

[9] R. Mazzeo, S. Prati, M. Quaranta, E. Joseph, E. Kendix, M. Galeotti, Attenuated total reflection micro FTIR characterisation of pigment-binder interaction in reconstructed paint films, Anal. Bioanal. Chem. 2008, 392 (1-2), pp 65-76.

[10] L. Brambilla,, C. Riedo, C. Baraldi, A. Nevin, M. C. Gamberini, C. D'Andrea, O. Chiantore, S. Goidanich, L. Toniolo, Characterization of fresh and aged natural ingredients used in historical ointments by molecular spectroscopic techniques: IR, Raman and fluorescence, Anal Bioanal Chem. 2011, 401(6), pp: 1827-37.

[11] I. Bonaduce, H. Brecoulaki, M.P. Colombini, A. Lluveras, V. Restivo, E. Ribechini, Gas chromatography-mass spectrometric characterization of plant gums in samples from painted works, J. Chromatogr. A 2007, 1175, pp 275-282.

[12] A. Lluveras, I. Bonaduce, A. Andreotti, M.P. Colombini, GC/MS analytical procedure for the characterization of glycerolipids, natural waxes, terpenoid resins, proteinaceous and polysaccharide materials in the same paint microsample avoiding interferences from inorganic media, Anal. Chem. 2010, 82 (1), pp 376-386.

[13] M.P. Colombini, F. Modugno (Eds.), Organic mass spectrometry in art and archaeology, John Wiley & Sons, 2009.

[14] C.M. Peres, “Vincent Van Gogh’s triptych of trees in blossom, Arles (1888), part II. On egg white varnishes”, in J.S. Mills and P. Smith (eds), Cleaning, retouching and coatings, Preprints of the contributions to the Brussels Congress, I.I.C., 1990, pp 131-133.

[15] E. De Witte, R. Guislan-Wittermann, L. Masschelein-Kleiner, Comparison de quelques matériaux et techniques de retouche, Bull. Inst. Royal Patrm. A. 1980/81, 18, pp 30-40.

[16] H. Lank, “Egg tempera as a retouching medium”, in J. S. Mills and P. Smith (eds.), Cleaning, retouching and coatings, Preprints of the contributions to the Brussels Congress, I.I.C., 1990, pp 156-157.

[17] N.C. Schellmann, Animal glues: a review of their key properties relevant to conservation, Revi. Conserv. 2007, 8, pp 55-66.

[18] A.V. Blom, Organic Coatings in Theory and Practice, Elsevier, Amsterdam, 1949.

[19] V.N. Yarosh, N.YU. Zakharova, Identification and quantitative analysis of organic materials in ground coats of wall paintings in sultan Sanjar’s tomb, 9th Triennial Meeting of the ICOM Committee for Conservation, Dresden, G. D. R., 1990, pp 545-547.

[20] R.J. Gettens, E.W. Fitzhugh, Azurite and Blue Verditer, in: A. Roy (Ed.), Artists pigments: a handbook of their history and characteristics, vol. 2, Oxford University Press, New York, 1993, pp. 23-35.

[21] J. Plesters, Ultramarine Blue, Natural and Artificial, in: A. Roy (Ed.), Artists pigments: a handbook of their history and characteristics, vol. 2, Oxford University Press, New York, 1993, pp. 37-65

[22] R.J. Gettens, G.L. Stout, Painting Materials, A Short Encyclopedia, Dover Publications, New York, 1966.

[23] H. Kühn, Conservation and Restoration of Works of Art and Antiquities, Butterworth Scientific, London, 1986.

[24] C. Defeyt, P. Vandenabeele, B. Gilbert, J. Van Pevenage, R. Cloots, D. Strivay, Contribution to the identification of α-, β- and ε-copper phthalocyanine blue pigments in modern artists’ paints by X-ray powder diffraction, attenuated total reflectance micro-fourier transform infrared spectroscopy and micro-Raman spectroscopy, J. Raman Spectrosc. 2012, 43, pp 1772-1780.

[25] Colour Index Dyes and Pigments, Vol 3 (3rd ed.), Society of Dyers and Colourists and the American Association of Textile Chemists and Colorists, Bradford, Yorkshire, 1971.

[26] R.J. Gettens, H. Kühn, W.T. Chase, Lead White, Stud. Conserv. 12, (1967) 125-13.

[27] R.J. Gettens, H. Kühn, W.T. Chase, Lead White, in: A. Roy (Ed.), Artists pigments: a handbook of their history and characteristics, vol. 2, Oxford University Press, New York, 1993, pp. 67-81.

[28] C.S. Tumosa, M.F. Mecklenburg, The influence of lead ions on the drying of oils, Rev. Conserv. 6 (2005) 39-47.

[29] L.A. O'Neill, R.A. Brett, Chemical reactions in paint films, J. Oil Col. Chem. Ass. 1969, 52, pp 1054–1074

[30] S.H. Bell, Controlling Loss of Gloss, Paint Varnish. Prod. 1970, 60, pp 55–60

[31] J. Van der Weerd, A. Van Loon, J.J. Boon, FTIR studies of the effects of pigments on the aging of oil, Stud. Conserv. 2005, 50 (1), pp 3-22.

[32] G. Chiavari, D. Fabbri, S. Prati, Effect of pigments on the analysis of fatty acids in siccative oils by pyrolysis methylation and silylation, J. Anal. Appl. Pyrol. 2005, 74, pp 39-44.

[33] R. Mazzeo, S. Prati, M. Quaranta, E. Joseph, E. Kendix, M. Galeotti, Attenuated total reflection micro FTIR characterisation of pigment-binder interaction in reconstructed paint films, Anal. Bioanal. Chem. 2008, 392 (1-2), pp 65-76.

[34] H. Kühn, Zinc White, in: R.L. Feller (Ed.), Artists pigments: a handbook of their history and characteristics, vol. 1, Cambridge University Press, London, 1986, pp. 169-186.

[35] C.E. Barnett, Physics and chemistry of pigments, Ind. Eng. Chem. 1949, 41(2), pp 272-279.

[36] E.J. Dunn Jr, Moisture Resistance of Paint Films, Official Digest 1954, 26, pp 387–407.

[37] G. Osmond, Zinc white: a review of zinc oxide pigment properties and implications for stability in oil-based paintings, AICCM Bulletin 2012, Vol. 33, pp 20-29.

[38] G. Osmond, B. Ebert, J. Drennan, Zinc oxide-centred deterioration in 20th century Vietnamise paintings by Nguyễn Trọng Kiệm (1933-1991), AICCM Bulletin 2014, Vol. 34, pp. 4-14.

[39] J.J. Hermans, K. Keune, A. Van Loon, P.D. Ledema, An infrared spectroscopic study of the nature of zinc carboxylates in oil paintings, J. Anal. At. Spectrom. 2015, 30 pp 1600-1608.

[40] C. Cennini, in: F. Frezzano (Ed.), Il libro dell'arte (XIV sec), 1st ed., Neri Pozza Editore, Vicenza, Italy, 2003.

[41] D.A. Burns, E.W. Ciurczak (Eds.), Handbook of Near-Infrared Analysis, Third edition, CRC Press, Boca Raton, FL, 2007.

[42] G.M. Barrow, Physical Chemistry, McGraw Hill Inc., New York, 1980.

[43] H.W. Siesler, Y. Ozaki, S. Kawata, H.M. Heise (Eds.), Near-infrared spectroscopy, Wiley-VCH, Weinheim, 2002.

[44] B. Schrader (Ed.), Infrared and Raman spectroscopy, Wiley-VCH, Weinheim, 1995.

[45] W. Groh, Overtone absorption in macromolecules for polymer optical fibers, Macromol. Chem. 1988, 189, pp 2861-2874.

[46] E.B. Wilson, J.C. Decius, P.C. Cross, Molecular Vibrations – The theory of infrared and Raman vibrational spectra, McGraw Hill, New York, 1955.

[47] P. Hendra, C. Jones, G. Warnes, Fourier Transform Infrared Spectrometry, Wiley-Interscience, New York, 1986.

[48] I.R. Lewis, H.G.M. Edwards (Eds.), Handbook of Raman spectroscopy, Marcel Dekker, New York, 2001.

[49] J. Workman, L. Weyer Practical Guide to Interpretative Near-Infrared Spectroscopy, CRC Press- Taylor and Francis, Boca Raton, 2007.

[50] C. Pasquini, Near Infrared Spectroscopy: Fundamentals, Practical Aspects and Analytical Applications, J. Braz. Chem. Soc. 2003, Vol. 14, No, 2, pp 198-219.

[51] P. Kubelka, F. Munk, Ein Beitrag zur Optik der Farbanstriche, Technische Physik 1931, 12, pp 593-601.

[52] P. Kubelka, New Contributions to the Optics of Intensely Light-Scattering Materials. Part I, J. of Opt. Soc. Am. 1948, 38 (5), pp 448-457.

[53] R. Johnston-Feller, Color science in examination of museum objects, non-destructive procedures, The Getty Conservation Institute, Los Angeles, 2001

[54] P.B. Mitton, Pigment Handbook, Vol. III, characterization and physical relationships, T.C. Patton (Ed.), Wiley & Sons, New York, 1973.

[55] D.R. Duncan, 'The Identification and Estimation of Pigments in Pigmented Compositions by Reflectance Spectrophotometry, JOCCA 1962, 45, pp 300-324.

[56] R.J. Lancashire, Selection Rules for electronic spectra of transition metal complexes, University of the West Indies, Mona, 2006.

[57] W. Vetter, M. Schreiner, Characterization of pigment-binding media systems – comparison of non-invasive in-situ reflection FT-IR with transmission FT-IR microscopy, e-PS 2011, 8, pp 10-22.

[58] R.L. McCreery, Photometric Standards for Raman Spectroscopy, in J.M. Chalmers and P.R. Griffiths (Eds.): Handbook of vibrational spectroscopy, John Wiley & Sons Ltd, Chichester, 2002.

[59] G.D Smith, R.J.H. Clark, Raman microscopy in archaeological science, J. Archeol. Sci. 2004, 31, pp 1137-1160.

[60] J.R. Lakowicz, Principles of Fluorescence Spectroscopy, 3rd ed, Springer Science+Business Media, LLC, New York, 2006.

[61] P.T.C So, C.Y. Dong, Fluorescence spectrometry, in Encyclopedia of life sciences, Macmillan Publishers Ltd, Nature Publishing Group, 2002, pp 1-4.

[62] A. Nevin, D. Anglos, S. Cather, A. Burnstock, The influence of visible light and inorganic pigments on fluorescence excitation emission spectra of egg-, casein and collagen-based painting media, Appl. Phys. A 2008, 92, pp 69-76.

[63] T.J. Reedy, C.L. Reedy, Statistical Analysis in Art Conservation Research, The Getty Conservation Institute, U.S.A., 1988.

[64] D.L. Massart, B.G.M. Vandeginste, S.N. Deming, Y. Michotte, L. Kaufman, Chemometrics: a Textbook, in Data Handling in Science and Technology, vol. 2, Elsevier, Amsterdam 2003.

[65] R. Todeschini, Introduzione alla Chemometria, EDiSES, Napoli, 1998.

[66] K.H. Esbensen, Multivariate Data Analysis – In Practice, An introduction to multivariate data analysis and experimental design, 5th edition, CAMO Software AS., Aalborg University, Esbjerg, 2009.

[67] M. Otto, Chemometrics: statistics and computer application in analytical chemistry; WILEY-VCH: Weinheim, New York, Chichester, Brisbane, Singapore, Toronto, 1999.

[68] M. Scholz, Approaches to analyse and interpret biological profile data, Ph.D. thesis, University of Postdam, Germany, 2006.

[69] H. Lohninger, Teach/Me Data Analysis, Springer-Verlag, Berlin-New York-Tokyo, 1999.

[70] D.W. Hopkins, What is a Norris derivative?, NIR News 2001, 12, pp 3-5.

[71] J.F. Kauffman, M. Dellibovi, C.R. Cunningham, Raman spectroscopy of coated pharmaceutical tablets and physical models for multivariate calibration to tablet coating thickness J. Pharm. Biomed. Anal. 2007, 43, p 39.

[72] N. Navas, J. Romero-Pastor, E. Manzano, C. Cardell, Raman spectroscopic discrimination of pigments and tempera paint model samples by principal component analysis on first-derivative spectra, J. Raman Spectrosc. 2010, 41, pp 1486-1493.

[73] A. Savitzky, M. Golay, Smoothing and Differentiation of Data by Simplified Least Squares Procedures, Anal. Chem. 1964. 36(8), pp 1627-1639.

[74] P. Vandenabeele, L. Moens, Micro-Raman spectroscopy of natural and synthetic indigo samples, Analyst 2003, 128, pp 187-193.

[75] A. Pallipurath, J. Skelton, P. Ricciardi, S. Buclow, S. Elliot, Multivariate Analysis of Combined Raman and Fibre-Optic Reflectance Spectra for the Identification of Binder Materials in Simulated Medieval Paints, J. Raman Spectrosc. 2013. 44(6), pp 866-874.

PART II

Chapter 1: FT-NIR and Raman spectroscopies for non-destructive identification and differentiation of traditional binding media

Abstract

In this chapter the main spectroscopic properties of all neat binding media, after an ageing of three months, will be explored and analysed by means of both FT-NIR and micro-Raman spectroscopies.
The application of PCA to the corresponding combined first derivative FT-NIR and Raman spectra will be further discussed to highlight its potentialities.

Introduction

In this work, FT-NIR and micro-Raman spectra of 13 traditional organic materials that have been commonly used by artists throughout history as binding media, are characterized. These materials have been analysed after a natural ageing of three months.
In order to further highlight significant differences inside each class of binders (protein-, polysaccharide- and lipid-based) the applying of Principal Component Analysis to the corresponding combined first derivative FT-NIR and Raman spectra has been also investigated.
These two vibrational spectroscopic methods provide complementary information and a deeper insight into the characteristic structural and binding properties of these organic materials.
Near infrared and Raman spectroscopies have the potential to overcome typical issues related to the application of separation methods (gas chromatography, capillary electrophoresis, and liquid chromatography) and mass spectrometry, such as large sample consumption, long experimental times, complex sample preparation and multi-parameter operating conditions. Both methodologies satisfy requirements necessary for analytical methods to be applied for the study of precious and unique artworks. They provide non-destructive and contactless measurements and could be performed *in-situ* by means of portable devices.
Whereas Raman spectroscopy has been extensively used [**1-4**] in the cultural heritage, near infrared (NIR) spectroscopy started to be applied most frequently in this field, only over the last few years [**5**].
NIR spectroscopy has been developed as a fast and less expensive-effective method of analysis. The low molar absorbance of near-infrared bands allows measurements in reflectance mode recording spectra of solid samples with

minimal or no pre-treatment [**5-8**]. These attractive features have increased the interest towards the application of NIR spectroscopy in a variety of fields: pharmaceutical, foods, polymers, etc. [**7-12**]. The main drawback of NIR spectroscopy is the difficult band assignment due to the fact that signals in this spectral region are originated by combination and overtone modes, generally broader and less resolved than the fundamental bands. For this reason, NIR is less specific than mid-infrared (Mid-IR) spectroscopy and in the case of mixtures of organic substances, single components cannot be well distinguished [**5, 7-9**]. Nevertheless, recent studies have demonstrated that NIR spectroscopy can be exploited to analyse binders and easel paintings, providing useful information [**5, 13-15**].
Literature about the application of NIR spectroscopy in different scientific fields points to the use of the first-derivative transformation as an effective approach to NIR spectra analysis [**5, 7-9**]. For this reason, first-derivative transformation has been applied in order to better perform PCA of neat binding media.

1.1 Materials and methods

1.1.1 Materials

All neat binding media analysed in this work, along with corresponding symbols, are listed in **Table 1**. The recipes followed to prepare each binder are described in **Part I** of this thesis.
These materials were analysed after an ageing of three months. As regards drying oils, they should be treated as "fresh" binding media because the drying process has not already been completed (according to previous studies, an oil paint can be regarded as aged only one year after its preparation [**16-17**]).

Table 1 List of analysed neat binding media, with their manufacturer and identification symbols.

Neat binder	Producer/Manufacturer	Symbol
Proteinaceous binders		
Rabbit Skin Glue	Zecchi	**RG**
Strong Glue	Zecchi	**SG**
Fish Glue	Zecchi	**FG**
Egg White	Local market	**EW**
Egg Yolk	Local market	**EY**
Whole Egg	Local market	**WE**
Casein	Zecchi	**C**
Drying oils		
Linseed Oil	Zecchi	**LOZ**
Linseed Oil	Maimeri	**LOM**
Linseed Oil	Ferrario	**LOF**
Poppy-seed Oil	Zecchi	**POZ**
Poppy-seed Oil	Talens	**POT**
Walnut Oil	Zecchi	**WOZ**
Walnut Oil	Ferrario	**WOF**
Stand-Oil	Zecchi	**SOLZ**
Polysaccharide media		
Arabic Gum	Zecchi	**AG**
Tragacanth Gum	Zecchi	**TG**

1.1.2 Fourier Transform-Near Infrared (FT-NIR) measurements.

FT-NIR reflectance spectra were acquired by using a portable ALPHA FT-IR spectrometer (Bruker Optics) equipped with an external reflection module. Total reflection spectra (including both the specular and diffuse reflection contributions) were collected in situ in the 7500–3900 cm^{-1} range, with a resolution of 4 cm^{-1} over 128 scans. The spectral sampling distance used for each scan was 2 cm^{-1}. The background was acquired using a gold mirror as reference sample. In total, 272 spectra were recorded, at four different positions for each sample (16 spectra for each binder).

1.1.3 Micro-Raman spectroscopy

Micro-Raman analysis was performed using a micro-Raman spectrometer (Renishaw 2000) equipped with a 785 nm diode laser, operating at the laser power on the sample (1.10 mW). The laser was focused onto the sample using a 50X objective lens, so that an area of about 2 μm in diameter was analysed. Spectra were recorded in the 2000–200 cm^{-1} spectral range, with a spectral resolution of 4 cm^{-1}. The integration time and the spectral sampling distance

used for each scan were 25 s and 1 cm^{-1}, respectively. For each scan, three acquisitions were recorded. The spectrometer was calibrated at the beginning of each measurement session by using the Raman signal from a silicon wafer at 520 cm^{-1}. No changes related to photochemical damage were observed on the samples. In total, 272 spectra were recorded, at four different positions for each sample (16 spectra for each binder).

1.1.4 Data analysis

Data analysis, employed in order to apply PCA to combined first derivative FT-NIR and micro-Raman spectra is discussed in detail in **Part I** of this thesis.
Micro-Raman and FT-NIR spectral datasets were pre-processed using the PCA method by means of The Unscrambler X version 10.3 software (CAMO).
Although micro-Raman spectra were registered between 2000 and 200 cm^{-1}, data analysis was performed in the 1800–750 cm^{-1} range, since the most important bands of binding media are located in this spectral region. The FT-NIR spectra were analysed in the 6000 and 3900 cm^{-1} range, where the signal was well defined and not affected by noise.
Each new combined spectrum includes 1575 data points, with the first 1050 derived from the FT-NIR spectrum abscissa, related to the spectral region 6000–3900 cm^{-1}, and the remaining 525 points taken from the micro-Raman spectrum abscissa in the 1800–750 cm^{-1} spectral region. Each combined spectrum is characterized by both fundamental and combination–overtone modes, as have been previously described in the FT-NIR and micro-Raman sections.

1.2 Results and discussion

1.2.1 FT-NIR and micro-Raman spectra of different binders

All raw FT-NIR and micro-Raman spectra acquired on neat binders, along with their corresponding first derivative spectra, are shown in **Appendix A**. For each of them, specific assignments for the main absorption/Raman bands are reported.

1.2.1.1 Proteinaceous binders

Firstly, we discuss the proteinaceous binders such as casein, egg white and glues; later, we analyse the egg yolk and whole egg, which differ from the other protein-based binding media for the lipid content [**4-5**].

FT-NIR spectra of casein, egg white and glues are shown in **Fig. 1A**, while the assignment of the most important near infrared bands for these binders is reported in **Table 2**, following the current literature [**5, 9**]. On the other hand, in **Fig. 1B**, the corresponding raw micro-Raman spectra are shown, whereas, the assignment for the most important bands is reported in **Table 3** [**1, 4**].

The raw FT-NIR spectra of these proteinaceous binding media do not show significant spectral differences. The characteristic signals of proteins are represented by the combination band of amide III (C-N stretching/N-H in plane bending), the first overtone of carbonyl stretching at about 4600 cm^{-1} and the combination band of the stretching and bending modes of N-H at around 4880 cm^{-1}. Furthermore, a weak absorption band, located at around 3988 cm^{-1} and ascribed to the first C-N-C stretching overtone in amides [**9**], can be observed. For all these binders, the methylenic overtones and combination bands result to be broad and weak, as can be seen in **Fig. 1A**.

Nevertheless, some differences can be observed: in the spectra of the glues, the combination band of asymmetric methylenic C-H stretching and bending is located at 4376 cm^{-1}, while in the spectra related to casein and egg white, this absorption band is located at around 4340 cm^{-1}. Furthermore, this absorption band results to be more intense than the symmetric one, always for the case of glues.

The raw micro-Raman spectra of casein, egg white and glues (**Fig. 1B**), are characterized by the vibrations related to amide I (at about 1665 cm^{-1}), CH_2 scissoring (at about 1450 cm^{-1}) and amide III (at about 1245 cm^{-1}). A sharp aromatic ring breathing band is present in all these spectra, which arises from phenylalanine amino acid residues (at about 1002 cm^{-1}). This last peak is especially pronounced in egg white and casein, for which phenylalanine is present in higher concentrations than in collagen-based glues (a total of approximately 12% of tyrosine plus phenylalanine is detected in egg white and casein, compared to approximately 4% total in animal glue) [**4**].

Furthermore, contributions due to tyrosine amino acid are present in all these protein-based binders (at around 826-850, 1210, and 1605-1610 cm^{-1}) [**4**].

Moreover, in the spectra of casein and egg white, peaks ascribable to tryptophan amino acid, at approximately 1550 and 880 cm^{-1}, and to phosphoproteins, at around at 954 cm^{-1}, can be found [**4**].

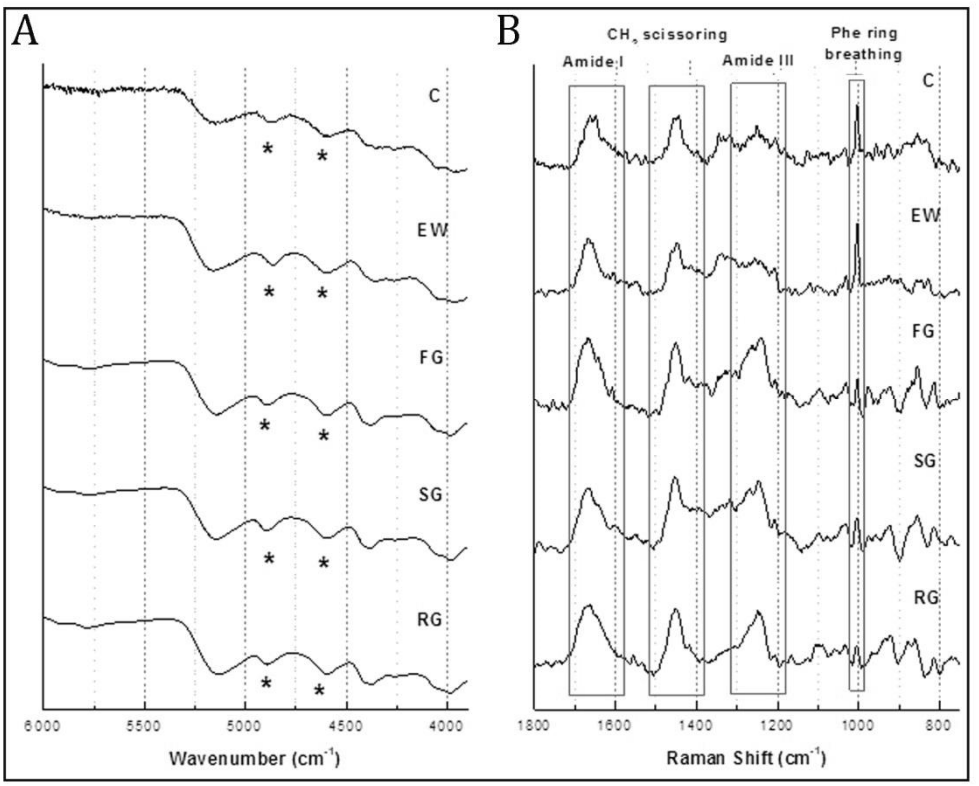

Fig. 1 FT-NIR (A) and Raman (B) spectra of C, EW, FG, SG and RG. Raman spectra are reported after background subtraction.

Table 2 Major peaks in the FT-NIR spectra (frequency shifts in cm-[1]) of C, EW, FG, SG and RG along with corresponding assignments.

EW	C	FG	RG	SG	Band Assignment	Ref.
5900	5900	5915	5915	5915	C-H aromatic/1st overtone $\nu_a(CH_2)$	[5, 9]
5740	5732	5780	5780	5780	1st overtone $\nu_s(CH_2)$	[5, 9]
5160	5146	5140	5140	5140	ν(OH)+ δ (OH)	[5, 9]
4865	4860	4896	4896	4896	ν_s(NH)+ δ (NH) [νN-H symmetric and Amide II deformation (N-H in plane bending) combination]	[5, 9]
4602	4612	4592	4592	4592	1st overtone ν(CO) amide I + amide III deformation (C-N stretching/N-H in plane bending)	[5, 9]
4352	4340	4376	4376	4376	$\nu_a(CH_2)$+ δ (CH_2)	[5, 9]
4260	4265	4260	4260	4260	$\nu_s(CH_2)$+ δ (CH_2)	[5, 9]
4050	4050	4045	4045	4045	CH combination (CH_2)/ 3rd overtone δ(CC)	[5, 9]
3984	3984	3988	3988	3988	1st overtone ν (C-N-C) amide	[9]

Table 3 Major peaks in the Raman spectra (frequency shifts in cm^{-1}) of C, EW, FG, SG and RG along with corresponding assignments.

EW	C	FG	RG	SG	Band Assignment	Ref.
1666	1658	1665	1666	1671	Amide I	[1, 4]
1605	1616	1607	1603	1603	Phe/Tyr	[4]
1550	1550				Trp	[4]
1446	1450	1450	1452	1450	C-H_2 scissoring	[1, 4]
1414	1410	1406	-	-	Aspartic and glutamic acids (C=O stretching)	[4]
1341	1322	1318	1312	1322	CH_2 deformation	[1, 4]
1256	1246	1246	1245	1246	Amide III	[1, 4]
1208	1212	1206	1209	1208	Phe/Tyr	[4]
1122	1120	-	-	-	C-CT stretching	[4]
1098	1090	-	-	-	ν(CC) (aliphatic)/C-N stretching	[1, 4]
1034	1041	1030	1033	1033	Phe	[4]
1002	1002	1002	1002	1002	Phe ring breathing	[1, 4]
-		975	-	-	C-C vibration δ (CH2)	[4]
954	955	-	-	-	C-C vibration, phosphate symmetric stretching	[4]
931	932	934	941	941	C-C stretching	[1, 4]
-	-	922	921	923	C-C vibration δ (CH3)	[4]
-	880				Trp	[4]
847	852	856	860	861	Tyr	[4]
827	826	-	-	-	Tyr	[4]
-	-	814	819	813	C-C stretching	[4]

The FT-NIR spectra related to egg yolk and whole egg, shown in **Fig. 2A**, highlight the methylenic combination bands and their overtones, in the ranges 4250-4350 cm^{-1} and 5600-5800 cm^{-1}, more intense in respect to the other protein-based binders, due to the lipid content of yolk. The shape and position of the methylenic combination bands from the lipid component in egg yolk/whole egg are different with respect to those from drying oils, thus providing distinctive features for their recognition. In particular, these combination bands in drying oils are located at about 4340 and 4265 cm^{-1}, while to lower wavenumbers in egg, at 4330 and 4260 cm^{-1}, respectively [**5**]. However, the main proteinaceous bands are detectable, as can be seen in **Fig. 2A** and in **Table 4**, where the assignment for the near infrared absorption bands for egg yolk/whole egg are reported, following the current literature [**5, 9**].

Concerning the corresponding Raman spectra (**Fig. 2B**), due to the presence of fatty acid esters, the characteristic carbonyl vibration at 1740 cm^{-1} is present [**4**]. Furthermore, bands arising from the following vibrations are predominant in their overall spectrum: at around 1302 cm^{-1} (in-phase methylene twist), at around 1442 cm^{-1} (scissoring mode of methylene) and at around 1655 cm^{-1} (*cis* double bond stretching). This last band is characterised by a frequency close to

amide I (at around 1665 cm^{-1}). Egg yolk and whole egg have the lowest values for polyunsaturated fatty acids in comparison with drying oils [**18**].
Nevertheless, characteristic proteinaceous bands are present, as can be seen in **Fig. 2B** and in **Table 5**, where the assignment for the most Raman bands are reported, according to literature [**1, 4, 18**]. A difference can be highlighted for the phenylalanine ring breathing (at around 1002 cm^{-1}) which results to be more intense in whole egg spectrum. Indeed, whole egg was prepared mixing one part of egg white with two parts of egg yolk and one part of vinegar. So, it is reasonable to assume a major proteinaceous content for it, with respect to the egg yolk.

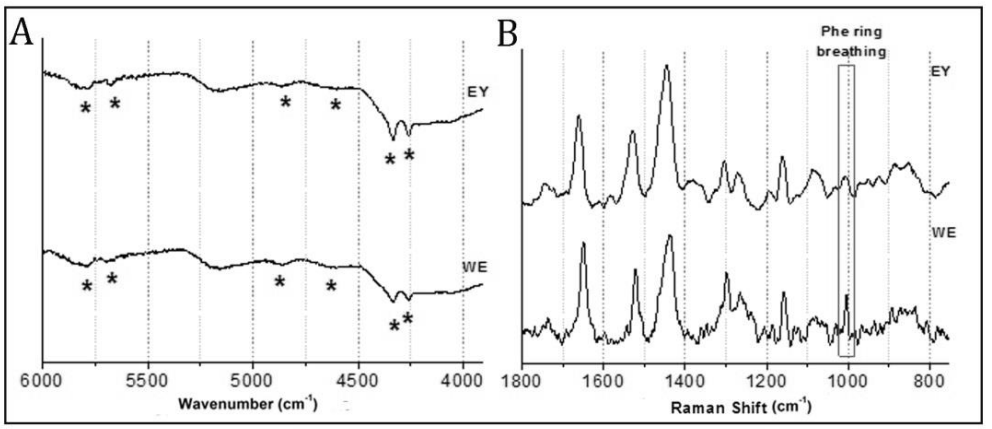

Fig. 2 FT-NIR (A) and Raman (B) spectra of EY and WE. Raman spectra are reported after background subtraction.

Table 4 Major peaks in the FT-NIR spectra (frequency shifts in cm^{-1}) of EY and WE along with corresponding assignments.

WE	EY	Band Assignment	Ref.
5808	5792	1st overtone $\nu_a(CH_2)$	[5, 9]
5680	5680	1st overtone $\nu_s(CH_2)$	[5, 9]
5160	5156	$\nu(OH)+\delta(OH)$	[5, 9]
4854	4860	$\nu(NH)+\delta(NH)$*	[5, 9]
4606	4602	1st overtone $\nu(CO)$amide I + amide III deformation (C-N stretching/N-H in plane bending)	[5, 9]
4330	4330	$\nu_a(CH_2)+\delta_a(CH_2)$*	[5, 9]
4260	4260	$\nu_s(CH_2)+\delta_s(CH_2)$*	[5, 9]
4058	4063	CH combination (CH_2)/ 3rd overtone $\delta(CC)$	[5, 9]

Table 5 Major peaks in the Raman spectra (frequency shifts in cm^{-1}) of EY and WE along with corresponding assignments.

EY	WE	Band Assignment	Ref.
1743	1740	C=O stretching	[4, 18]
1660	1660	Amide I/*cis* ν(C=C)	[1, 4, 18]
1526	1522	Trp	[4]
1442	1435	C-H_2 scissoring	[1, 4, 18]
1300	1300	In phase methylene twisting motion δ$(CH_2)_2$	[18]
1268	1264	Amide III	[1, 4]
1192	1187	Phe/Tyr	[4]
1156	1156	C-CT stretching	[4]
1081	1080	C-C,C-N stretching	[1, 4]
1028	1030	Phe	[4]
1005	1003	Phe ring breathing	[1, 4]
884	892	Trp	[4]
848	836	Tyr	[4]

1.2.1.2 Drying oils

FT-NIR spectra of drying oils are reported in **Fig. 3A**, while in **Table 6**, the assignment of the most important near infrared bands for these binders is given, following the current literature [**5, 9, 19-20**].

As regards drying oils, the main near infrared absorption bands are represented by the combination of methylenic C-H stretching and bending between 4250 and 4350 cm^{-1} and first CH_2 stretching overtone bands, which occur in the 5700-5800 cm^{-1} spectral range. The second overtone of ester carbonyl stretching mode is observed at 5176 cm^{-1}, whereas the combination of ester C=O and methylenic C-H stretching modes occurs at about 4690 cm^{-1}.

Raw FT-NIR spectra of drying oils do not show significant spectral differences between each other. Also, the FT-NIR spectrum related to stand-oil does not show any information which could be inferred about the effect of the heating process.

On the other hand, the major Raman bands are represented by symmetric rock in *cis* double bond (at about 1265 cm^{-1}), in-phase methylene twist mode (at about 1302 cm^{-1}), scissoring mode of methylene (at 1442 cm^{-1}), *cis* double bound stretching mode (at about 1655 cm^{-1}) and ester stretching (at about 1745 cm^{-1}), as can be seen in **Fig. 3B**. So, the Raman spectra of drying oils predominantly contain bands arising from vibrations of the hydrocarbon chains and it is possible to distinguish them from the Raman spectra of egg yolk/whole egg for the absence of proteinaceous bands.

As can be seen in **Fig. 3B**, the major difference between the different drying oils is located at the band 1655 cm^{-1} which is more intense for linseed oil and stand-oil. Linseed oil, indeed, contains around 52-55% of linolenic acid in its chemical

composition [**1, 18**], whereas poppy-seed oil 0.4-0.6% and walnut oil 10-15% [**18**]. Concerning stand-oil, accordingly to Zovi *et al.* [**21**], the heating process generates a double rearrangement of the polyunsaturated fatty acids into conjugated systems, which represents the first step to trigger Diels–Alder reactions. Nevertheless, a hydrogen abstraction from the methylene group located between two non-conjugated double bonds is also possible. This step can induce a radical addition and either combination or elimination reactions. According to the methylene radical delocalization or the double bond environment, additional products with conjugated double bonds can also be obtained.

In **Table 7** are reported the assignments for the main Raman bands, following the current literature [**18, 21-23**].

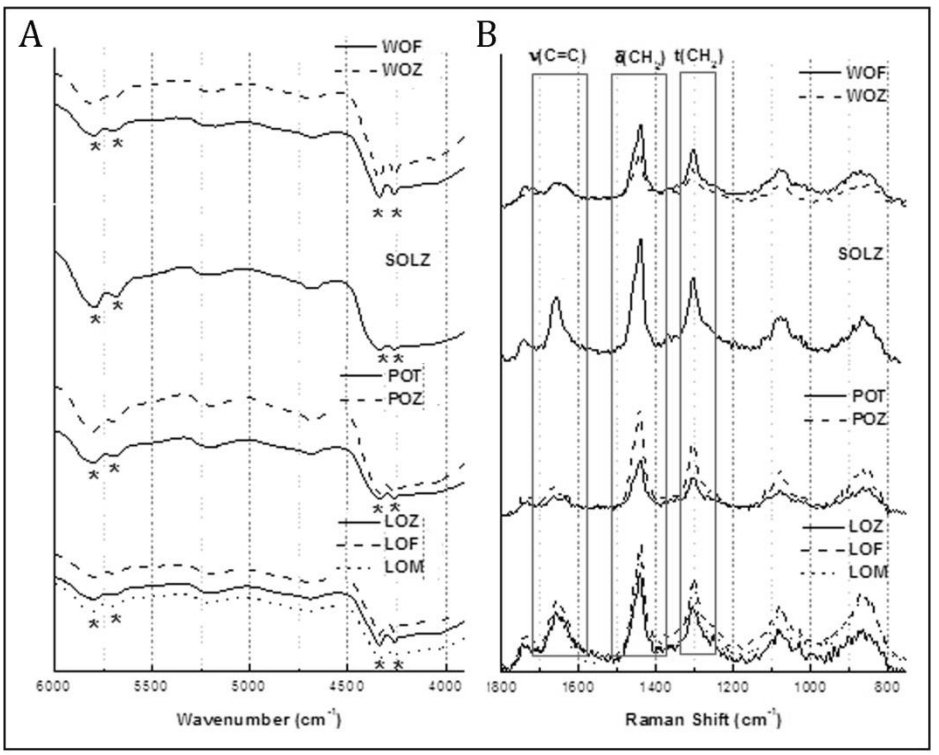

Fig. 3 FT-NIR (A) and Raman (B) spectra of drying oils. Raman spectra are reported after background subtraction. In **Table 1** all symbols are explained.

Table 6 Major peaks in the FT-NIR spectra (frequency shifts in cm^{-1}) of drying oils along with corresponding assignments.

Drying oil	Assignment	Ref.
5790	1st overtone $\nu_a(CH_2)$	[5, 9]
5676	1st overtone $\nu_s(CH_2)$	[5, 9]
5260	2nd overtone ν(C=O)	[9]
5176	2nd overtone ν(C=O) ester	[5, 9]
4686	ν(CH) + ν(C=O)	[5, 9, 19]
(4595)	[ν_s(CH) + ν(C=C)]	[20]
4340	$\nu_a(CH_2)$ + $\delta(CH_2)$	[5, 9]
4262	$\nu_s(CH_2)$ + $\delta(CH_2)$	[5, 9]

Table 7 Major peaks in the Raman spectra (frequency shifts in cm^{-1}) of drying oils along with corresponding assignments.

Drying oil	Assignment	Ref.
1746	Stretching ν(C=O) esters	[22, 23]
1655	Stretching ν(C=C) [*cis* dialkyl C=C double bond]	[18]
1445	Bending $\delta(CH_2)$	[18]
1302	In phase methylene twisting motion $\delta(CH_2)_2$	[18]
1267	Rocking deformation of *cis* dialkyl ethylenes r(CH=CH)	[18]
1085	Stretching ν(C-C)	[21]
864	Stretching ν(C-C)	[21]

1.2.1.3 Gums

FT-NIR spectra of gums, shown in **Fig. 4A**, are characterized by broad bands. The characteristic signals of polysaccharides are represented by the combination bands of O-H stretching and bending (at around 5140 cm^{-1}), of O-H bending and C-O stretching (at around 4800 cm^{-1}) and of C-H and C-C/C-O-C stretching modes (at around 4010 cm^{-1}) [**9**]. Also, a very broad band, ascribed to combination band of C-H stretching and bending [**9**], at about 4270 cm^{-1}, can be observed.

As regards the near infrared region, the main difference between two gums is represented by the combination band of O-H stretching and bending. In the spectrum of Tragacanth gum, this band is shifted of around 20 cm^{-1} towards longer wavenumbers in comparison with Arabic gum.

In **Table 8** are reported the assignments for the main near infrared absorption bands for these polysaccharide binding media, following the current literature [**9**]. Concerning Raman spectra, shown in **Fig. 4B**, there are no intense peaks in the 1800-1500 cm^{-1} spectral range and this differentiates the gums from the other binding media, previously described. These materials, indeed, do not contain aromatic or aliphatic C=C double bonds. Also, no amide I and amide III bands are present, in contrast to proteinaceous binders. The rather broad peaks in the 1500-1200 cm^{-1} region, are ascribed to C-H deformations, whereas

the peaks at lower wavenumbers are associated with C-C and C-O symmetrical stretching modes (1200-950 cm^{-1}) and C-O-C sugar ring vibrations (950-800 cm^{-1}). The Raman spectrum of Arabic gum shows a doublet at around 850 cm^{-1} (882 cm^{-1} and 841 cm^{-1}), whereas Tragacanth gum has a singlet (857 cm^{-1}). This feature is useful to distinguish between two gums. In **Table 9** are reported the assignments for the main Raman bands of these polysaccharide binding media, following the current literature [**1, 24**].

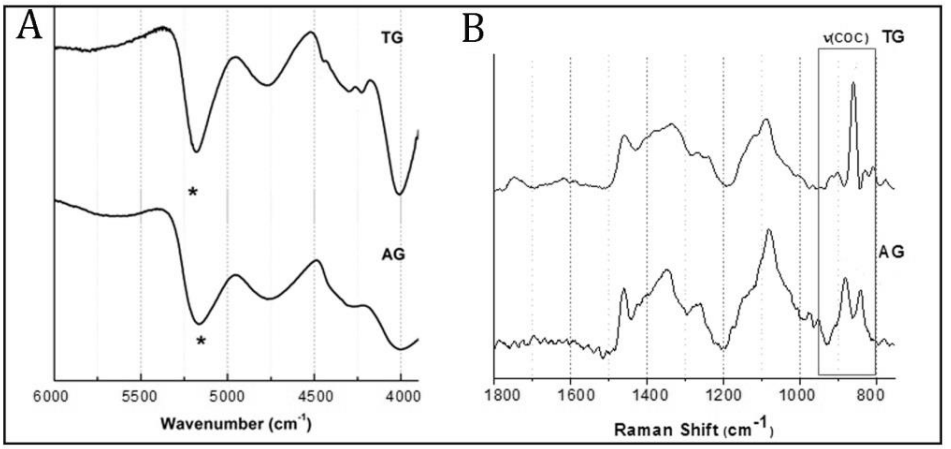

Fig. 4 FT-NIR (A) and Raman (B) spectra of Tragacanth gum and Arabic gum. Raman spectra are reported after background subtraction.

Table 8 Major peaks in the FT-NIR spectra (frequency shifts in cm^{-1}) of AG and TG along with corresponding assignments.

AG	TG	Band Assignment	Ref.
5164	5181	O-H stretching and HOH bending combination (O-H and HOH)	[9]
4761	4812	O-H bending and C-O stretching combination. O-H/C-O polymeric (.O-H and .C-O)	[9]
4268	4454-4228	C-H stretching and CH_2 deformation combination	[9]
4000	4016	C-H stretching and C-C (and C-O-C) stretching combination	[9]

Table 9 Major peaks in the Raman spectra (frequency shifts in cm^{-1}) of AG and TG along with corresponding assignments.

AG	TG	Band Assignment	Ref.
1460	1445	$\delta(CH_2)$ scissoring	[1, 24]
1348	1349	$\delta(CH_2)$ wagging	[1, 24]
1264	1250	$\tau(CH_2)$	[1, 24]
1078	1084	ν(COC) ether group (ring)	[1, 24]
974	-	$\delta(CH_3)$	[1, 24]
950	-	CC symmetrical stretching	[1, 24]
-	941	ν(COC)	[1, 24]
882	857	ν(COC)	[1, 24]
841		ν(COC)	[1, 24]

1.2.2 PCA applied to combined first derivative FT-NIR and micro-Raman spectra

In this section, the application of PCA to combined first derivative FT-NIR and micro-Raman spectra of all neat binders is evaluated.
Taking into account separately the two spectroscopic techniques, it is possible to describe each class of binders, as can be seen in the **Fig. S1** and **Fig. S2** in the **supplementary section**. Nevertheless, their combination enables to gather valuable information from the data, allowing a meaningful and rapid description of different binding media and a better differentiation between them. The application of a multivariate analytical tool, such as PCA, to combined spectra, indeed, provides the concomitant extraction of important information.
A significant percentage (83%) of the cumulative variability is explained by the first four PCs. PC1 explains 49% of the total variance contained in the data, whereas PC2, PC3 and PC4 explain 19, 11 and 4% of the total variance, respectively. In **Fig. 5** the two-dimensional score plot in the space defined by PC1 and PC2 is reported, showing four different data groups with good data separation: gums; drying oils; egg yolk and whole egg; glues, casein and egg white. The vibrations mainly responsible for sample distinguishing can be observed by inspection of the loading plots for each variable for the first and second principal components, as shown in **Fig.6**. In **Fig. 7**, **Fig. 8** and **Fig. 9** the loading plots of PC1 and PC2 are reported, highlighting the contributions which can be ascribed to polysaccharide-, lipid- and protein-based binding media, respectively. In these loading plots, the "plus" symbol is used to indicate that the 1st derivative contribution is concordant with the starting combined spectra, while a "minus" sign is used when its behaviour is reversed. Furthermore, the main contributions related to binders are highlighted by means of different colours/patterns.

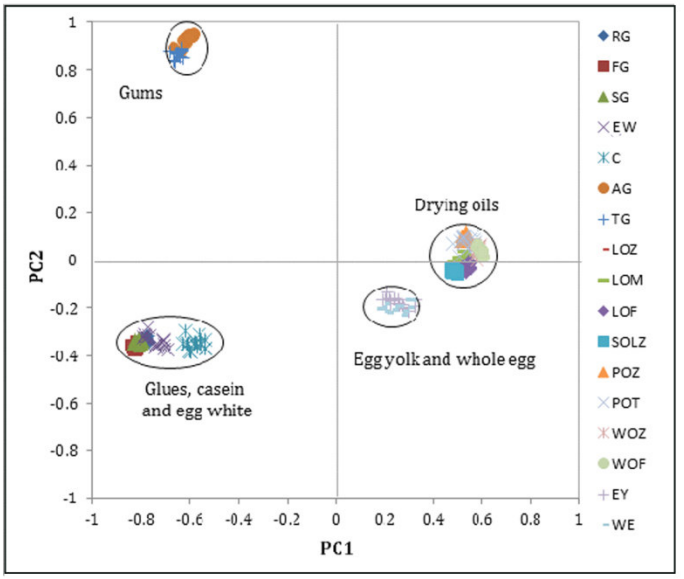

Fig. 5 PCA applied to combined FT-NIR and Raman spectra, taking into account all neat binding media: score plot of PC1-PC2.

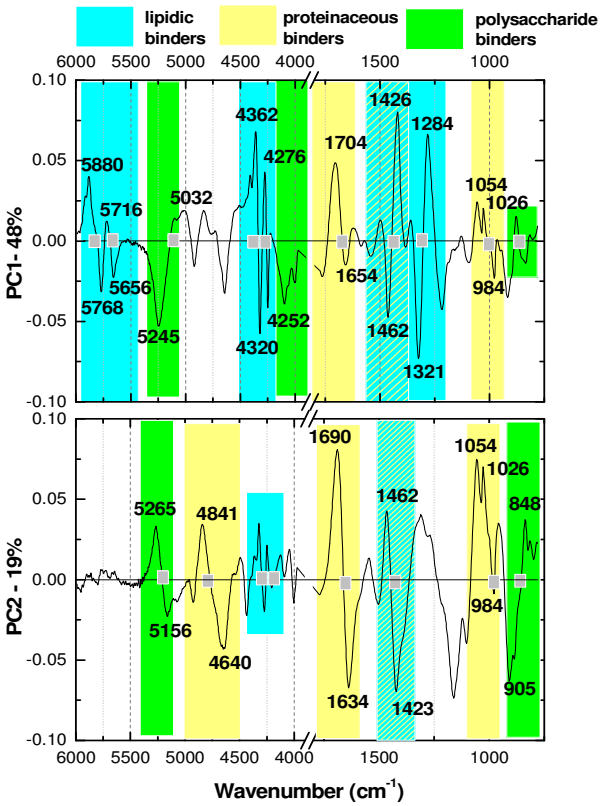

Fig. 6 PCA applied to combined FT-NIR and Raman spectra, taking into account all neat binding media: loading plots of PC1 and PC2.

AG and TG display a negative score value for PC1, whereas they have a positive score value for PC2 (**Fig. 5**). As can be seen in **Fig. 6** and **Fig. 7**, the greatest contributions to PC1 related to polysaccharide-based binding media are the combination band of O-H stretching and bending (at around 5140 cm^{-1}), the combination band of C-H and C-C/C-O-C stretching modes (at around 4010 cm^{-1}) [**9**] and the C-O-C sugar ring vibrations (950-800 cm^{-1}) [**1, 24**]. As regards PC2, the main highlighted polysaccharide vibrations are the combination band of O-H stretching and bending and the C-O-C sugar ring vibrations (as can be seen in **Fig. 6** and **Fig. 7**). So, the first two PCs describe this class of binders, immediately focusing on its principal spectral properties in NIR and Raman regions, but do not provide any differentiation between two gums.

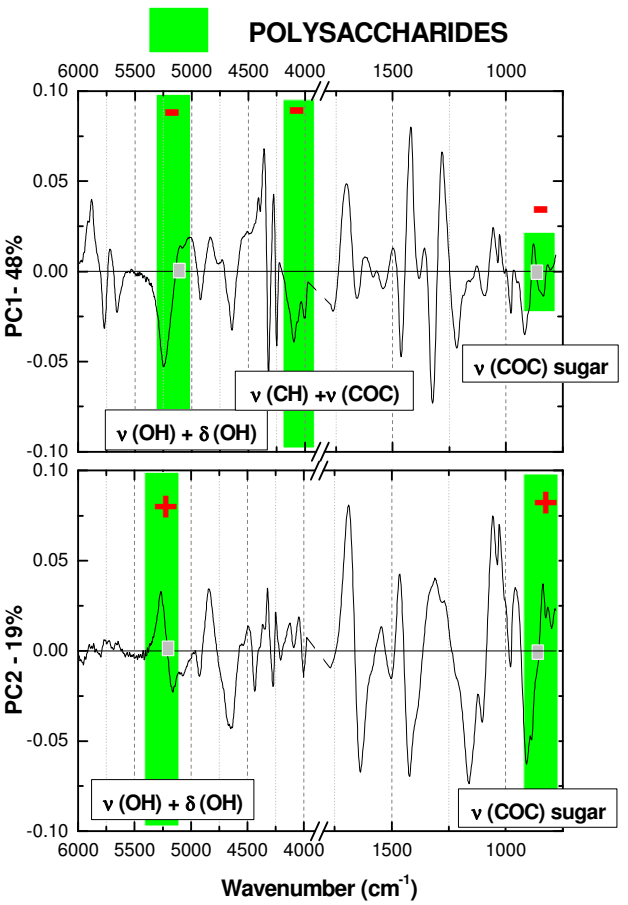

Fig. 7 PCA applied to combined FT-NIR and Raman spectra, taking into account all neat binding media: loading plots of PC1 and PC2, highlighting polysaccharide bands.

Drying oils show a positive score value for PC1, whereas result to be very close to a zero value for PC2, as can be seen in **Fig. 5**.

As regards lipid-based binding media, the loading plot of PC1, shown in **Fig. 6** and **Fig. 8**, is characterized by first CH_2 stretching overtone band (in the 5700-5800 cm^{-1} spectral range), combination band of methylenic C-H stretching and bending (between 4250 and 4350 cm^{-1}) [**5, 9**], scissoring mode of methylene (at 1442 cm^{-1}) and in-phase methylene twist mode (at about 1302 cm^{-1}) [**18**]. In PC2, the main lipidic contributions are related to combination band of methylenic C-H stretching and bending, in NIR region, and scissoring mode of methylene, in Raman region. These contributions cause a very low score value for PC2, because are opposed: the former is positive, while the latter is negative (**Fig. 5**).

Also for drying oils, this model immediately highlights their characteristic spectral bands. No differentiation between various drying oils is observed.

Concerning glues, C and EW, these display a negative score value for PC1, while a negative one for PC2 (**Fig. 5**).

As regards proteinaceous binders, in the loading plot of PC1 (**Fig. 6** and **Fig. 9**), specific contributions due to amide I (at about 1665 cm^{-1}), CH_2 scissoring (at about 1450 cm^{-1}) and phenylalanine ring breathing (at 1002 cm^{-1}) vibrations can be observed [**1, 4**]. Nevertheless, PC2 better describes protein-based binding media. Indeed, in the corresponding loading plot (**Fig. 6** and **Fig. 9**) intense contributions related to the combination band of the stretching and bending modes of N-H at around 4880 cm^{-1} [**5, 9**], amide I mode, CH_2 scissoring vibration and phenylalanine ring breathing mode, can be highlighted.

Going to focus on EY and WE, as can be seen in **Fig. 5**, they are located at an intermediate position between drying oils and the other protein-based binding media. As previously discussed, these binders are characterized by a lipid content, completely absent in C, EW and glues.

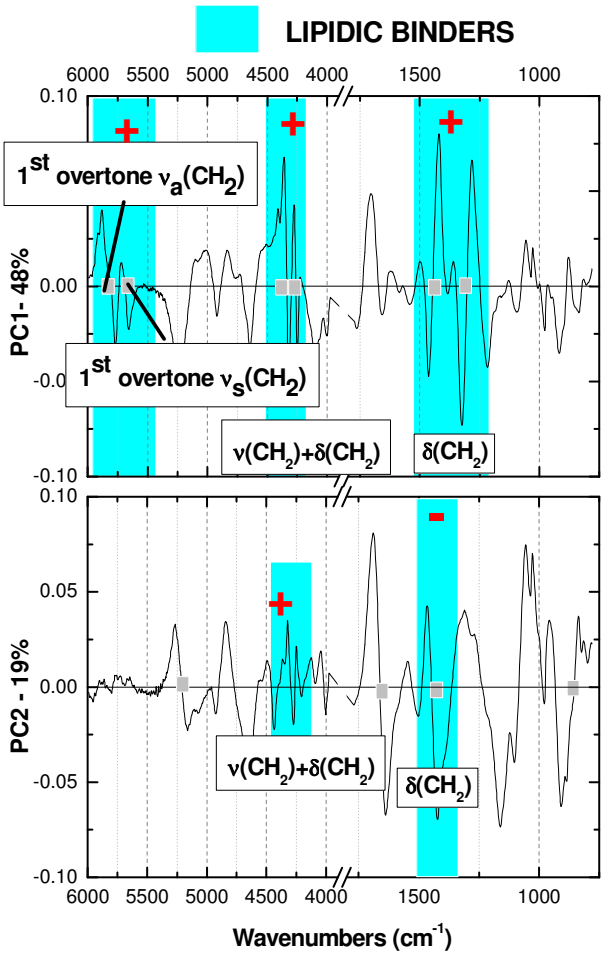

Fig. 8 PCA applied to combined FT-NIR and Raman spectra, taking into account all neat binding media: loading plots of PC1 and PC2, highlighting lipidic bands.

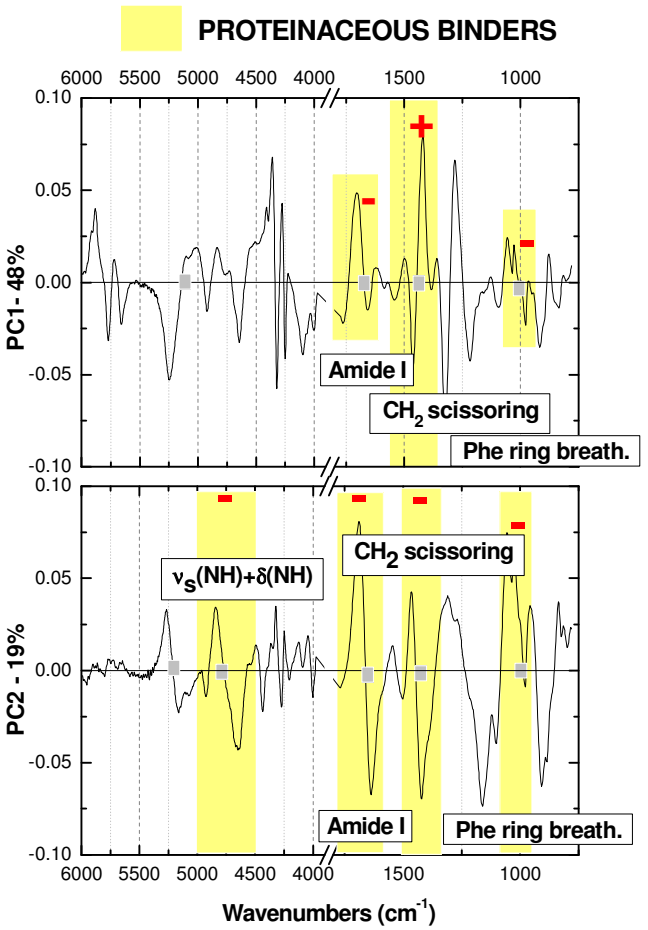

Fig. 9 PCA applied to combined FT-NIR and Raman spectra, taking into account all neat binding media: loading plots of PC1 and PC2, highlighting proteinaceous bands.

The score plot defined by PC2 and PC4 (**Fig. 10A**) is notably interesting, because a better differentiation between various classes of binders can be highlighted. A clear separation between AG and TG can be observed. EW and C are also distinguished between each other and from glues.

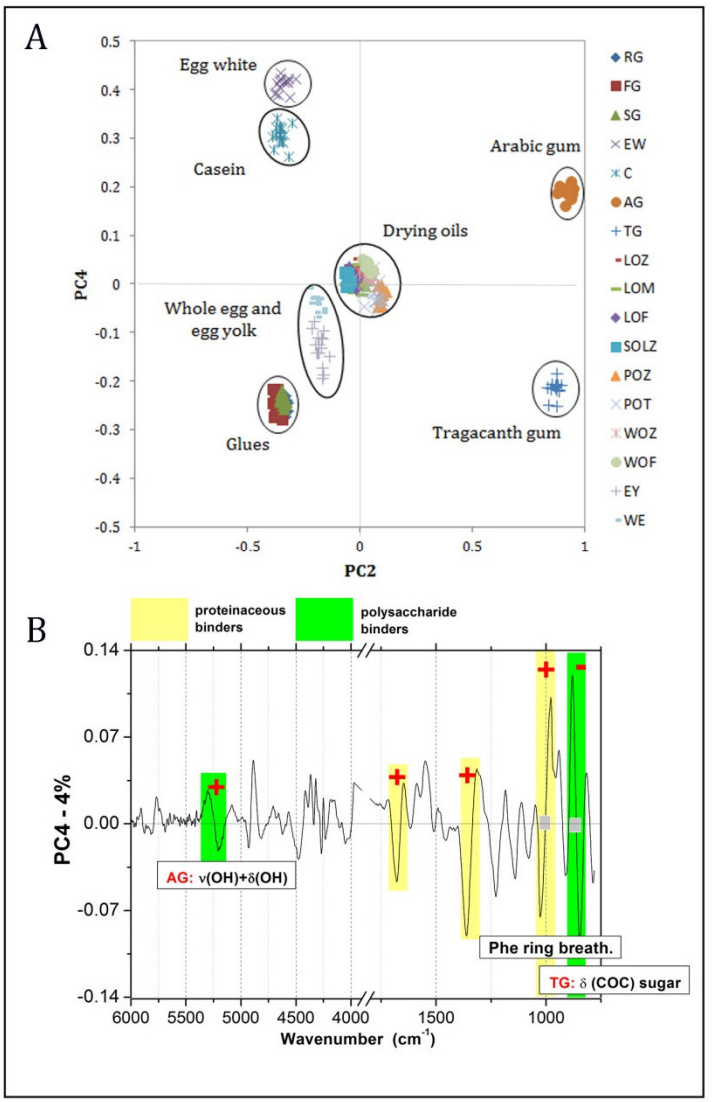

Fig. 10 PCA applied to combined FT-NIR and Raman spectra, taking into account all neat binding media: score plot of PC2-PC4 (A) and loading plot of PC4 (B).

The loading plot of PC4, reported in **Fig. 10B**, is, indeed, characterized by two main contributions: phenylalanine ring breathing and C-O-C ring vibration. This last contribution shows the specific frequency related to TG. This gum, as discussed above, shows in the corresponding Raman spectrum a characteristic singlet at 857 cm^{-1}, while in the same spectral range AG highlights a doublet

(882 cm^{-1} and 841 cm^{-1}) [**1, 24**]. Additionally, another minor contribution could be ascribed to gums: the combination band of OH stretching and bending. In this case, the corresponding frequency is 5180 cm^{-1}, which is close to that observed for AG.
Concerning phenylalanine ring breathing vibration, PC4 seems to describe the different content of this amino acid in proteinaceous binding media. The peak at 1002 cm^{-1}, as previously described, is especially pronounced in EW and C Raman spectra, for which phenylalanine is present in higher concentrations than in collagen-based glues (a total of approximately 12% of tyrosine plus phenylalanine is detected in egg white and casein, compared to approximately 4% total in animal glue) [**4**].

In **Table 10** a summary of the main spectral properties highlighted by this PCA model for the different classes of binding media is reported.

Table 10 Main near infrared and Raman bands, characteristic for different classes of binding media, highlighted by PCA applied to combined spectra referred to all neat binders.

Class of binders	FT-NIR	Micro-Raman
Polysaccharide-based	ν(OH)+δ(OH) ν(CH)+ν(COC)	δ(COC) sugar ring vibrations
Lipid-based	1st overtone CH_2 ν(CH_2)+δ(CH_2) [ν(OH)+ν(OH)]	δ(CH_2) ν(C-C)
Protein-based	ν(NH)+δ(NH) ν(OH)+ν(OH)	Amide I δ(CH_2) Phe ring breathing

1.3 Conclusions

Model films of protein-, polysaccharide- and lipid-based binding media have been analysed after a natural ageing of three months, highlighting the applicability of FT-NIR and Raman spectroscopies for their characterization. Assignment of main near infrared and Raman bands, revealed significant differences between spectra related to various classes of binders, which have been further highlighted by PCA applied to the corresponding combined first derivative FT-NIR and Raman spectra.

The application of PCA to combined first-derivative spectra immediately focused the main spectral properties, in both regions investigated, of these materials. The proposed method has provided a novel non-destructive approach for their identification and differentiation.

Additionally, the results described, highlighted the capability of this methodology to differentiate egg white and casein between each other and from glues, on the basis of different content in the amino acid phenylalanine. It has been also possible to distinguish between Arabic gum and Tragacanth gum. Nevertheless, no differentiation within drying oils or glues groups has been observed. This result indicates and suggests the need for further PCA modelling of each such group in order to fine-tune the analysis and to understand the characteristic features of the different classes of binders.

1.4 Supplementary material

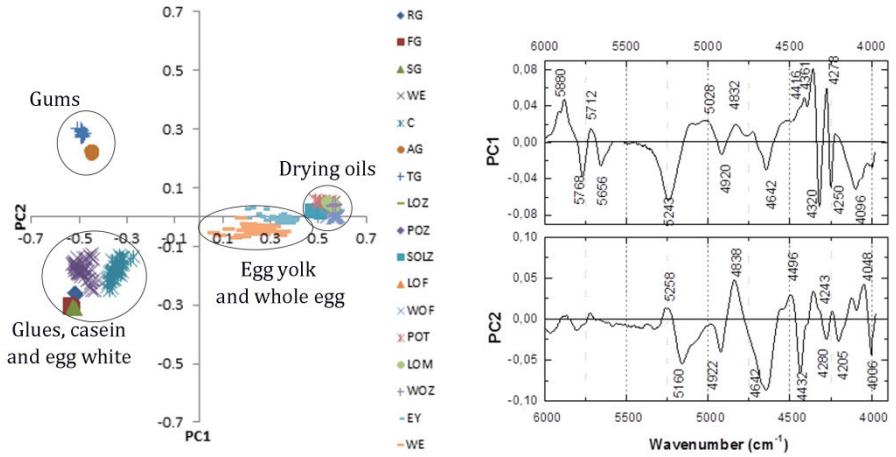

Fig. S1 Principal Component Analysis (PCA) of FT-NIR first derivative spectra of all neat binding media films: PC1-PC2 score is reported along with PC loadings related to the first two principal components. PC1 explains the 60% of the total variance contained in the data. PC2 explains only 15% of the total variance, corresponding with 75% of cumulative variability.

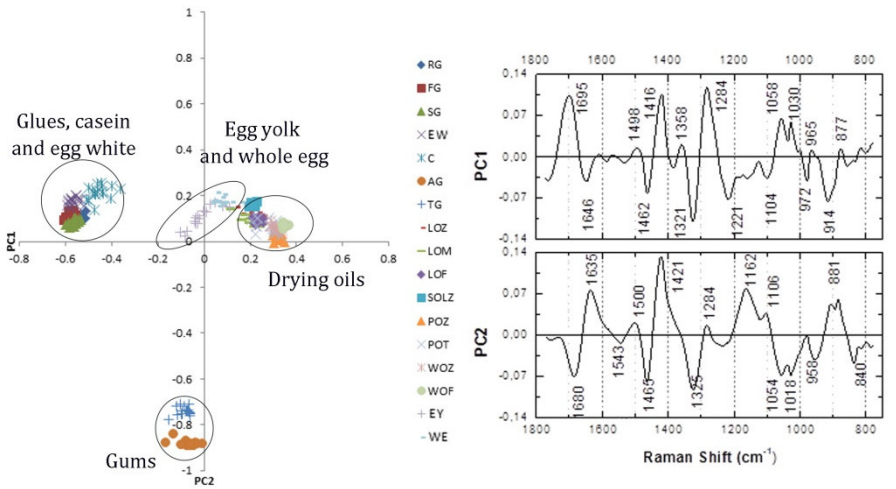

Fig. S2 Principal Component Analysis (PCA) of micro-Raman first derivative spectra of all neat binding media films: PC1-PC2 score is reported along with PC loadings related to the first two principal components. PC1 explains the 36% of the total variance contained in the data. PC2 explains the 30% of the total variance, corresponding with 66% of cumulative variability.

References

[1] P. Vandenabeele, B. Wehling, L. Moens, H. Edwards, M. De Reu, G. Van Hooydonk, Analysis with Micro-Raman Spectroscopy of Natural Organic Binding Media and Varnishes Used in Art, Anal. Chim. Acta. 2000, 407(1-2), pp 261-274.

[2] L. Burgio, R.J.H. Clark, Library of FT-Raman spectra of pigments, minerals, pigment media and varnishes, and supplement to existing library of Raman spectra of pigments with visible excitation, Spectrochim. Acta A 2001, 57, pp 1491-1521.

[3] M. Bouchard, D.C. Smith, Catalogue of 45 reference Raman spectra of minerals concerning research in art history or archaeology, especially on corroded metals and coloured glass, Spectrochim. Acta A 2003, 59, pp 2247-2266.

[4] A. Nevin, I. Osticioli, D. Anglos, A. Burnstock, S. Cather, E. Castellucci, Raman Spectra of Proteinaceous Materials Used in Paintings: A Multivariate Analytical Approach for Classification and Identification, Anal. Chem. 2007, 79(16), pp 6143-6151.

[5] M. Vagnini, C. Miliani, L. Cartechini, P. Rocchi, B.G. Brunetti, A. Sgamellotti, FT-NIR Spectroscopy for Non-Invasive Identification of Natural Polymers and Resins in Easel Paintings, Anal. Bioanal. Chem. 2009, 395(7), pp 2107-2118.

[6] M. Blanco, J. Coello, H. Iturriaga, S. Maspoch, C. De la Pezula, Near-infrared spectroscopy in the pharmaceutical industry, Analyst 1998, 123(8), pp 135R-150R.

[7] C. Pasquini, Near Infrared Spectroscopy: Fundamentals, Practical Aspects and Analytical Applications, J. Braz. Chem. Soc. 2003, Vol. 14, No, 2, pp 198-219.

[8] J. Workman, L. Weyer Practical Guide to Interpretative Near-Infrared Spectroscopy, CRC Press-Taylor and Francis, Boca Raton, 2007.

[9] D.A. Burns, E.W. Ciurczak (Eds.), Handbook of Near-Infrared Analysis, third edition, CRC Press-Taylor and Francis, Boca Raton, 2008.

[10] J. Cruz, M. Bautista, J.M. Amigo, M. Blanco, Nir-chemical imaging study of acetylsallicylic acid in commercial tablets, Talanta 2009, 80, pp 473-478.

[11] L.M. Reid, C.P. O'Donnell, G. Downey, Recent technologies advances for the determination of food authenticity, Trends Food Sci. Tech. 2006, 17(7), pp 344-353.

[12] R. Karoui, J. De Baerdemaeker, A review of the analytical methods coupled with chemometric tools for the determination of the quality and identity of dairy products, Food Chem. 2007, 102, pp 621-640.

[13] D. Lichtblau, M. Strlič, T. Trafela, J. Kolar, M. Anders, Determination of mechanical properties of historical paper based on NIR spectroscopy and chemometrics – a new instrument, Appl. Phys. 2008, 92(1), pp 191-195.

[14] A. Jurado-Lopez, M.D. Luque de Castro, Use of near infrared spectroscopy in a study of binding media used in paintings, Anal. Bioanal. Chem. 2004, 380, pp 706–711.

[15] T. Trafela, M. Strlic, J. Kolar, D.A. Lichtblau, M. Anders, D. Pucko Mencigar. B. Pihlar, Non-destructive Analysis and Dating of Historical Paper Based on IR Spectroscopy and Chemometric Data Evaluation, Anal. Chem. 2007, 79(15), pp 6319-6323.

[16] L. Masschelein-Kleiner, Ancient Binding Media, Varnishes and Adhesives, ICCROM, Italy, Rome, 1995.

[17] I. Bonaduce, L. Carlyle, M.P. Colombini, C. Duce, C. Ferrari, E. Ribechini, P. Selleri, M.R. Tine´, New Insights into the Ageing of Linseed Oil Paint Binder: A Qualitative and Quantitative Analytical Study, PLoS ONE. 2012. 7(11): e49333.

[18] E. Manzano, J. García-Atero, A. Dominguez-Vidal, M.J. Ayora-Cañada, L. Fermín Capitán-Vallvey, N. Navas, Discrimination of aged mixtures of lipidic paint binders by Raman spectroscopy and chemometrics, J. Raman Spectrosc. 2011, 43, pp 781-786.

[19] J.B. Lambert, H.F. Shurvell, R.G. Cooks, Introduction to Organic Spectroscopy, Macmillan Publ., New York, 1987.

[20] J.S. Shenk, J.J. Workman, M.O. Westrhaus, "Application of NIR spectroscopy to agricultural products" in D.A. Burns and Ciurczak E.W. (eds), Handbook of Near-Infrared Spectroscopy Marcel Dekker Inc., New York,2001, pp 419-474

[21] O. Zovi, L. Lecamp, C. Loutelier-Bourhis, C.M. Lange, C. Bunel, Stand reaction of linseed oil, J. Lipid Sci. Technol. 2011, 113, pp 616-626.

[22] D. Lin-Vien, N.B. Colthup, W.G. Fately, J.G. Grasselli, The handbook of Infrared and Raman characteristic frequencies of organic molecules, Academic Press, San Diego, 1991.

[23] H. Yang, J. Irudayaraj, Characterization of semi-solid fats and oils by fourier transform infrared photoacoustic spectroscopy, J. Am. Oil Chem. Soc. 2001, 78, pp 889-895.

[24] L. Brambilla, C. Riedo, C. Baraldi, A. Nevin, M.C. Gamberini, C. D'Andrea, O. Chiantore, S. Goidanich, L. Toniolo, Characterization of fresh and aged natural ingredients used in historical ointments by molecular spectroscopic techniques: IR, Raman and fluorescence, Anal. Bioanal. Chem. 2011, 401, pp 1827-1837

<u>Chapter 2</u>: Multivariate analysis of combined Fourier Transform Near-Infrared Spectrometry (FT-NIR) and Raman datasets for improved discrimination of drying oils

Abstract

This work explores the application of chemometric techniques to combined Raman and near infrared spectra for the analysis of lipidic paint binders (i.e. drying oils), materials that were widely used by artists throughout history, both individually and in mixtures. We prepared various model samples of the pure binders (linseed, poppy-seed and walnut oils) obtained from different suppliers.
These model samples were left to dry and characterized by Raman and reflectance near infrared spectroscopies. Multivariate analysis was performed by applying Principal Component Analysis (PCA) on the first derivative of the corresponding Raman spectra (1800-750 cm^{-1}), near infrared spectra (6000-3900 cm^{-1}) and their combination to test whether spectral differences allowed the distinction of samples on the basis of their composition. The combination of the methylenic C-H stretching and bending region and the ν(C=C) stretching region were found to be especially useful for differentiation among the different binders and companies.
Comparison with HPLC data was furthermore realized to check the PCA results.

THIS CHAPTER HAS BEEN PUBLISHED ON "APPLIED SPECTROSCOPY" [S. Carlesi, M. Ricci, C. Cucci, J. La Nasa, C. Lofrumento, M. Picollo, M. Becucci, Multivariate Analysis of Combined Fourier Transform Near-Infrared Spectrometry (FT-NIR) and Raman Datasets for improved Discrimination of Drying Oils, Appl. Spectrosc. 2015, 69(7), pp 865-876]

Introduction

Analytical procedures such as separation methods (gas chromatography, capillary electrophoresis, and liquid chromatography), mass spectrometry, and hyphenated techniques are well suited for the analysis of organic compounds [**1-2**], even if their relatively large sample consumption, long experimental times, complex sample preparation, and the multi-parameter operating conditions imply obvious problems for the analyses of samples of historical interest. Vibrational spectroscopic methods, i.e., infrared (IR) and Raman, extensively used in the cultural heritage field [**3-4**], have the potential to overcome the aforementioned issues.

The differentiation of the organic materials classes, such as the proteinaceous and the fat-based classes, is relatively straightforward by spectroscopic analysis. In contrast, the differentiation of organic compounds of the same class, for example, different kinds of glues or oils, is likely to be more challenging. Several methods of multivariate analysis have been used [**5-7**] to simplify the classification of spectra. One of the most commonly applied is Principal Component Analysis (PCA) [**8**]. PCA can be used to explain the variance–covariance structure of a set of data by the original variables' linear combination that form a new set of independent coordinates, called Principal Components (PCs). The PCs are hierarchically ordered to describe the largest variance of the dataset, so that most of the information from the original dataset can be accounted for by a smaller number of variables. The application of PCA to large spectral datasets can therefore be exploited to extract meaningful information to support the spectra classification, but it is not always sufficient to identify different compounds belonging to the same organic class [**9**].

Although IR and Raman are often referred to as complementary spectroscopic techniques, their joint application for quantitative analysis (calibration or classification) does not necessarily result in a gain [**9-10**]; hence, in this work we investigated the potential of applying PCA to combined near-infrared (NIR) and Raman and first derivative spectra. To our knowledge, this application is novel with respect to previous published work, and its introduction is aimed at increasing the differentiation capability among compounds belonging to the same organic class. Recently, Fourier transform (FT)-Raman and fibre optic reflectance spectra, originating from the same samples, were combined for the identification of binder materials, bound pigments, and pigment–binder interactions in a range of lead-based paints [**9**]. It was pointed out that the quality of PCA was greatly improved by using combined spectra, giving a more accurate classification for the differentiation of proteinaceous and polysaccharide-based media in paint mixtures. Bueno *et al.* [**10**] used the combination of Raman and FT-IR methods into a single dataset to improve statistical differentiation of gunshot residues. The combined data, obtained from the same analyte, enhanced any potential statistical differentiation between the two non-equivalent samples.

In this study, drying oils that have been commonly and traditionally used as binding media by artists throughout history were analysed by means of FT-NIR and micro-Raman. The combination of these two vibrational spectroscopic methods provides complementary information, due to the different physical processes involved, there is the possibility to obtain deeper insight into the characteristic structural and binding properties of the investigated compounds.

Lipidic paint binders consist of triglycerides condensed into a wide range of fatty acids, together with small amounts of other compounds, such as sterols and vitamins. The differences among the various binders lie mostly in their relative fatty acid composition. Thus, the characterization of drying oils in paintings is a complex task, complicated by the natural drying and the spontaneous aging processes, due to a complex set of reactions. Oils are classified as drying oils when they undergo oxidation and crosslinking reactions to form solid films after exposure to light and oxygen. Linseed oil is the most common binder oil, because of its excellent performance in terms of pigment dispersion, drying time, optical transparency, and resulting film stability [**11**].
Stand-oil is generated by heating linseed oil to near 300 °C for a few days in the absence of air; it is highly viscous and forms coatings that are more elastic than those produced by linseed oil itself [**12**]. Drying oils are characterized by a high content of unsaturated fatty acids (>50%) [**13**].

2.1 Materials and methods

2.1.1 Materials

Four representative typologies of drying oils were chosen for this study: linseed oil, walnut oil, poppy oil, and stand-oil (originated from linseed oil). The drying oils examined in this study were obtained from different manufacturers. Oils produced from different manufacturers were purchased from international stores. The producers are labelled with randomly selected letters (**Table 1**): F, M, T, and Z.
Linseed oil was produced by F, M, and Z; walnut oil by F and Z; and poppy seed oil by T and Z. Stand-oil from a single source (Z) was analysed.

Table 1 Drying oils analysed.

Typology	Company	Symbol
Linseed Oil	**Z**	**LOZ**
Linseed Oil	**M**	**LOM**
Linseed Oil	**F**	**LOF**
Poppy seed Oil	**Z**	**POZ**
Poppy seed Oil	**T**	**POT**
Walnut Oil	**Z**	**WOZ**
Walnut Oil	**F**	**WOF**
Stand Oil	**Z**	**SOLZ**

All these drying oils were individually applied as a film on a microscope glass slide and left to dry on a shelf for three months before analysis. Thirty-two

model samples were prepared. These drying oils have to be considered as "fresh" binding media because the drying process has not already been completed (according to previous studies, an oil paint can be regarded as aged only one year after its preparation [**12-13**]).
Polyunsaturated fatty acids in triacylglycerol molecules are subjected to oxidative cleavage of the double bond, present in fatty acid hydrocarbon chains, possibly forming a polymeric network of saturated fatty acids that appears as a solid paint film. Also, compounds such as dicarboxylic fatty acids, hydroxycarboxylic acid, and other oxidized derivatives are formed as a result of aging of the drying oil [**14-15**].
Table 2 shows the typical fatty acids composition of the various drying oils for a better interpretation of the corresponding differences between the Raman and FT-NIR spectral features [**14**].

Table 2 Typical fatty acid composition (%) of the drying oils.[a] [14]

Binder	Palmitic acid C16:0	Stearic acid C18:0	Oleic acid C18:1	Linoleic acid C18:2	Linolenic acid C18:3
Linseed	7-8	3.4-4.6	18.5-22.6	14.2-17.2	52-55
Poppy seed	10-14	2.5-3.2	16-24	56-70	0.4-0.6
Walnut	6.4-7.5	1.3-2.0	14-20	57-62	10-15

[a] Each reported fatty acid is described by two numbers: the first one represents the length of the chain, while the second one indicates the number of unsaturations

2.1.2 Fourier Transform-Near Infrared (FT-NIR) measurements.

We measured FT-NIR reflectance spectra by using a portable ALPHA FT-IR spectrometer (Bruker Optics) equipped with an external reflection module. Total reflection spectra (including both the specular and diffuse reflection contributions) were collected in situ in the 7500–3900 cm^{-1} range, with a resolution of 4 cm^{-1} over 128 scans. The spectral sampling distance used for each scan was 2 cm^{-1}. The background was acquired using a gold mirror as reference sample. In total, 128 spectra were recorded, at four different positions for each sample.

2.1.3 Micro-Raman spectroscopy

Micro-Raman analysis was performed using a micro-Raman spectrometer (Renishaw 2000) equipped with a 785 nm diode laser, operating at the maximum available laser power on the sample (1.10 mW). The laser was focused onto the sample using a 50X objective lens, so that an area of ~2 μm in diameter was analysed. Spectra were recorded in the 2000–200 cm^{-1} spectral

range, with a spectral resolution of 4 cm^{-1}. The integration time and the spectral sampling distance used for each scan were 25 s and 1 cm^{-1}, respectively. For each scan, three acquisitions were recorded. The spectrometer was calibrated at the beginning of each measurement session by using the Raman signal from a silicon wafer at 520 cm^{-1}. No changes related to photochemical damage were observed on the samples.
In total, 128 spectra were recorded, at four different positions for each sample (16 spectra for each type of drying oil).

2.1.4 High-Performance Liquid Chromatography Coupled with Electrospray Ionization and Quadrupole Time-of-Flight Mass Spectrometry (HPLC-ESI-QTOF) analysis

High-performance liquid chromatography coupled to electrospray ionization and quadrupole time-of-flight (HPLC-ESI-QTOF) analyses were carried out using a 1200 Infinity HPLC, coupled with a quadrupole time-of-flight tandem mass spectrometer 6530 Infinity QTOF detector by a Jet Stream ESI interface (Agilent Technologies). The HPLC conditions were as follows: Poroshell 120 EC-C18 column (3.0 mm X 35.0 mm, 2.7 μm particle size) with a Zorbax eclipse plus C-18 guard column (4.6 mm X 12.5 mm, 5 μm particle size), flow rate of 0.3 mL/min, and column temperature of 45 °C. Separation was achieved using a gradient of methanol (eluent A) and iso-propanol (eluent B). The elution gradient was programed as follows: 90% A for 5 min, followed by a linear gradient to 90% B in 25 min, and then held for 5 min. The ESI conditions and the tandem mass spectrometry experimental setup were adapted from previous work [**16**].

2.1.5 Data analysis

Micro-Raman and FT-NIR spectral datasets were pre-processed using the PCA method by means of The Unscrambler X version 10.3 software (CAMO). Although micro-Raman spectra were registered between 2000 and 200 cm^{-1}, data analysis was performed in the 1800–750 cm^{-1} range, since the most important bands of drying oils are located in this spectral region [**17-18**]. The FT-NIR spectra were analysed in the 6000 and 3900 cm^{-1} range, where the signal was well defined and not affected by noise. After pre-processing, spectra were loaded into a data matrix; each spectrum-row represented the sample, whereas each wavenumber-column was the variable.
The micro-Raman and FT-NIR datasets were treated separately. There are several different causes that can lead to random noise in Raman and FT-NIR spectra, thus making the identification of spectral bands more difficult,

particularly in computational analyses, as in the present work. To identify small differences in the original spectra, first derivatives of the spectral data were obtained before extracting the PCs.
In detail, micro-Raman spectra were subjected to baseline subtraction, average reduction of variables (factor two), and first derivative calculation. To perform the transformation of average reduction, a minimum of two variables was chosen, obtaining a new spectral data step of 2 cm^{-1}. The first derivative transformation was made by applying the Savitzky–Golay algorithm [**19**]. The derivative algorithm used in this study permits a simultaneous smoothing of the spectra (15 data points, second order polynomial), which reduces the noise produced by the derivative transformation. The FT-NIR spectra were subjected to the Savitzky–Golay derivative algorithm (15 data points, second order polynomial) without any other pre-processing.
Both the FT-NIR and micro-Raman spectra were vector normalized, because the use of absolute peak heights could lead to erroneous sample classification [**9**]. Principal component analysis was applied to the combined first derivative FT-NIR and micro- Raman spectra in the region 6000–3900 cm^{-1} together with the 1800–750 cm^{-1} region. The combined spectra were obtained as follows: the 128 pre-processed FT-NIR and Raman spectra were combined into 128 spectra, generating a new set of ''combined first derivative FT-NIR-Raman'' spectra, 16 for each typology of drying oils.
The uncertainty test was performed to estimate the significance of the variables. Successively, PCA was performed by using the nonlinear iterative partial least squares algorithm. This model was validated by leave-one-out cross-validation. Finally, the PCA model was further validated by a test set, consisting of a series of 32 spectra. These spectra were acquired on the same samples (four spectra for each type of drying oil).
To check our results and considerations, linseed and walnut oils were further analysed by means of HPLC-ESI-QTOF. This comparison was possible as the analysed drying oils are fresh binding media, thus their drying process was still incomplete.

2.2 Results and discussion

2.2.1 Raw and first derivative Fourier Transform Near-Infrared (FT-NIR) spectra

Fourier transform near infrared spectra of drying oil films are reported in **Fig. 1**. The assignment of the most important bands for each oil spectrum is given in **Table 3**, following the current literature [**20-23**].

The raw spectra of the eight lipidic standards do not show significant spectral differences (**Fig. 1**), but when considering their derivative transformation (**Fig. 2**), some distinctive features clearly appear, especially in the 5980–5590 and 4800–4000 cm^{-1} spectral ranges. In particular, the first derivative maxima and minima, which correspond to the inflection points of the original FT-NIR spectra, show different relative intensity ratios and wavenumbers [**20**]. Looking back on the correspondence between the zero-crossing-point first derivative and the maximum or minimum in the original FT-NIR spectrum, first derivative spectra enable better individuation of the main absorption bands.

In the 4800–4200 cm^{-1} spectral region, zero first derivative related to the combinations of the methylenic antisymmetric C–H stretching and bending is observable at 4340 cm^{-1}, whereas that of the methylenic symmetric C–H stretching and bending is at 4261 cm^{-1}.

An initial observation was that the intensity of many of these peaks in the first derivative spectra, reported in **Fig. 2** (namely, those at 4252, 4276, 4320, and 4360 cm^{-1}), follows the content in polyunsaturated fatty acids. Also, the drying oils show a different trend in the 4500– 4350 cm^{-1} spectral range; especially, the first derivative stand-oil spectrum that shows a shift toward lower wavenumbers for the antisymmetric combination band (at 4335 cm^{-1}). Moreover, analysis of the 5980–5590 cm^{-1} spectral region shows the same trend for intensities of the peaks. Also, it highlights that the zero-crossing points first derivative, referred to the first overtone of antisymmetric and symmetric methylenic C–H, is not exactly coincident for all types of oils, as shown in **Fig. 2** and reported in **Table 3**. Again, the first derivative stand-oil spectrum shows a shift toward lower wavenumbers for the overtone band (at 5685 cm^{-1}).

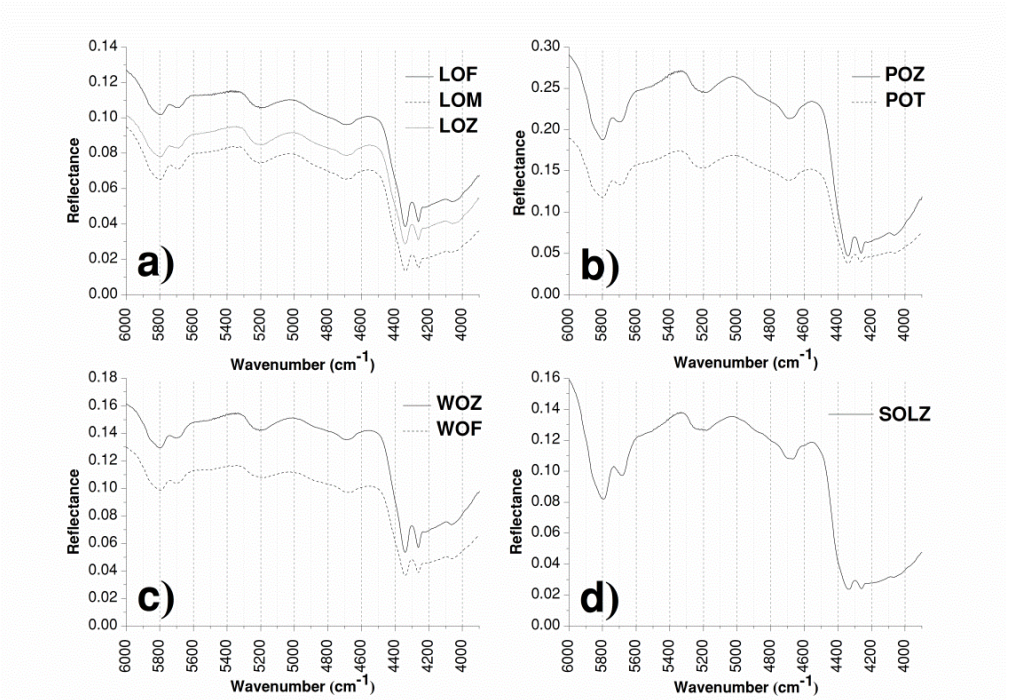

Fig. 1 FT-NIR spectra of the drying oils shown in the range 6000-3900 cm^{-1}.

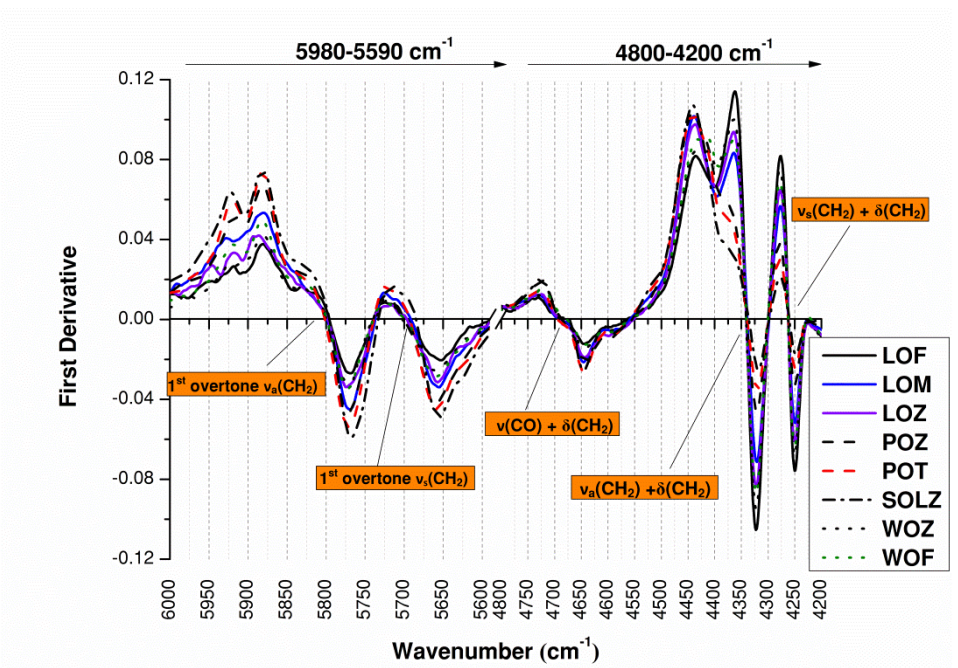

Fig. 2 First derivative FT-NIR spectra of the drying oils shown in the ranges 5980-5590 and 4800-4000 cm^{-1}.

Table 3 Major peaks in the FT-NIR spectra (frequency shifts in cm^{-1}) of the eight different drying oils compared to current reference values and assignments.

LOZ	LOF	LOM	WOZ	WOF	POZ	POT	SOLZ	cm^{-1}	Functional group	Assignments	Ref.
5792 (s-sh)[a]	5796 (s-sh)	5798 (s-sh)	5800 (s-sh)	5800 (s-sh)	5800 (s-sh)	5802 (s-sh)	5796 (s-sh)	5794	$-CH_2-$	1st overtone antisymmetric stretching $\nu_a(CH)$	[20-21]
5698 (s-sh)	5694 (s-sh)	5688 (s-sh)	5704 (s-sh)	5700 (s-sh)	5698 (s-sh)	5694 (s-sh)	5685 (s-sh)	5698	$-CH_2-$	1st overtone symmetric stretching $\nu_s(CH)$	[20-21]
							5258 (m-br)	5260	.C=OOH	2nd overtone stretching ν(C=O) Acids, carboxylic	[21]
5202 (m-br)	5200 (m-br)	5205 (m-br)	5202 (m-br)	5190 (m-br)	5181 (m-br)	5205 (m-br)	5181 (m-br)	5179	.C=OOR	2nd overtone stretching ν(C=O) Acids and esters	[20-21]
4707 (m-br)	4707 (m-br)	4707 (m-br)			4707 (m-br)	4707 (m-br)	4707 (m-br)	4707	-COOR	stretching ν(CH) + stretching ν(C=O)	[20-21]
			4690 (m-br)	4680 (m-br)				4690		stretching ν(CH) + stretching ν(C=O)	[22]
4595 (vw)	4597 (vw)	4597 (vw)	4597 (vw)	4600 (vw)	4610 (vw)	4597 (vw)	4604 (w)	4595	-HC=CH-	symmetric stretching $\nu_s(CH)$ + stretching ν(C=C)	[23]
4340 (s-sh)	4340 (s-sh)	4340 (s-sh)	4340 (s-sh)	4340 (s-sh)	4340 (s-sh)	4340 (s-sh)	4335 (s-sh)	4340	$-CH_2-$	antisymmetric stretching $\nu_a(CH)$ + bending δ(CH)	[20-21]
4261 (s-sh)	4261 (s-sh)	4261 (s-sh)	4261 (s-sh)	4261 (s-sh)	4261 (s-sh)	4261 (s-sh)	4261 (s-sh)	4261	$-CH_2-$	symmetric stretching $\nu_s(CH)$ + bending δ(CH)	[20-21]
4060 (w-sh)	4060 (w-sh)	4062 (w-sh)	4063 (w-sh)	4063 (w-sh)	4063 (w-sh)	4067 (w-sh)	4063 (w-sh)	4060	$-CH_2-$	Combination bending	[21]

[a]sh (sharp); br (broad); m (medium); s (strong); w (weak); sd (shoulder)

Table 4 Major peaks in the Raman spectra (frequency shifts in cm-1) of the eight different drying oils compared to current reference values and assignments.

LOZ	LOM	LOF	WOZ	WOF	POZ	POT	SOLZ	cm-1	Assignment	Ref.
1735 (m-br)[a]	1735 (m-br)	1735 (m-br)	1732 (m-br)	1734 (m-br)	1734 (m-br)	1734 (m-br)	1735 (m-br)	1740 1730	Stretching ν(C=O) esters	[24-25]
1654 (s)	1658 (s)	1654 (s)	1652 (m)	1652 (m)	1654 (m)	1660 (m)	1654 (s)	1655	Stretching ν(C=C) [*cis* dialkyl C=C double bond]	[18]
1441 (s-sh)	1441 (s-sh)	1441 (s-sh)	1441 (s-sh)	1441 (s-sh)	1441 (s-sh)	1441 (s-sh)	1441 (s-sh)	1440	Bending $\delta(CH_2)$	[18]
1306 (s-sh)	1303 (s-sh)	1303 (s-sh)	1303 (s-sh)	1303 (s-sh)	1303 (s-sh)	1303 (s-sh)	1303 (s-sh)	1300	In phase methylene twisting motion $\delta(CH_2)_2$	[18]
(1265) (w)	(1265) (w)	(1260) (w)	(1262) (w)	(1258) (w)	(1258) (w)	(1258) (w)	(1262) (w)	1265	Rocking deformation of *cis* dialkylethylenes r(CH=CH)	[18]
1072 (s-br)	1078 (s-br)	1078 (s-br)	1078 (s-br)	1078 (s-br)	1078 (s-br)	1078 (s-br)	1075 (s-br)	1085	Stretching ν(C-C)	[26]
865 (s-br)	865 (s-br)	862 (s-br)	862 (s-br)	870 (s-br)	862 (s-br)	867 (s-br)	865 (s-br)	864	Stretching ν(C-C)	[26]

[a]s (strong); m (medium); w (weak); sh (sharp); br (broad)

2.2.2 Raw and first derivative micro-Raman spectra

The raw micro-Raman spectra of the drying oils (**Fig. 3**) are characterized mainly by the vibrations corresponding to the hydrocarbon chains. The assignment of the most important bands (**Table 4**) follows current literature [**18, 24-26**].

As expected, by analysing the first derivative spectra, the intensity variation among the different oils appears mainly in the region between 1800 and 1500 cm^{-1}, where the stretching of ν(C=C) cis double bond is located (**Fig. 4**). The signal corresponding to the ν(C=O) stretching vibration is shifted at higher wavenumbers in stand-oil spectra. The related zero-crossing-point first derivative is located at about 1735 cm^{-1} (**Fig. 4**). Furthermore, other small differences are evident for the ν(C–C) stretching at 865 cm^{-1} (**Fig. 4**).

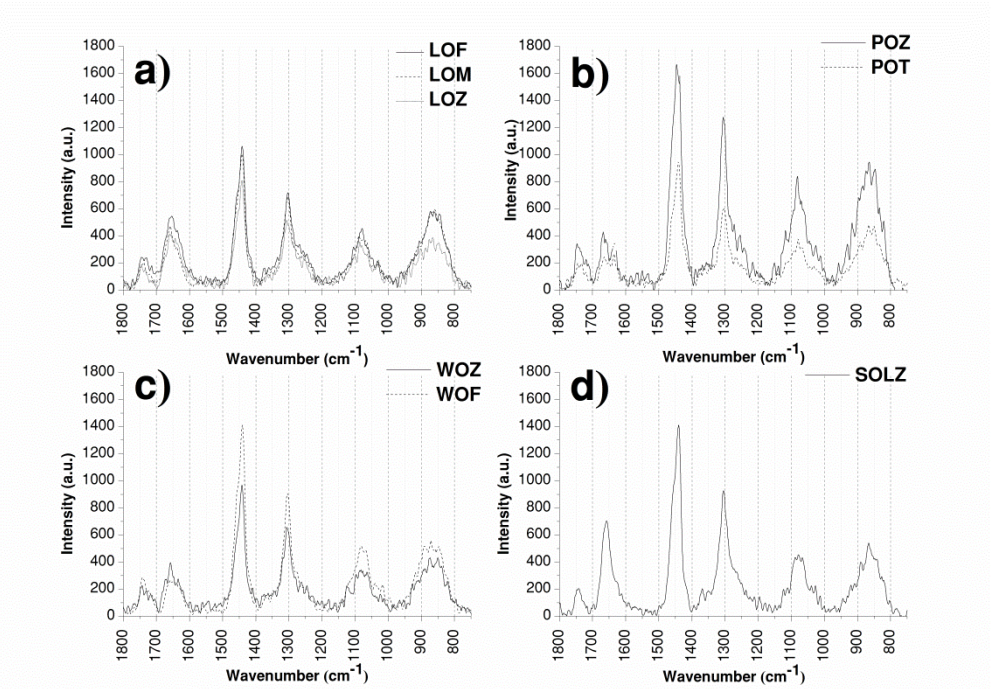

Fig. 3 Raman spectra of drying oils in the range 1800-750 cm^{-1} after background subtraction.

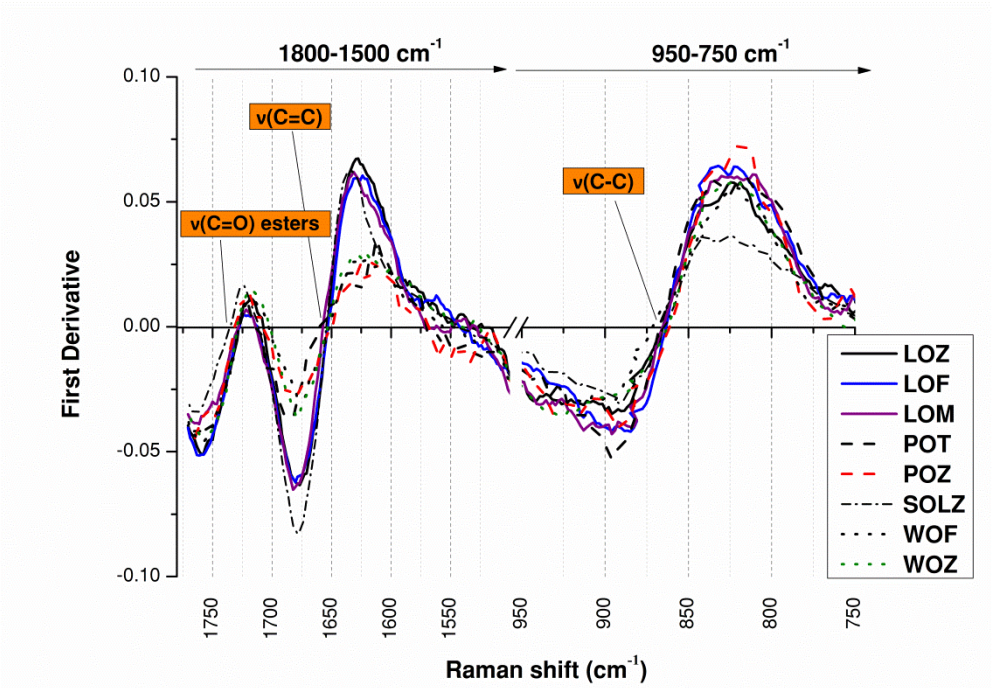

Fig. 4 First derivative micro-Raman spectra of the drying oils shown in the ranges 1800-1500 and 950-750 cm^{-1}.

2.2.3 Principal Component Analysis

Fig. 5 shows the combined first derivative FT-NIR-Raman spectra for each typology of drying oils. Each new combined spectrum includes 1575 data points, with the first 1050 derived from the FT-NIR spectrum abscissa, related to the spectral region 6000–3900 cm^{-1}, and the remaining 525 points taken from the micro-Raman spectrum abscissa in the 1800–750 cm^{-1} spectral region. Each combined spectrum is characterized by both fundamental and combination–overtone modes, as have been previously described in the FT-NIR and micro-Raman sections.

Principal component analysis has been applied to the separated first derivative spectra, and their score plots together with the relative PC loadings are shown in the **Supplemental material** (**Fig. S1** and **Fig. S2**). Only the results concerning PCA to the combined spectra are discussed in detail.

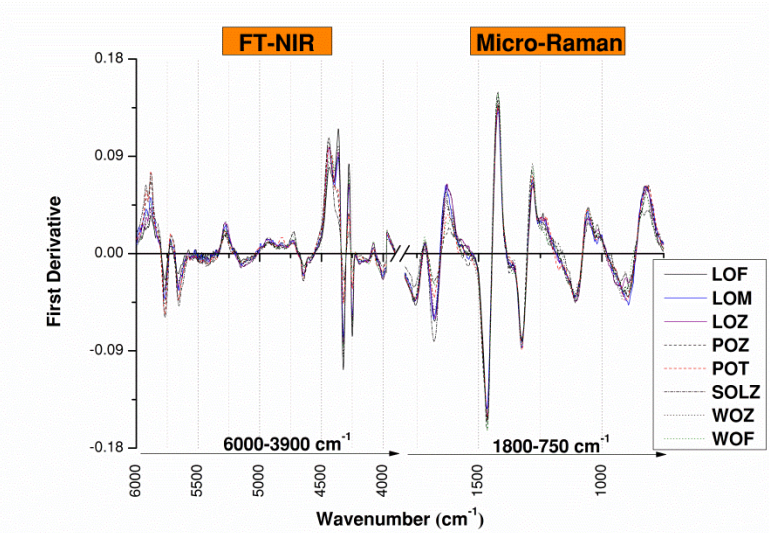

Fig. 5 Combined first derivative FT-NIR-Raman spectra for each typology of drying oils. The break is the demarcation between the NIR (left) and micro-Raman (right) contributions.

Of note, for linseed oils, PCA applied to first derivative micro-Raman spectra highlighted a homogenous trend for the different samples, whereas PCA of first derivative FT-NIR spectra revealed dissimilarities in samples obtained from the various manufacturers, mainly due to a different contribution of methylenic C–H stretching and bending combination bands. Alternatively, PCA of first derivative FT-NIR spectra of walnut oils revealed a homogenous behaviour between the two selected manufacturers. Furthermore, PCA of micro-Raman first derivative spectra did not completely separate walnut from poppy seed oils. On the contrary, PCA on the pre-processed combined spectra grouped satisfactorily the different typologies of drying oils and also somehow differentiated the various manufacturers (**Fig. 6**).

Fig. 6a reports the loading plots of the first three PCs identified by the uncertainty test and is useful to describe the statistical model; they can be used to define the most significant spectral range contributing to each PC. A significant percentage (86%) of the cumulative variability was explained by the first three PCs. PC1 explains 68% of the total variance contained in the data, whereas PC2 and PC3 explain 14 and 4% of the total variance, respectively.

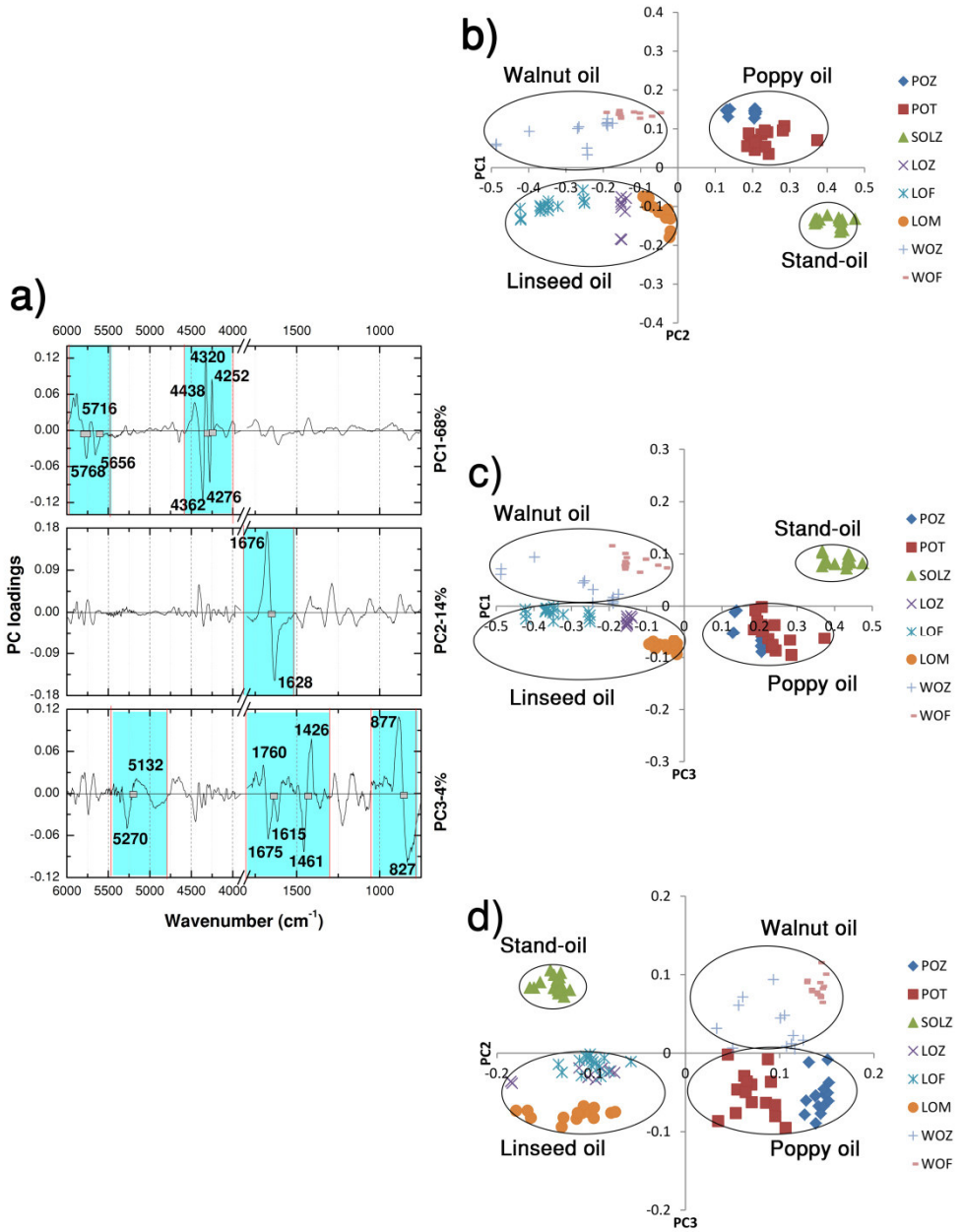

Fig. 6 PCA applied to combined FT-NIR–Raman spectra: loadings of PC1, PC2, and PC3 (a) and score plots of PC1-PC2 (b), PC1-PC3 (c), and PC2-PC3 (d).

PC1 highlights a major contribution by the FT-NIR dataset, whereas PC2 is most influenced by the micro-Raman dataset; in addition, PC3 shows an equal contribution by both datasets (**Fig. 6a**).

As shown in **Fig. 6**, the greatest contributions to PC1 are due to the regions between 5980 and 5590 cm^{-1} and between 4560 and 4200 cm^{-1}. Furthermore, PC1 shows the first derivative maximum at 4438 cm^{-1} (**Fig. 6a**), which is characteristic of stand-oil and poppy seed oils, a feature that all other oils have associated to a second maximum at 4360 cm^{-1} (**Fig. 2**).
By observing the loading plot for PC2 (**Fig. 6a**), the most relevant spectral region is that between 1730 and 1560 cm^{-1}.
Analysing the score plot PC1-PC2 shown in **Fig. 6b**, PC1 differentiates linseed and walnut oils (with a negative score) from the rest of the samples (with a positive score), whereas PC2 separates walnut and poppy seed samples (positive values) from stand-oil and linseed oils (negative values). Thus, the four classes of oils are grouped into four separated clusters.
Linseed oils present a negative score for PC1 (**Fig. 6b**); they are indeed characterized by intense methylenic C–H stretching and bending combination bands, as pointed out in the FT-NIR section. Moreover, PC1 underlines a separation among the three linseed oil different manufacturers based on these vibrations.
This characteristic could lead us to hypothesize that the aforementioned differences highlighted by PC1 might be related to the contribution from the combination band of C–H stretching and bending vibrations of both the methylene groups located between non-conjugated bonds, and the methylene groups situated along the hydrocarbon chains. Indeed, LOF (see drying oil symbols in **Table 1**) showed the highest negative score for PC1, whereas LOM showed the lowest score, following a similar trend with respect to the related linolenic acid content (three non-conjugated double bonds).
The most reactive site is represented by the methylenic group as a result of the aging process of a drying oil that resides between double bonds where the autoxidation reactions start [**26-27**], and it is reasonable to hypothesize a major contribution of such peculiar methylenic groups in the resulting combination band of methylenic stretching and bending. Indeed, the trend of the various oil groups is in accordance with the corresponding polyunsaturated fatty acids content, as evidenced in **Table 2**. LOF is the richest, among the linseed oils, in polyunsaturated fatty acids content, so it dries faster than the other oils.
In addition, PC2, for which linseed oils have a negative score (**Fig. 6b**), reveals the high content of ν(C=C) cis double bonds, which is characteristic of this type of drying oil. Linseed oil has a lot of linolenic acids in its triglycerides composition, and it is characterized by a faster drying process than other typologies of drying oil [**14**].
Walnut oils display a negative score for PC1, whereas they have a positive score for PC2 (**Fig. 6b**). They are characterized by intense combination bands

between 4400 and 4000 cm^{-1} (represented by PC1), like linseed oils, but they have a lower amount of ν(C=C) cis double bonds (represented by PC2), like poppy seed oils, with respect to linseed oil. Hence, walnut oils show an intermediate trend. PC2 displays a little separation between the two walnut oil manufacturers. Therefore, a major content of unsaturation could be hypothesized for WOZ, which is closer to linseed oils for both PCs.

Poppy seed oils are located in the spatial region characterized by positive values for both PC1 and PC2 (**Fig. 6b**). PC1 displays a high contribution due to the spectral region between 6000 and 5600 cm^{-1}. Moreover, the positive score for PC1 is also due to the maximum at 4438 cm^{-1}, which is related to the combination band of antisymmetric methylenic C–H stretching and bending (**Fig. 2**). In addition, PC2 reveals a lesser contribution of ν(C=C) cis double bonds stretching for poppy seed oils. Hence, these PCs underline the minor content of polyunsaturated fatty acids, such as linolenic fatty acid, for both the poppy seed oils, with respect to linseed oil.

Although there is no clear spectral evidence regarding the effect of the heating process, stand-oil shows a clear separation from the rest of the analysed oils in all the score plots (**Fig. 6**). In the score plot PC1-PC2 (**Fig. 6b**), stand-oil has a positive score for PC1 and a negative score for PC2. PC1 indicates that stand-oil is characterized by combination and overtone bands related to antisymmetric methylenic C–H stretching and bending modes as poppy oils. A high content of double bonds is, instead, underlined by PC2 (**Fig. 6b**), as for linseed oils.

The PCA for stand-oil is in agreement with the observation of the stand process of linseed oil studied by Zovi *et al*. [**26**]. They pointed out that this process can cause a series of possible reactions. The heating process generates a double rearrangement of the polyunsaturated fatty acids into conjugated systems, which represents the first step to trigger Diels–Alder reactions. Nevertheless, a hydrogen abstraction from the methylene group located between two non-conjugated double bonds is also possible. This step can induce a radical addition and either combination or elimination reactions. According to the methylene radical delocalization or the double bond environment, additional products with conjugated double bonds can also be obtained. All these processes cause a slowdown in the drying process with respect to linseed oil that has not been pre-treated, because this oil loses part of the methylenic groups between non-conjugated double bonds. The PC1-PC2 score plot highlights that stand-oil is similar to poppy seed oil, which is less rich in linolenic acid, but it is similar to linseed oil in terms of its high content in double bonds.

In PC3 (**Fig. 6a**), the greatest contributions are observable in the ranges between 1800 and 1570 cm^{-1}, 1500 and 1400 cm^{-1}, and 1000 and 750 cm^{-1} (**Fig. 6a**), whereas the FT-NIR range displays a contribution between 5500 and 5000

cm^{-1} (**Fig. 6a**). Walnut and stand-oils (positive scores) are separated from the rest of the samples (negative scores) (**Fig. 6c** and **Fig. 6d**).
The most negative values for PC3 within the linseed oil group are for LOM (**Fig. 6c** and **Fig. 6d**); these results confirm the previous hypothesis that it has different polyunsaturated fatty acid content. Furthermore, walnut oils, which are characterized by an intense contribution due to the $\delta(CH_2)$ bending (1445 cm^{-1}) and a less intense ν(C–C) stretching (860 cm^{-1}) compared to linseed oils, show a quite clear separation between the two different manufacturers. WOZ, indeed, has the smallest positive values. PC3 is also influenced by the ν(C=C) cis double bond stretching spectral range (**Fig. 6a**), so a minor contribution could be hypothesized for WOF. Consequently, in the score plot PC1-PC3 (**Fig. 6c**) WOZ is located again near to the linseed oils group. Stand-oil samples (SOLZ) show the highest values for PC1 (**Fig. 6c**), because of a more intense contribution by the $\delta(CH_2)$ scissoring mode of methylene, along with the lower intensity of the ν(C–C) stretching. The score plot PC1-PC2 (**Fig. 6b**) reveals a similar trend to that shown in the score plot PC1-PC3 (**Fig. 6c**). Moreover, the score plot PC2-PC3 (**Fig. 6d**) better underlines the previous observations obtained from the first two score plots regarding the separation of LOM from the other manufacturers.
To validate the results, an evaluation set of 32 samples (spectra acquired on the same drying oil films but not used in the creation of the model) was projected into the PCA model. Furthermore, the 32 spectra could be perfectly superimposed on the original clusters previously defined by the model for each type of drying oil (**Fig. 7**). PC1 describes 68% of the total variance contained in the unknown data, whereas PC2 and PC3 explain 13 and 3% of the total variance, respectively.

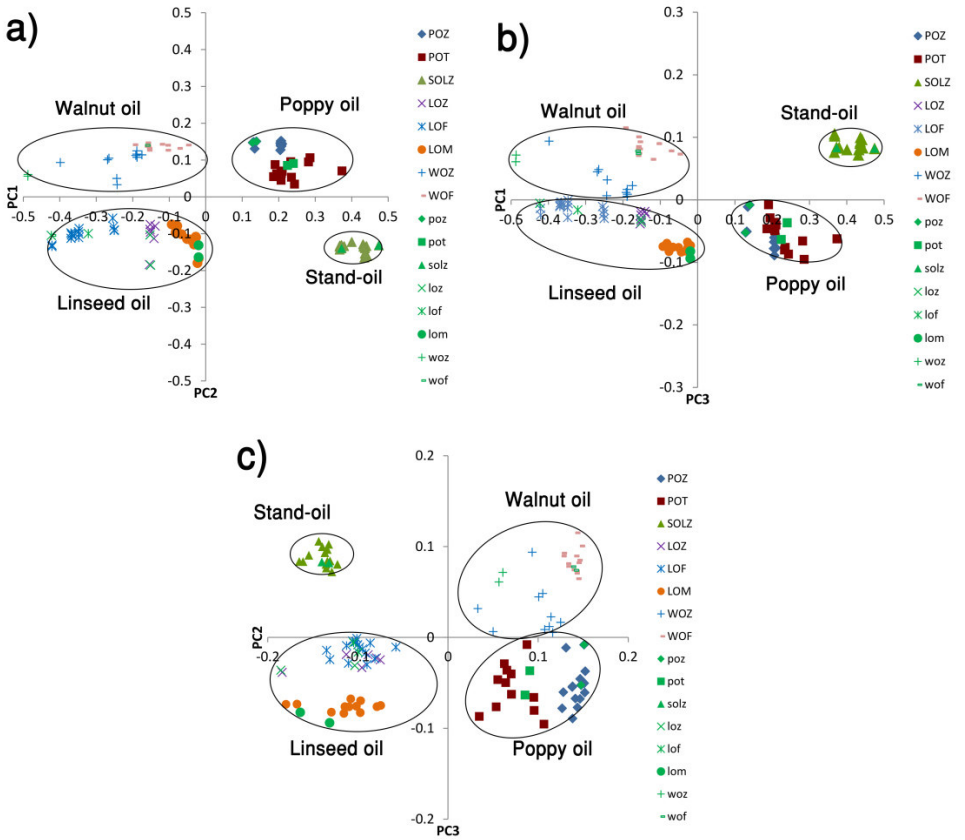

Fig. 7 Projection of the evaluation set comprising 32 samples into PCA model. The projected samples are shown in brilliant green. Every projected sample depicted uses the same shape of the specific type of drying oil. Score plots of PC1-PC2 (a), PC1-PC3 (b), and PC2-PC3 (c).

2.2.4 High-Performance Liquid Chromatography Coupled with Electrospray Ionization and Quadrupole Time-of- Flight Mass Spectrometry (HPLC-ESI-QTOF) analysis

Linseed and walnut oils were further analysed by means of HPLC-ESI-QTOF to verify the PCA results. For the characterization of the oils, 3–5 mg of each was submitted to dissolution in n-hexane (500 µL) in an ultrasonic bath at 60 °C with for 5 min. The extracted lipid fraction was dried under nitrogen flux, diluted with 500 µL of the elution mixture, and filtered with 0.45 µm PTFE filters (Grace Davison Discovery Sciences). Then, 10 µL of the filtered solution was diluted to 1 mL and injected into the HPLC system. The solvents used were isopropanol, n-hexane, and methanol (HPLC MS grade; Fluka).

The relative abundances for the main triglycerides identified in the analysed oils are reported in **Table 5**. A first differentiation between linseed and walnut oils is highlighted: linseed oils have a major content of triglycerides with linolenic acid (i.e., LnLnLn, LnLnL, LnLnP, LnLL), whereas linoleic acid (L) represents the most important fatty acid present in the chemical composition of walnut oil (i.e., LLL, LLO, LLP).

Taking into account the three types of linseed oil, linolenic acid (as a constituent of all the different triglycerides) is the major contributor for LOF, whereas it is a minor contributor for LOM. This difference confirms the previous PCA observations and our hypothesis that the combination bands of methylene C–H stretching and bending could be related to the methylene groups located between non-conjugated double bonds. Indeed, LOF showed the highest negative score for PC1, whereas LOM showed the lowest score, following a similar trend with respect to the related linolenic acid (three non-conjugated double bonds) content.

For walnut oils, WOZ has a linolenic contribution in its triglycerides composition, which is absent in WOF. This characteristic confirms our previous hypothesis. The PC2 displays a little separation between the two walnut oil manufacturers. Therefore, a major content of unsaturation could be hypothesized for WOZ, which results to be closer to linseed oils for both PCs.

Table 5 Relative abundances for the main triglycerides identified in the analysed oils.[a]

TAG[b]	LOM	LOZ	LOF	WOZ	WOF
LnLnLn	100	100	98	12	0
LnLnL	83	94	100	46	0
LnLnP	48	58	68	0	0
LnLL	95	86	93	85	0
LnLP	96	96	86	33	0
LLL	34	45	28	100	100
PLnP	18	28	32	0	0
LLP	0	0	0	58	76
LLO	72	76	68	83	78
PLP	0	0	0	0	14
LOP	12	11	10	38	55
LLS	13	12	15	0	0
OOL	0	0	0	58	62
OOP	59	57	68	14	24
POP	0	0	0	0	0
OOO	0	0	0	0	0
OLS	10	12	13	21	32
ALL	0	0	0	0	7
OOS	12	11	12	9	14
GLO	4	8	3	0	0
ALO	0	0	0	0	4
BLL	0	0	0	0	4

[a] Triglycerides are named according to the following fatty acid abbreviations: B, behenyl (C22:0); G, gadolenyl (C20:1); A, arachidyl (C20:0); Ln, linolenyl (C18:3); L, linoleyl (C18:2); O, oleyl (C18:1); S, stearyl (C18:0); P, palmityl (C16:0).

[b] TAG, triacylglyceride.

2.3 Conclusions

In this work, the analysis of FT-NIR and Raman spectra of different fresh drying oil films, together with the multivariate analysis of the combined spectra, demonstrates the potential of this analytical approach and provides a non-destructive novel method for differentiation among compounds belonging to the same organic class. In the analysis of real paintings, more problems should be faced as the materials change with time and more complex mixtures are present. We are currently working on the extension of this study to more realistic systems.

In particular, as the two techniques can highlight properties of different functional groups in the molecular systems, model films of drying oils have been analysed to provide complementary information. We developed a correct data pre-processing procedure able to avoid loss of information. For this procedure, FT-NIR and Raman spectra, individually and in combination, were analysed by applying PCA to highlight the spectral differences of the samples. Indeed, the differentiation among the drying oils and their manufacturers was greatly improved by using combined FT-NIR and Raman spectra (see Supplemental material for the PCA data relative to the separate FT-NIR and Raman datasets). The information from the spectral regions of the ν(C=C) fundamental stretching (1700–1600 cm^{-1}) and of methylenic stretching and bending combination bands (4800–4200 cm^{-1}) enabled an increase in the sensitivity and specificity of the statistical differentiation to be achieved. Our hypothesis is that this information is mostly carried by stretching and bending combination bands of methylenic groups located between non-conjugated double bonds and by the C=C stretchings. These structural features are those more directly involved by the chemical reactions that take place with cross-linking and aging of these drying oils. These two spectral regions are not commonly accessible to either FT-NIR or Raman spectroscopy alone. The application of PCA to combined different spectral regions allowed more information to be extracted from the spectral data, leading to a more complete analysis with respect to separate datasets.

The four types of drying oils studied—linseed, stand-oil, poppy seed, and walnut—are correctly separated by the chemometric PCA. Indeed, the differentiation between linseed and walnut oils from different manufacturers achieved by this approach was also confirmed by HPLC-ESI-QTOF analysis.

The non-destructive analysis method presented here in is a valuable and rapid tool able to distinguish organic compounds; moreover, it allows the identification of the producer of the binder in use (at least within the present set of samples). Theoretically, this analytical approach, which should be considered as a satisfactory procedure for the handling of the problem, can be

further expanded, taking into account other spectral regions for the creation of new combined spectra, and evaluating the dependence on the experimental conditions.

These results represent a step toward computer assisted analysis of artwork; however, more needs to be done to investigate the application of this method to real artwork, where the effects of pre-processing of products, substrate, and aging may become apparent. Furthermore, partial least squares discriminant analysis models could be applied to spectral intervals that are able to distinguish drying oils produced by different manufacturing plants.

2.4 Supplementary material

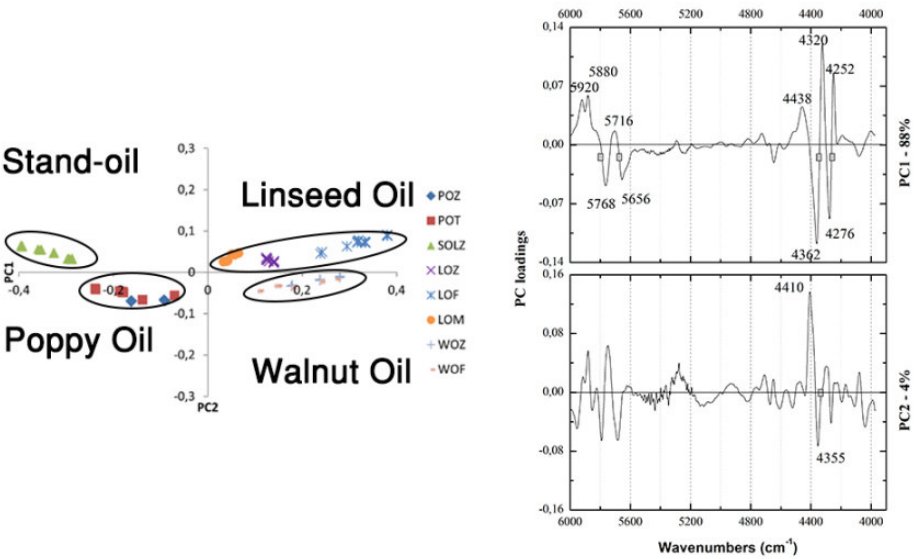

Fig. S1 Principal Component Analysis (PCA) of FT-NIR first derivative spectra of drying oils films: PC1-PC2 score is reported along with PC loadings related to the first two principal components. PC1 explains the 88% of the total variance contained in the data. PC2 explains only 4% of the total variance, corresponding with 92% of cumulative variability.

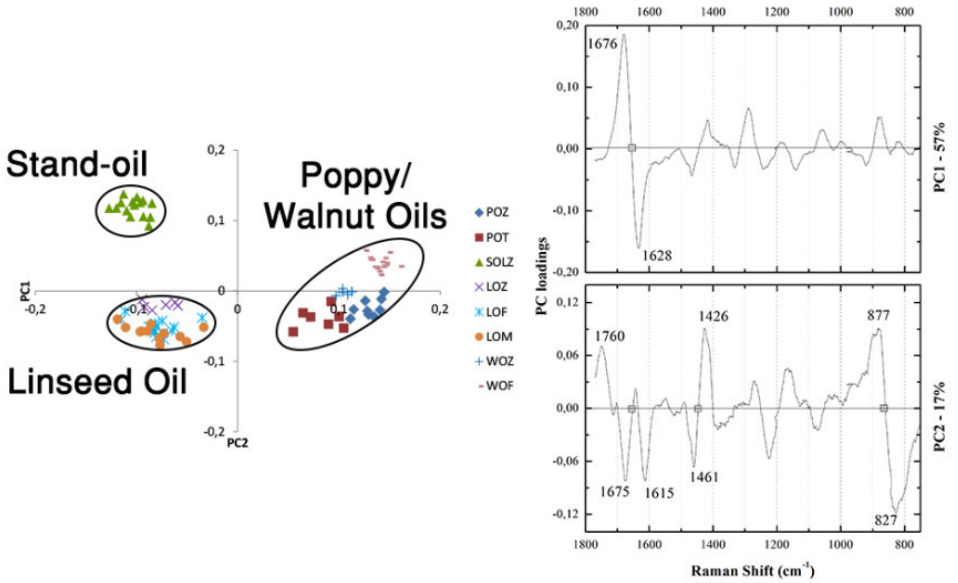

Fig. S2 Principal Component Analysis (PCA) of micro-Raman first derivative spectra of drying oils films: PC1-PC2 score is reported along with PC loadings related to the first two principal components. PC1 explains the 57% of the total variance contained in the data. PC2 explains the 17% of the total variance, corresponding with 74% of cumulative variability.

References

[1] I. Bonaduce, V. Castelvetro, M.P. Colombini, A. Lluveras-Tenorio, M. Raihane, M. Ibnoussina, A. Boujamid, Characterization of the Organic Materials Used in the Painting of the Vaulted Ceiling at the Saadian Tomb of Mulay Ahmed Al-Mansour (Marrakech), J. Cult. Herit. 2014, 15(3), pp 300-307.

[2] M.P. Colombini, F. Modugno (eds.), Organic Mass Spectrometry in Art and Archaeology, John Wiley and Sons, UK, Chichester, 2009, pp. 6-9.

[3] E. Platania, J.R. Lombardi, M. Leona, N. Shibayama, C. Lofrumento, M. Ricci, M. Becucci, E. Castellucci, Suitability of Ag-agar Gel for the Micro-Extraction of Organic Dyes on Different Substrates: The Case Study of Wool, Silk, Printed Cotton and a Panel Painting Mock- Up, J. Raman Spectrosc. 2014, 45(11-12), pp 1133-1139.

[4] C. Lofrumento, F. Arci, S. Carlesi, M. Ricci, E. Castellucci, M. Becucci, Safranin-O Dye in the Ground State. A Study by Density Functional Theory, Raman, SERS and Infrared spectroscopy, Spectrochim. Acta, Part A. 2015, 137, pp 677-684.

[5] K. Castro, A. Sarmiento, M. Maguregui, I. Martínez-Arkarazo, N. Etxebarria, M. Angulo, M. Urrutikoetxea Barrutia, J.M. González- Cembellín, J.M. Madariaga, Multianalytical Approach to the Analysis of English Polychromed Alabaster Sculptures: μRaman, μEDXRF, and FTIR Spectroscopies, Anal. Bioanal. Chem. 2008, 392(4), pp 755-763.

[6] A. Nevin, I. Osticioli, D. Anglos, A. Burnstock, S. Cather, E. Castellucci, Raman Spectra of Proteinaceous Materials Used in Paintings: A Multivariate Analytical Approach for Classification and Identification, Anal. Chem. 2007, 79(16), pp 6143-6151.

[7] C. Lofrumento, M. Ricci, L. Bachechi, D. De Feo, E.M. Castellucci, The First Spectroscopic Analysis of Ethiopian Prehistoric Rock Painting, J. Raman Spectrosc. 2012. 43(6), pp 809-816.

[8] M. Otto. Chemometrics: Statistics and Computer Application in Analytical Chemistry, Wiley-VCH, Germany, Weinheim, 1999.

[9] A. Pallipurath, J. Skelton, P. Ricciardi, S. Buclow, S. Elliot, Multivariate Analysis of Combined Raman and Fibre-Optic Reflectance Spectra for the Identification of Binder Materials in Simulated Medieval Paints, J. Raman Spectrosc. 2013, 44(6), pp 866- 874.

[10] J. Bueno, I.K. Lednev, Advanced Statistical Analysis and Discrimination of Gunshot Residue Implementing Combined Raman and FT-IR Data, Anal. Methods. 2013, 5(22), pp 6292-6296.

[11] U. Poth, Drying Oils and Related Products, in: Ullmann's Encyclopedia of Industrial Chemistry, Wiley- VCH, Germany, Weinheim, 2002.

[12] L. Masschelein-Kleiner, Ancient Binding Media, Varnishes and Adhesives, ICCROM, Italy, Rome, 1995.

[13] I. Bonaduce, L. Carlyle, M.P. Colombini, C. Duce, C. Ferrari, E. Ribechini, P. Selleri, M.R. Tine´, New Insights into the Ageing of Linseed Oil Paint Binder: A Qualitative and Quantitative Analytical Study, PLoS ONE. 2012. 7(11): e49333.

[14] J.S. Mills, R. White. The Organic Chemistry of Museum Objects, 2nd ed, Butterworth-Heinmann, UK, Oxford, 1994.

[15] A. Schönemann, H.G.M. Edwards, Raman and FTIR Microspectroscopic Study of the Alteration of Chinese Tung Oil and Related Drying Oils During Ageing, Anal. Bioanal. Chem. 2011, 400(4), pp 1173-1180.

[16] J. La Nasa, E. Ghelardi, I. Degano, F. Modugno, M.P. Colombini, Core Shell Stationary Phases for a Novel Separation of Triglycerides in Plant Oils by High Performance Liquid Chromatography with Electrospray-Quadrupole-Time of Flight Mass Spectrometer, J. Chromatogr. A. 2013, 1308, pp 114-124.

[17] P. Vandenabeele, B. Wehling, L. Moens, H. Edwards, M. De Reu, G. Van Hooydonk, Analysis with Micro-Raman Spectroscopy of Natural Organic Binding Media and Varnishes Used in Art, Anal. Chim. Acta. 2000, 407(1-2), pp 261-274.

[18] E. Manzano, J. García-Atero, A. Dominguez-Vidal, M.J. Ayora- Caňada, L. Fermín Capitán-Vallvey, N. Navas, Discrimination of Aged Mixtures of Lipidic Paint Binders by Raman Spectroscopy and Chemometrics, J. Raman Spectrosc. 2012, 43(6), pp 781-786.

[19] A. Savitzky, M. Golay, Smoothing and Differentiation of Data by Simplified Least Squares Procedures, Anal. Chem. 1964, 36(8), pp 1627-1639.

[20] M. Vagnini, C. Miliani, L. Cartechini, P. Rocchi, B.G. Brunetti, A. Sgamellotti, FT-NIR Spectroscopy for Non-Invasive Identification of Natural Polymers and Resins in Easel Paintings, Anal. Bioanal. Chem. 2009, 395(7), pp 2107-2118.

[21] J. Workman, L. Weyer Practical Guide to Interpretative Near-Infrared Spectroscopy, CRC Press- Taylor and Francis, Boca Raton, 2007.

[22] B. Lambert, H.F. Shurvell, R.G. Cooks, Introduction to Organic Spectroscopy, Macmillan Publ., New York, 1987.

[23] J.S. Shenk, J.J. Workman, M.O. Westrhaus, “Application of NIR spectroscopy to agricultural products” in D.A. Burns and Ciurczak E.W. (eds), Handbook of Near-Infrared Spectroscopy Marcel Dekker Inc., New York,2001, pp 419-474.

[24] D. Lin-Vien, N.B. Colthup, W.G. Fately, J.G. Grasselli, The Handbook of Infrared and Raman Characteristic Frequencies of Organic Molecules, Academic Press, CA, San Diego, 1991.

[25] H. Yang, J. Irudayaraj, Comparison of Near-Infrared, Fourier Transform-Infrared, and Fourier Transform-Raman Methods for Determining Olive Pomace Oil Adulteration in Extra Virgin Olive Oil, J. Am. Oil Chem. Soc. 2001, 78(9), pp 889-895.

[26] O. Zovi, L. Lecamp, C. Loutelier-Bourhis, C.M. Lange, C. Bunel, Stand Reaction of Linseed Oil, Eur. J. Lipid Sci. Technol. 2011, 113(5), pp 616-626.

[27] M. Lazzari, O. Chiantore, Drying and Oxidative Degradation of Linseed Oil, Polym. Degrad. Stab. 1999, 65(2), pp 303-313.

Chapter 3: Multivariate analysis of combined reflectance FT-NIR and micro-Raman spectra on oil-paint models

Abstract

The potential of principal component analysis (PCA), on combined first derivative near infrared and Raman spectra, was explored and tested in order to exhaustively characterize different oil-paint models, prepared with linseed and poppy-seed oil, and to verify the behaviour of these binders in the presence of a pigment.

A series of oil-paint models, selecting pigments used in artworks both in antiquity (like lead white, azurite, Afghanistan ultramarine) and contemporary art (such as phthalocyanine blue, zinc oxide and synthetic ultramarine blue), were prepared and analysed by means of reflectance near infrared and micro-Raman spectroscopic techniques.

At first, PCA was applied by taking into account all oil-paint models, pigments and drying oils. Subsequently, new statistical models were built focusing only on single pigment subsets; hence, offering a more realistic application of this method, once the pigment had been identified. The proposed procedure allowed us to recognize the pigments and binding media used to prepare each model. In addition, it proved to be even sensitive to the drying oil used in the oil-paint mixture, enabling its identification. The application of PCA to a combination of different spectral regions (6000-3900 cm^{-1} along with 1900-260 cm^{-1}) allowed an enhanced level of spectral information to be extracted, with respect to its application on separated data-sets. It represents also a powerful tool to differentiate oil-paint models on the basis of their composition, including oils and pigments.

Moreover, we verified that after a natural ageing of nine months, and in presence of a pigment, it is still possible to obtain information regarding the functional groups directly involved in the drying process (e.g. the 1st overtones of methylenic stretching, 5800 cm^{-1} and 5698 cm^{-1}, the C-H combination bands of methylenic stretching and bending modes, 4340 and 4261 cm^{-1}, and the ν(C=C) stretching, 1654 cm^{-1}).

THIS CHAPTER WILL BE PUBLISHED ON "MICROCHEMICAL JOURNAL" [S. Carlesi, M. Ricci, C. Cucci, C. Lofrumento, M. Picollo, M. Becucci, Multivariate analysis of combined reflectance FT-NIR and micro-Raman spectra on oil-paint models, Microchem. J. 2016, 124, pp 703-711; doi: 10.1016/j.microc.2015.10.023]

Introduction

The knowledge of the materials present in artworks is crucial to ensure appropriate conservation procedures and to gain insight into their historical evolution. This knowledge is especially important when dealing with paintings, because they are complex systems, composed of various supports, preparation layers and painting materials, such as pigments and binders.

While the identification of pigments in paintings is today a relatively straightforward process in most cases, the identification of binding media remains a challenge [**1**]. The fact that organic materials are often added in scant quantity, in contrast with the presence of the high amounts of inorganic materials, as pigments and dryers, may hinder their reliable identification [**2**]. Furthermore, organic materials are less stable and deteriorate faster than the inorganic components, so that they often only remain at trace levels in centuries-old paintings, thus making their identification even more difficult. Consequently, the analytical techniques should provide high sensitivity and specific information to avoid ambiguities or misinterpretations. To achieve this requirement, the most prudent approach is to apply, more than one analytical procedure, in order to gather complementary information. The most common techniques used in this type of study are chromatography [**3-4**] and spectroscopy [**5**].

The main advantages of spectroscopic techniques, such as reflectance and Raman, are that in many cases they can be applied without sampling or in a non-destructive way. In addition, they do not need any sample pre-treatment, the time of analysis is short, and they allow very small areas of the surface of the artwork to be studied [**6-7**]. Nevertheless, data analysis performing one-by-one or peak-by-peak comparison of sample spectra with those of the standard materials, especially in the case of natural binding media, is a tedious time-consuming methodology that is not always effective. The management of all the information obtained from the data collected by the different spectroscopy techniques is improved considerably by using chemometric analysis assistance. Indeed, it is highly worthwhile to characterize artworks by non-destructive analytical techniques combined with statistical methods, such as multivariate chemometric tools, in order to extract the maximum information concerning composition, and to detect slight disparities between the spectroscopic data [8-9]. One of the most common exploratory tools in chemometrics is Principal Component Analysis (PCA). The main benefit of PCA is its capability to reduce dimensionality of the original data-set by representing them in terms of new coordinates, the principal components (PCs), which contain more interpretable and representative information of the system under investigation [**10**].

This work is aimed at exploring the possibility of fully characterizing complex systems, such as oil-paint models, using multivariate analysis on combined Fourier Transform Near Infrared (FT-NIR) and Raman spectroscopic techniques, and to differentiate between the oil-paint models according to the spectral differences attributable to the binder.
A set of model samples were prepared by mixing linseed oil, which was used in the Middle Ages, and poppy-seed oil, which has been utilized especially for artistic purposes since the seventeenth century [**11**], with a series of pigments used in artworks, both in antiquity (like lead white, azurite, Afghanistan ultramarine) and contemporary art (such as phthalocyanine blue, zinc oxide and synthetic ultramarine blue). These models were analysed by means of reflectance NIR and micro-Raman spectroscopic techniques.
The combination of FT-NIR and micro-Raman spectroscopy techniques, which furnish complementary information due to the different physical processes involved, has already demonstrated the ability to provide a much deeper insight into the characteristic structure and binding properties of different and partially aged (three months of natural ageing) drying oils. [12] Indeed, the application of PCA to a combination of different spectral regions allowed an enhanced level of spectral information to be extracted. This non-invasive approach revealed to be a valuable, rapid and meaningful tool able to distinguish these organic compounds, up to the tracing of the manufacturer (in the case of drying oils) [**12**].
The results obtained by the present work are very beneficial for research concerning the characterization and the identification of the materials present in a pictorial layer, because they mark an important step forward with respect to similar former studies, due to the choice of the laser source (785 nm wavelength) to acquire Raman spectra, which is important both to prevent fluorescence issues, and to work in a non-destructive way, contrary to FT-Raman analysis [**13**].

3.1 Materials and methods

3.1.1 Oil-paint model samples

For this work four blue pigments (azurite (A), Afghanistan ultramarine (AU), synthetic ultramarine (SU) and phthalocyanine blue (PB)) and two white pigments (lead white (LW) and zinc white (ZW)) were selected on the basis of their chemical and mineralogical properties, according to their widespread use in easel paintings throughout history. The A, AU, SU, PB pigments were purchased from Zecchi (Florence, Italy), while the rest of pigments were supplied by Sigma-Aldrich (Milano, Italy). Linseed oil (L) and poppy-seed oil (P)

from Zecchi (Florence, Italy) were selected as binding media and were used as supplied.

Twelve oil-paint models were prepared according to the recipes reported in original treaties and artists' accounts [**14**] by mixing these pigments with linseed or poppy-seed oils on the smooth surface of a panel glass. The list of samples together with their denomination is reported in **Table 1**. The powdered pigments were initially crushed in an agate mortar in order to obtain a homogenously-fine particle grain size without lumps. The exact concentration of the pigment with respect to drying oil was not determined *a priori*; instead for each case, a mixture of similar consistency was used to prepare the paint models, so that they could be applied with a fine brush as a single thick layer onto microscope glass slides and left to dry on a bench top. Four sets of oil-paint models were prepared, obtaining a total of forty-eight samples. The paint films had rough non-homogeneous surfaces as would be expected in real samples. Neat samples of the binding materials were also applied as films on four microscope glass slides and left to dry for a total of eight samples. All oil-paint models and neat binders were analysed after a natural ageing of nine months. It has been shown that it represents a time-lapse during which the polymerization process is not yet completed and the hydrolysis or (photo-) oxidation reactions, characteristic for the degradation of these materials, have not started yet [**15-16**]. We are then evaluating a sort of intermediate step in the natural ageing process of both the drying oils and the oil-paint models.

The neat powdered pigments were directly analysed without any preparation.

Table 1 The oil mixtures analysed and their corresponding identification symbols.

Pigment	Drying Oil	Symbol
Lead White (**LW**), $2PbCO_3*Pb(OH)_2$	+ linseed oil(**L**)	**LWL**
	+ poppy-seed oil (**P**)	**LWP**
Zinc White (**ZW**), ZnO	+ linseed oil (**L**)	**ZWL**
	+ poppy-seed oil (**P**)	**ZWP**
Phthalocyanine Blue (**PB**), $C_{32}H_{16}N_8Cu$/copper phthalocyanine	+ linseed oil (**L**)	**PBL**
	+ poppy-seed oil (**P**)	**PBP**
Azurite (**A**), $Cu_3(CO_3)_2(OH)_2$	+ linseed oil (**L**)	**AL**
	+ poppy-seed oil (**P**)	**AP**
Synthetic Ultramarine Blue (**SU**), $Na_{8-10}Al_6Si_6O_{24}S_{2-4}$	+ linseed oil (**L**)	**SUL**
	+ poppy-seed oil (**P**)	**SUP**
Afghanistan Ultramarine Blue (**AU**), $(Na,Ca)_8[(S,Cl,SO_4,OH)_2/(Al_6Si_6O_{24})]$	+ linseed oil (**L**)	**AUL**
	+ poppy-seed oil (**P**)	**AUP**

3.1.2 FT-NIR spectroscopy

FT-NIR reflectance spectra were recorded using a portable ALPHA FTIR spectrometer (Bruker Optics), equipped with the external reflection module.

Total reflection spectra (including both the specular and diffuse reflection contributes) were collected in situ, in the 7500-3900 cm^{-1} spectral range with a resolution of 4 cm^{-1} over 128 scans. The spectral sampling distance used for each scan was 2 cm^{-1}. An area of approximately 3 mm diameter was analysed. The background was acquired using a gold mirror as reference sample.
A total of 320 spectra were recorded at four different positions for each sample.

3.1.3 Micro-Raman spectroscopy

The Raman spectra were collected using a Renishaw 2000 micro-Raman spectrometer equipped with a 785 nm diode laser. To analyse neat drying oils and powdered pigments, the laser was focused using a 50x objective lens, so that an area of approximately 2 μm diameter was considered. For the study of oil-paint models, a 20x objective lens was used so an area of about 5 μm diameter was investigated. In order to have an adequate sampling, we marked on the samples the spots characterized by FT-NIR and we made 16 different Raman measurements within the FT-NIR areas. We noticed that for each Raman single measurement we always obtained signals both from the pigment and the binder, furthermore the repeatability within the 16 measurements was quite good. Spectra were recorded in the 2000-200 cm^{-1} spectral range with a spectral resolution of 4 cm^{-1}. To improve signal/noise ratios, we acquired spectra of 25 s and 100 s exposure time (averaged 3 times) for neat binders/pigments and for oil-paint models, respectively. The spectral sampling distance used for each scan was 1 cm^{-1}. Precautions were taken to avoid any damage to the samples (i.e. laser–induced degradation of paint materials). This was done by visually confirming the absence of damage in the sampling area with the help of a video-camera. Thus, laser power was kept between 1 mW (with 50x objective lens) and 1.5 mW (with 20x objective lens) on the samples during the analysis. The spectrometer was calibrated at the beginning of each measurement session using the Raman signal from a silicon crystal at 520 cm^{-1}.
A total of 320 spectra were recorded, as in case of FT-NIR.

3.1.4 Data analysis

Data processing of the micro-Raman and FT-NIR spectra along with Principal Component Analysis (PCA) were performed using The Unscrambler® X software version 10.3 (CAMO).
The initial data analysis was carried out in the spectral ranges where the prominent signals are located. Therefore, the FT-NIR spectra were analysed in the 6000-3900 cm^{-1} range, where signals appear well-defined and less affected

by noise. The micro-Raman spectra were evaluated in the 1900-260 cm^{-1} range, where both drying oils and pigments show significant contributions.
The FT-NIR and micro-Raman datasets were pre-processed separately to discern variability in the original spectra. In detail, the FT-NIR spectra were subjected to the Savitzky-Golay derivative algorithm (2^{nd} order polynomial, 15 data points) [**17**] without any other pre-processing. The micro-Raman spectra were, instead, subjected to baseline subtraction, average reduction of variables (factor two) and first derivative calculation by applying the Savitzky-Golay algorithm (2^{nd} order polynomial, 15 data points). Then, both the FT-NIR and micro-Raman spectra were vector normalized, as the use of absolute band heights could lead to erroneous sample classifications [**13**]. For convenience, we report in **Fig. 1** the raw data obtained from the ZWL oil-paint model and the associated first derivative and combined spectra.

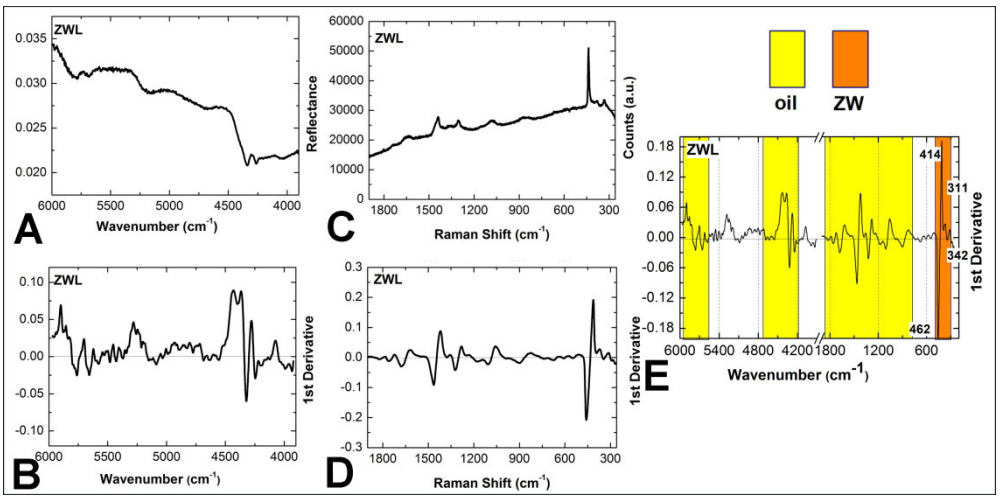

Fig. 1 Results from the spectroscopic characterization of the ZWL oil-paint model: the FT-NIR (A) and micro-Raman (B) spectra, the associated first derivative spectra (C and D, respectively) and the combined spectrum (E).

The combined spectra were obtained as follows: the first derivative Raman and FT-NIR spectra were joined, generating the new combined Raman-FT-NIR spectrum, 16 for each typology of sample. Each new combined spectrum includes 1870 data points, with the first 1050 derived from the FT-NIR spectrum abscissa and the remaining 820 points from the micro-Raman spectrum abscissa. The total number of combined spectra analysed was 320.
The Uncertainty Test was always performed to estimate the significance of variables. Then, PCA was performed by applying a mean-centering onto data column-wise and the Non Linear Iterative Partial Least Squares (NIPALS) algorithm. Each model was always validated by Leave One Out (LOO) cross-

validation and by a projection of evaluated sets of spectral data acquired by the same samples (four spectra for each type of sample).

3.2 Results and discussion

3.2.1 PCA applied to all the samples

In this study, the application of PCA to combined first derivative FT-NIR and micro-Raman spectra of oil-paint models was evaluated.
Taking into account the two spectroscopic techniques separately, it is not possible to exhaustively describe each oil-paint model; on the contrary, their combination allowed this goal to be achieved. PCA has been also applied on the separated first derivative spectra (**Fig. S1** and **Fig. S2** in the **supplementary material**).
The PCA applied only to first derivative FT-NIR spectra showed that all oil-paint models are close to the binders and separated from their corresponding pigment, as can be deduced taking into account the first two PCs.
On the other hand, the PCA on first derivative micro-Raman spectra highlighted that each pigment is always very close to the corresponding mixtures. The only exception is represented by zinc white mixtures which are close to both the drying oils. Hence, whereas the FT-NIR technique furnishes a characterization mainly focused on the binder, micro-Raman spectroscopy gives information related principally to the pigment, thus their combination enables to gather additional and valuable information from the data. The application of a multivariate analytical tool, such as PCA, to the combined spectra allows the concomitant extraction of important information. Moreover, the different behaviour, highlighted by the binder in the presence of a pigment, should be also taken into account in the discussion of the final results. In a previous study [**11**], we demonstrated that the information obtained from selected spectral regions could be useful to differentiate among different and partially aged (three months of natural ageing) drying oils. Now, we would like to test this assumption in a more realistic model where both drying oils and pigments are present.
In the present study, from PCA performed as described previously, five principal components (PCs) were selected, explaining 81% of the total variance of the samples. PC1 explains 23% of the total variance contained in the data, while PC2 to PC5 explain 18, 16, 13 and 11% of the total variance, respectively.
In **Fig. 2** the two-dimensional score plots in the spaces defined by PC1 and PC2 (**Fig. 2A**), PC1 and PC3 (**Fig. 2B**) and PC3 and PC4 (**Fig. 2C**) are reported showing different data clusters with good data separation. The vibrations mainly responsible for sample clustering can be observed by inspection of the

loading plots for each variable for the first, second, third and fourth principal components, as shown in **Fig. 3**. In these loading plots, the "plus" symbol is used to indicate that the 1st derivative contribution is concordant with the starting combined spectra, while a "minus" sign is used when its behaviour is reversed. Furthermore, the main contributions related to pigments and binders are highlighted by means of different colours/patterns.

As can be seen in **Fig. 2A**, the influence of the drying oils is reflected in PC1, establishing a clear separation between oils, pigments and the corresponding mixtures (oil: negative score value; pigments: positive score values; mixtures: intermediate score values). The only exception is the azurite pigment (A) and its oil mixtures (AL and AP), which have a PC1 score value similar to that of the oils. This behaviour can be understood taking into account the overlap of the Raman signal of azurite pigment at 1430 cm^{-1} (antisymmetric stretching of carbonate ion [**18**]) with the oil signal at around 1441 cm^{-1}, due to the $\delta(CH_2)$ bending mode [**12**].

PC2 is instead much more sensitive to the presence of the different pigments. As shown in **Fig. 2A**, it is also possible to highlight the separation between natural (negative score value) and synthetic (positive score value) ultramarine blues. Furthermore, the PC2 score values locate PB pigment very far from the corresponding mixtures, while both ZW and LW pigments show a similar score value to their corresponding mixtures.

The major contributions to PC1 (**Fig. 3A**), can be ascribed to both drying oils (at 5792 and 5698 cm^{-1}, 1st overtones of methylenic stretching; at 1654 cm^{-1}, ν(C=C) fundamental stretching; 1441 cm^{-1}, $\delta(CH_2)$ bending; at 1304 cm^{-1}, in phase methylene twisting motion $\delta(CH_2)$ [**12**]), according to previous spectral assignments. Instead, in PC2 (**Fig. 3B**) the main contributions are related to PB (at 5944 cm^{-1} and 4640 cm^{-1} in near infrared region; at 1524 cm^{-1}, 1340 cm^{-1}, 1140 cm^{-1}, 747 cm^{-1} and 682 cm^{-1} in Raman range [**19**]), LW (at 1053 cm^{-1}, symmetric stretching carbonate ion [**11**]) and ZW (at 437 cm^{-1}, E_2 phonon in the ZnO crystal [**20**]) pigments, as noted above. In addition, in the near infrared region of PC2 loading plot (**Fig. 3B**) the vibrations characteristic of AU [**21**], located at 4300 cm^{-1} and 4200 cm^{-1}, can be observed. These latter bands enable natural and synthetic ultramarine blue pigments to be distinguished. The PC1-PC3 score plot (**Fig. 2B**) distinctly clusters A, PB and AU/SU pigments with their corresponding mixtures. In **Fig. 2B**, also a clear separation between ZW mixtures can be observed on the basis of PC3; this represents a peculiarity of such a pigment/oil system due to the fact that the spectral features referred to the pigment and to the binder are not in the same spectral range. The distance between the mixtures and the corresponding oil in the PC1-PC3 space is different. Possibly this can be explained by small differences in the pigment/binder ratio, which was not controlled during the oil-paint

preparation. PC3 loading plot, shown in **Fig. 3C**, reflects the drying oils contributions (at 4340 and 4261 cm^{-1}, stretching ν(CH) + bending δ(CH); 1650 cm^{-1}) which, in agreement with our previous study [**12**], might be used to differentiate between these two drying oils.

The other main contributions underlined by the PC3 loading plot (**Fig.3C**) can be ascribed to the PB (at 5944 cm^{-1} and 4640 cm^{-1} in near infrared region; at 1524 cm^{-1}, 1340 cm^{-1}, 747 cm^{-1} and 682 cm^{-1} in Raman range [**19**]), LW (at 1053 cm^{-1}[**11**]), ultramarine blues (symmetric stretching ν_s (S_3^-), at 547 cm^{-1} [**22-23**]) and finally, A pigments (ν(Cu-OH), at 400 cm^{-1} [**24**]), as reported in **Fig. 2B**.

The score plot PC3-PC4 (**Fig. 2C**) confirms the separation between ultramarine blue mixtures from the corresponding pigments. Moreover, these mixtures along with PB and ZW mixtures are characterized by a positive PC4 score value, as that of the binders. For PC4, the influence of drying oils is intense, as can be observed in **Fig. 3D**.

In conclusion, PCA of the first derivative FT-NIR and micro-Raman of the whole combined spectra allows additional information to be extracted from each simulated paint system. The main result is that from the analysis of the full set of data we can separate samples containing different pigments and, within these groups we distinguish pure pigments from their mixtures with binders. The first two PCs highlight that the data corresponding to the LW and ZW mixtures are positioned near to both the binder and pigment used to prepare them (**Fig. 2A**). The grouping of the data referred to the other oil-paint models is possible thanks to the spaces defined by the others PCs, up to the fourth, while the groups of A, alone and in mixtures, are close to each other in all the spaces reported in **Fig. 2**.

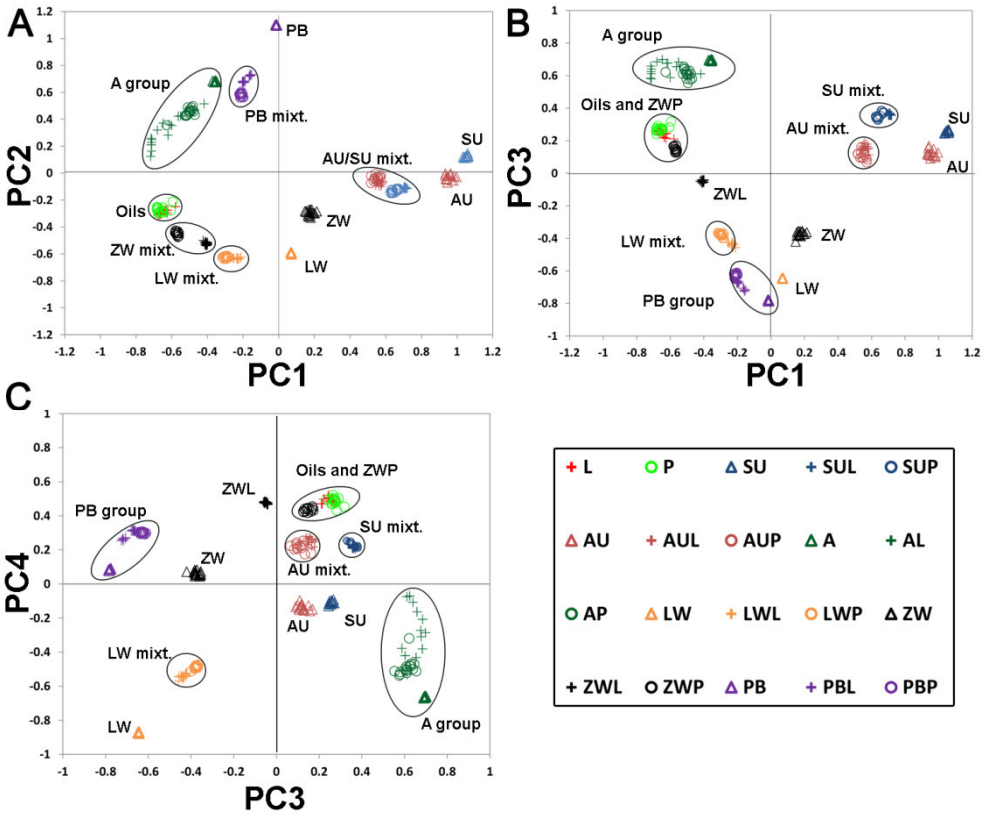

Fig. 2 Score plots of PC1-PC2 (A), PC1-PC3 (B) and PC3-PC4 (C).

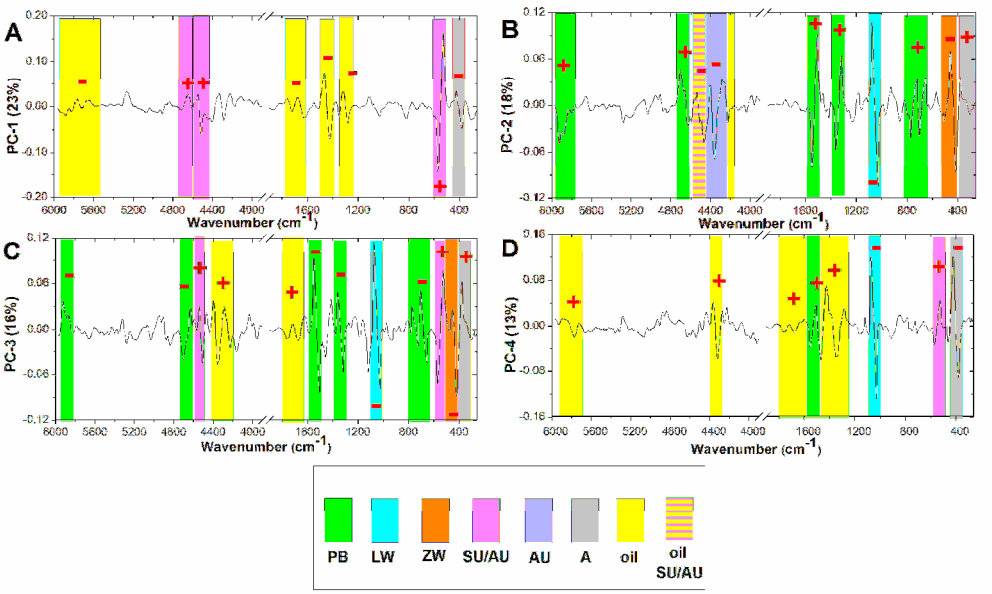

Fig. 3 Loading plots of the first three PCs: PC1 (A), PC2 (B), PC3 (C) and PC4 (D).

3.2.2 PCA applied to each single pigment data group

As discussed in the Introduction, in order to achieve a more realistic application of this method, we worked on data subsets, each including only a single pigment, whose identification is straightforward by means of the micro-Raman technique. This second step consists in the extraction of more precise information regarding the binders used in the oil-paint models by means of this analytical approach, despite the complexity that may occur due to their interactions with the different pigments.
Therefore, we built new statistical models, processing combined first derivative FT-NIR and micro-Raman spectra related to a specific pigment, two drying oils and their corresponding paint mixtures.
LW, ZW, SU and PB datasets, showed similar PCA results. Instead, the same approach was not completely successful when dealing with A and AU datasets. Therefore, for these latter cases, we re-processed the data in selected spectral sub-ranges, in order to better focus on specific spectroscopic features and discard less relevant information.
The results of the corresponding PCA in terms of explained variance (%) and cumulative variance (%) with the spectral ranges analysed for each oil-paint model are summarized in **Table 2**.
Hereafter we discuss in detail only the results of oil-paint models prepared with LW (a lead basic carbonate) and A (a basic copper carbonate) pigments, with the aim of demonstrating the potential of the method.

Table 2 The results of PCA performed on each oil-paint model dataset for the reported spectral ranges.

Oil-paint model	PCs	Variance account (%)	Variance accumulated (%)	Spectral ranges
LW group	PC1	83	83	6000-3900 cm^{-1}/ 1900-260 cm^{-1}
	PC2	12	95	
	PC3	4	99	
ZW group	PC1	74	74	6000-3900 cm^{-1}/ 1900-260 cm^{-1}
	PC2	10	84	
	PC3	7	91	
A group	PC1	76	76	6000-3900 cm^{-1}/ 1900-260 cm^{-1}
	PC2	14	90	
	PC3	4	94	
	PC1	63	63	6000-5500 cm^{-1}/ 1900-1200 cm^{-1}
	PC2	27	90	
	PC3	4	94	
AU group	PC1	61	61	6000-3900 cm^{-1}/ 1900-260 cm^{-1}
	PC2	19	80	
	PC3	3	83	
	PC1	57	57	6000-5500 cm^{-1}/ 4800-3900 cm^{-1}/ 1900-1200 cm^{-1}
	PC2	25	82	
	PC3	4	86	
SU group	PC1	78	78	6000-3900 cm^{-1}/ 1900-260 cm^{-1}
	PC2	16	94	
	PC3	4	98	
PB group	PC1	80	80	6000-3900 cm^{-1}/ 1900-260 cm^{-1}
	PC2	15	95	
	PC3	4	94	

3.2.2.1 Lead White data group

LW pigment is commonly known as an inorganic material able to catalyse the oxidation of drying oils [**25**].

In **Fig. 4**, the first derivative combined spectra related to both the drying oils and their oil-paint models containing LW (LWL and LWP) are reported.

While in the region between 6000 and 5500 cm^{-1} the LW pigment does not show any absorption bands, in the region between 4500 and 4000 cm^{-1} this pigment shows an absorption band centered at 4294 cm^{-1} (ν(OH) + deformation modes (Pb-OH) [**27**]) and the neat oils have two absorption bands at 4261 cm^{-1} (C-H combination band of symmetric methylenic stretching and bending) and at 4340 cm^{-1} (C-H combination band of antisymmetric methylenic stretching and bending). The spectral modifications due to this pigment's peculiar bands are noticeable solely upon considering the changes in the corresponding first derivative spectra, indicative of the effect of the lead white

pigment on the drying oil binders, and which are more evident for the paint mixture containing linseed oil (LWL).

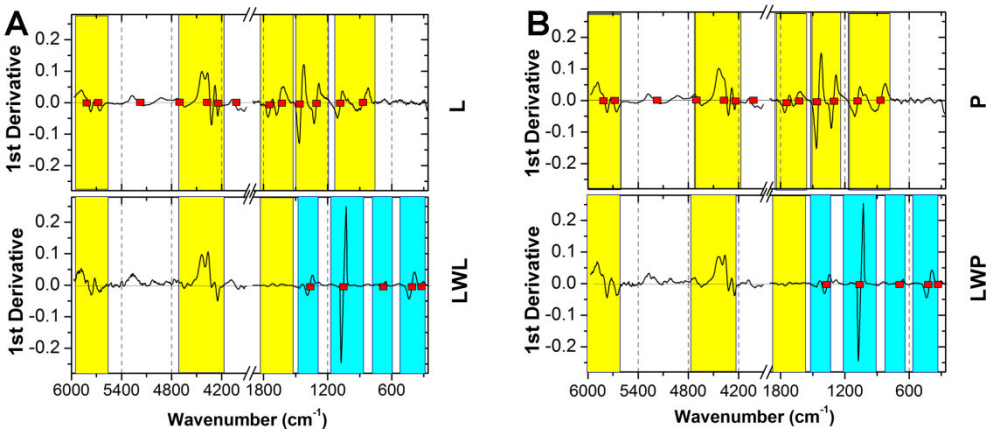

Fig. 4 First derivative FT-NIR and micro-Raman combined spectra related to neat linseed oil along with the corresponding mixture (A) and to neat poppy-seed oil along with the corresponding mixture (B) for LW pigment. Major contributions referred to the oils are reported in "yellow", while those related to the pigment are "light blue".

The statistical model related to LW group, can be described by means of the first three principal components, which account for 99% of the total variance. In **Fig. 5** the score plots PC1-PC2 and PC1-PC3 along with the corresponding PC3 loading plot are reported.

As can be seen in **Fig. 5A** and **Fig. 5B**, PC1 clearly separates pigment and mixtures from both drying oils, while PC2 separates both mixtures, from pigment and binders. Nevertheless, the most interesting information is obtained from the PC3. The PC3 loading, shown in **Fig. 5C**, is characterized by contributions due to both drying oils (at 5792 cm^{-1}, 5698 cm^{-1}, 4664 cm^{-1}, 4340 cm^{-1}, 4261 cm^{-1}, 4060 cm^{-1}, 1650 cm^{-1}, 1441 cm^{-1}). It has been demonstrated that these spectral vibrations are able to characterize and distinguish among different drying oils [**12**], even in presence of a pigment and after a natural ageing of nine months. The C-H combination bands for methylenic stretching and bending (4800-4200 cm^{-1}) along with the stretching of ν(C=C) *cis* double bond (1700-1600 cm^{-1}) [**12**] might be mainly related to linseed oil and give a positive contribution in the related score plot (**Fig. 5B**). On the other hand, the 1st overtones of methylenic stretching (6000-5500 cm^{-1}) [**12**] might be related to poppy-seed oil and cause a negative contribution. Hence, according to PC3, both LWL and LWP oil-paint mixtures are grouped correctly (**Fig.5B**).

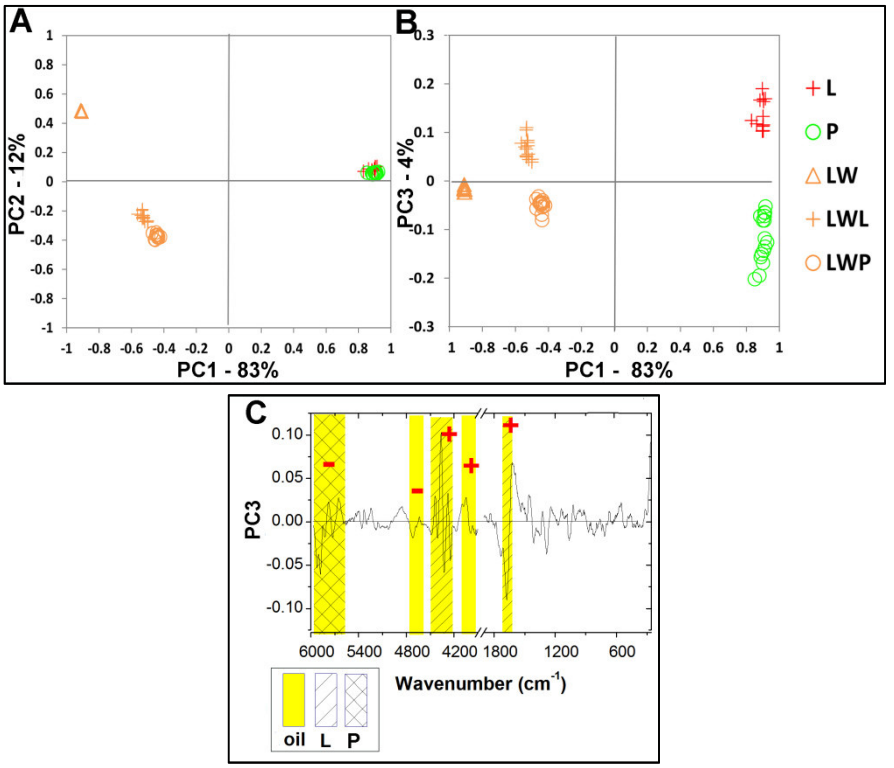

Fig. 5 Score plots of PC1-PC2 (A) and PC1-PC3 (B) along with the corresponding loading plot of PC3 (C) related to statistical model of LW group.

3.2.2.2 Azurite data group

The spectra obtained on oil-paint models containing A were characterized by a smaller signal-to-noise ratio with respect to other data-sets. However, pigment bands, in the all spectral ranges considered for PCA, are intense (**Fig. 6**). In the near infrared region, the most intense bands of A, that we observe in both pigment and oil-paint samples, are located at 5206 cm^{-1}, 5055 cm^{-1}, 4521 cm^{-1} [**26**], 4377 cm^{-1}, 4242 cm^{-1} [**26-27**], while in the Raman region they are at 1430 cm^{-1}, 1095 cm^{-1} [**18**] and at 400 cm^{-1} [**24**].

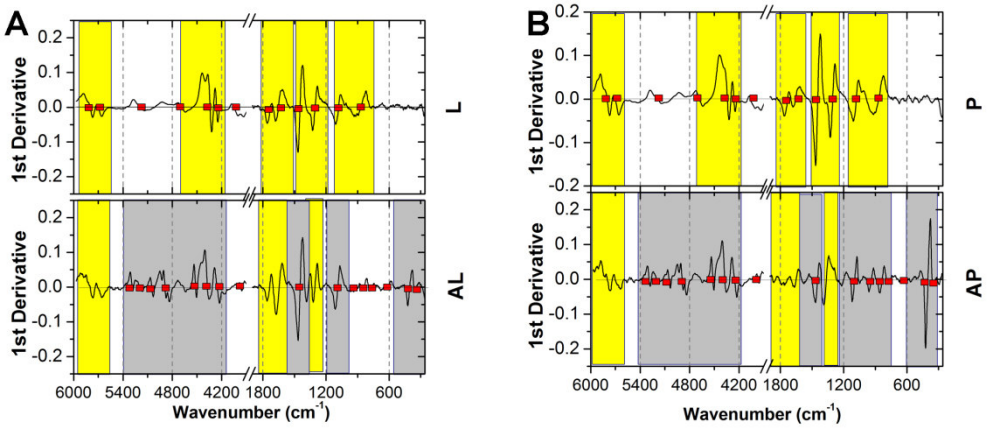

Fig. 6 First derivative FT-NIR and micro-Raman combined spectra related to neat linseed oil along with the corresponding mixture (A) and to neat poppy-seed oil along with the corresponding mixture (B) for A pigment. Major contributions referred to the oils are reported in "yellow", while those related to the pigment in "grey".

The simultaneous presence of such a considerable number of vibrational bands in the mixtures hindered the PCA in the 6000-3900 cm^{-1} and the 1900-260 cm^{-1} spectral ranges.

Therefore, for AL and AP models, PCA was further applied on regions characterized by binder contributions (6000-5500 cm^{-1} and 1900-1200 cm^{-1} spectral ranges). The statistical model related to A group can be described almost completely by means of the first three principal components, which accounted for 94% of the total variance. In **Fig. 7** the PC1-PC2 (**Fig. 7A**) and the PC1-PC3 (**Fig.7B**) score plots obtained for the A group with the PC3 loading plot (**Fig. 7C**) are reported.

As shown in **Fig. 7A**, the influence of the presence of drying oils is reflected in PC1, which separates drying oils (positive score values) from both pigment and mixtures (negative score values). In contrast, the major contributions to PC2 are related to the presence of pigment (positive score value).

PC3 makes it possible to distinguish both azurite mixtures and drying oils as shown in **Fig. 7B**: AL samples show a negative score value, while AP samples are positive. The analysis of the corresponding loading plot (**Fig. 7C**) shows that its major contributions are due to the vibrations of the previously identified drying oils. In fact, the 1st overtones of both the $\nu(CH_2)$ antisymmetric and symmetric stretching at 5800 and 5694 cm^{-1} can be ascribed to P, while the stretching of ν (C=C) *cis* double bond at around 1650 cm^{-1} can be mainly related to L [**12**].

These smaller and more defined spectroscopic ranges better describe these oil-paint models, redistributing the information that can be extracted related to the binding media used, despite the remarkable weight of the pigment.

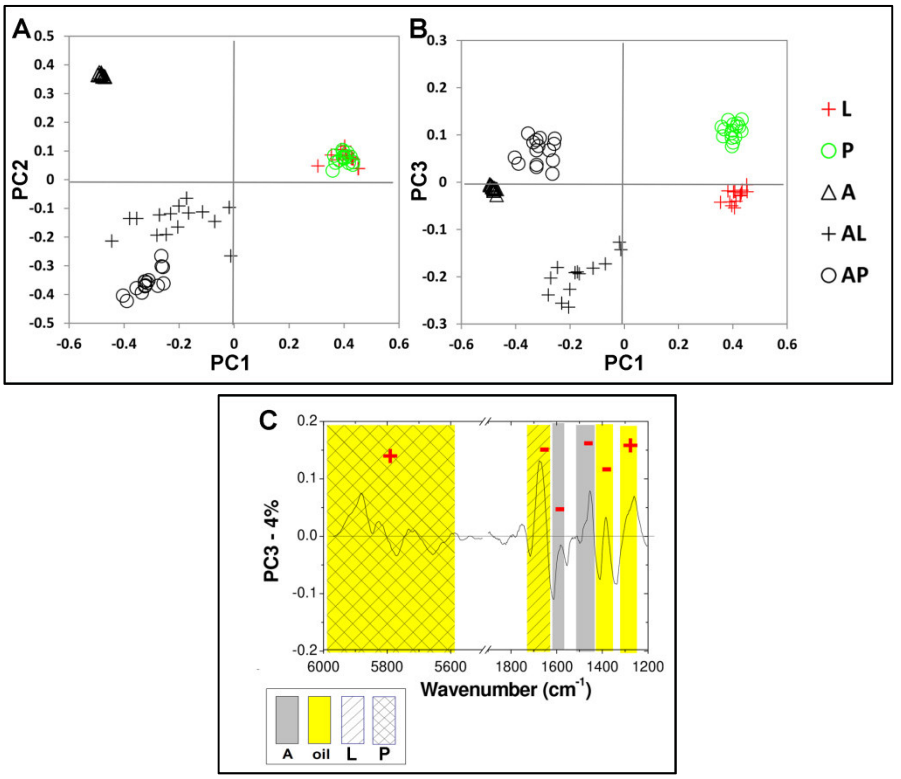

Fig. 7 Score plots of PC1-PC2 (A) and PC1-PC3 (B) along with the corresponding loading plot of PC3 (C) for A group.

3.2.2.3 Other pigment data groups

The PCA results obtained on the other pigment data groups (PB, SU, ZW and AU) confirmed that the separation of the different mixtures is possible and that the third principal component is able to differentiate between two drying oils and corresponding oil-paint mixtures, as is summarized in **Fig. 8**.

The corresponding loading plots related to each oil-paint model, are always characterized by contributions due to the spectral regions of the 1st overtones of methylenic stretching (6000-5500 cm^{-1}), of C-H combination bands for methylenic stretching and bending (4800-4200 cm^{-1}) and of ν(C=C) fundamental stretching (1700-1600 cm^{-1}).

A special case is represented by the AU data group (**Table 2**). The analysis of the full spectral data-set does not allow for the differentiation of the oil-paint models. The analysis of the reduced number of data points (**Fig. 8D**) carries out two consequences: a defined grouping of the oil-paint samples and the neat oils is observed while the pure pigment data spread-out. This could be ascribable to the small intensity of the pigment combination vibrational bands present in the reduced spectral region for the micro-Raman data-set (1900-1200 cm^{-1}) that limits the amount of information available on the pigment itself [**28**].

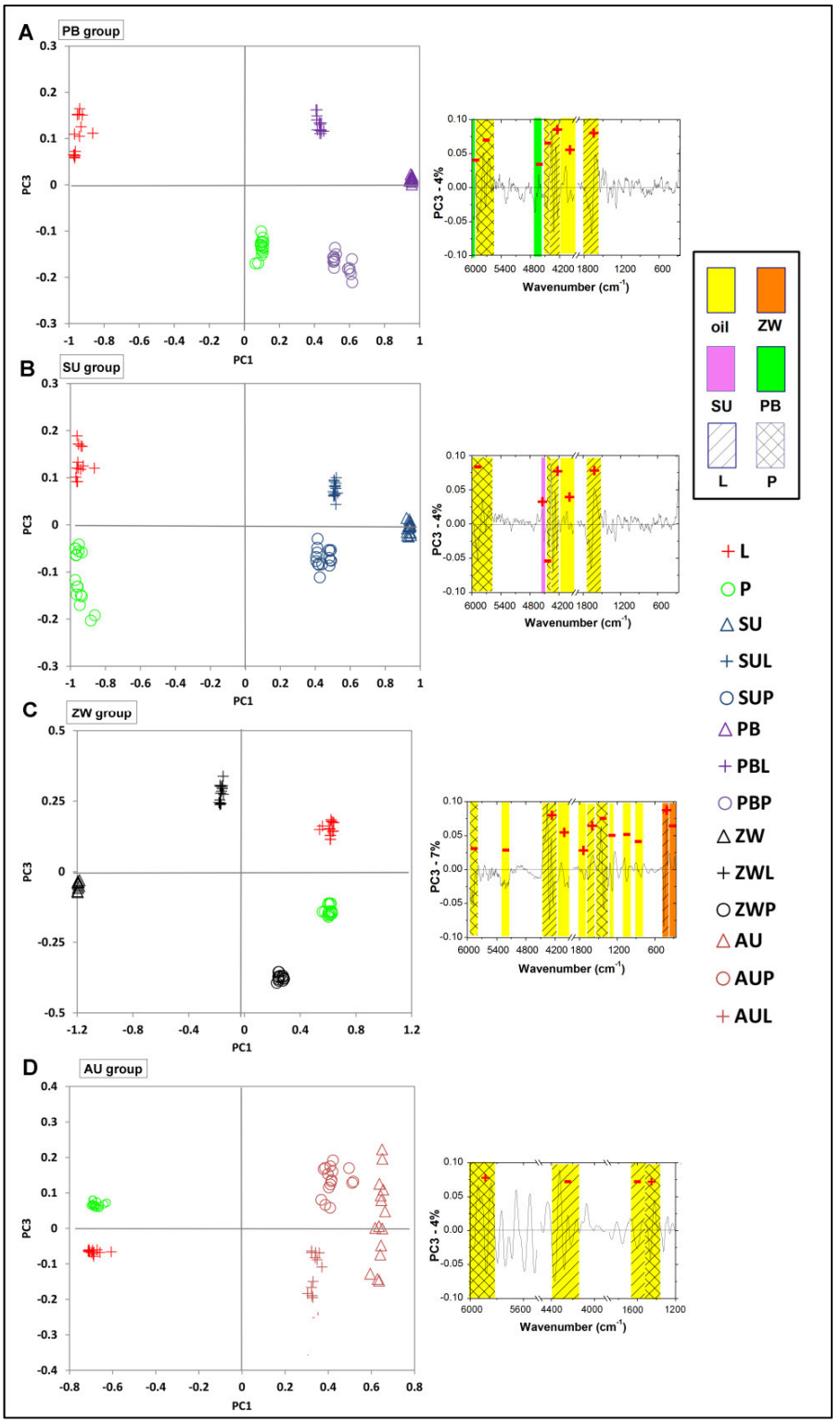

Fig. 8 Score plots of PC1-PC3 along with the corresponding loading plot of PC3 relate to the statistical models of PB (A), SU (B), ZW(C) and AU (D) groups.

3.3 Conclusions

This work explores the application of chemometric techniques to combined near infrared and Raman spectra for the discrimination of both binding media and pigments. This study demonstrates the potential of the proposed analytical approach, and provides a non-destructive novel method for the differentiation among constituents of oil-paint models and their identification, after a natural aging of nine months.

A model set of samples with different pigments and linseed/poppy-seed oil was prepared and analysed by FT-NIR and micro-Raman spectroscopic techniques that provide complementary and useful information on the properties of the various functional groups in the molecular systems.

The combined use of the FT-NIR and micro-Raman spectroscopic techniques, together with the choice of the proper spectral range, represents a significant advantage to distinguish the various mixtures even on the basis of the oil binder, thanks to the different physical phenomena that the two techniques represent. All these aspects were successful in demonstrating the sensitivity of this analytical approach and in extending it to the study of oil-paint mixtures.

We showed that the data-sets referred to lead white (LW), zinc white (ZW), synthetic ultramarine (SU), and phthalocyanine blue (PB) gave optimal results in the grouping of the different samples, when considering the 6000-3900 cm^{-1}/1900-260 cm^{-1} spectral ranges. In contrast, the oil-paint models prepared with azurite (A) and Afghanistan ultramarine (AU) needed to take into consideration further limited spectral ranges, characterized by the binder spectral contributions, thus reducing the noise due to not relevant spectral components.

An additional and important perspective arose from this research work regards the chemical information provided by the PC3s obtained from the analysis of all the different data groups; it can be ascribable to the drying oil's spectral contributions, and helps to differentiate the oils present in the oil-paint models.

This method appears thus promising to proceed with further studies on real samples and more aged models in order to investigate the interactions that take place after a longer air exposure.

3.4 Supplementary material

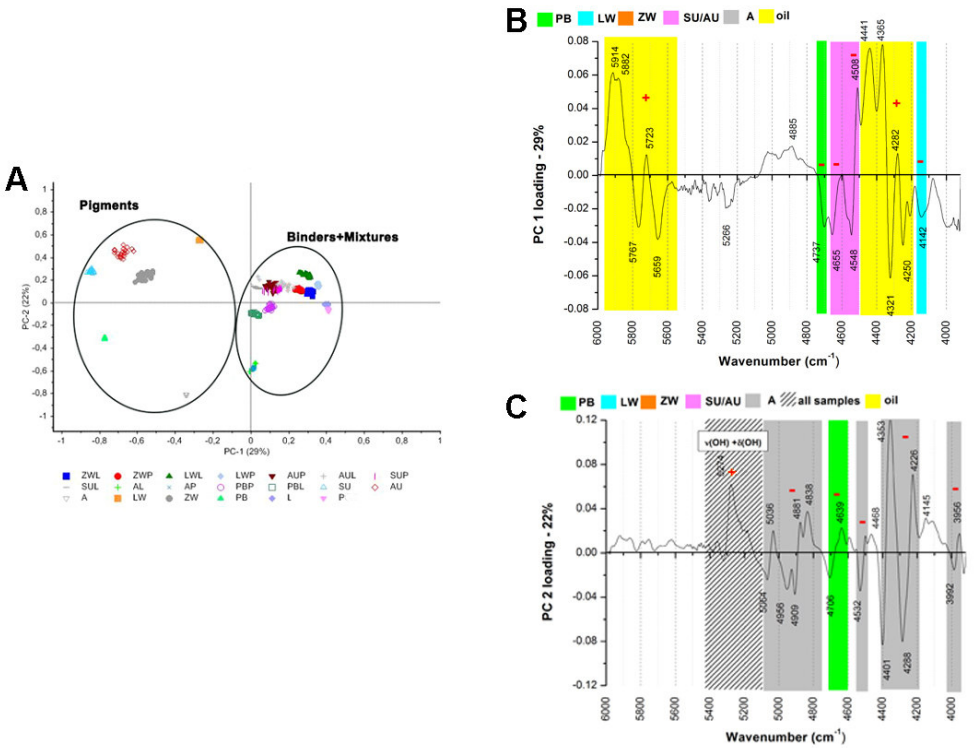

Fig. S1 Score plot of PC1-PC2 (A) along with the corresponding loading plots: PC1 (B) and PC2 (C) related to the statistical model built, processing only FT-NIR first derivative spectra of all samples.

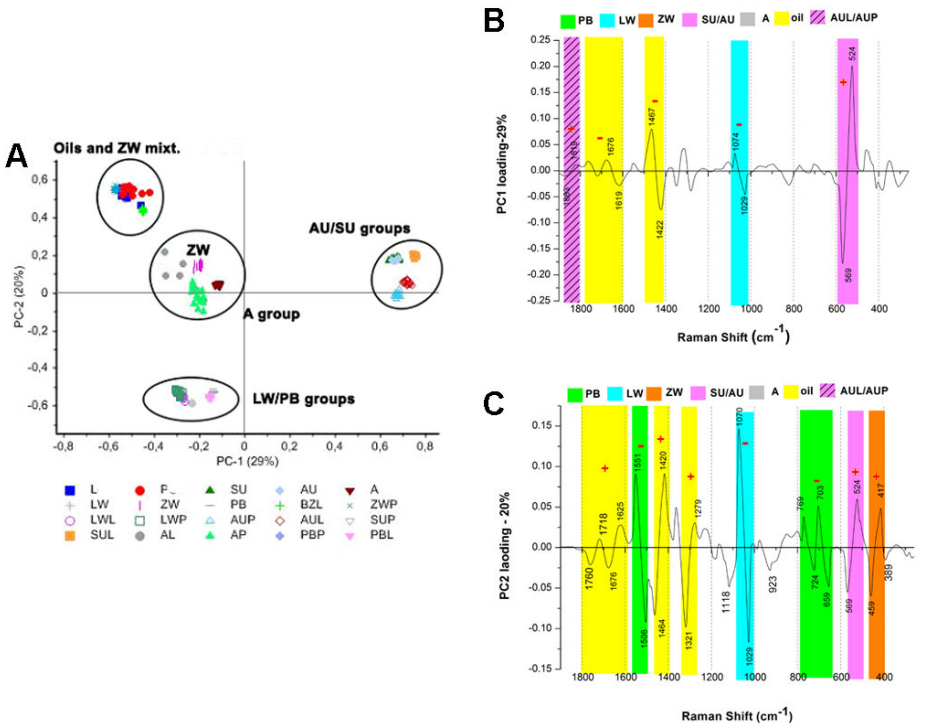

Fig. S2 Score plot of PC1-PC2 (A) along with the corresponding loading plots: PC1 (B) and PC2 (C) related to the statistical model built, processing only micro-Raman first derivative spectra of all samples.

References

[1] B. Stuart, Analytical techniques in materials conservation, John Wiley and Sons Ltd., Chichester, UK, 2007.

[2] I. Bonaduce, M. Cito, M.P. Colombini, The development of a gas chromatographic-mass spectrometric analytical procedure for the determination of lipids, proteins and resins in the same paint micro-sample avoiding interferences from inorganic media, J. Chromatogr. A 2009, 1216, pp 5931-5939.

[3] E. Manzano, L.R. Rodriguez-Simón, N. Navas, R. Checa-Moreno, M. Romera, L.F. Capitan-Vallvey, Study of the GC–MS determination of the palmitic–stearic acid ratio for the characterization of drying oil in painting: La Encarnación by Alonso Cano as a case study, Talanta 2011, 84, pp 1148-1154.

[4] M.P. Colombini, A. Andreotti, I. Bonaduce, F. Modugno, E. Ribechini, Analytical strategies for characterizing organic paint media using Gas Chromatography/Mass Spectrometry, Acc. Chem. Res. 2010, 43, pp 715-727.

[5] A. Zoppi, C. Lofrumento, M. Ricci, E. Cantisani, T. Fratini, E. M. Castellucci, A novel piece of Minoan art in Italy: the first spectroscopic study of the wall paintings from Phaistos, J. Raman Spectrosc. 2012, 43, pp 1663-1670.

[6] N. Navas, J. Romero-Pastor, E. Manzano, C. Cardell, Raman spectroscopic discrimination of pigments and tempera paint model samples by principal component analysis on first-derivative spectra, J. Raman Spectrosc. 2010, 41, pp 1196-1203.

[7] J. Romero-Pastor, N. Navas, S. Kuckova, A. Rodríguez-Navarro, C. Cardell, Collagen-based proteinaceous binder-pigment interaction study under UV ageing conditions by MALDI-TOF-MS and principal component analysis, J. Raman Spectrosc. 2012, 47, pp 322-330.

[8] E. Manzano, J. García-Atero, A. Dominquez-Vidal, M. J. Ayora-Cañada, L.F. Capitán-Vallvey, N. Navas, Discrimination of aged mixtures of lipidic paint binders by Raman spectroscopy and chemometrics, J. Raman Spectrosc. 2012, 43, pp 781-786.

[9] N. Navas, J. Romero-Pastor, E. Manzano, C. Cardell, Benefits of applying combined diffuse reflectance FTIR spectroscopy and principal component analysis for the study of blue tempera historical painting, Anal. Chim. Acta 2008, 630, pp 141-149.

[10] M. Otto, Chemometrics: statistics and computer application in analytical chemistry, Wiley-VCH, Weinheim, Germany, 1999.

[11] R. J. Gettens, H. Kühn, W.T. Chase, Lead White, in: A. Roy (Ed.), Artists pigments: a handbook of their history and characteristics, vol. 2, Oxford University Press, New York, 1993, pp. 67-81.

[12] S. Carlesi, M. Ricci, C. Cucci, J. La Nasa, C. Lofrumento, M. Picollo, M. Becucci, Multivariate analysis of combined Fourier transform near-infrared spectrometry (FT-NIR) and Raman datasets for improved discrimination of drying oils, Appl. Spectrosc. 2015, 69, pp 865-876.

[13] A. Pallipurath, J. Skelton, P. Ricciardi, S. Buklow, S. Elliot, Multivariate analysis of combined Raman and fibre-optic reflectance spectra for the identification of binder materials in simulated medieval paints, J. Raman Spectrosc. 2013, 44, pp 866-874.

[14] C. Cennini, in: F. Frezzano (Ed.), Il libro dell'arte (XIV sec), 1st ed., Neri Pozza Editore, Vicenza, Italy, 2003.

[15] M. Lazzari, O. Chiantore, Drying and oxidative degradation of linseed oil, Polym. Degrad. Stab. 1999, 65, pp 303-313.

[16] C.S. Tumosa, M.F. Meckleburg, Oil Paints: The chemistry of drying oils and the potential for solvent disruption, in: Marion F. Mecklenburg, A. Elena Charola, Robert J. Koestler (Ed.), New Insights into the Cleaning of Paintings, Smithsonian Institution Scholarly Press, Washington, 2013, pp 51-58.

[17] A. Savitzky, M. Golay, Smoothing and differentiation of data by simplified least squares procedures, Anal. Chem. 1964, 36, pp 1627-1639.

[18] M.J. Genge, A.P. Jones, G.D. Price, An infrared and Raman study of carbonate glasses: Implications for the structure of carbonatite magmas, Geochim. Cosmochim. Ac. 1995, 59(5), pp927-937.

[19] Li Daocong, P. Zhenghe, D. Lizhi, S. Yufang, Z. Yunhong, Theoretical studies on molecular structure and vibrational spectra of copper phthalocyanine, Vib. Spectrosc. 2005, 39, pp 191-199.

[20] M.F. Cerqueira, A.G., Rolo T. Viseu, J.Ayres de Campos, T. De Lacerda-Arôso, F. Oliveira, M.I. Vasilevskiy, E. Alves, Raman study of doped-ZnO thin films grown by rf sputtering, Phys. Status Solidi C 2010, 7(9), pp 2290-2293.

[21] M. Bacci, C. Cucci, E. Del Federico, A. Ienco, A. Jerschow, J.M. Newman, M. Picollo, An integrated spectroscopic approach for the identification of what distinguishes Afghan lapis lazuli from others, Vib. Spectrosc. 2009, 49, pp 80-83.

[22] I. Osticioli, N.F.C. Mendesa, A. Nevin, F.P. Gil, M. Becucci, E. Castellucci, Analysis of natural and artificial ultramarine blue pigments using laser induced breakdown and pulsed Raman spectroscopy, statistical analysis and light microscopy, Spectrochim. Acta A 2009, 73, pp 523-531.

[23] R.J.H. Clark, M.L. Curri, C.L. Laganara, The Identification of Lapis Lazuli on Medieval Pottery Fragments from the South of Italy, Spectrochim. Acta A 19997, 53, pp 597-603.

[24] R.L Frost., W.N. Martens, L. Rintoul, E. Mahmutagic, J.T. Kloprogge, Raman spectroscopic study of azurite and malachite at 298 and 77 K, J. Raman. Spectrosc. 2002, 33, pp 252-259.

[25] C.S. Tumosa, M.F. Mecklenburg, The influence of lead ions on the drying of oils, Rev. Conserv. 2005, 6, pp 39-47.

[26] M. Vagnini, C. Miliani, L. Cartechini, P. Rocchi, B.G. Brunetti, A. Sgamellotti, FT-NIR spectroscopy for non-invasive identification of natural polymers and resins in easel paintings, Anal. Bioanal. Chem. 2009, 395, pp 2107-2118.

[27] S.J. Gaffey, Spectral reflectance of carbonate minerals in the visible and near infrared (0.35–2.55 microns): calcite, aragonite, and dolomite, Am. Mineral., 1986, 71, pp 151-162.

[28] A.R. De Torres, S. Ruiz-Moreno, A. López-Gil, P. Ferrer, M.C. Chillón, Differentiation with Raman spectroscopy among several natural ultramarine blues and the synthetic ultramarine blue used by the Catalonian modernist painter Ramon Casas I Carbó, J. Raman. Spectrosc. 2014, 45, pp 1279-1284.

Chapter 4: Characterization and differentiation of aged neat linseed oil and white-oil mixtures

Abstract

In this chapter, a comprehensive study of the effects of natural ageing on neat linseed oil and on two oil-paint models, prepared with lead and zinc white pigments, is carried out by FT-NIR and micro-Raman spectroscopies. Both raw and first-derivative spectra are analysed in order to better extract information on the linseed oil behaviour.

The potentiality of applying Principal Component Analysis (PCA) to combined first derivative FT-NIR and micro-Raman spectra is further exploited in order to individuate and define probable ageing trends for these two oil-white mixtures.

Two 10-year old oil-mock-ups are also studied and used to verify the robustness of the investigated statistical models; they can be regarded as nearly a real contemporary oil painting.

To be thorough, the application of 2D-fluorescence spectroscopy to describe how the presence of these two white pigments may change the emission of linseed oil and consequently influence the associated ageing/degradation process is further investigated.

The observations of the chemical changes correlated with the drying/ageing process of linseed oil and its interactions with these two white pigments have been found in line with the literature.

Introduction

The drying process of oils has been investigated thoroughly over the past 140 years, and a detailed description of the mechanisms involved can be found in the literature. It appears to be a very complicated process, in which a number of different mechanisms are simultaneously occurring [**1-8**].

However, it is not clear to what extent the models developed are valid description of a normal ageing paint. The time-scale of most chemical studies is very short; the changes on a longer time-scale are simulated by using thermally- or light-accelerated ageing [**9-12**]. However, the assumption that this accelerated ageing does not change the ageing processes is not easily verified. The most important restriction of the majority of ageing studies is the absence of pigment, which is a crucial and potentially reactive compound in paint [**13**].

Fourier Transform Infrared (FT-IR), Attenuated Total Reflection (ATR), Gas Chromatography-Mass Spectrometry (GC-MS), Proton Nuclear Magnetic

Resonance (H-NMR) analysis have provided to be very useful tools in the study of the drying process of the oils and the investigation of traditional paints [**7, 11, 13-18**].
In this chapter, the applicability of Fourier Transform Near Infrared (FT-NIR) and micro-Raman spectroscopies for the characterization of the spectral changes due to the ageing of linseed oil, both neat and in presence of two white pigments, is investigated. Despite Raman studies have been already effectuated with a similar purpose [**7, 12, 19-20**], it is the first time that the FT-NIR capability to highlight some modifications related to the ageing process of linseed oil is tested and evaluated. Literature about the application of near-infrared spectroscopy in different scientific fields points to the use of the first-derivative transformation as an effective approach to NIR spectra analysis [**21-24**]. For this reason, first-derivative transformation has been applied in order to better extract information on linseed oil behaviour.
So, a FT-NIR and micro-Raman study of the natural ageing of neat linseed oil and corresponding paint-models prepared with lead and zinc white pigments is presented and discussed. Only naturally aged models/paints have been investigated, to minimize the bias due to the ageing method. Furthermore, the analysis of two 10-year old oil mock-ups prepared using lead white and zinc white pigments is described. These last paint models should be regarded as nearly a real contemporary oil painting.
In this chapter the potentiality of applying Principal Component Analysis (PCA) to combined first derivative FT-NIR and Raman spectra is further exploited. In this case, the goal is aimed at the evaluation of the possibility to define an ageing trend for oil-white mixtures. The investigated statistical models are further tested to project the spectra related to the 10-year old mock-ups.
Finally, to be thorough, the application of 2D-fluorescence spectroscopy to describe how the presence of these two white pigments may change the emission of linseed oil and consequently influence the associated ageing/degradation is further investigated.

4.1 Materials and methods

4.1.1 Linseed oil-paint models

For this work two white pigments (lead white and zinc white) were selected on the basis of their chemical and mineralogical properties, according to their widespread use in easel paintings throughout history. Both pigments were supplied by Sigma-Aldrich (Milano, Italy). Linseed oil from Zecchi (Florence, Italy) was selected as binding medium and was used as supplied.

Two oil-paint models were prepared according to the recipes reported in original treaties and artists' accounts [**25**], by mixing these pigments with linseed oil on the smooth surface of a panel glass.
The powdered pigments were initially crushed in an agate mortar in order to obtain a homogenously-fine particle grain size without lumps. The exact concentration of the pigment with respect to that of the drying oil was not determined *a priori*; instead, for each case, a mixture of similar consistency was used to prepare the paint models, so that they could be applied with a fine brush as a single thick layer onto microscope glass slides and left to dry on a bench top. Four sets of oil-paint models were prepared, obtaining a total of eight samples. The paint films had rough non-homogeneous surfaces as would be expected in real samples. Neat linseed oil was also applied as film on four microscope glass slides and left to dry.
All oil-paint models and neat linseed oil films were left to age on a shelf at room temperature (T: ~20°C) with indoor conditions (RH: ~50-55% and light: sunlight through a window).
Neat linseed oil was analysed after a natural ageing of three, nine and twelve-four months, while all linseed oil-paint models after nine and twelve-four months. The list of samples, together with their denomination and the evaluated ageing time, is reported in **Table 1**.
The neat powdered pigments were further directly analysed without any preparation.
Finally, it was possible analysing two 10-year old oil paint mock-ups (**Table 1**) prepared using lead white and zinc white, both purchased from Sigma-Aldrich mixed with linseed oil from Zecchi (Florence, Italy). These last paint models can be regarded as nearly a real contemporary oil painting. For each of them, the prepared canvas had a ground made by gypsum, calcite and rutile mixed with linseed oil.

Table 1 List of analysed samples with corresponding identification symbols and evaluated ageing times.

	Pigment	Drying Oil	Symbol	Ageing time
Neat dring oil	/	Linseed oil	L	3 months_L3 9 months_L9 24 months_L24
Oil-paunt models	Lead White (LW), $2PbCO_3*Pb(OH)_2$	+ linseed oil	LWL	9 months_LWL9 24 months_LWL24
	Zinc White (ZW), ZnO	+ linseed oil	ZWL	9 months_ZWL9 24 months_ZWL24
Oil-paint mock-ups	Lead White (LW), $2PbCO_3*Pb(OH)_2$	+ linseed oil	LWL	120 months_LWL120
	Lead White (LW), $2PbCO_3*Pb(OH)_2$	+ linseed oil	ZWL	120 months_ZWL120

4.1.2 FT-NIR spectroscopy

FT-NIR reflectance spectra were recorded using a portable ALPHA FTIR spectrometer (Bruker Optics), equipped with the external reflection module. Total reflection spectra (including both the specular and diffuse reflection contributes) were collected *in situ*, in the 7500-3900 cm^{-1} spectral range with a resolution of 4 cm^{-1} over 128 scans. The spectral sampling distance used for each scan was 2 cm^{-1}. An area of approximately 3 mm diameter was analysed. The background was acquired using a gold mirror as reference sample.
A total of 16 spectra were recorded for each model.

4.1.3 Micro-Raman spectroscopy

The Raman spectra were collected using a Renishaw 2000 micro-Raman spectrometer equipped with a 785 nm diode laser. To analyse neat linseed oil and powdered pigments, the laser was focused using a 50x objective lens, so that an area of approximately 2 μm diameter was considered. For the study of oil-paint models and oil-mock-ups a 20x objective lens was used so an area of

about 5μm diameter was investigated. In order to have an adequate sampling, we marked on the samples the spots characterized by FT-NIR and we made 16 different Raman measurements within the FT-NIR areas. We noticed that for each Raman single measurement we always obtained signals both from the pigment and the binder, furthermore the repeatability within the 16 measurements was quite good. Spectra were recorded in the 2000-200 cm^{-1} spectral range with a spectral resolution of 4 cm^{-1}. To improve signal/noise ratios, we acquired spectra of 25 s and 100 s exposure time (averaged 3 times) for neat binder/pigments and for oil-paint models, respectively. The spectral sampling distance used for each scan was 1 cm^{-1}. Precautions were taken to avoid any damage to the samples (i.e. laser–induced degradation of paint materials). This was done by visually confirming the absence of damage in the sampling area with the help of a video-camera. Thus, laser power was kept between 1 mW (with 50x objective lens) and 1.5 mW (with 20x objective lens) on the samples during the analysis. The spectrometer was calibrated at the beginning of each measurement session using the Raman signal from a silicon crystal at 520 cm^{-1}.
A total of 16 spectra were recorded for each model, as in case of FT-NIR.

4.1.4 2D-Fluorescence spectroscopy

Films were analysed using a scanning spectrofluorimeter with excitation provided by a xenon arc lamp (Jobin- Yvon/Horiba Fluoromax-P). Excitation-Emission (EE) spectra were constructed by recording a series of excitation spectra with an interval of 20 nm between successive excitation scans and with a resolution of 1 nm for emission spectra; scans were recorded with excitation from 250 to 550 nm, first- and second-order Rayleigh scattering was electronically eliminated and spectra were corrected for detector efficiency. Contour plots were constructed with spectra normalised to the maximum emission and are presented in all figures with 8 different colour levels with the least intense emissions represented in black and the strongest peaks in red.
All the films were analysed after an ageing of eighteen months.
This analysis was performed at the laboratories of IELS - FORTH (Institute of Electronic Structure and Laser – Foundation for Research and Technology) at Heraklion (Crete).

4.1.5 Data analysis

Multivariate analysis of spectral data was performed using the Principal Component Analysis (PCA) functionality of The Unscrambler® X software version 10.3 (CAMO).

The region of micro-Raman spectra between 1800 and 1000 cm^{-1} was taken for the Raman analysis, while FT-NIR spectra were analysed in the 6000-3900 cm^{-1} range, where signals appear well-defined and less affected by noise.
Before the construction of PCA-training matrices, spectra were processed separately. FT-NIR spectra were subjected to the Savitzky-Golay derivative algorithm (2^{nd} order polynomial, 15 data points) [**26**] without any other pre-processing. The micro-Raman spectra were, instead, subjected to baseline subtraction, average reduction of variables (factor two) and first derivative calculation by applying the Savitzky-Golay algorithm (2^{nd} order polynomial, 15 data points). Then, both the FT-NIR and micro-Raman spectra were vector normalized, as the use of absolute peak heights could lead to erroneous sample classifications [**27**].
Before the construction of PCA-trainings, the composite spectra were created: the pre-processed Raman and FT-NIR spectra were joined, generating a new combined first derivative Raman-FT-NIR spectrum. Each new combined spectrum includes 1450 data points, with the first 1050 derived from the FT-NIR spectrum abscissa and the remaining 400 points from the micro-Raman spectrum abscissa.
The Uncertainty Test was always performed to estimate the significance of variables. Then, PCA was performed by applying a mean-centering onto data column-wise and the Non Linear Iterative Partial Least Squares (NIPALS) algorithm. Each model was always validated by Leave One Out (LOO) cross-validation and by a projection of evaluated sets of spectral data acquired by the same samples (four spectra for each type of sample).
At the end, the pre-processed spectra, related to two 10-year old oil-mock-ups, were projected into the proper models.

4.2 State of art: the curing and the ageing processes of linseed oil

A mechanism of early reactions in the curing of linseed oil is presented and illustrated, followed by a brief review on how lead and zinc white pigments can influence the linseed oil properties.

4.2.1 The curing of neat linseed oil

In order to better understand the spectral features which can be observed for the neat linseed oil film after three, nine and twenty-four months of natural ageing (by means of FT-NIR and micro-Raman spectroscopies), a basic knowledge about the curing process and its main reaction steps may be fundamental.

Linseed oil was extensively used as medium for paintings, since the fifteenth century, owing its capacity, after being spread out in thin layer, to form a continuous film with good optical and mechanical properties within a reasonable time. Linseed oil highlighted the best performance compared with other common oils, mainly thanks to its faster drying, due to the highest concentration of linolenic acid [**11**], as can be seen in **Table 2**.

Table 2 Typical fatty acid composition (%) of the drying media studied [**20**].

Drying oil	Palmitic Acid C16:0	Stearic Acid C18:0	Oleic Acid C18:1	Linoleic Acid C18:2	Linolenic Acid C18:3
Linseed	7-8	3.4-4.6	18.5-22.6	14.2-17.2	52-55
Poppy-seed	10-14	2.5-3.2	16-24	56-70	0.4-0.6
Walnut	6.4-7.5	1.3-2.0	14-20	57-62	10-15

The curing of this drying oil has been the subject of several studies [**5, 7, 11, 13, 19, 28-29**], even if there are still some steps which need to be completely understood. Nevertheless, many scientists are in agreement with the curing of this drying oil has to be considered a process of autoxidation of the unsaturated fatty acid components, followed by a polymerisation. After an induction period attributed to the presence of natural antioxidants, the oil absorbs large amount of oxygen, giving rise to the formation of hydroperoxides with concomitant conjugation and *cis-trans* isomerization of the double bonds. The drying process is promoted by the reactive hydrogen atoms on the allylic positions of the molecules. Hydroperoxide formation is easier on linoleic and linolenic components where one and two methylene groups, respectively, are situated between two unconjugated double bonds. As an example, in scheme of **Fig. 1** is reported the mechanism of hydroperoxidation for a linoleic chain. Three hydroperoxides, A, B, C, could potentially form. It has been demonstrated that the formation of non-conjugated hydroperoxide C is not favoured. The subsequent decomposition of hydroperoxides into alkoxy (RO$^{\bullet}$) and peroxy (ROO$^{\bullet}$) free radicals, in presence of oxygen leads to the formation of by-products (e.g. alcohols, aldehydes, ketones, carboxylic acids and peresters) (**Fig. 2** and **Fig. 3**) and cross-links, mainly through radical recombination. A rapid decrease in the double bond concentration is also recorded when the curing continues, since the addition of free radicals (R$^{\bullet}$, RO$^{\bullet}$ and ROO$^{\bullet}$) on the conjugated double bonds becomes a probable mechanism (**Fig. 4**) [**7, 11**].
More precisely, once R$^{\bullet}$, RO$^{\bullet}$ and ROO$^{\bullet}$ radicals are formed, the occurrence of β-scission and/or Russel termination and/or other possible reactions appears inevitable (**Fig. 2** and **Fig. 3**), and so the formation of non-volatile aldehydes, carboxylic acids and ketones is possible, even during the very early stage. During the early stage of oxidation, the concentrations of R$^{\bullet}$, RO$^{\bullet}$ and ROO$^{\bullet}$ are likely not very high; as a consequence, termination by radical-radical

recombination results to be less favourable. In other words, the probability of the two radicals finding each other is rather low. As the amounts of radicals increases, the chance for the termination by radical-radical recombination increases, leading to cross-linking. The cross-linking can be also partially ascribed to the addition of these free radicals to the conjugated double bonds that are formed at the same time of hydroperoxides being generated (**Fig. 4**). Ether and peroxy linkages are present in roughly the same amount, whereas C-C cross-links are formed to a minor extent [**19**].

So, the polymerization process essentially consists in the intermolecular coupling of radicals originated by the decomposition of the relatively unstable peroxide groups, with the formation of cross-linked structures [**11**].

Although a film of linseed oil becomes *touch-dry* in a few days, the drying reactions continue for many years, as cross-linking proceeds, and a progressive hardening occurs. On the other hand, this hardening is moderated by the presence of unchanged glycerides which act as plasticisers [**11**].

The oil can gain up to 40% of its original weight during oxidation phase with some weight loss due the decomposition and disappearance of volatile compounds [**30-31**]. Linseed oil loses far less weight than the other drying oils [**31**].

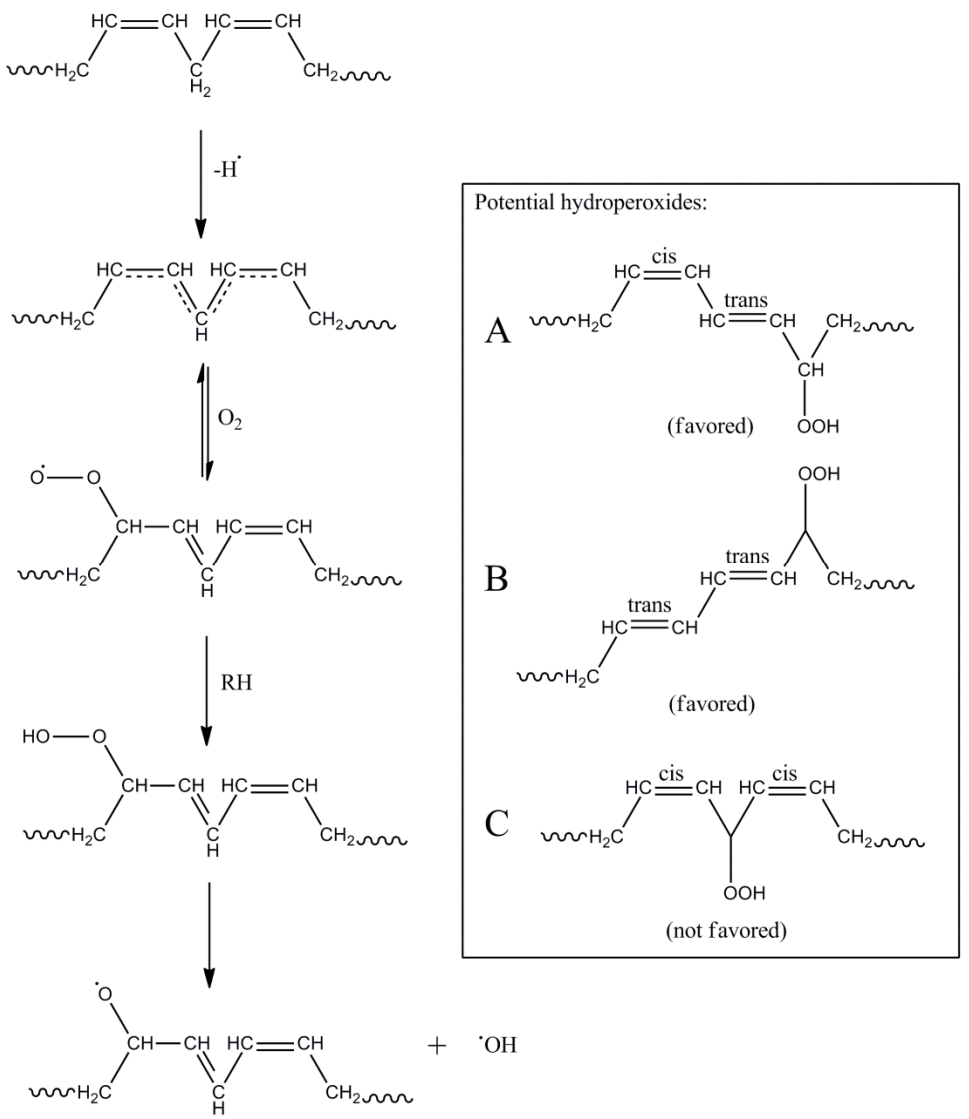

Fig. 1 Hydroperoxidation for a linoleic chain [**7**].

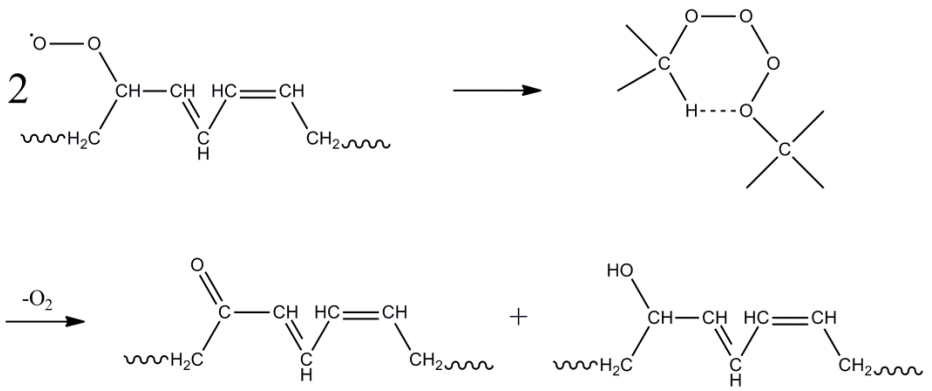

Fig. 2 Russel termination reaction [**11**].

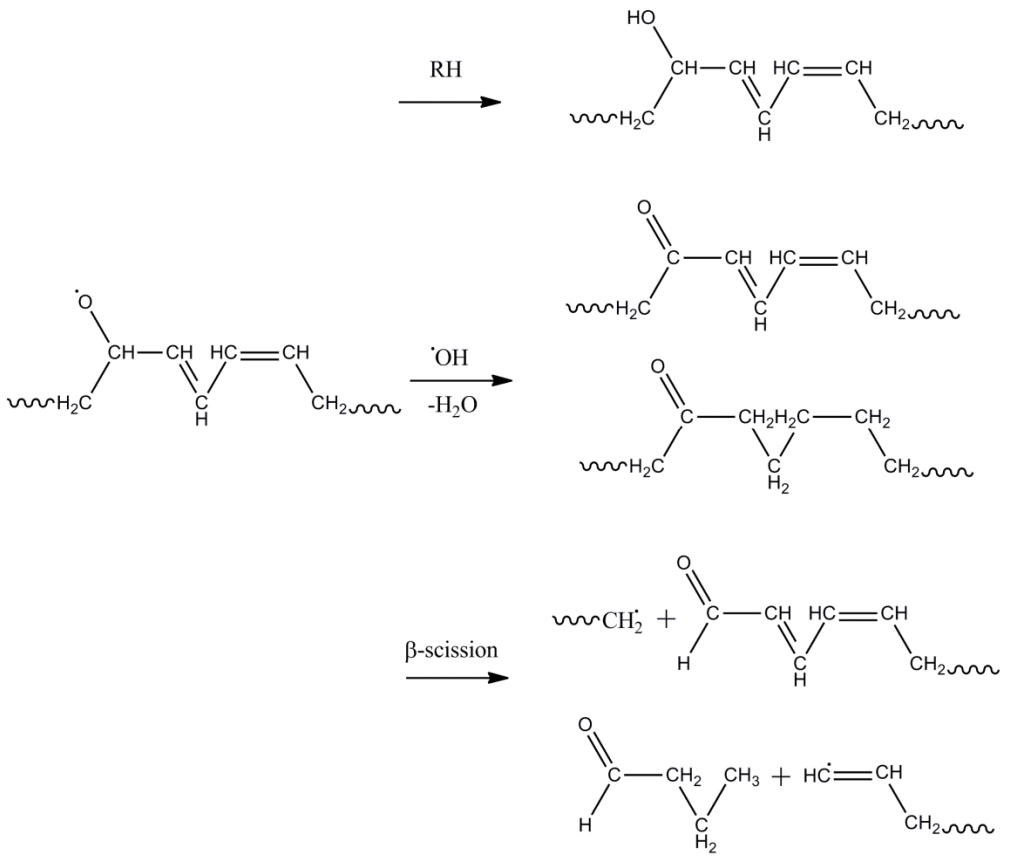

Fig. 3 Possible reactions of an alkoxy radical: formation of an alcohol; formation of ketones (saturated or unsaturated); formation of aldehydes by means of β-scission [**7**].

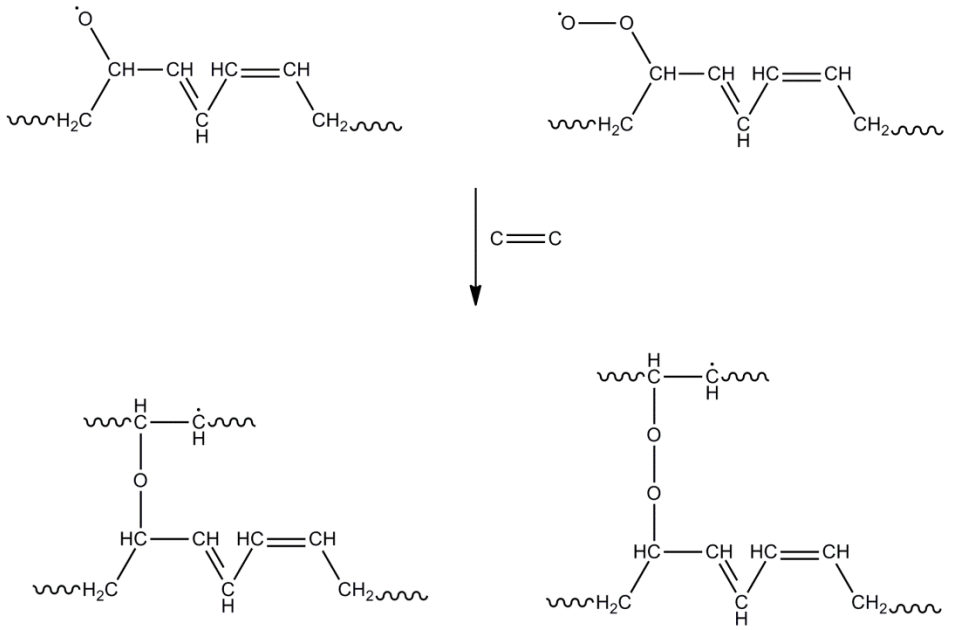

Fig. 4 Addition of alkoxy and peroxy radicals on conjugated double bonds with consequence formation of cross-links (ether and peroxy linkages) [**11**].

4.2.2 Ageing and degradation of linseed oil network

The numerous mechanisms that play a role in the ageing process of linseed oil paint are certainly more complicated than that explained in the previous figures (**Fig. 1**, **2**, **3** and **4**), which focus mainly on the general aspects of the reactions. These figures do not take into consideration the nature of the different types of fatty acids involved, the important role of catalysts in the different steps, the *cis-trans* transformation as a result of successive oxygen additions, the role of photooxidation in the formation of hydroperoxides [**32**], and several other reactions that take place on heat-bodying oil [**33**]. However, the cited publications provide a detailed overview of the afore-mentioned effects.

If no pigments or other additives are present, the ageing/degradation process of linseed oil may simply be considered as the continuation of the hardening process. After hardening, the dried oil shows a noteworthy stability, and degradation occurs only at long ageing times, through slow and progressive oxidation on the alkyl chains. The stiffening of the chains, due to the progressive formation of cross-links, is likely to hinder further coupling reactions, making more and more competitive other degradative pathways, in particular the decomposition by β–scission [**11**]. The autoxidation can also produce small chain acids, and oxidation at the C9 position of the unsaturated

acids can result in the formation of azelaic acid, found in the analysis of almost oil paintings [**5, 31, 34**].
Metals, light, heat and enzymes can accelerate the oxidation of unsaturated acids in linseed oil, and also influence the ageing and the degradation processes. In the case of photooxidation (oxidation reactions induced by light) no induction period and no inhibition by antioxidants are needed [**35**].
It is generally assumed that the role of pigments in the initial stages of drying is catalytic or inhibitive, influencing the activation of oxygen or the breakdown of hydroperoxides [**13**]. Nevertheless, several papers have been published on the interaction between metal salts, present as driers or pigments in painted artworks and linseed oil [**13-16, 31, 36**]. The main effect of pigments on the linseed oil ageing is represented by the triglyceride hydrolysis process which mainly takes place in presence of particular pigments, such as lead and zinc white (basic pigments) along with environmental humidity [**16**]. The hydrolysis reaction frees fatty acids from their esters, capable of migrating and/or reacting [**31**]. The most important consequence is the *saponification* process which leads to the formation of metal carboxylates/metal soaps. Generally, the saponification causes a darkening and a brittling of the painting [**16**]. Metal soaps defects may appear in the paint system in many different forms: as large aggregates that deform paint layers, as deposits on the surface of paint or homogeneously spread throughout paint layers. Besides causing a loss of pigment and change in surface texture, the formation of metal carboxylates has been linked to cases of brittleness, loss of strength and delamination of paint layers [**37**].

4.2.3 Lead White in oil-painting

The most important lead pigment is the basic carbonate or lead white. Reviews of its history and use in painting have been published by various authors [**38-41**].
It is common knowledge that this pigment has the capability to decrease the drying time of drying oils and to better polymerize films [**36**]. Driers may act in different ways to alter the drying behaviour of oils, and they may either increase the oxygen uptake through catalytic action, or they may accelerate the oxygen uptake (the induction period) through precipitation/deactivation of antioxidants. Besides, they can also promote the decomposition of hydroperoxides into free radicals, affecting the polymerization. Lead white can be considered both an oxidizing and a polymerization affecting drier [**36**].
In spite of cobalt- or manganese-based compounds, which easily touch-dry the surface of a film, but leave the subsurface soft, lead white is defined as a *through drier* able to dry also the subsurface [**42**]. The film made of basic

carbonate and linseed oil, does not necessarily become brittle, but maintains its flexibility for a considerable time [**43**].
Nevertheless, several papers have demonstrated that lead white in oil-paintings can lead to the formation of lead-carboxylates, promoting the triglyceride hydrolysis process [**13, 15-16, 44-45, 31, 36**]. After ten years, one paint film stored under museum conditions was found to have its saturated fatty acid ester linkages reduced by almost 25% [**46**]. Commercial lead white outdoor paints in contact with light and moisture can reach this level in less than three years [**47**]. The study of a series of old oil paintings by Turner and Sargent showed hydrolysis levels of paints of up to 90% after two hundred years [**48**].

4.2.4 Zinc White in oil-painting

Zinc oxide white pigment has been widely diffuse across Europe for about a century, from the second half of the nineteenth to the late sixties of the twentieth century, when the introduction of titanium white progressively replaced it. The history of zinc oxide as pigment is well covered in the literature [**49-52**].
Compared to lead white, the practical benefits associated to this pigment are the great fineness, the lesser tendency to yellowing and the resistance to darkening, when mixed with hydrogen sulphide pigments [**51-52**].
Despite its many advantages, zinc white shows some aspects potentially dangerous when applied in oil-paintings. It is indeed able to absorb UV radiation below 366 nm, which is a property that may help to protect an organic binder from destructive radiation, but at the same time this capability may also be the source of troublesome photochemical reactions [**53**]. As previously discussed, the drying and degradation processes in drying oils can be influenced by light. Moreover, zinc white is hygroscopic, thus it can absorb water if exposed to air and may become sticky [**54**]. Consequently, if a "sticky" zinc white is used to make an oil colour, some moisture can be trapped inside the paint, which may lead to cracking and peeling.
Furthermore, recently researchers have found that zinc white can rapidly form a hard and brittle oil-film (in about three years), following a particular drying process. Indeed, they found a significant amount of oleic acid in aged paint films, in spite of the expected azelaic acid, in addition to this brittleness [**55-56**].
According to them, zinc oxide in oil would form a tightly packed crystalline structure with a highly ordered lamellar distribution. Because of this layered structure the paint film would appear very stiff in a short time, and the tight packing of hydrocarbon chains would make double bonds more difficult to oxidize. As a result, unsaturated chains could remain trapped within the aged

paint layers for years, this way leading to a lower polymerization degree. Cross-linking is therefore hindered and overall structural stability results minor than that of a normally oxidized oil-paint film. This condition produces outwardly the effect of a film that prematurely appears hard and becomes brittle in a short time. The absence of an adequate number of cross-links together with the stiff lamellar structure would be responsible of episodes of planar fracture within zinc white oil-films [**55-56**]. Use the stand-oil is recorded by Khün [**51**] precisely to counteract zinc oxide tendency to form hard and brittle films.
So, zinc white should be considered as a *hardener* than a drier for linseed oil, because it causes the oil solidification at an earlier stage in the oxidation [**57**]. Zinc white is also defined as an auxiliary or a secondary drier [**36**].
Finally, also zinc white pigment tends to react with drying oils, forming metal carboxylates, due to its high reactivity with certain fatty acids, e.g., stearic acid [**37, 58-59**].

4.3 Results and discussions

The whole FT-NIR and micro-Raman raw spectra acquired on neat linseed oil and the corresponding white-models are reported in **Appendix D**.

4.3.1. 2D-Fluorescence spectroscopy

To be thorough, 2D-fluorescence spectroscopy application is discussed in this section, in order to describe how the presence of lead white (LW) or zinc white (ZW) pigments may change the emission of linseed oil, consequently influencing its ageing/degradation.
In **Fig. 5**, all Excitation-Emission (EE) maps of pure pigments, neat linseed oil, LWL and ZWL mixtures, are reported. It is noteworthy to recall that all the films were analysed after an eighteen months ageing, after the curing process had started.
For neat linseed oil, as can be better seen in **Fig. 5F**, the main fluorescent maximum is located at about 496-500 nm. The origin of the broad fluorescence in solid linseed oil can be explained as a consequence of the polymerization, resulting from the autoxidation reactions of fatty acids. Unluckily, more precise attributions are not possible [**60-61**].
De la Rie [**60**] observed that pigment may have a great influence on the fluorescence and the yellowing of dried linseed oil. Many pigments have an inhibiting effect on fluorescence (e.g. ochres, siennas, umbers, bone black). However, some other pigments, such as lead white or cobalt blue, stimulate the development of fluorescence in linseed oil. By contrast, another group of pigments, such as titanium white and vermillion, are considered inert [**60**].

When LW and ZW pigments are mixed with linseed oil, the intensity emission increases, as can be observed in both EE maps (**Fig. 5D** and **Fig. 5E**) and associated emission spectra of LWL (**Fig. 5G**) and ZWL (**Fig. 5H**). Simultaneously, a broadening for the emission band can be detected, along with a slight blue shift for both excitation and emission ranges (**Fig. 5D** and **Fig. 5E**). On the contrary, the corresponding emission spectra (**Fig. 5G** and **Fig. 5H**) do not show any emission maximum shift in comparison with that of neat linseed oil (**Fig. 5F**).

These results agree with the increasing of fluorescence intensity observed for a lead white oil-paint upon storage in daylight [**60**]. Further, this behaviour has been explained by taking into consideration the drier capability of this pigment, which is able to immediately react with linseed oil [**60**].

Additionally, as regards EE map related to ZWL (**Fig. 5E**), a specific emission at 384 nm, for excitation wavelengths below about 370 nm (**Fig. 5H**), can be detected. This emission is characteristic of ZW pigment [**62**], which absorbs UV-radiation below 366 nm [**53**].

In order to better visualize the actual contribution of these pigments, we calculated the *spectra-sum* of the emission spectra referred to neat linseed oil and pure pigment at the excitation wavelength of 430 nm. This excitation wavelength, as can be seen in **Fig. 5F**, causes the maximum in emission for neat linseed oil. In **Fig. 6** the LW+L and ZW+L spectra-sum are shown along with the spectra of neat linseed oil, pure pigments and oil-paint mixtures.

We can observe that the spectra of both mixtures are characterized by the highest intensity emission. The emission of LWL model results to be approximately four times that of LW+L, while the emission of ZWL is around three times that of ZW+L.

So, it is reasonable to presume these pigments actually interact with linseed oil and the resulting emission is not only due to scattering phenomena.

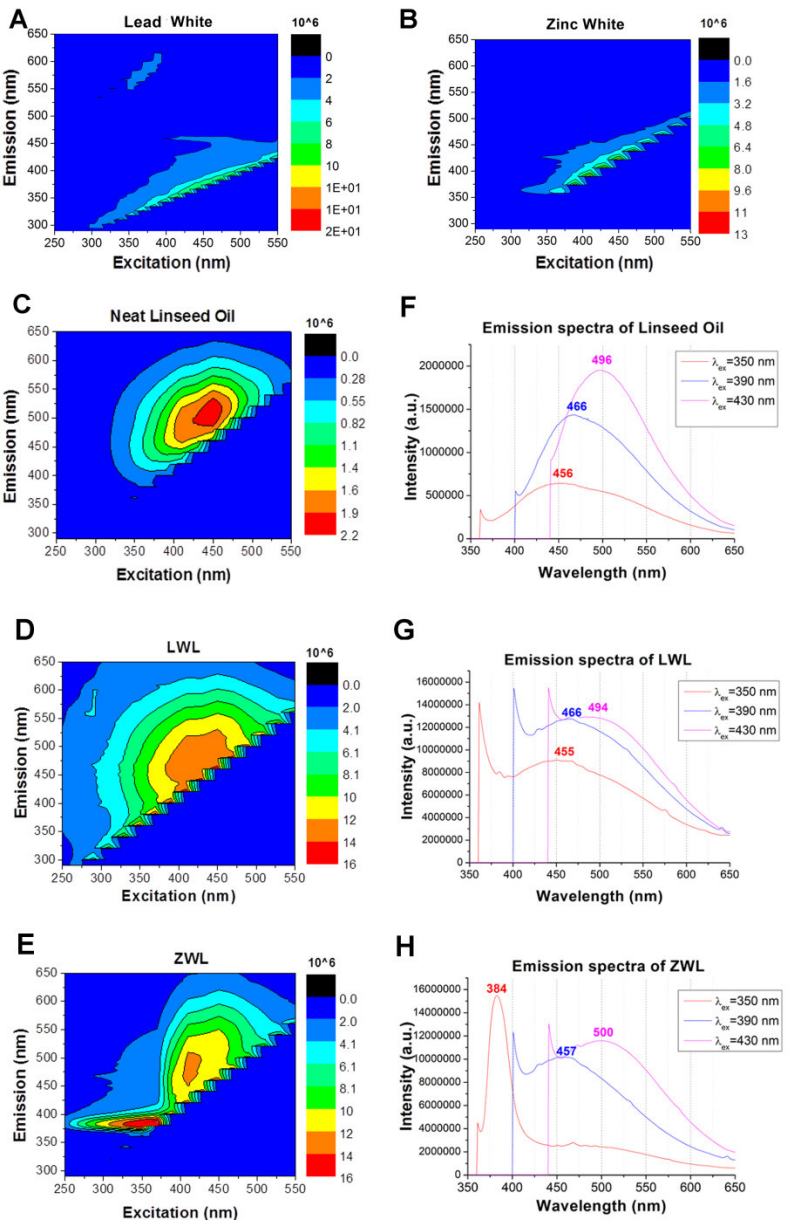

Fig. 5 2D-fluorescence maps of LW (A), ZW (B) pigments, neat linseed oil (C), LWL (D) and ZWL (E) mixtures, along with associated emission spectra (F, G and H).

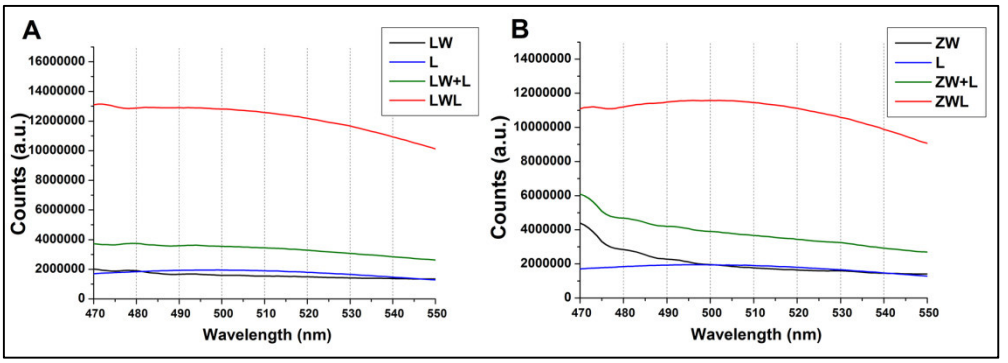

Fig. 6 Comparison between related emission spectra of L (blue line), LW pigment (black line), LWL mixture (red line) and the sum LW+L, green line (A); and between emission spectra of L (blue line), ZW pigment (black line), ZWL mixture (red line) and the sum ZW+L, green line (B). Excitation wavelength is 430 nm.

4.3.2 Neat linseed oil

4.3.2.1 The main spectral features detectable by means of FT-NIR and Raman spectroscopy

The drying of linseed oil has been monitored by FT-NIR and micro-Raman spectroscopies to study the mechanisms involved.

In order to better highlight the changes related to the drying process, a description of the main spectral bands detectable by means of these two techniques may be useful. The description of the neat linseed oil spectra acquired after a three months natural ageing is reported below. Linseed oil, after three months ageing period, is considered as a ''fresh'' binding medium, because the drying process has not been completed yet; according to previous studies, an oil paint can be regarded as aged only one year after its preparation [**18, 63**].

In **Fig. 7** the raw FT-NIR and micro-Raman spectra (**Fig. 7A** and **Fig. 7C**, respectively) are displayed along with the first derivative associated (**Fig. 7B** and **Fig. 7D**). The various absorption bands in the FT-NIR spectrum are assigned in **Table 2**, whereas the Raman bands are described in **Table 3**, following the current literature [**22, 24, 64-68**].

The main NIR absorption bands, characteristic for linseed oil, are represented by the combination of methylenic C-H stretching and bending between 4250 and 4350 cm^{-1} and first CH_2 stretching overtone bands, which occur in the 5700-5800 cm^{-1} spectral range (**Fig. 7A**). The second overtone of ester carbonyl stretching mode is observed at about 5176 cm^{-1}, whereas the combination of ester C=O and methylenic C-H stretching modes occurs at about 4690 cm^{-1} (**Fig. 7A**). Moreover, the combination band between methylenic C-H stretching and

C-O stretching is located at 4060 cm^{-1}. All these bands distinctively appear with clear features in the associated first derivative spectrum (**Fig. 7B**). By comparing the zero-crossing-point first derivative and the maximum or minimum in the original FT-NIR spectrum, it is clear that the first derivative spectrum enables a better individuation of the main absorption bands.
Additionally, a weak absorption band at around 4600 cm^{-1}, related to the combination between methylenic C-H stretching and double bond C=C stretching [**65**], can be observed in the FT-NIR spectrum (**Fig. 7A**). As can be seen in **Fig. 7B**, this band appears as a "shoulder" of the most intense absorption band due to the combination of ester C=O and methylenic C-H stretching modes located at 4690 cm^{-1}.
Going to focus on Raman spectrum, shown in **Fig. 7C**, the major Raman bands are represented by symmetric rock in *cis* double bond (at about 1265 cm^{-1}), in-phase methylene twist mode (at about 1302 cm^{-1}), scissoring mode of methylene (at 1442 cm^{-1}), unconjugated *cis* double bound stretching mode (at about 1655 cm^{-1}) and ester stretching (at about 1735-40 cm^{-1}). So, the Raman spectrum of linseed oil predominantly contains bands arising from vibrations of the hydrocarbon chains. For further information, the corresponding first derivative spectrum is also reported (**Fig. 7D**), even if the main Raman bands are all detectable from the raw one.

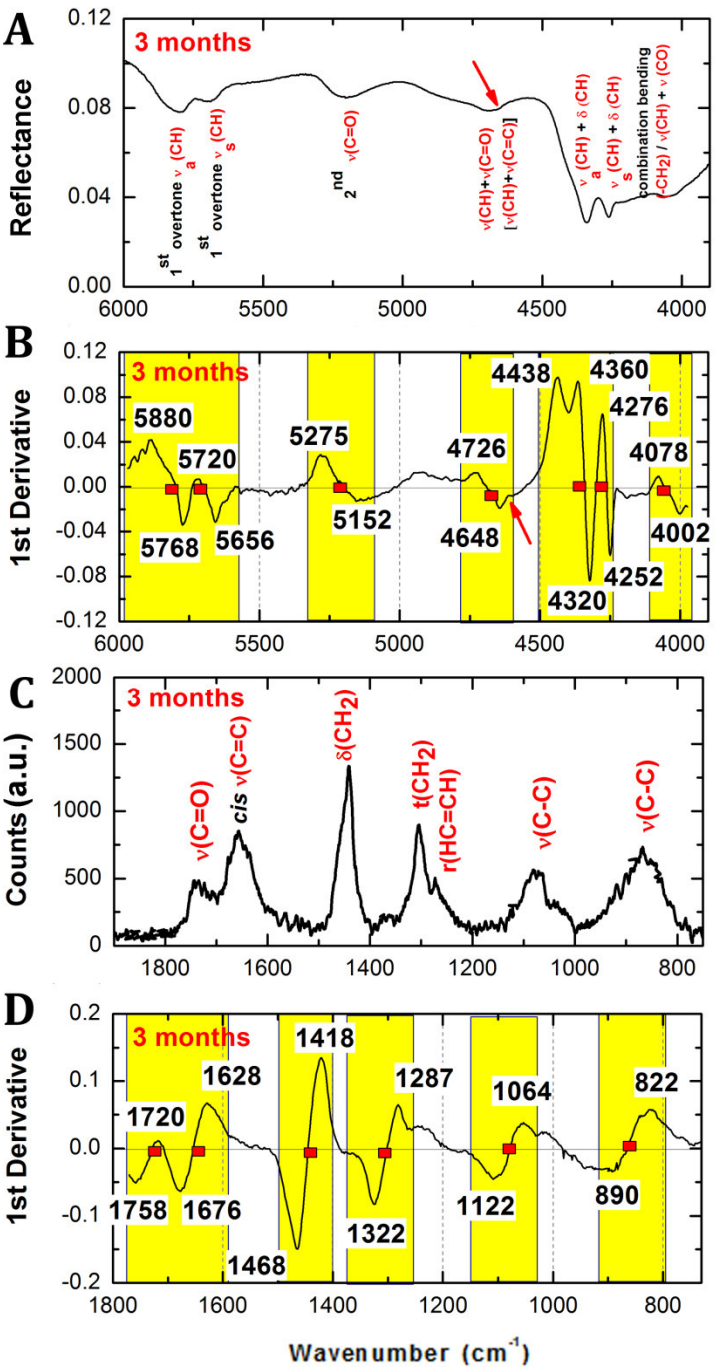

Fig. 7 Results from the spectroscopic characterization of neat linseed oil after a three months ageing period: FT-NIR (A) and micro-Raman (C) spectra and the associated first derivative spectra (B and D, respectively).

Table 2 Major bands in FT-NIR spectra (frequency shifts in cm^{-1}) of linseed oil (L), after an ageing of three months, compared to current reference values and assignments.

L	cm^{-1}	Functional group	Assignment	Ref.
5792	5794	$-CH_2-$	1st overtone asymmetric stretching $\nu_a(CH)$	[22]
5698	5698	$-CH_2-$	1st overtone symmetric stretching $\nu_s(CH)$	[22]
	5260	.C=OOH	2nd overtone stretching $\nu(C=O)$Acids, carboxylic	[24]
5202	5180	.C=OOR	2nd overtone stretching $\nu(C=O)$ Acids and esters	[22]
4707	4707	-COOR	stretching $\nu(CH)$ + stretching $\nu(C=O)$	[22]
	4690		stretching $\nu(CH)$ + stretching $\nu(C=O)$	[64]
4595	4610	-HC=CH-	asymmetric stretching $\nu_s(CH)$ + stretching $\nu(C=C)$	[65]
4340	4340	$-CH_2-$	asymmetric stretching $\nu_a(CH)$ + bending $\delta(CH)$	[22]
4261	4261	$-CH_2-$	symmetric stretching $\nu_s(CH)$ + bending $\delta(CH)$	[22]
4060	4060	$-CH_2-/CO$	Combination bending/ ν (CH) + $\nu(CO)$	[24]

Table 3 Major bands in Raman spectra (frequency shifts in cm^{-1}) of linseed oil (L), after an ageing of three months, compared to current reference values and assignments.

L	cm^{-1}	Assignment	Ref
1735	1740	Stretching $\nu(C=O)$ esters	[66-67]
	1730		
1654	1655	Stretching $\nu(C=C)$ [unconjugated *cis* dialkyl C=C double bond]	[20]
1441	1440	Bending $\delta(CH_2)$	[20]
1306	1300	In phase methylene twisting motion $\delta(CH_2)_2$	[20]
1265	1265	Rocking deformation of *cis* dialkylethylenes r(CH=CH)	[20]
1072	1085	Stretching $\nu(C-C)$	[68]
865	864	Stretching $\nu(C-C)$	[68]

4.3.2.2 Raman and FT-NIR spectra of aged linseed oil

Raman spectroscopy can be useful to follow chemical changes affecting C=C bonds during the drying process of linseed oil, because the relative modifications are reflected in spectral changes [**7, 12, 19-20, 28**]. The following figure (**Fig. 8**) displays the properly selected parts of the spectra with the aim to visualize the changes more clearly.

In the early stage (**Fig. 8A**), below 1800 cm^{-1} two main Raman bands related to unsaturation bonds present on long-chains of fatty acids can be found: 1265 and 1654 cm^{-1}.

The spectra before and after ageing in **Fig. 8** evidence the main effect of the curing process is the reduction of *cis* double bonds, with the concomitant broadening of the two Raman bands located between 1800 and 1500 cm^{-1}. As previously described, the oxidation of unsaturated fatty acids is accompanied by considerable isomerization of double bonds, leading to products containing *trans* double bonds and conjugated double bonds systems [**7, 12, 19-20, 28**]. Conjugated C=C stretching modes are located at around 1599 cm^{-1} (*cis*) and at 1634 cm^{-1} (*trans*), whereas isolated *trans* C=C stretching at about 1670 cm^{-1} [**19, 28**].

When the curing continues, a rapid decrease in the double bond concentration can be also recorded, since the addition of free radicals, originated from the unstable hydroperoxides ($R^{\bullet}$, $RO^{\bullet}$ and $ROO^{\bullet}$), on the conjugated double bonds becomes a probable mechanism.

To better visualize the general tendency of the unconjugated *cis* double bond band to decrease, the intensity of this band was compared to that related to ester stretching vibration, located at 1735 cm^{-1}. The obtained results are shown in **Table 4**.

After 24 months, as can be seen in **Fig. 8C**, the unsaturation bonds are still present. So, it is reasonable to assume that the curing process of this neat linseed oil model has not already been completed. However, the intense decreasing of C=C content can be observed, as highlighted by **Table 4**.

Table 4 Comparison between intensities of *cis* double bond band (1654 cm^{-1}) and ester stretching band (1735 cm^{-1}) during 24 months of ageing.

Ageing time	$I_{1654cm^{-1}}/I_{1735\ cm^{-1}}$
L3	1.81
L9	1.66
L24	1.28

Furthermore, the rapid decomposition of the hydroperoxides facilitates the formation of a multitude of volatile and non-volatile secondary oxidation

products, such as alcohols, saturated and unsaturated ketones, aldehydes, carboxylic acids and epoxy compounds [**7, 12, 19-20, 28**], and the broadening of the Raman band related to C=O stretching, could be mainly explained thanks to the appearance of the C=O stretching modes of saturated and conjugated unsaturated ketones (1725 cm^{-1} and 1690 cm^{-1} respectively) and of aldehydes (at 1748 cm^{-1}) [**7, 28**]. The bands not involved in C=C losses or isomerizations do not changes during the oxidation process.

In **Fig.9** the associated first derivative spectra referred to the neat linseed oil film during the 24 months of ageing are reported.

Fig. 9A agrees with the discussion about the intensity reduction of *cis* double bond band and concomitant broadening, as consequence of the oxidation process.

On the other hand, only slightly changes can be observed in the 1600-1000 cm^{-1} spectral range (**Fig. 9B**). By focusing on the spectral interval characterized by the presence of the symmetric rock in *cis* double bond (at about 1265 cm^{-1}), clear changes are not evident, except the intensity reduction of the maximum at about 1250 cm^{-1}.

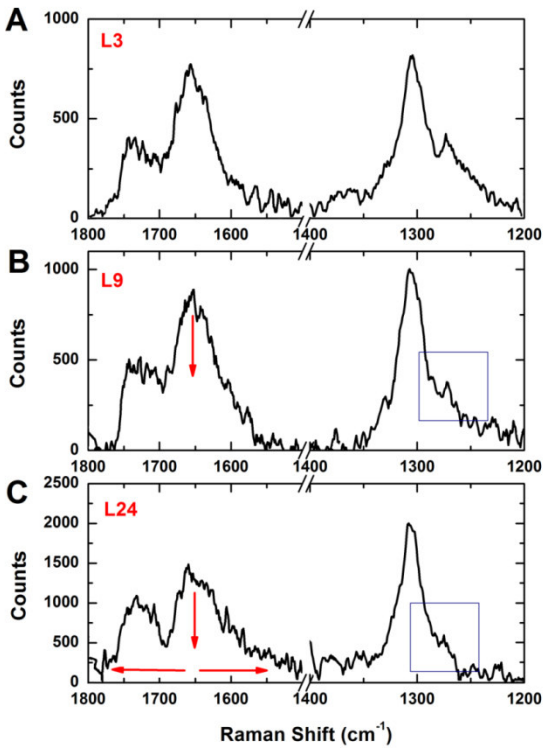

Fig. 8 Raman study of the drying of linseed oil at different ageing periods: L3 (A); L9 (B) and L24 (C). The analysed spectral ranges are the following: 1800-1500 cm^{-1} and 1400-1200 cm^{-1}. Raman spectra are shown after background subtraction.

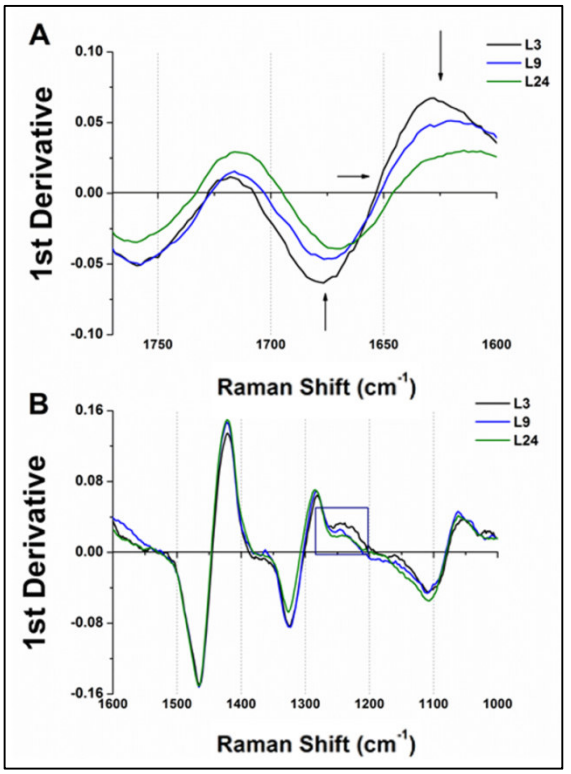

Fig. 9 First derivative Raman spectra referred to L3, L9 and L24. The analysed spectral ranges are the following: 1770-1600 cm^{-1} (A) and 1600-1000 cm^{-1} (B).

The raw FT-NIR spectra do not show significant spectral differences, even if when considering their first derivative transformation (**Fig. 10**), some changes, as consequence of the drying process, can be highlighted. For this reason, the raw FT-NIR spectra are directly reported in **Appendix D**.

If we compare spectra, reported in **Fig. 10**, it is possible to underline the following changes: an intensity decreasing for the combination bands of methylenic C-H stretching and bending between 4250 and 4350 cm^{-1} (**Fig. 10A**); a disappearance of the shoulder previously associated to the combination band between methylenic C-H stretching and C=C double bond stretching, located at 4600 cm^{-1} (**Fig. 10A**) and an increasing for the second overtone of ester carbonyl stretching mode at about 5176 cm^{-1} (**Fig. 10B**). On the other hand, only slightly changes can be observed for the first CH_2 stretching overtone bands, which occur in the 5700-5800 cm^{-1} spectral range (**Fig. 10C**).

In previous studies, focused on the application of FT-IR/ATR/Raman spectroscopies to follow the drying process of linseed oil [**11, 13, 20, 28, 69**] the decreasing of the C-H stretching vibration bands, located at about 2930 and 2855 cm^{-1}, has been observed, being interpreted accordingly to the decrease of aliphatic moieties due to the loss of volatile products, which formed since the

early stage. The increase of the carbonyl stretching second overtone could be explained by taking into account some considerations. The second overtones of carbonyl stretching modes of ketones, aldehydes, carboxylic acids are effectively located in the spectral range between 5260-5180 cm^{-1} [**24**]. These products, formed during the drying and ageing processes, are non-volatile. This consideration agrees with the broadening observed for the Raman band centered at 1735 cm^{-1}, referred to the C=O stretching.

Furthermore, after a longer ageing time, the decreasing of C-H stretching vibrations should be also related to the hydrolysis process or metal carboxylates formation [**13**].

In addition, the disappearance of the combination band between methylenic C-H stretching and C=C double bond stretching is in accordance with the curing reactions described for linseed oil.

Finally, it is noteworthy to underline that the chemical changes highlighted by FT-NIR technique can be mainly related to the C-H and C=O vibrations, whereas Raman spectroscopy better describes modifications referred to the C=C content, as expected.

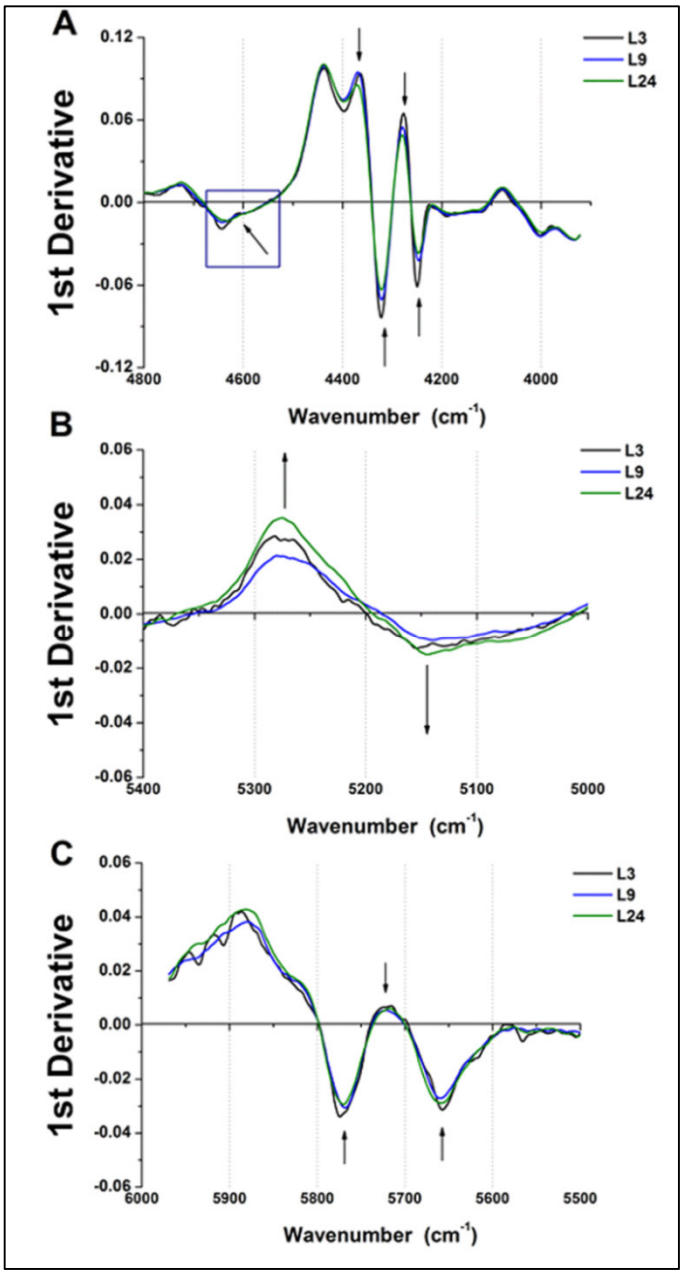

Fig. 10 First derivative FT-NIR spectra referred to L3, L9 and L24. The analysed spectral ranges are the following: 4800-3900 cm^{-1} (A), 5400-5000 cm^{-1} (B) and 6000-5500 cm^{-1} (C).

4.3.3 Lead white oil-paint model (LWL)

4.3.3.1 Raman and FT-NIR spectra of aged LWL model

As previously discussed, lead white has the capability to decrease the drying time of drying oils and to give better polymerized films [**36**]. So, it is reasonable to assume that it should modify the spectral properties of linseed oil, since early stages. In order to better understand how it influences the near infrared absorption bands of linseed oil, a comparison between the raw FT-NIR spectra of the lead white pigment (LW) and lead white mixtures (LWL is the linseed oil mixture and LWP is the poppy-seed oil mixture), after the ageing time of 9-months, is shown in **Fig. 11A**. LWP is reported and discussed only for completeness.

The FT-NIR spectrum of LW is characterized by the following combination bands: the OH stretching and Pb-OH deformation modes (at about 4294 cm^{-1}) [**22**]; the carbonate ion stretching and bending (at about 4407 cm^{-1}) [**70**]; the OH stretching and C-O stretching (at 4980 cm^{-1}) [**22**] and that related to water presence (at 5150 cm^{-1}) [**24**]. In spite of this, the raw FT-NIR spectra referred to LWL and LWP models are mainly influenced by the contributions due to the oils. This behaviour can be better highlighted by considering their first derivative transformation (**Fig.11B** and **Fig. 11C**).

Previously we observed that one of the main changes, due to the drying process of neat linseed oil and detectable by means of FT-NIR spectroscopy, is the intensity decreasing of the combination bands of methylenic C-H stretching and bending (between 4250 and 4350 cm^{-1}). It has been interpreted, for the early stages, as a decrease of aliphatic moieties consequent to the loss of volatile products, formed during the oxidation process [**7, 12, 19-20, 28**]. Focusing on the **Fig. 11B** and **Fig. 11C**, it is possible to highlight an intense intensity decreasing for the combination bands of methylenic C-H stretching and bending in both spectra of LWL and LWP. This decreasing should be explained by means of two principal reasons: the actual contribution from the pigment in this spectral interval, and the dryer capability of lead white. The decreasing is more evident for LWL.

Due to the fact that the drying process is promoted by the reactive hydrogen atoms on the allylic positions of the molecules, the hydroperoxide formation is easier on linoleic and linolenic components, where one and two methylene groups, respectively, are situated between two unconjugated double bonds. Linseed oil is characterised by the fastest drying bent, thanks to its higher concentration of linolenic acid (**Table 2**), with respect to poppy-seed oil.

By contrast, the raw Raman spectra referred to LWL model result to be more influenced by the contributions from the pigment. The very intense symmetric

and asymmetric stretching modes of carbonate ion (at 1053 and 1049 cm^{-1}, respectively) [**41**], indeed, prevail. For this reason, they are directly reported in **Appendix D.**

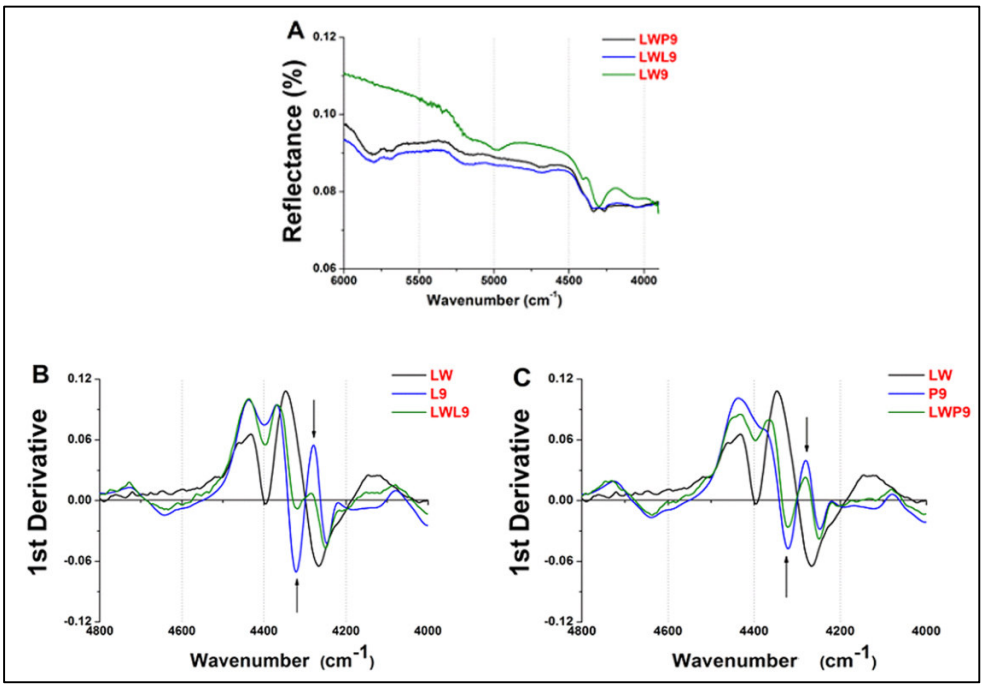

Fig. 11 Comparisons between the raw FT-NIR spectra of LW pigment, LWL9 and LWP9 mixtures (A); between the first derivative spectra of LW, L9 and LWL9 (B); and between the first derivative spectra of LW, P9 and LWP9 (C).

As regards the drying/ageing process of LWL model, only the significant spectra and intervals are shown and discussed. In addition, the spectrum referred to the 10-year old mock-up is also reported (LWL120) to make a comparison with our model.

Neither the Raman spectra, nor their corresponding first derivative transformation provide significant information, so they are directly shown in **Appendix D**, together with the raw FT-NIR spectra, which do not show any substantial spectral difference.

Considering the first derivative FT-NIR spectra (**Fig. 12**), some changes can be highlighted, such as the intensity decreasing of the combination bands of methylenic C-H stretching and bending between 4250 and 4350 cm^{-1} (**Fig. 12A**) and the increase of the second overtone of ester carbonyl stretching mode at about 5176 cm^{-1} (**Fig. 12B**), accordingly to the previous observations about neat linseed oil.

Considering the LWL120 mock-up spectrum, it is reasonable to assume that the observable changes are related to both the formation of secondary oxidative

products, and to the hydrolysis process and/or metal carboxylates formation. Van der Weerd *et al.* [**13**] and Mazzeo *et al.* [**16**], indeed, found high contents of lead carboxylates, in lead white mixtures prepared with linseed oil, after 50 and 10 years of natural ageing, respectively. Furthermore, it is possible to note that the zero-crossing-point first derivative (**Fig. 12B**) is located between 5200 and 5150 cm^{-1}, consequently the water absorption cannot be completely excluded, despite the increasing trend towards higher wavenumbers.
Finally, as can be seen in **Fig. 12**, LWL120 mock-up spectrum seems to follow the ageing trend defined by LWL9 and LWL24.
Nevertheless, a more detailed description for the drying/ageing of LWL model cannot be obtained by the direct observation of the raw and first derivative spectra.

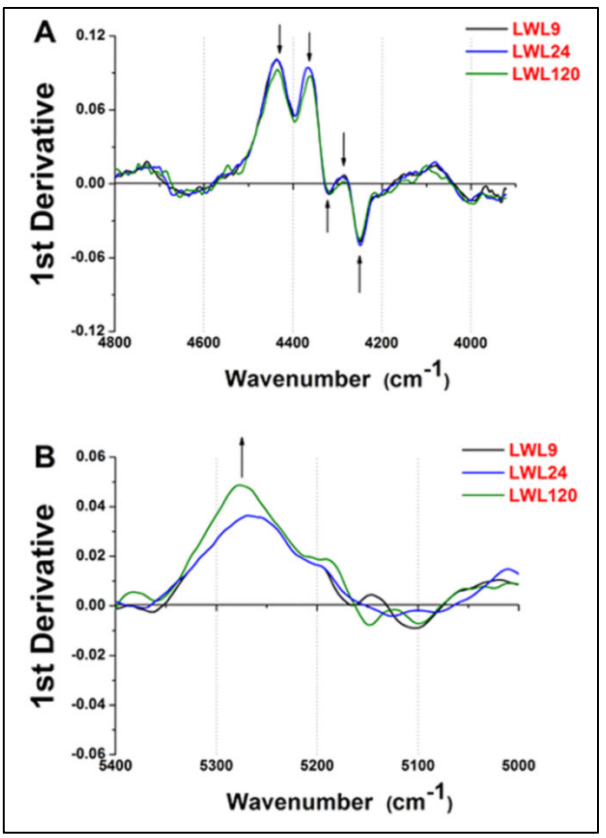

Fig. 12 First derivative FT-NIR spectra referred to LWL9, LWL24 and LWL120. The analysed spectral ranges are the following: 4800-3900 cm^{-1} (A) and 5400-5000 cm^{-1} (B).

4.3.3.2 PCA applied to combined first derivative FT-NIR and micro-Raman spectra of aged LWL model

In this section, the potentiality of PCA to improve the description for the drying/ageing process of the LWL model is evaluated and discussed.
Taking into account separately FT-NIR and micro-Raman spectroscopies, it is possible to define an ageing trend, as can be seen in the **Fig. S1** and **Fig. S2** in the **supplementary section**, which is in agreement with the changes/modifications previously highlighted analysing raw and associated first derivative spectra.
Nevertheless, their combination enables to gather valuable information from the data, allowing a more complete and rapid description of the different properties involved in the drying process related to both spectral ranges (6000-3900 cm^{-1} and 1800-1000 cm^{-1}). The application of a multivariate analytical tool, such as PCA, to the combined spectra, indeed, allows the concomitant extraction of important information.
The statistical model has been elaborated by processing the combined spectra referred to lead white pigment (LW), linseed oil (with ageing of 3, 9 and 24 months: L3, L9 and L24) and lead white oil-paint mixture (with ageing of 9 and 24 months: LWL9 and LWL24), so that a total of 96 spectra has been processed.
Successively, in order to verify the robustness of this statistical model, the combined first derivative FT-NIR and micro-Raman spectra, referred to the 10-year old mock-up (LWL120), have been projected.
The obtained statistical model explains a significant percentage (99%) of the cumulative variability by the first three PCs. In detail, PC1 explains 88% of the total variance contained in the data, whereas PC2 and PC3 explain 8 and 3% of the total variance, respectively.
In **Fig. 13A** the two-dimensional score plot in the space defined by PC1 and PC2 is reported, showing a clear differentiation between LW pigment, linseed oil and LWL mixture. In this score plot, no information referred to drying/ageing changes can be highlighted. The vibrations mainly responsible for sample distinguishing can be observed by the inspection of the associated loading plots, shown in **Fig. 13C**. In all loading plots, the "plus" symbol is used to indicate that the first derivative contribution is concordant with the starting spectra, while a "minus" sign is used when its behaviour is reversed. Moreover, the main contributions related to pigment and linseed oil are highlighted by means of different colours.

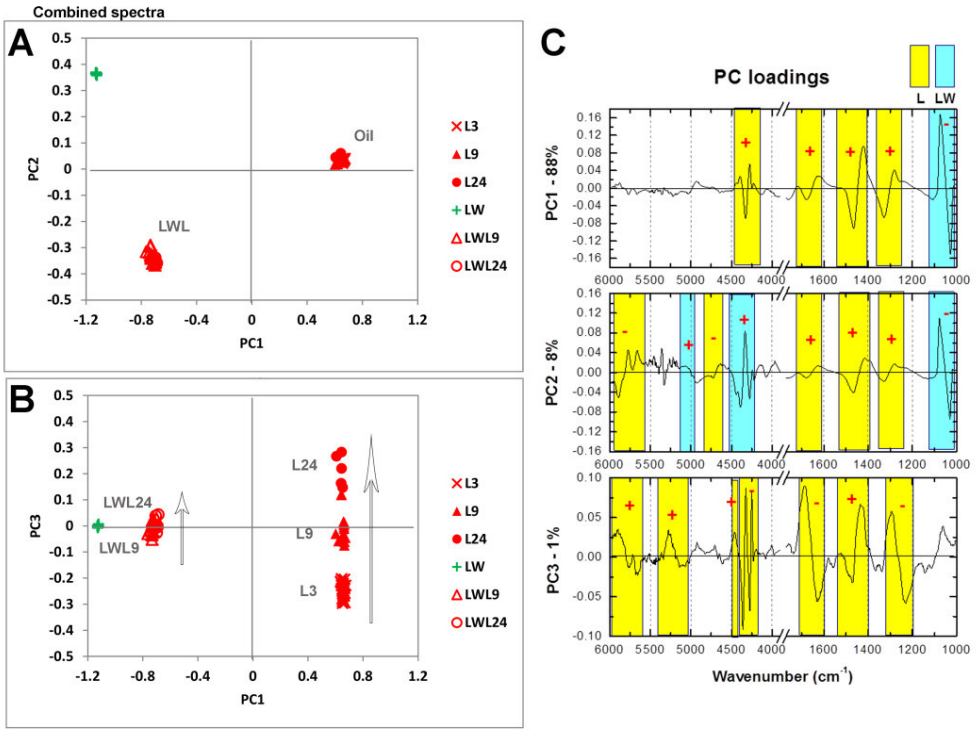

Fig 13 PCA applied to combined FT-NIR and Raman first derivative spectra for LWL model: score plots of PC1-PC2 (A) and PC1-PC3 (B); loading plots of PC1, PC2 and PC3 (C).

As regards the drying/ageing process, the most useful principal component is represented by the third one (PC3). The associated loading plot (**Fig. 13C**) is characterized exclusively by linseed oil contributions (Positive ones: at 5792 cm^{-1} and 5698cm^{-1}, first methylenic CH stretching overtone bands; at 5260 cm^{-1}, the second overtone of carbonyl stretching; at 4690 cm^{-1}, combination of ester C=O and methylenic C-H stretching modes; at 1441 cm^{-1}, methylenic bending. Negative ones: at 4340 cm^{-1} and 4261 cm^{-1}, combination bands of methylenic C-H stretching and bending; at 1650 cm^{-1}, *cis* double bond stretching mode, and at 1306 cm^{-1}, in phase methylene twisting motion).

The decreasing in abundance of C=C double bond, the intensity decreasing of methylene stretching and bending combination bands, along with the intensity increasing of the second overtone of carbonyl stretching, are all described by PC3, going from negative to positive score values, so that a trend related to the drying process of LWL/linseed oil can be defined (**Fig. 13B**). For LWL model, LWL9 is characterised by the minor score value in comparison with LWL24, even if the LWL group, since the influence of the pigment, shows a limited inner differentiation in comparison with that observed for neat linseed oil group (**Fig. 13B**).

These results are in agreement with the previous discussion on the raw/first derivative spectra, and PCA extracted information, also from micro-Raman spectra.
Finally, the combined first derivative FT-NIR and micro-Raman spectra related to LWL120 mock-up have been projected into this statistical model, giving as a result that PC1 describes 72% of the total variance contained in the unknown data, whereas PC2 and PC3 explain 14 and 3% of the total variance, respectively.
In the score plot defined by the first two PCs the spectra referred to LWL 120 mock-up result to be superimposed on the original cluster previously defined for LWL model (**Fig. 14A**).
Focusing on the score plot defined by PC1 and PC3, shown in **Fig. 14B**, LWL120 is located in an upper position in comparison with LWL9 and LWL24, in agreement with the trend previously individuated to describe the drying/ageing process of this oil-paint model.

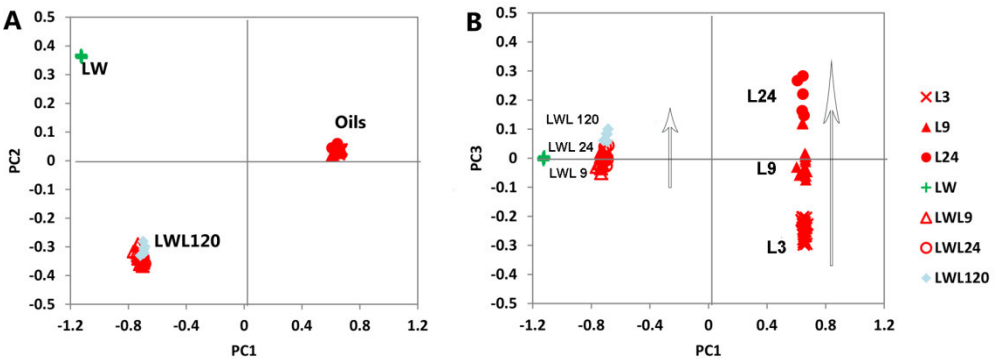

Fig 14 PCA applied to combined FT-NIR and Raman first derivative spectra for LWL model: projection of the first derivative combined spectra related to LWL120 mock-up. Score plots of PC1-PC2 (A) and PC1-PC3 (B).

4.3.4 Zinc white oil-paint model (ZWL)

4.3.4.1 Raman and FT-NIR spectra of aged ZWL model

In order to better understand how zinc white pigment influences the near infrared absorption bands of linseed oil a comparison between the raw spectra of zinc white pigment (ZW) and corresponding oil-paint model, analysed after an ageing of 9-months (ZWL9) is reported in **Fig. 15A**. The FT-NIR spectrum of ZW does not show characteristic absorption bands. The main contribution is related to the absorbed water (at around 5150 cm^{-1}), as can be better highlighted by the associated first derivative transformation (**Fig. 15C**). This aspect is in agreement with its hygroscopic capability [**54**].

Nevertheless, if we compare the first derivative FT-NIR spectra of ZW, ZWL9 and L9 (**Fig. 15B**), a decreasing for the combination bands of methylenic C-H stretching and bending between 4250 and 4350 cm^{-1} can be observed, "highlighting" that a reactivity is actually present.

ZW pigment is not characterized by characteristic Raman bands in the investigated region between 1800 and 1000 cm^{-1}, and then the oils contributions are all detectable.

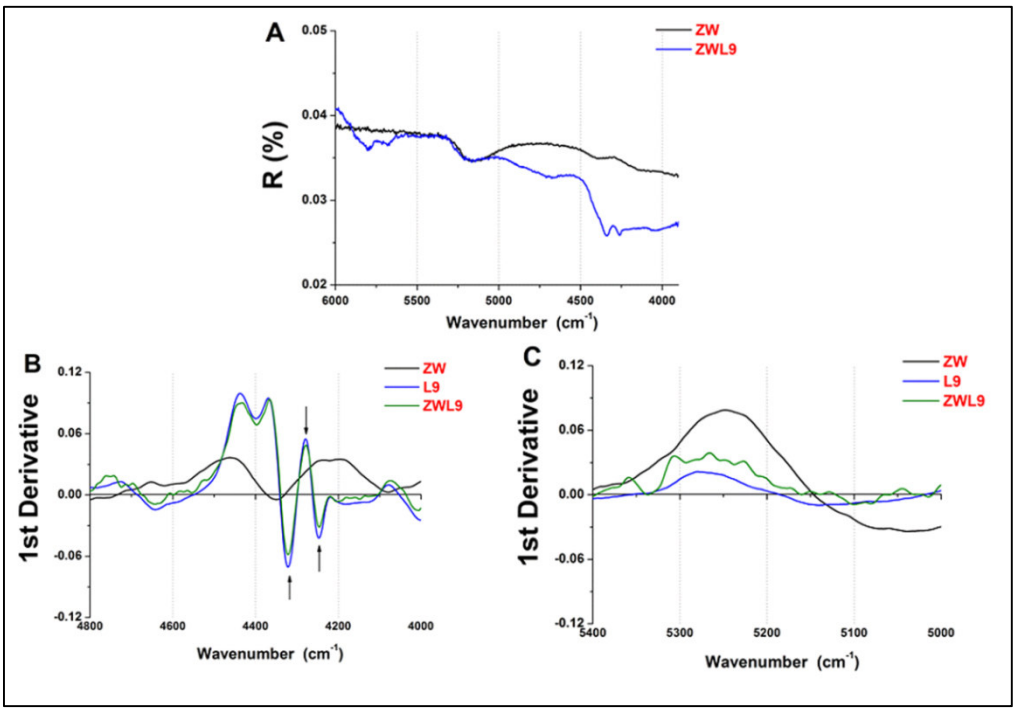

Fig. 15 Comparison between the raw FT-NIR spectra of ZW pigment and ZWL9 mixture (A); and between the first derivative spectra of ZW, L9 and ZWL9 in the range 4800-4000 cm^{-1} (B). Zoom on the spectral range between 5400-5000 cm^{-1} of the first derivative spectra of ZW, L9 and ZWL9 (C).

As concerns the drying/ageing of ZWL model, the following figures display only some selected parts of the significant spectra to visualize the changes more clearly, while the whole spectra (FT-NIR and Raman) are directly reported in **Appendix D**. In addition, the spectrum referred to the 10-year old mock-up (ZWL120) is also shown to make a comparison with the calculated model.
By comparing the first derivative FT-NIR spectra (**Fig. 16**) it is possible to underline the intensity decreasing of the combination bands of methylenic C-H stretching and bending between 4250 and 4350 cm^{-1} (**Fig. 16A**) and the

increasing of the second overtone of ester carbonyl stretching mode at about 5176 cm^{-1} (**Fig. 16B**), exactly as detected for neat linseed oil and LWL model.

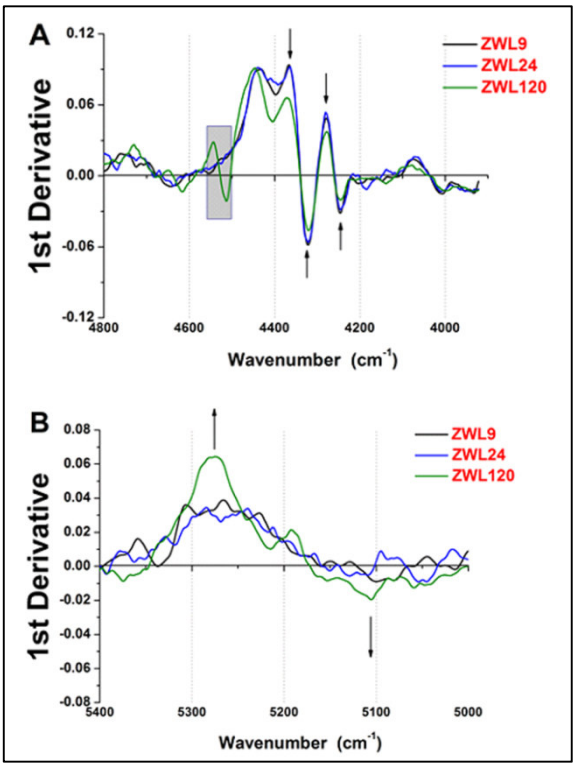

Fig. 16 First derivative FT-NIR spectra referred to ZWL9, ZWL24 and ZWL120. The analysed spectral ranges are the following: 4800-3900 cm^{-1} (A) and 5400-5000 cm^{-1} (B).

ZWL120 mock-up spectrum seems to respect the ageing trend defined by ZWL9 and ZWL24, and it is reasonable to assume that the observed changes should be related to the formation of secondary oxidative products and to the hydrolysis process and/or metal carboxylates formation [**13, 16**]. The only difference with neat linseed oil is that these modifications are more evident. Zinc white is, indeed, considered to be more reactive than lead white, as regards the formation of metal carboxylates [**44, 59, 71**]. Furthermore, it is also UV-absorbent [**53**] and highly hygroscopic [**54**], as previously discussed.
Additionally, the first derivative FT-NIR spectrum of ZWL120 shows a contribution around 4530 cm^{-1}, which is not associated to any compound/material used for the ground (gypsum, calcite, rutile and linseed oil). It could be related either to aldehydes (ν(C=O) + ν(CH) and 2δ(CH)+ν(C=O) [**24**]) and to epoxides (epoxy stretching and bending [**72**]). Obviously, this is only a tentative explanation, since deeper analysis is needed to formulate a proper assignment.

Furthermore, it is possible to note that the zero-crossing-point first derivative, in **Fig. 16B**, is located between 5200 and 5150 cm^{-1}, exactly as observed for LWL model. Consequently, the water absorption should not be completely excluded, since ZW is hygroscopic. Nevertheless, the trend of the increasing is shifted towards higher wavenumbers (greatly in the ZWL120 spectrum).

Raman spectroscopy appears to be useful to follow the chemical changes affecting C=C bonds during the drying process of ZWL model.

The comparison between the Raman spectra of ZWL in **Fig. 17** underlines that the main effect of the curing process is the reduction of *cis* double bounds, with concomitant broadening of the two Raman bands located between 1800 and 1500 cm^{-1}, as previously described for neat linseed oil.

It is interesting to observe that in the spectrum related to ZWL120, unsaturation bonds evidences are still present. This result might be explained through studies effectuated by Rogala *et al.* [**55**] and Maines *et al.* [**56**], previously discussed.

Fig. 18, which shows the 1770-1600 cm^{-1} spectral range of the associated first derivative spectra, is in agreement with the previous discussion about the intensity reduction of *cis* double bond band and concomitant broadening as consequence of the oxidation process.

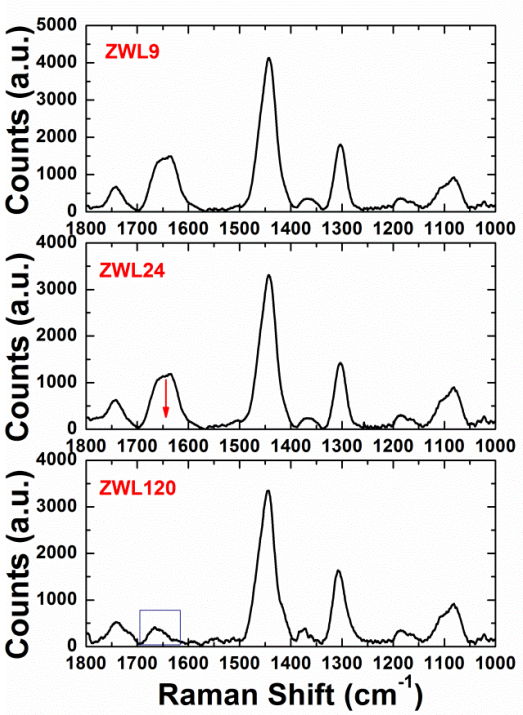

Fig. 17 Raman study of the drying of linseed oil mixed with zinc white at different ageing periods: ZWL9 (A); ZWL24 (B) and ZWL120 (C). The analysed spectral range is 1800-1000 cm^{-1}.

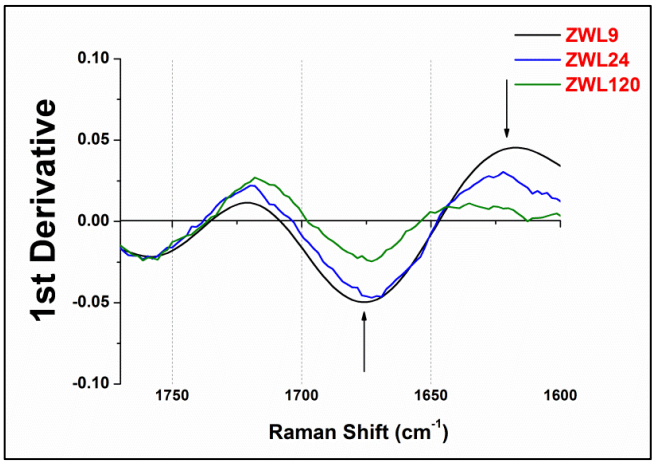

Fig. 18 First derivative Raman spectra referred to ZWL9, ZWL24 and ZWL120. The analysed spectral range is the following: 1770-1600 cm^{-1}.

4.3.3.2 PCA applied to combined FT-NIR and micro-Raman first derivative spectra of aged ZWL model

In this section, the potentiality of Principal Component Analysis (PCA) to improve the description for the drying/ageing process of the ZWL model is evaluated and discussed.

Also for ZWL, taking into account separately FT-NIR and micro-Raman spectroscopies, it is possible to define an ageing trend, as can be seen in the **Fig. S3** in the **supplementary section**, in agreement with the changes/modifications, previously highlighted analysing raw and associated first derivative spectra. Nevertheless, their combination enables to gather valuable information from the data, allowing a more rapid description of the different properties involved in the drying process.

The statistical model has been elaborated processing the combined spectra referred to zinc white pigment (ZW), linseed oil (with ageing of 3, 9 and 24 months: L3, L9 and L24) and zinc white oil-paint mixture (with ageing of 9 and 24 months: ZWL9 and ZWL24). A total of 96 spectra has been processed.

Successively, in order to verify the robustness of this statistical model, the combined first derivative FT-NIR and micro-Raman spectra, referred to the 10-year old mock-up (ZWL120), have been projected within/inside.

The obtained statistical model explains a significant percentage (85%) of the cumulative variability is explained by the first two PCs. In detail, PC1 explains 81% of the total variance contained in the data, whereas PC2 explains 4% of it.

In **Fig. 19A** the two-dimensional score plot in the space defined by PC1 and PC2 is reported, showing a clear differentiation between ZW pigment, linseed oil and ZWL mixture. The vibrations mainly responsible for sample distinguishing can be observed by inspection of the associated loading plots, shown in **Fig.**

19B. In all the loading plots the "plus" symbol is used to indicate that the first derivative contribution is concordant with the starting spectra, while the "minus" sign is used when its behaviour is reversed. Moreover, the main contributions related to pigment and linseed oil are highlighted by means of different colours.

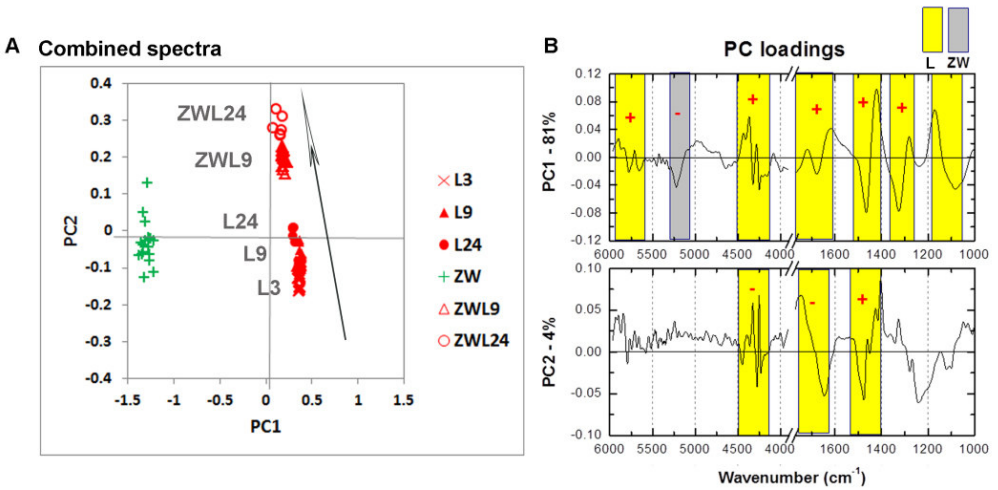

Fig. 19 PCA applied to combined FT-NIR and Raman first derivative spectra for ZWL model: score plot of PC1-PC2 (A) and associated loading plots (B).

The main negative contribution in the loading plot of PC1 can be ascribed to ZW pigment (at 5150 cm^{-1}, combination of OH stretching and bending related to absorbed water), whereas all the positive ones are related to the linseed oil (at 5792 and 5698 cm^{-1}, first overtones of methylenic stretching; at 4340 cm^{-1} and 4261 cm^{-1}, the methylene stretching and bending combination bands; at 1654 cm^{-1}, ν(C=C) fundamental stretching; at 1440 cm^{-1}, methylenic bending; at 1306 cm^{-1}, in phase methylene twisting motion).

According to PC1, ZWL group is positive, exactly as linseed oil model, whereas ZW pigment results to be negative (**Fig. 19A**). As previously described, this pigment in the spectral ranges investigated, only shows the absorption band related to the absorbed water (at about 5150 cm^{-1}).

As regards the ageing process, the most useful principal component is represented by the second one (PC2). The associated loading plot (**Fig. 19B**) is exclusively characterized by linseed oil contributions (Positive ones: at 1441 cm^{-1}, methylenic bending. Negative ones: at 4340 cm^{-1} and 4261 cm^{-1}, combination bands of methylenic C-H stretching and bending; at 1650 cm^{-1}, *cis* double bond stretching mode).

The decreasing in abundance of C=C double bond and the intensity decreasing of methylene stretching and bending combination bands are all described by

PC2, going from negative to positive score values. Consequently, a trend related to the drying process of ZWL/linseed oil can be defined (**Fig. 19A**).
These results are in agreement with the previous discussion on the raw/first derivative spectra.
Finally, the combined first derivative FT-NIR and micro-Raman spectra related to the 10-year old mock-up (ZWL120) have been projected into this PCA model, so that PC1 describes 54% of the total variance contained in the unknown data, whereas PC2 explains 2% of it.
In the score plot defined by the first two PCs the spectra referred to the 10-year-old mock-up (ZWL120) are located in an upper position in comparison with ZWL9 and ZWL24, in agreement with the trend previously individuated to describe the ageing process of zinc-white-linseed oil-model.

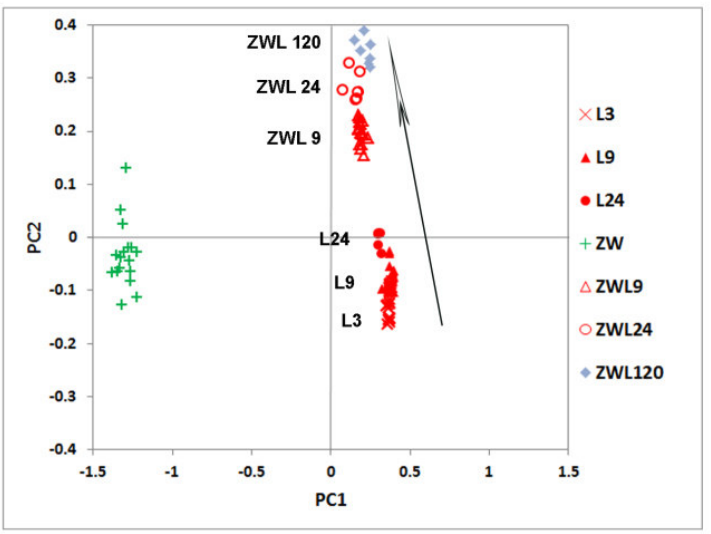

Fig. 20 PCA applied to combined FT-NIR and Raman first derivative spectra for ZWL model: projection of the first derivative combined spectra related to ZWL120 mock-up. Score plot of PC1-PC2.

4.4 Conclusions

In this chapter, FT-NIR and micro-Raman spectroscopies have been successfully applied in the study of aged neat linseed oil and two white oil-paint models prepared with lead and zinc white pigments.
The comparison between the near infrared (NIR) and Raman features for fresh and aged samples highlighted the decreasing of all the bands related to the double bonds (in FT-NIR range, the combination band between methylenic C-H stretching and double bond C=C stretching, at 4600 cm^{-1}; whereas in Raman range, the bands at 1265 and 1654 cm^{-1}, which correspond to symmetric rock

in *cis* double bond and to unconjugated *cis* double bound stretching mode, respectively). Additionally, the intensity decreasing for the combination methylenic stretching and bending between 4250 and 4350 cm^{-1}, along with a broadening for all the bands referred to C=O groups (in FT-NIR range, the second overtone of carbonyl stretching at about 5176 cm^{-1}; whereas for Raman range, the ester stretching at about 1735-40 cm^{-1}) has been observed. All these results are in line with the curing reactions of linseed oil and with the rapid decomposition of the hydroperoxides, which leads both the cross-linking of this binder and to the formation of a multitude of volatile and non-volatile secondary oxidation products, such as alcohols, ketones, aldehydes, carboxylic acids and epoxy compounds.

As expected, the main chemical changes highlighted by FT-NIR technique have been those related to the C-H and C=O vibrations, whereas Raman spectroscopy better described all modifications referred to the C=C content. This study demonstrated the usefulness of the complementarity of these two spectroscopic techniques to follow the drying/ageing process of linseed oil.

Moreover, the potentiality of Principal Component Analysis (PCA) on the combined first derivative FT-NIR and micro-Raman spectra to define and individuate drying/ageing trends for lead and zinc white pigments oil-mixtures has been demonstrated. Indeed, the direct analysis of raw and first derivative spectra has not always allowed a description of the ageing process involved in these models. So, the description of the drying/ageing process for LWL and ZWL models has been improved through the application of PCA to the associated combined spectra, highlighting more easily the different chemical changes involved in the curing process.

Two 10-year old oil mock-ups prepared with lead and zinc white have been further analysed and they verified the robustness of ageing trends defined for two oil-white models.

Finally, the reactivity of lead and zinc white with linseed oil has been analysed thanks to the application of 2D-fluorescence spectroscopy. An increasing in intensity emission for both oil-paint models has been detected.

4.5 Supplementary material

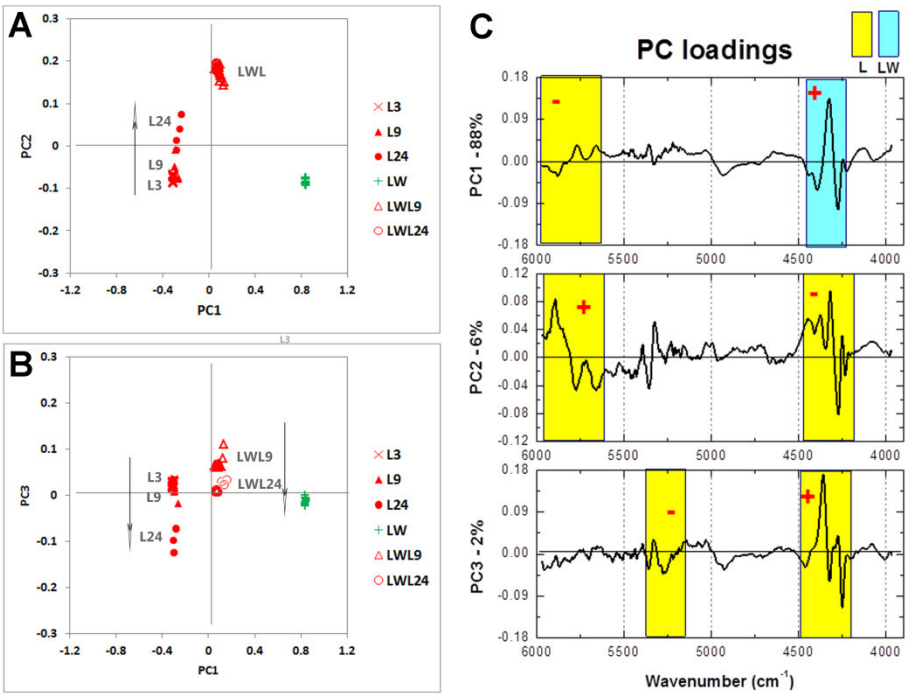

Fig S1 PCA applied to FT-NIR first derivative spectra for LWL model: score plots of PC1-PC2 (A) and PC1-PC3 (B); loading plots of PC1, PC2 and PC3 (C).

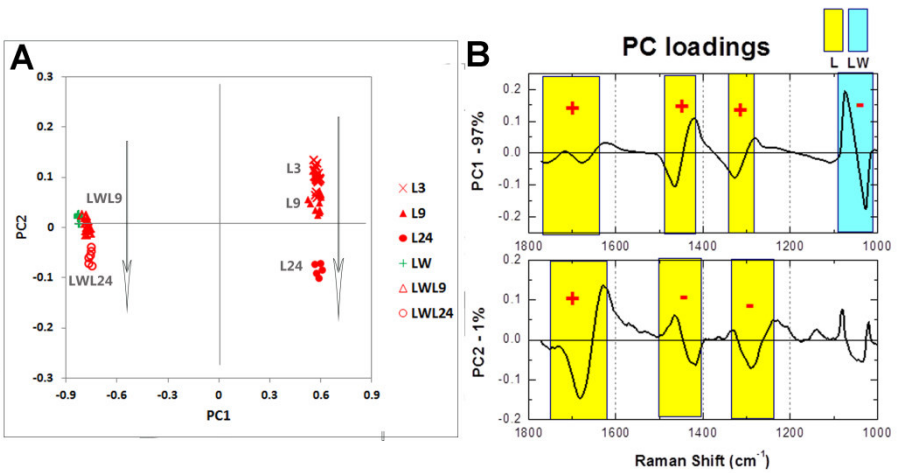

Fig S2 PCA applied to Raman first derivative spectra for LWL model: score plot of PC1-PC2 (A); loading plots of PC1 and PC2 (B).

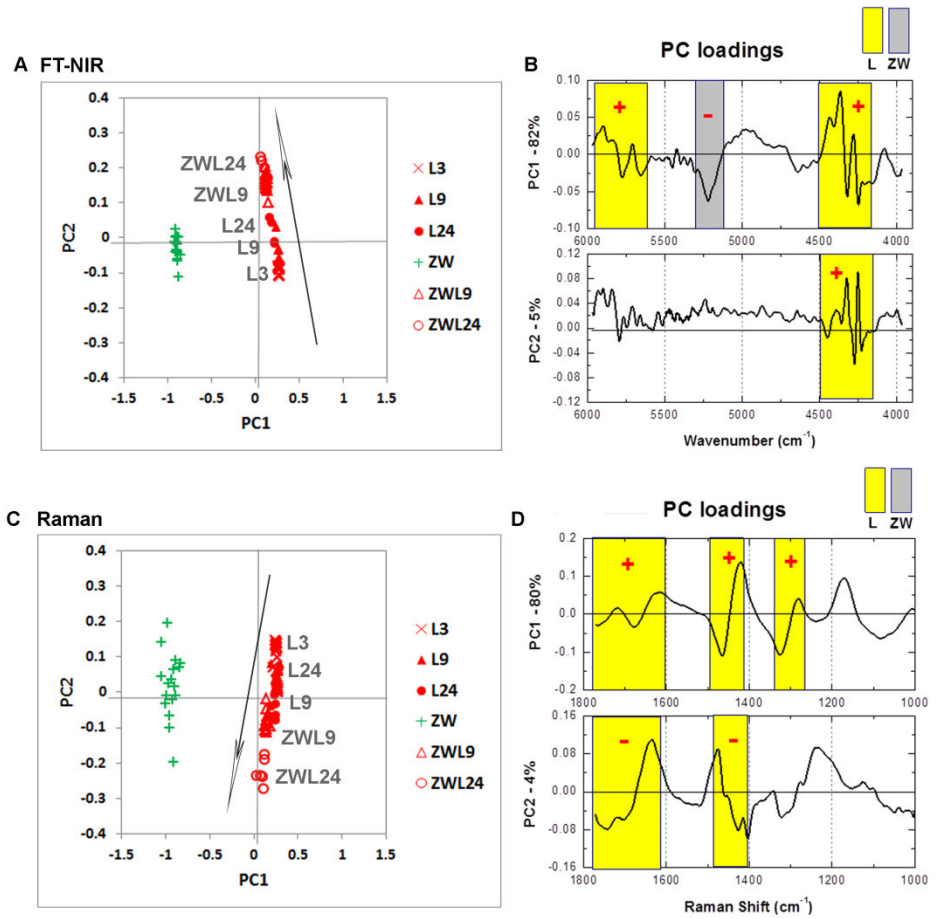

Fig. S3 PCA applied to FT-NIR first derivative spectra for ZWL model: score plots of PC1-PC2 (A) along corresponding loading plots (B). PCA applied to Raman first derivative spectra for ZWL model: score plot of PC1-PC2 (A); loading plots of PC1 and PC2 (B).

References

[1] D. Swern, J.T. Scanlan, H.G. Knight, Mechanism of the reactions of oxygen with fatty materials. Advances from 1941 through 1946, JAOCS 1948, pp 193-200.

[2] H. Wexler, Polymerization of drying oils, Chem. Rev. 1964, 64(6), pp 591-611.

[3] N.A. Porter, L.S. Lehman, B.A. Weber, K.J. Smith, Unified mechanism for polyunsaturated fatty acid autoxidation. Competition of peroxy radical hydrogen atom abstraction, b-scission, and cyclization, JAOCS 1981, 103, pp 6447-6455.

[4] N.A. Porter, Mechanisms for the autoxidation of polyunsaturated lipids, Accounts of Chemical Research 1986, 19, pp 262 268.

[5] J.S. Mills, R. White,The Organic Chemistry of Museum Objects, 2nd ed, Butterworth-Heinmann, UK, Oxford, 1994.

[6] W.J. Muizebelt, J.J. Donkerbroek, M.W.F. Nielen, J.B. Hussem, M.E.F. Biemond, R.P. Klaasen, K.H. Zabel, Oxidative crosslinking of unsaturated fatty acids studied with mass spectrometry, J. Mass Spectrom. 1996, 31(5), pp 545-554.

[7] J. Mallégol, J.-L. Gardette, J. Lemaire, Long-term behavior of oil-based varnishes and paints I. Spectroscopic analysis of curing drying oils, JAOCS 1999, 76, pp 967-976.

[8] W.J. Muizebelt, M.W.F. Nielen, R.P. Klaasen, K.H. Zabel, Crosslink mechanisms of high-solids alkyd resins in the presence of reactive diluents, Progr. Org. Coat. 2000, 40, pp 121-130.

[9] R.J. Meilunas, J.G. Bentsen, A. Steinberg, Analysis of aged paint binders by FTIR spectroscopy, Stud. Conserv. 1990, 35, pp 33-51.

[10] M.P. Luxan, F. Dorrego, Reactivity of earth and synthetic pigments with linseed oil, Jocca-Surf. Coat. Int. 1999, 82, p 390.

[11] M. Lazzari, O. Chiantore, Drying and oxidative degradation of linseed oil, Polym. Degrad. Stab. 65 (1999) 303-313.

[12] A. Schönemann, H.G.M. Edwards, Raman and FTIR microspectroscopic study of the alteration of Chinese tung oil and related drying oils during ageing, Anal. Bioanal. Chem 2011, 400, pp 1173-1180.

[13] J. Van der Weerd, A. Van Loon, J. Boon, FTIR studies of the effects of pigments on the aging of oil, Stud. Conserv. 2005, 50 (1), pp 3-22.

[14] M.P. Colombini, F. Modugno, M. Giacomelli, S. Francesconi, Characterization of proteinaceous binders and drying oils in wall painting samples by gas chromatography–mass spectrometry, J. Chromatogr. A 1999, 846, pp 113-124.

[15] G. Chiavari, D. Fabbri, S. Prati, Effect of pigments on the analysis of fatty acids in siccative oils by pyrolysis methylation and silylation, J. Anal. Appl. Pyrol. 2005, 74, pp 39-44.

[16] R. Mazzeo, S. Prati, M. Quaranta, E. Joseph, E. Kendix, M. Galeotti, Attenuated total reflection micro FTIR characterisation of pigment-binder interaction in reconstructed paint films, Anal. Bioanal. Chem. 2008, 392 (1-2), pp 65-76.

[17] G. Cipriani, A. Salvini, L. Dei, A. Macherelli, F.S. Cecchi, C. Giannelli, Recent advances in swollen-state NMR spectroscopy for the study of drying oils, J. Cult. Herit. 2009, 10, pp 388-395.

[18] I. Bonaduce, L. Carlyle, M.P. Colombini, C. Duce, C. Ferrari, E. Ribechini, P. Selleri, M.R. Tine´, New Insights into the Ageing of Linseed Oil Paint Binder: A Qualitative and Quantitative Analytical Study, PLoS ONE. 2012. 7(11): e49333.

[19] Z.O. Oyman, W. Ming, R. Van Der Linde, Oxidation of drying oils containing non-conjugated and conjugated double bonds catalyzed by a cobalt catalyst, Progr. Org. Coat. 2005, 54, pp 198-204.

[20] E. Manzano, L.R. Rodriguez-Simón, N. Navas, R. Checa-Moreno, M. Romera, L.F. Capitan-Vallvey, Study of the GC–MS determination of the palmitic–stearic acid ratio for the characterization of drying oil in painting: La Encarnación by Alonso Cano as a case study, Talanta 84 (2011) 1148-1154.

[21] C. Pasquini, Near Infrared Spectroscopy: Fundamentals, Practical Aspects and Analytical Applications, J. Braz. Chem. Soc. 2003, Vol. 14, No, 2, pp 198-219.

[22] M. Vagnini, C. Miliani, L. Cartechini, P. Rocchi, B.G. Brunetti, A. Sgamellotti, FT-NIR spectroscopy for non-invasive identification of natural polymers and resins in easel paintings, Anal. Bioanal. Chem. 2009, 395, pp 2107-2118.

[23] D.A. Burns, E.W. Ciurczak (Eds.), Handbook of Near-Infrared Analysis, Third edition, CRC Press, Boca Raton, FL, 2007.

[24] J. Workman, L. Weyer Practical Guide to Interpretative Near-Infrared Spectroscopy, CRC Press- Taylor and Francis, Boca Raton, 2007.

[25] C. Cennini, in: F. Frezzano (Ed.), Il libro dell'arte (XIV sec), 1st ed., Neri Pozza Editore, Vicenza, Italy, 2003.

[26] A. Savitzky, M. Golay, Smoothing and differentiation of data by simplified least squares procedures, Anal. Chem. 36 (1964) 1627-1639.

[27] A. Pallipurath, J. Skelton, P. Ricciardi, S. Buklow, S. Elliot, Multivariate analysis of combined Raman and fibre-optic reflectance spectra for the identification of binder materials in simulated medieval paints, J. Raman Spectrosc. 44 (2013) 866-874.

[28] B. Muik, B. Lendi, A. Molina-Diaz, M.J. Ayora-Canada, Direct monitoring of lipid oxidation in edible oils by Fourier transform Raman spectroscopy, Chemi. Phys. Lipids 2005, 134, pp 173-182.

[29] J. Juita, B.Z. Dlugogorski, E.M. Kennedy, J.C. Mackie, Low temperature oxidation of linseed oil: a review, Fire Science Reviews 2012, 1 (3), pp 1-36.

[30] P. Fjällström, B. Andersson, C. Nilsson, K. Andersson, Drying of linseed oil paints: A laboratory study of aldehyde emissions, Ind. Crops. Prod. 2002, 16, pp 173-184.

[31] C.S. Tumosa, M.F. Meckleburg, Oil Paints: The chemistry of drying oils and the potential for solvent disruption, in: Marion F. Mecklenburg, A. Elena Charola, Robert J. Koestler (Ed.), New Insights into the Cleaning of Paintings, Smithsonian Institution Scholarly Press, Washington, 2013, pp 51-58

[32] H.W.S. Chan, D.T. Coxon, Lipid Peroxides in: H.W.S Chain (ed.), Autoxidation of Unsaturated Lipids, Academic Press, London, 1987, pp 17-50.

[33] K. Figge, Dimeric fatty acid [1-^{14}C] methil esters. I. Mechanisms and products of thermal and oxidative-thermal reactions of unsaturated fatty acid esters – literature review, Chemi. Phys. Lipids 1971, 6, pp164-182.

[34] J.D. Van den Berg, Analytical chemical studies on traditional linseed oil paints, Molart (FOM), Amsterdam, 2002, pp 9-52.

[35] F. Gunstone, Fatty Acid and Lipid Chemistry, Blackie Academic and Professional, London, 1996.

[36] C.S. Tumosa, M.F. Mecklenburg, The influence of lead ions on the drying of oils, Rev. Conserv. 6 (2005) 39-47.

[37] J.J. Hermans, K. Keune, A. Van Loon, P.D. Ledema, An infrared spectroscopic study of the nature of zinc carboxylates in oil paintings, J. Anal. At. Spectrom. 2015, 30 pp 1600-1608.

[38] H. Kühn, Bleiweiss und seine Verwendung in der Malerei, Farbe und Lack 1967, 73, pp 99–105.

[39] H. Kühn, Bleiweiss und seine Verwendung in der Malerei, Vol. 2, Farbe und Lack 1967, 73, pp 209–213.

[40] W.H. Pulsifer, Notes for a History of Lead, D. Van Nostrand Company, New York, 1888.

[41] R.J. Gettens, H. Kühn, W.T. Chase, Lead white, in A. Roy (ed.): Artists' Pigments. A Handbook of Their History and Characteristics, Vol. 2, National Gallery of Art, Washington, D.C., Oxford University Press, Oxford, 1993, pp 67–81.

[42] H.H. Morgan, Cobalt and other metals as driers in the paint and allied industries, Paint Manufacture 1951, 21, pp 239–248, 259.

[43] M.F. Mecklenburg, C.S. Tumosa, Traditional oil paints: the effects of long-term chemical and mechanical properties on restoration efforts, Mater. Res. Bull. 2001, 26, pp 51–54.

[44] L.A. O'Neill, R.A. Brett, Chemical reactions in paint films, J. Oil Col. Chem. Ass. 1969, 52, pp 1054–1074

[45] S.H. Bell, Controlling Loss of Gloss, Paint Varnish. Prod. 1970, 60, pp 55–60

[46] D. Erhardt, C.S. Tumosa, M.F. Mecklenburg, Longterm chemical and physical processes in oil paint films, Stud. Conserv. 2005, 50, pp 143–150.

[47] W.J. Stewart, Lead pigments and paints, Official Digest - Federation of Paint and Varnish Production Clubs 1950, 311, pp 1100–1113.

[48] J.D.J. Van den Berg, K.J. Van den Berg, J.J. Boon, Chemical changes in curing and ageing oil paints, in J. Bridgland (ed.): 12th Triennial Meeting Lyon 29 August–3 September 1999. ICOM Committee for Conservation, Preprints Vol. I, James & James, London, 1999, pp 248–253.

[49] H.A. Gardner, Paint researches and their practical application, Press of Judd and Detweiler, Inc., Washington D.C., 1917.

[50] H.E. Brown, Zinc oxide rediscovered, New Jersey Zinc Company, New York, 1957.

[51] H. Kühn, Zinc white, in R.L. Feller(ed): Artists' pigments, Cambridge University Press, Cambridge, 1986, Vol. 1, pp 169–86.

[52] L. Carlyle, The artist's assistant: oil painting instruction manuals and handbooks in Britain 1800-1900 with reference to selected eighteenth-century sources, Archetype Publications, London, 2001.

[53] C.E. Barnett, Physics and chemistry of pigments, Ind. Eng. Chem. 1949, 41(2), pp 272-279.

[54] E. J. Dunn Jr, Moisture Resistance of Paint Films, Official Digest 1954, 26, pp 387–407.

[55] D. Rogala, S. Lake, C. Maines, M. Mecklenburg, Condition problems related to zinc oxide underlayers: examination of selected Abstract Expressionist paintings from the collection of the Hirschhorn Museum and Sculpture Garden, Smithsonian Institution, JAIC 2010, Vol. 49, 2, pp 96–113.

[56] C.A. Maines, D. Rofala, S. Lake, M. Mecklenburg, Deterioration in Abstract Expressionist Paintings: Analysis of Zinc Oxide Paint Layers in Works from the Collection of the Hirshhom Museum and Sculpture Garden, Smithsonian Institution, in MRS Proceedings 2011, Vol. 1319, pp. 275-284.

[57] F.H. Rhodes, R.A. Mathes, Effect of zinc oxide pigments upon rate of oxidation of linseed oil, Imdustrial and engineering chemistry 1923, Vol.18, 1, pp 30-31.

[58] G. Osmond, Zinc white: a review of zinc oxide pigment properties and implications for stability in oil-based paintings, AICCM Bulletin 2012, Vol. 33, pp 20-29.

[59] G. Osmond, B. Ebert, J. Drennan, Zinc oxide-centred deterioration in 20th century Vietnamise paintings by Nguyễn Trọng Kiệm (1933-1991), AICCM Bulletin 2014, Vol. 34, pp. 4-14.

[60] E.R. De la Rie, Fluorescence of paint and varnish layers (part II), Stud. Conserv. 1982, 27, pp.-65-68.

[61] T. Miyoshi, Fluorescence from Oil Colours, Linseed Oil and Poppy Oil under N2 Laser Excitation, Jpn. J. Appl. Phys. 1985, 24(3), pp 371-372.

[62] T. Miyoshi, Laser-Induced Fluorescence of oil colours and its application to the identification of pigments in oil paintings, Jpn. J. Appl. Phys. 1982, 21(7), pp 1032-1036.

[63] L. Masschelein-Kleiner, Ancient Binding Media, Varnishes and Adhesives, ICCROM, Italy, Rome, 1995.

[64] J.B. Lambert, H.F. Shurvell, R.G. Cooks, Introduction to Organic Spectroscopy, Macmillan Publ., New York, 1987.

[65] J.S. Shenk, J.J. Workman, M.O. Westrhaus, Application of NIR spectroscopy to agricultural products, in D.A. Burns and Ciurczak E.W. (eds), Handbook of Near-Infrared Spectroscopy Marcel Dekker Inc., New York,2001, pp 419-474.

[66] D. Lin-Vien, N.B. Colthup, W.G. Fately, J.G. Grasselli, The handbook of infrared and raman characteristic frequencies of organic molecules, Academic Press, San Diego, 1991.

[67] H. Yang, J. Irudayaraj, Characterization of semi-solid fats and oils by fourier transform infrared photoacoustic spectroscopy, J. Am. Oil Chem. Soc. 2001, 78, pp 889-895.

[68] O. Zovi, L. Lecamp, C. Loutelier-Bourhis, C.M. Lange, C. Bunel, Stand reaction of linseed oil, J. Lipid Sci. Technol. 2011, 113, pp 616-626.

[69] A. Pallipurath, J. Skelton, S. Bucklow, S. Elliot, A chemometric study of ageing in lead-based paints, Talanta 2015, 144, pp 977-985.

[70] M. Bacci, D. Magrini, M. Picollo, M. Vervat, A study of the blue colors used by Telemaco Signorini, 1835–1901, J. Cult. Herit. 2009, 10, pp 275-280.

[71] E. Pratali, Zinc oxide grounds in 19th and 20th century oil paintings and their role in picture degradation processes, CeROArt [En ligne], | 2013, mis en ligne le 10 mai 2013, consulté le 25 octobre 2015. URL : http://ceroart.revues.org/3207 [Last visit: 18/11/2015]

[72] J. Mijovic, S. Andjelic, C.F. Winnie Yee, A study of reaction kinetics by near-infrared spectroscopy. 2. Comparison with dielectric spectroscopy of model and multifunctional epoxy/amine systems, Macromolecules 1995, 34(17), pp 2797-2806.

PART III

2D-Fluorescence spectroscopy combined with Principal Component Analysis for studying aged traditional binding media

Abstract

In this chapter, the results obtained by the application of 2D-fluorescence spectroscopy to analyse the fluorescent properties of all neat binding media and their modifications with ageing will be debated.
Moreover, the applying of PCA to Excitation-Emission (EE) maps of all these materials will be investigated in an effort to examine the use of chemometrics for screening and classifying between the different types of binders.

This work represents a preliminary study to evaluate potentialities and limits of the 2D-fluorescence spectroscopy, and to individuate the main advantages of its combination with multivariate analytical tools in cultural heritage/painting field. In a future, a joined application of this analysis with vibrational spectroscopies might be explored.

Introduction

Spectrofluorometric analysis of binding media can be particularly useful, because organic materials used in paintings are often fluorescent and binding media from different origin have an own fluorescence spectral profile. 2D-fluorescence spectroscopy provides distinct advantages in the investigation of samples that are mixtures of various molecules, as binding media, revealing the presence of different fluorophores in the sample, moreover their wavelength dependence, emission and excitation maxima [**1**]. Furthermore, the excitation-emission maps often convey information on the extent of sample aging and degradation.
Binding media are complex molecular mixtures of natural products containing residues and/or individual chromophores that are fluorescent [**2**] In addition, the ageing process influences the overall fluorescence emission of a binder, leading to the formation of degradation products which can change the original emission profile of the fresh material [**1**].
In this work, the fluorescence excitation-emission profiles of neat binding media and their modifications with ageing are discussed, in order to define limits and potentialities of this spectroscopic technique.
Furthermore, Principal Component Analysis (PCA) is applied to Excitation-Emission (EE) maps of all these materials in an effort to examine the use of

chemometrics for screening and classifying different types of binding media. This work represents a preliminary study to evaluate the potentialities of the combination of 2D-fluorescence analysis with multivariate analytical tools in cultural heritage/painting field.
This study was performed at the laboratories of IELS-FORTH (Institute of Electronic Structure and Laser–Foundation for Research and Technology) at Heraklion (Crete).

1.1 Materials and methods

1.1.1 Materials

All neat binding media, along with the corresponding symbols, are listed in **Table 4** of **Part I** of this thesis. All binders were analysed after an ageing of eighteen months.

1.1.2 2D-Fluorescence spectroscopy

Films were analysed using a scanning spectrofluorimeter with excitation provided by a xenon arc lamp (Jobin-Yvon/Horiba Fluoromax-P). Excitation-Emission (EE) spectra were constructed by recording a series of excitation spectra with an interval of 20 nm between consecutive excitation scans and with a resolution of 1 nm for emission spectra; first- and second-order Rayleigh scattering was electronically eliminated and spectra were corrected for detector efficiency. Scans were recorded with the following excitation-emission spectral ranges:

- Proteinaceous binders (Ex: 250-530 nm; Em: 290-800 nm)
- Lipidic binders (Ex: 250-550 nm; Em: 290-750 nm)
- Polysaccharide binders (Ex: 250-550 nm; Em: 290-750 nm)

Contour plots were constructed with spectra normalised to the maximum emission and are presented in all figures with 8 different colour levels with the least intense emissions represented in black and the strongest peaks in red.
In order to apply PCA to 2D-fluorescence maps of all neat binding media, 5 new EE maps were acquired for each sample at 5 different positions, taking into account the same excitation and emission ranges (ex: 250-550 nm; em: 290-750 nm).

1.1.3 Data analysis

Data analysis, employed in order to apply PCA on 2D-fluorescence maps, is discussed more in detail in **Part I**.

All Excitation-Emission (EE) maps were processed using the Principal Component Analysis (PCA) tool of the Matlab® software version R2012b (MathWorks Inc., USA) which works, performing SVD (Singular Value Decomposition) algorithm.
In order to take into consideration each cell of the starting matrices, a proper code written in Matlab, allowed the transformation of each map into one vector, carrying the total information. Each loading plot is shown as a proper matrix with the same parameters of the starting analysed matrices. A colour scale aids differentiation among positive and negative contributions.
All the processed matrices had the same dimensions and for each neat binder five different excitation-emission maps were acquired for a total of eighty-five maps.

1.2 Results and discussion

All Excitation-Emission (EE) maps acquired are reported in **Appendix E** along with single emission spectra extracted from each of them. For each EE map, tentative assignments for the main emission maxima/bands are shown, according to literature references.

1.2.1 Fluorescence excitation emission spectra of binding media

In this study, 2D-fluorescence spectroscopy was exploited for the mapping of fluorophores present within traditional binding media, which are complex mixtures of molecules. The interpretation of Excitation-Emission (EE) spectra is not straightforward, because of the large number of fluorophores and impurities inside and also the limited knowledge regarding fluorophores in solid and aged artists' materials. Furthermore, reactions and oxidation products which may develop during ageing processes are numerous. For instance, the oxidation reactions can involve many molecules found in binding media, which include specific amino acids, terpenoids and fatty acids. Therefore, rather than the identification of specific fluorophores, EE spectra can instead be used for a rapid differentiation between binding media [**2**].
Regarding proteinaceous materials, over the last few years, studies focused on the characterization of general class of protein-based binders, such as casein, egg white, egg yolk, animal glues, on the basis of fluorescence emission, arising from the presence of certain amino acids and their degradation by-products, were carried out [**3**]. On the other hand, for oils and gums, the isolation of individual fluorophores has been more limited [**2**].

Below, a description of each EE map (and related single emission spectra) is reported, in order to define the different fluorescent profiles of the examined neat binding media.

1.2.1.1 EE maps of proteinaceous binders

Proteins exhibit intrinsic fluorescence, mainly due to the aromatic amino acids *tryptophan* (**Fig. 1A**), *tyrosine* (**Fig. 1B**) and *phenylalanine* (**Fig. 1C**).

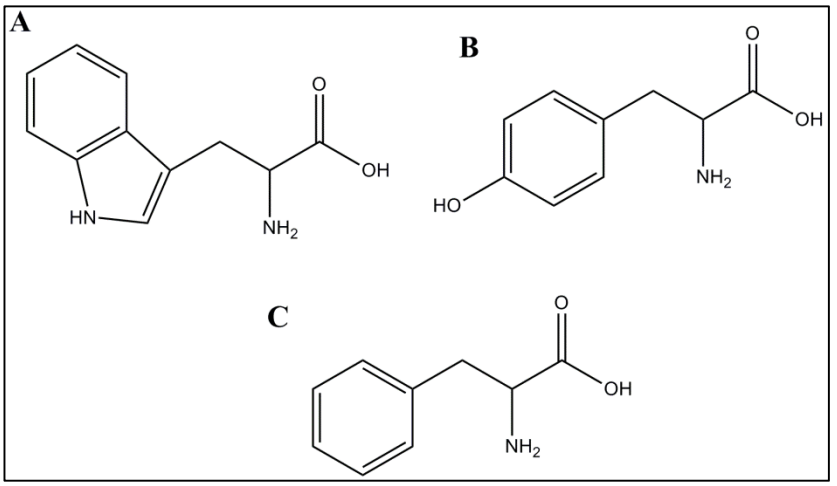

Fig. 1 Chemical structures of tryptophan - Trp (A), tyrosine – Tyr (B) and phenylalanine - Phe (C) amino acids.

The optical properties of these free amino acids differ significantly, as can be seen in **Table 1**. Differences in extinction coefficient and quantum yield can explain the dominating fluorescence observed with tryptophan and tyrosine in the presence of phenylalanine [**3**].

Table 1 Excitation and emission maxima of fluorescence spectra, absorption coefficient, lifetime of emission and quantum yield of autofluorescent amino acids [**3**].

	$\lambda_{Excitation}$ (nm)	$\lambda_{Emission}$ (nm)	ε_{max} (X 10^{-3})	Lifetime (ns)	Quantum yield
Phenylalanine	257	282	0.2	6.4	0.04
Tryptophan	280	348	5.6	3.6	0.20
Tyrosine	274	303	1.4	2.6	0.14

EE spectra of proteinaceous binders can be also rationalised on the basis of the aromatic amino acids composition media, as shown in **Table 2**. Additionally, ageing process can further modify and make more complex these EE spectra, owing to the modifications of amino acids and the formation of photooxidation

and “cross-linkage” products (e.g. between amino acids and free sugars by means of Maillard reactions).

Table 2 Autofluorescent amino acid composition (percent of amino acids) of materials used as binding media: egg, casein and collagen [**3**].

	Egg White	Egg Yolk	Casein	Collagen
Phenylalanine	5.3	4.3	3.2	2.3
Tryptophan	1.2	1.2	1.4	n/a
Tyrosine	3.9	4.5	2.7	1.0

The EE map related to the protein film of **casein**, shown in **Fig. 2**, highlights a strong peak located at excitation/emission of 288/340 nm which could be associated with the amino acid *tryptophan* (Trp) [**3**].
Furthermore, a broader, but weaker band, can be detected between emissions of 406-440 nm for excitations of 340-370 nm. This emission could be ascribed to the photooxidation products of Trp (e.g. *N-formyl kynurenine* which has been seen to show a fluorescent emission at 440 nm [**1**]) and to the derivative products of Tyr (e.g. *di-tyrosine*, emission at 420 nm [**1**], which has been documented to be present in solid protein films of casein [**4**]).

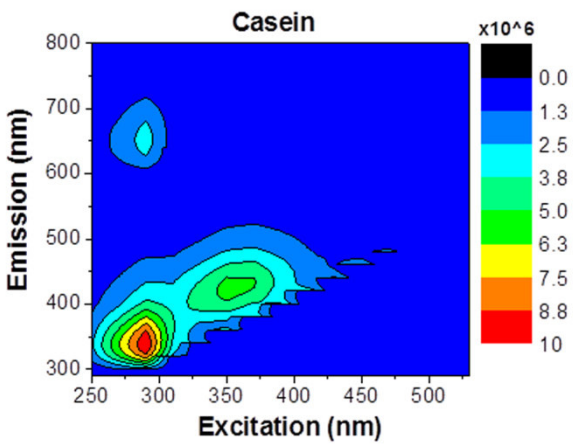

Fig. 2 EE map of casein.

A different situation is observed in 2D-fluorescence maps of glues, reported in **Fig. 3**.
In the EE spectrum of **rabbit skin glue** (**Fig. 3A**), a broad fluorescence band, centered approximately between 394 and 455 nm (for excitation range of 340-390 nm), can be detected. This broad emission could be related to various fluorophores originated by both “cross-linkage” and photooxidation reactions: *Maillard reaction* products (from the reaction between free glucose, or other sugars, and amino acids; emission above 400 nm [**3**]); glycation products, such as

pentosidine (an adduct formed between the side chains of lysine and arginine and free sugar like ribose; emission at 385 nm [**3**]) and *pyridinoline* (formed from two hydroxylysine residues and a helical lysine residue; emission at 440 nm [**3**]), which are naturally formed in collagen, the chief-protein of animal glues [**5**] and derivative products of Tyr (e.g. *di-tyrosine*, emission at 420 nm [**1**]). In addition, a weaker and smaller band, which could be ascribable to the amino acid *tyrosine* (Tyr), at excitation/emission of 268/307 nm can be observed. Moreover, a weak emission contour, centered at about 480 nm, can be noted. This last could be referred to derivative products of *dihydroxyphenylalanine* (DOPA) amino acid, other ageing fluorescent products which have been observed in aged animal glues films [**3**].

The EE map of **strong glue**, reported in **Fig. 3B**, shows an emission profile close to that observed for rabbit skin glue. The only difference is a slightly more intense emission. As discussed in **Part I**, rabbit skin glue is essentially refined rabbit collagen, whereas strong-glue is produced, using bones coming from various bovines [**6**]. Therefore, a different amino acid/impurities content could be hypothesized [**7**] and might explain this slight difference in intensity emission. Further analysis is needed to verify this evaluation (e.g. by means of GC-MS, Gas Chromatography Mass Spectroscopy).

Finally, going to observe the EE map related to the protein film of **fish glue** (**Fig. 3C**), a broad emission band, located between 385 and 430 nm for excitations of about 320-360 nm, can be observed. It is reasonable to assume that the responsible fluorophores for it might be the same described/hypothesized for the previous animal glues, since, also, fish glue is a collagen-based binder. In spite of this, the global emission intensity observed for fish glue is the weakest, taking into account all the protein-based binding media. This behaviour seems to be in agreement with the lowest proportion of amino acids (with corresponding derivative products) and impurities highlighted for this glue [**7-8**].

It is interesting to underline that the emission contribution which could be ascribable to Tyr amino acid (at excitation/emission of 270/307 nm, [**1**]) results to be more evident within the fluorescence profile of fish glue (**Fig. 3C**). This aspect might be explained thanks to the recipe followed to prepare it. Fish glue is extracted with slight hot water without alkaline or acid treatment, from sturgeon swim-bladders [**7**]; whereas rabbit skin glue/strong glue are extracted at high temperatures, using an alkaline or acid hydrolysis from membranes, tendons and cartilage of animals. So, it is reasonable to assume that a more drastic treatment, as that applied for rabbit skin glue/strong glue, could lead to a major loss of Tyr amino acid. Obviously, further analysis would be needed.

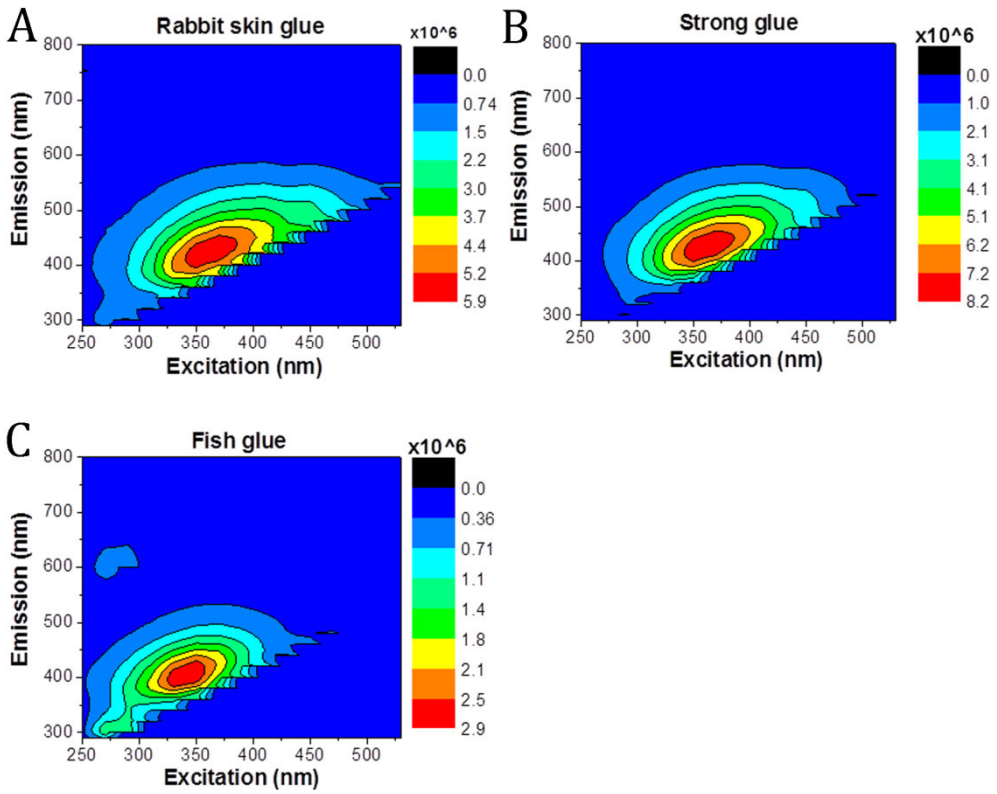

Fig. 3 EE maps of rabbit skin glue (A), strong glue (B) and fish glue (C).

In the EE map of **egg white**, reported in **Fig. 4A**, a broad emission between 405 and 460 nm can be detected for excitations of 345-390 nm. This broad emission can be ascribed to various compounds present in the complex mixtures found within egg and to the generation of ageing/degradation products: *Maillard reaction* products (emission above 400 nm), the photooxidation products of Trp (e.g. *N-formyl kynurenine* which has been seen to show a fluorescent emission at 440 nm [**1**]) and derivatives products of Tyr (e.g. *di-tyrosine*, emission at 420 nm [**1**]). In addition, a weaker emission at ~330 nm (for excitation at 290 nm) can be also observed, ascribable to the amino acid *tryptophan*. Additionally, a weak emission contour centered at about 480 nm can be noted. This last could be referred to derivative products of *dihydroxyphenylalanine* (DOPA) amino acid, other ageing fluorescent products which have been observed in aged animal glues films [**3**].

On the other hand, in the EE map of **egg yolk** (**Fig. 4B**), the broad band fluorescence emission centered between 425 and 515 nm could be ascribed to various compounds characterized by a fluorescence emission in this range: *vitamin A* (emission at 410 nm [**3**]); a build-up of multiple fluorophores from the complex mixtures in egg, including *flavins, free glucose* and *cross-linked lipids* (emission above 400 nm [**1**]); *Maillard reactions* products [**1**];photo-

oxidation products of Trp (e.g. *N-formyl kynurenine*, emission at approximately 435 nm [**3**]) and derivative products of *dihydroxyphenylalanine* (DOPA) amino acid (emission approximately at 480 nm, [**3**]). In addition, the fluorescence from cross-linking of fatty acids polymerization cannot be excluded at longer excitation/emission wavelengths (emission at approximately 520 nm), since a lipidic content is present in its chemical composition, as discussed in **Part I**.

The EE map of **whole egg** (**Fig. 4C**) shows a similar fluorescent broadband to that observed for egg yolk. It was prepared, mixing one part of egg white with two parts of egg yolk and one part of vinegar, as described in **Part I**. Consequently, we could expect that its fluorescence behaviour results to be more similar to that observed for egg yolk.

The single emission spectra (**Appendix E**) extracted from each EE map, better highlight the aforementioned emission contributions.

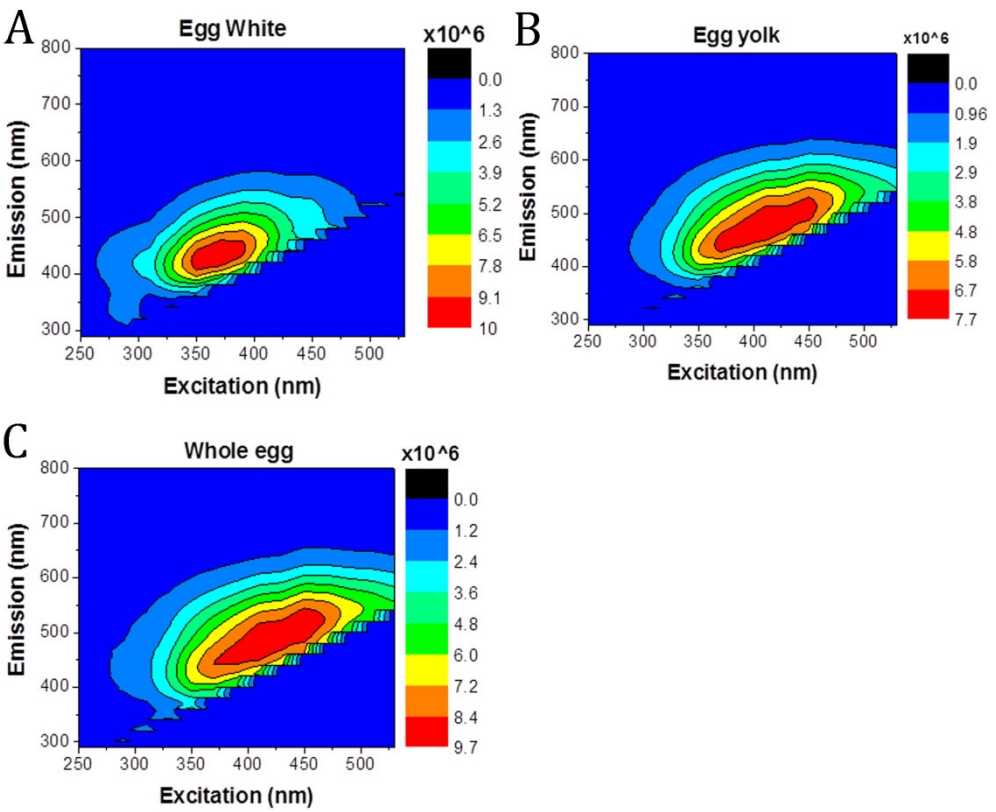

Fig. 4 EE maps of egg white (A), egg yolk (B) and whole egg (C).

1.2.1.2 EE maps of drying oils

The origin of fluorescence in drying oils is a consequence of their polymerization, in contrast to that of fresh oils, for which it is instead ascribed

to tocopherols, chlorophyll and phenolic antioxidants [**9**]. During the autoxidation process, a great number of low molecular weight compounds are formed as by-products. Among these, there are saturated and unsaturated acids, ketones, aldehydes and epoxides. At same time, also fluorescent polymeric structures are formed, but the information that can be obtained by application of fluorescence spectroscopy results to be limited [**10-11**].

Four representative typologies of drying oils were chosen for this study: linseed oil, walnut oil, poppy oil, and stand-oil (originated from linseed oil). Furthermore, the drying oils examined in this study were obtained from different manufacturers, as described in **Part I**, in order to take into account a more significant representation/description for each class of drying oils.

Moreover, we remind that, fresh linseed and walnut oils were further analysed by means of High-Performance Liquid Chromatography Coupled with Electrospray Ionization and Quadrupole Time-of - Flight Mass Spectrometry (HPLC-ESI-QTOF) analysis to characterize their triglycerides composition (**Table 5** of **chapter 2** of **Part II** of this thesis).

From an inspection of the EE spectra recorded from different drying oils (**Fig. 5**, **Fig. 6**, **Fig. 7**, **Fig. 8**), it is clear that the samples share common features: all are characterized by a broad-band emission. Some variations between samples can be observed in the shape of contour plots and in emission intensity.

As can be seen in **Table 3**, the maximum fluorescence emission for linseed oils is located at longest wavelengths (490-500 nm, [**10-11**]), whereas for poppy-seed oils is located at shorter (460 nm, [**11**]). On the other hand, walnut oils show an intermediate fluorescence behaviour (maximum emission at 460-490 nm). The main emission for stand-oil is, instead, located at around 440 nm, confirming its lower tendency to yellowing, as described in **Part I**.

As can be seen in **Table 3**, WOZ shows the strongest intensity emission.

By means of HPLC-ESI-QTOF analysis, this oil resulted to have a linolenic contribution in its triglycerides composition, which is completely absent in WOF (**Table 5**of **chapter 2** of **Part II** of this thesis). So, the EE spectrum of WOZ seems to confirm that this oil will be subject to a different ageing in respect to WOF. In spite of this, further analysis would be however needed to determine which by-products or possible impurities/additives could explain this different intensity emission.

Additionally, it is interesting to note that the fluorescence behaviour of LOF and WOF results very similar, as can be observed in **Table 3** and in **Fig. 5C** and **Fig. 7B**. Nevertheless, this similarity does not mean an identical chemical composition for these materials.

In conclusion, the 2D-fluorescence spectroscopy was found to be useful to highlight the main emission maxima of the various drying oils, but the extraction of information remains however limited, since a more precise

description of which “fluorophores/fluorescent by-products” are actually present has not still been explored.

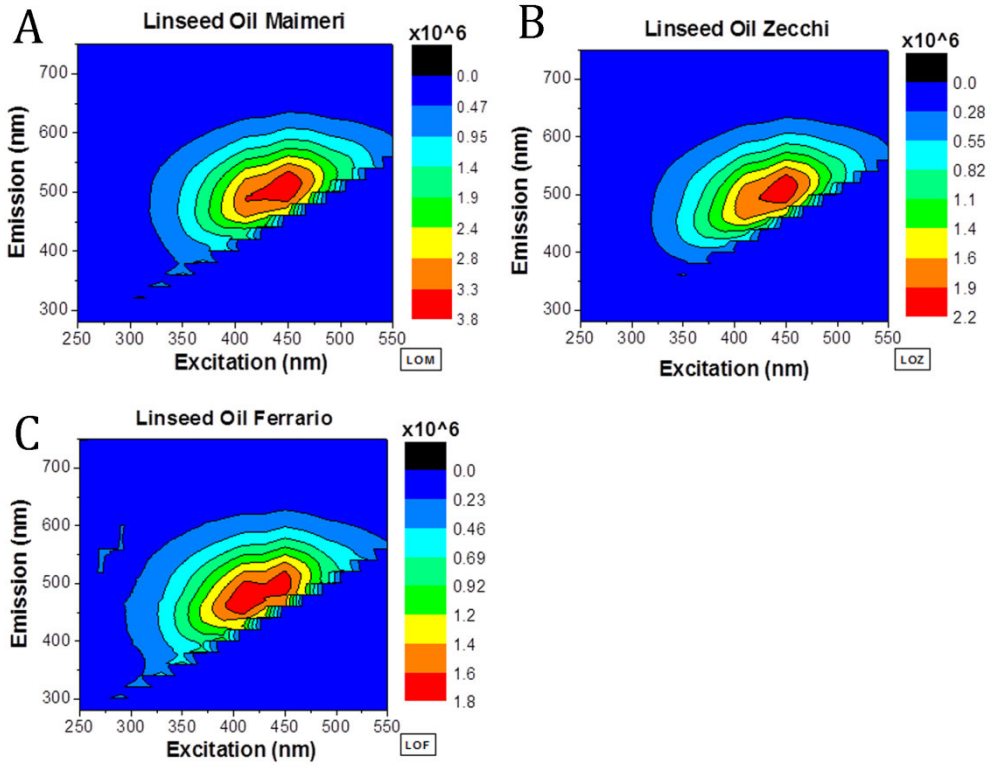

Fig. 5 EE maps of LOM (A), LOZ (B) and LOF (C).

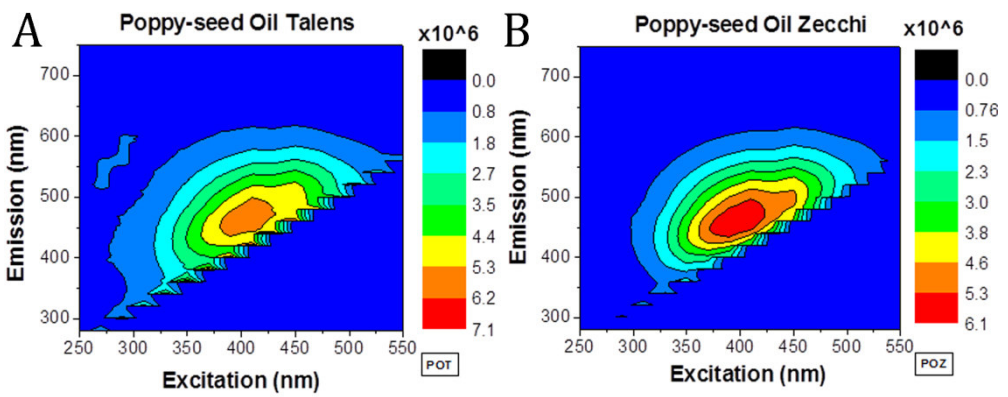

Fig. 6 EE maps of POZ (A) and POT (B).

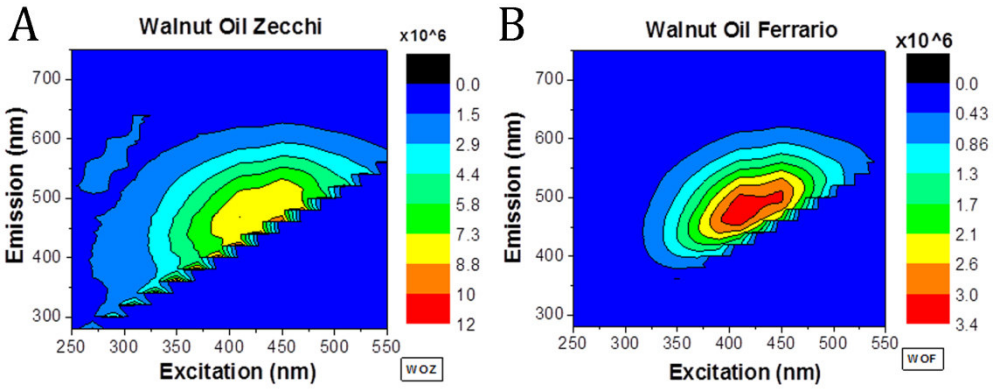

Fig. 7 EE maps of WOZ (A) and WOF (B).

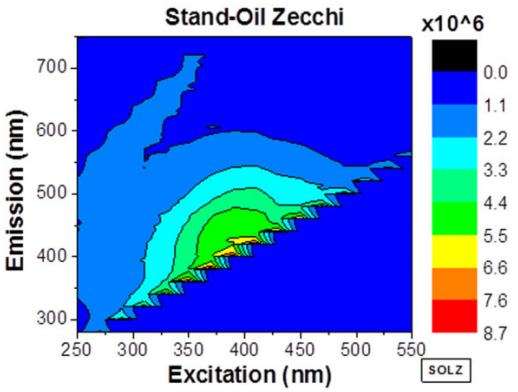

Fig. 8 EE maps of stand-oil.

Table 3 Fluorescence properties of each drying oil.

Drying oil	Band max intensity/ 10^6 counts	Excitation range/nm	Emission range/nm	Ex/Em maximum (nm)[a]
LOM	3.8	410-460	486-536	430/498
LOZ	2.2	420-460	485-536	430/496
LOF	1.8	390-450	450-520	(390)-430/(460)-490
POZ	6.1	380-430	436-500	390/460
POT	6.2	370-420	434-500	390/460
WOZ	8.8	380-470	390-530	390-430/460-490
WOF	3.4	390-450	450-505	390-430/460-490
SOLZ	5.5	350-450	390-490	386/440

[a] By the analysis of single emission spectra extracted from each EE map (**Appendix E**)

1.2.1.3 EE maps of gums

Fluorescence spectroscopy provides limited information for polysaccharide-based binding media, since these binders are complex mixtures mainly made of carbohydrates, uronic acids and proteins. In addition, chemical analysis revealed the presence of residues of tryptophan and phenolic compounds, both also being contributors to fluorescence emission [**12-14**]. For both, Arabic gum and Tragacanth gum, a noised emission band between ~375 and 475 nm for excitations of 330-420 nm can be highlighted in the related EE maps (**Fig. 9**). This broad band emission results mainly centered at about 440 nm, as can be better highlighted, analysing single emission spectra, reported in **Appendix E**.
Nevertheless, the similarity observed for the EE maps of Arabic gum and Tragacanth gum, does not mean an identical chemical composition. The biogenesis of each gum appears to be quite different, and the ratio of their neutral monosaccharides, arabinose and galactose, are widely different (as discussed in **Part I**). Therefore, chemical characterization, such as Gas Chromatography-Mass Spectrometric analysis, GC-MS [**15**], remains more meaningful for the characterization of these binding media.

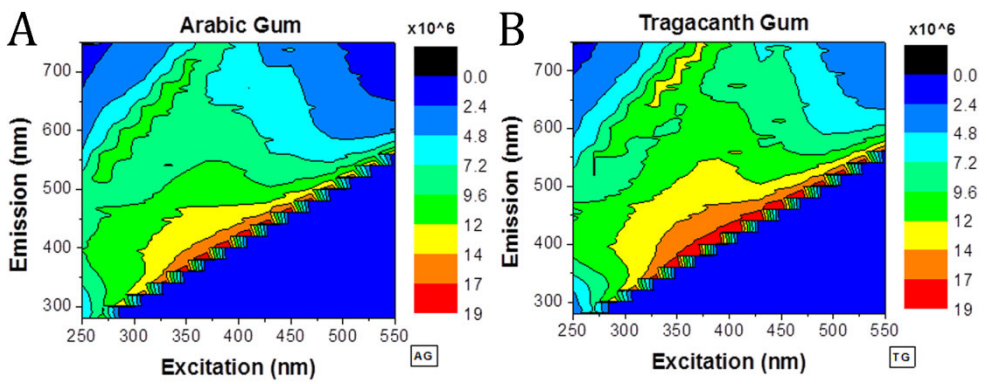

Fig. 9 EE maps of Arabic gum (A) and Tragacanth gum (B).

1.2.2 PCA results

First of all, PCA has been applied to EE maps related to all neat binding media. Successively, in order to evaluate if other meaningful information could be extracted, new statistical models were built only focusing on protein- and oil-based binders.

1.2.2.1 PCA applied to EE maps of all neat binding media

A total of 85 EE maps were processed.
A significant percentage (99.16 %) of the cumulative variability contained in the dataset is explained by the first three PCs. PC1 explains 88.36 % of the total variance, whereas PC2 and PC3 explain 8.9 and 3.9 % of the total variance, respectively.
As previously described, each loading plot is reported as "a fluorescence map" with the same parameters of the starting analysed matrices. A colour scale aids differentiation among positive and negative contributions.
In **Fig. 10** the score plots defined by the first three PCs are shown along with the related loading plots. In **Table 4** all the emission ranges with corresponding excitation intervals, for both positive and negative contributions, are reported for each PC.
The major contribution to PC1, shown in **Fig. 10A**, is represented by the emission range between 378 and 470 nm (for excitations of 320-430 nm) centered at around 440 nm. This contour is very close to that observed in both EE maps of Arabic gum and Tragacanth gum. Then, both gums show a positive score value for this PC, as can be seen in **Fig 10D** and **Fig 10E**. Furthermore, EE maps related to egg-based binders are also characterized by a positive score value for PC1, even if this is lower. All these binders, indeed, show an emission between around 405 and 500 nm, ascribable to various fluorophores, as previously discussed, including the photooxidation products of the amino acid Trp (e.g. *N-formyl kynurenine* characterized by an emission at 440 nm [**1**]). The presence of residues of tryptophan in gums was also revealed [**13-14**]. According to this, it could be explained this slight similarity between these different binding media.
Nevertheless, PC1 principally describes polysaccharides materials.

Table 4 Excitation and emission ranges of each loading plot related to the first three PCs. Also, the positive or negative contributions are specified.

PC	Excitation (nm)	Emission (nm)	Contribution
PC1	A broad emission similar to that of gums (~320-430)	A broad emission similar to that of gums (~378-470)	Positive contribution
PC2	(406-476)	(480-558)	Positive contribution
	(270-307)/288	(310-390)/346	Negative contribution
PC3	(341-381)	(400-454)	Positive contribution
	290	337	Positive contribution
	308	405	Positive contribution
	II order: 290	660	(Positive contribution)

On the other hand, the loading plot of PC2 (**Fig. 10B**) highlights two main contributions: the first one is represented by the emission range centered at around 330 nm (for an excitation wavelength of 288 nm), which could be ascribed to the amino acid *tryptophan* (emission at 330 nm) [**1**], and leads to a negative score value. This emission range could be partly related to the emission of the amino acid *tyrosine* (emission at 304 nm) [**1**]. The second contribution is, instead, represented by a broad emission range between 480 and 558 nm (for excitations of 406-476 nm) which can be found in the 2D-Fluorescence maps of all egg-based binding media (principally in those of egg yolk and whole egg,) and drying oils (except stand-oil). This last contribution leads to a positive score value. So, casein and glues show a negative score for PC2, whereas egg-based binders and drying oils (except stand oil) highlight a positive one. Egg yolk and whole egg show the highest score positive value. PC2 differentiates drying oils/egg-based binders from casein/glues.

Summarising, the score plot defined by the first two PCs, shown in **Fig. 10D**, defines four different spatial regions, each corresponding to a different type of binding medium: drying oils, egg-based binders, casein with glues and gums. In this case, the only exception is represented by stand-oil which results close to glues and casein.

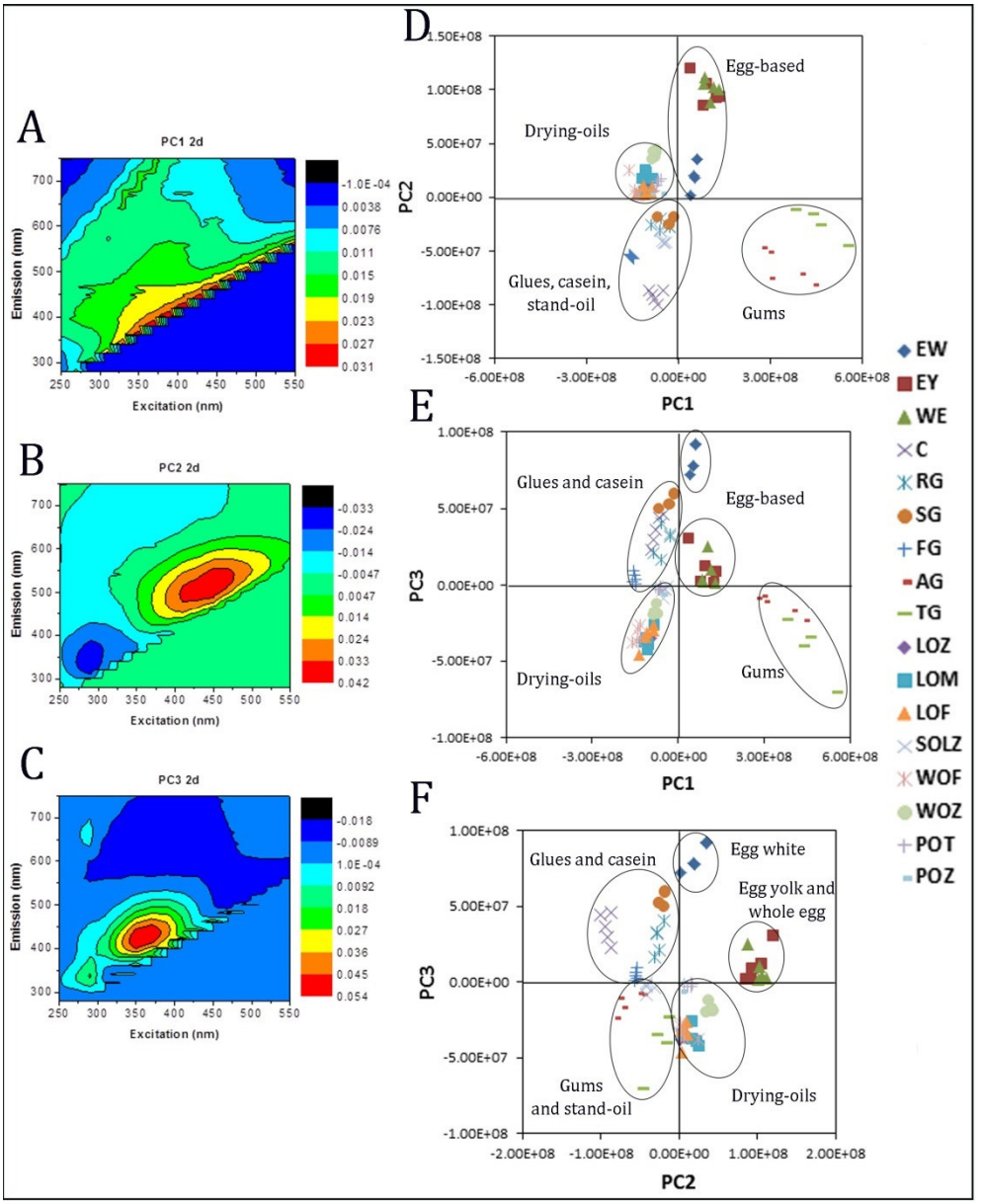

Fig. 10 Loading plots of PC1 (A), PC2 (B) and PC3 (C); along with score plots PC1-PC2 (D), PC1-PC3 (E) and PC2-PC3 (F).

PC3, as can be seen in **Fig. 10E** and **Fig. 10F**, describes proteinaceous materials. The corresponding loading plot (**Fig. 10C**), is characterized by two main different contributions, all leading to a positive score value. The most intense emission is located between 400 and 454 nm (for excitations of 341-381 nm) and it can be observed in the EE maps of egg-based binders, casein and glues. The second emission results to be centered at around 330 nm (excitation of 290 nm) with corresponding second order emission at 660 nm, which could be

related to the amino acid *tryptophan* (emission at 330 nm). This emission range could partly be also attributed to the emission of the amino acid *tyrosine* (emission at 304 nm). Consequently, all proteinaceous binding media own a positive score value for this PC.
The score plot PC1-PC3, shown in **Fig. 10E**, properly "distinguishes" the different types of binders: egg-based, drying oils, polysaccharides and proteinaceous; whereas the score plot PC2-PC3, shown in **Fig. 10F**, better differentiates egg white from egg yolk/whole egg.
Results suggest that multivariate analysis can be used to differentiate samples on the basis of their fluorescence spectra, because the placement of the different materials in all score plots reflects their origin and chemical composition, but similarities between oils, proteinaceous, polysaccharides may be such that additional data analysis is required.

1.2.2.2 PCA applied to EE maps of all proteinaceous binders

A total of 35 EE maps were processed.
A significant percentage (92.1 %) of the cumulative variability contained in the dataset is explained by the first two PCs. PC1 explains 82.3 % of the total variance, whereas PC2 explains 9.8 % of the total variance, respectively.
In **Fig. 11**the score plot defined by the first two PCs is shown along with the related loading plots. In **Table 5** all the emission ranges with corresponding excitation intervals, for both positive and negative contributions, are reported for each PC.
The major contribution to PC1 (**Fig. 11A**), is represented by the positive emission range between 453 and 550 nm (for excitations of 400-475 nm). This contour is very close to that observed in EE maps of egg-based binders (principally in those of egg yolk and whole egg,). Egg-based binding media show a positive score value for this PC, as can be seen in **Fig 11C**.
Furthermore, the loading plot of PC1 (**Fig. 11 A**) also highlights the presence of a second weak contribution, which results to be centered at around 330 nm (excitation of 290 nm) with corresponding second order emission at 660 nm, that could be related to the amino acid *tryptophan* (emission at 330 nm). This emission range could partly be also attributed to the emission of the amino acid *tyrosine* (emission at 304 nm). Consequently, both casein and glues own a negative score value for this PC, as can been seen in **Fig. 11C**.
Egg white highlights an intermediate score value for PC1 (**Fig. 11 C**), since its corresponding EE map shows a contribution ascribable to tryptophan amino acid. Additionally, this binder has not a lipidic content, such as egg yolk and whole egg (which leads to an emission approximately centered at around 520 nm).

Therefore, PC1 better describes egg-based binders and differentiates them from casein/glues.

The loading plot of PC2 highlights three main different contributions, as can be observed in **Fig. 11B**: the first one is represented by the positive emission range between 394 and 457 nm (for excitations of 330-394 nm) which can be found in the EE maps of casein, glues and egg-white. The second emission results centered at around 330 nm (excitation of 290 nm) with corresponding second order emission at 660 nm, which could be related to the amino acid *tryptophan* (emission at 330 nm). This emission range could partly be also attributed to the emission of the amino acid *tyrosine* (emission at 304 nm). This emission leads to a positive score value for this PC. The last contribution to PC2 is represented by a negative broad emission, between 500 and 594 nm (for excitations of 432-530 nm) which can be found in EE maps of egg yolk and whole egg (emission ascribed to the polymerization of fatty acids present in their chemical composition [**1**]).

So, egg yolk and whole egg show a negative score value for PC2, whereas rabbit skin glue, strong glue, casein and egg white highlight a positive one, as can be seen in **Fig. 11C**.

Fish glue for PC2 is characterized by a negative score value (**Fig. 11C**). As previously discussed, its corresponding EE map shows the weakest emission intensity. Furthermore, this binder highlights the most evident contribution (emission at 304 nm) which could be ascribable to tyrosine amino acid and a broad emission slightly shifted towards shorter wavelengths than those observed for the other two animal glues.

Table 5 Excitation and emission ranges of each loading plot related to the first two PCs. Also, the positive or negative contributions are specified.

PC	Excitation (nm)	Emission (nm)	Contribution
PC1	400-475	453-550	Positive contribution
	(258-305)/285	(306-386)/340	Negative contribution
	II order (270-298)/285	(630-710)/660	Negative contribution
PC2	330-394	394-457	Positive contribution
	288	340	Positive contribution
	II order (254-305)	(610-740)	Positive contribution
	432-530	500-594	Negative contribution

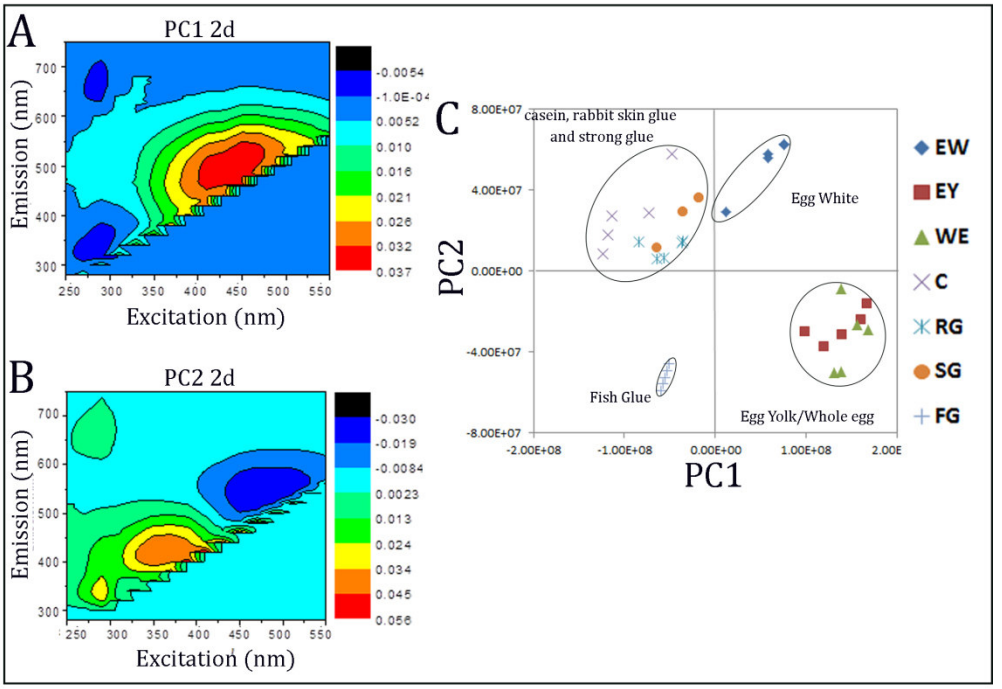

Fig. 11 Loading plots of PC1 (A) and PC2 (B); along with score plot PC1-PC2 (C).

Summarising, the score plot defined by the first two PCs, shown in **Fig. 11C**, defines four different spatial regions, each corresponding to a different type of proteinaceous binding medium: egg-based binders; casein with rabbit skin glue/strong glue; egg white and fish glue.

These results suggest that the application of PCA to EE spectra related to protein-based binders allows the enhancement in their distinguishing and in the extraction of meaningful information. It resulted to be sensitive at the inner differences present in their chemical composition, leading, for instance, to differentiate between fish glue and the other two glues.

As discussed in **Chapter 1** of **Part II**, no differentiation between glues was observed by the application of PCA to combined first derivative FT-NIR and micro-Raman spectra.

1.2.2.3 PCA applied to EE maps of all drying oils

A total of 40 EE maps were processed.

From PCA performed on EE maps of drying oils, two principal components (PCs) were selected, explaining 85.6 % of the total variance of the samples. PC1 explains 68.8 % of the total variance contained in the data, while PC2 explains 16.8 % of the total variance.

In **Fig. 12** the score plot defined by the first two PCs is shown along with the related loading plots. In **Table 6** all the emission ranges with corresponding excitation intervals, for both positive and negative contributions, are reported for each PC.

The major contribution to PC1, as can be observed in **Fig. 12A**, is represented by a positive emission located at around between 420 and 470 nm (for excitations wavelengths of 376-428 nm). This contour is very close to that observed in the EE maps of stand-oil. Thus stand oil, poppy-seed oil and WOZ shows a positive score value for this PC (**Fig. 12C**).

As previously discussed, the main emission maximum for poppy-seed oils is located at 460 nm, whereas for stand-oil is located at around 440 nm. The closeness of the emission maxima may let us suppose that these drying oils could have similar score values for PC1, while linseed oils highlight a negative one, since their main emission is bathochromically shifted (500 nm).

WOZ shows the highest positive score value for PC1, probably due to the highest emission intensity highlighted in its corresponding EE map, which predominates in this model.

By contrast, WOF shows a negative PC1 score value, so in the score plot defined by the first two PCs results to be near to LOF (**Fig. 12C**). This similarity has been previously discussed.

The loading plot of PC2 shown in **Fig. 12B** is characterized by a negative emission between 485 and 552 nm (for excitations of 421-474 nm) which can be partly observed in all EE maps of dying oils, except for stand-oil, which shows its broad emission hypsochromically shifted. Stand-oil results to be positive for this PC, as can be seen in **Fig. 12C**.

This PCA model defines four different groups (linseed oil with WOF; poppy-seed oils; stand-oil and WOZ), but it does not succeed in the description of each type of drying oil. PC1 could define a trend for the main emission maxima, but the highest emission of WOZ limits this “capability”. Additionally, as previously detected, LOF and WOF are not differentiated.

The information which could be obtained is however limited in comparison to that highlighted by the application of PCA to combined first derivative FT-NIR and micro-Raman spectra, as discussed in **Chapter 3** of **Part II**, by which even information on the various manufactures was extracted (analyses after three months of natural ageing).

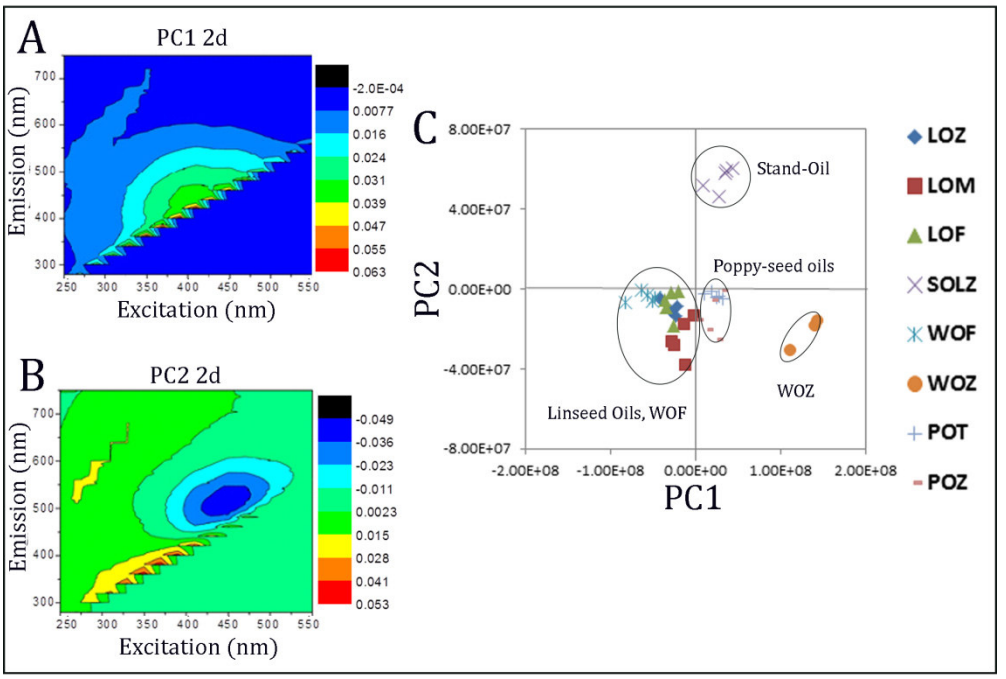

Fig. 12 Loading plots of PC1 (A) and PC2 (B); along with score plot PC1-PC2 (C).

Table 6 Excitation and emission ranges of each loading plot related to the first two PCs. Also, the positive or negative contributions are specified.

PC	Excitation (nm)	Emission (nm)	Contribution
PC1	376-428	420-470	Positive contribution
	Background contour	Background contour	Positive contribution
PC2	421-474	485-552	Negative contribution

1.3 Conclusions

This work represented a preliminary study to evaluate the potentialities and limits of 2D-fluorescence spectroscopy for the analysis of neat binding media, and to individuate the main advantages of its combination with multivariate analytical tools in cultural heritage/painting field.

Within the context of the analysis of paintings, fluorescence spectroscopy is indeed an important tool, since it can provide indications and guide to further analytical investigations. An improvement of its sensitivity could be particularly beneficial.

First of all, 2D-fluorescence spectroscopy provided an effective differentiation between the various classes of neat binding media, even without a complete

characterization of the multiple fluorophores present. This capability was found particularly evident for protein-based binders.
All binders were analysed after a natural ageing of eighteen months. Ageing and degradation processes can cause modifications in emission shape (i.e. a broadening of bands) and intensity and/or generate the appearance of new emission bands. An example regards proteinaceous materials, for which a progressive oxidation of amino acids has been observed. By means of 2D-fluorescence spectroscopy it has been also possible to highlight the main emission maxima of the different typologies of drying oils.
Successively, Principal Component Analysis (PCA) of Excitation-Emission (EE) maps was investigated to differentiate some neat binders. The results obtained stressed the potentiality of the proposed methodology, thanks to the position of the different materials in the score plots, which reflected their origin and chemical composition, i.e. egg-based, drying oils, polysaccharides and proteinaceous binders.
Additionally, PCA was also applied to separated data-subsets, such as drying oils and proteinaceous media, proving a good sensitivity for them. An enhancement in their distinguishing and in the extraction of meaningful information was indeed observed (mainly for proteinaceous ones).
This analytical approach, based on fluorescence properties, represents a useful way to differentiate between various types of binding media, even if the similarities observed do not necessarily imply an identical chemical composition (e.g. stand oil with gums in score plot PC2-PC3 or with glues in score plot PC1-PC3/or LOF and WOF). Therefore, in order to exhaustively characterize these materials, this method should be assisted by other complementary techniques, such as Gas Chromatography Mass Spectroscopy (GC-MS).
In a future, a joined application of 2D-fluorescence spectroscopy with vibrational techniques might be explored, also in combination with multivariate analytical tools (e.g. for proteinaceous materials, whose "differentiation/characterization" is often difficult, especially by means of non-destructive and non-invasive methodologies).

References

[1] A. Nevin, D. Anglos, S. Cather and A. Burnstock, The influence of visible light and inorganic pigments on fluorescence excitation emission spectra of egg-, casein-and collagen-based painting media, Appl. Phys. A 2008, 92, pp 69-76.

[2] A. Nevin, D. Comelli, G. Valentini and R. Cubeddu, Total synchronous fluorescence spectroscopy combined with multivariate analysis: method for the classification of selected resins, oils, and protein-based media used in paintings, Anal. Chem. 2009, 81, pp 1784-1791.

[3] A. Nevin, S. Cather, D. Anglos, C. Fotakis, LIF of protein-based media, Anal. Chim. Acta 2006, 573-574, pp 341-346.

[4] M.P. Colombini, F. Modugno (Eds.), Organic mass spectrometry in art and archaeology, John Wiley & Sons, 2009.

[5] D. Sell, V. Monnier, Structure elucidation of a senescence cross-link from human extracellular matrix, J. Biol. Chem. 1989, 264, pp 21597-21602.

[6] L. Masschelein-Kleiner, Ancient Binding Media, Varnishes and Adhesives, ICCROM, Rome, Italy, 1995.

[7] N.C. Schellmann, Animal glues: a review of their key properties relevant to conservation, Revi. Conserv. 2007, 8, pp 55-66.

[8] J. Mills, R. White, The organic chemistry of museum objects, 2nd ed, Butterworth-Heinemann, Oxford, 1994.

[9] E. Sikorska, T. Gorecki, I.V. Khmelinskii, M. Sikorski, J. Koziol, Classification of edible oils using synchronous scanning fluorescence spectroscopy, Food Chem. 2005, 89, pp 217-225.

[10] E.R. De la Rie, Fluorescence of paint and varnish layers (part II), Stud. Conserv. 1982, 27, pp.-65-68.

[11] T. Miyoshi, Fluorescence from Oil Colours, Linseed Oil and Poppy Oil under N2 Laser Excitation, Jpn. J. Appl. Phys. 1985, 24(3), pp 371-372.

[12] J.L. Larson, K.S. Kim Shin, J.I. Zink, Photoluminescence spectroscopy of natural resins and organic binding media of paintings, JAIC 1991, Vol. 30, No. 1 (7), pp 89-104.

[13] L. Brambilla,, C. Riedo, C. Baraldi, A. Nevin, M. C. Gamberini, C. D'Andrea, O. Chiantore, S. Goidanich, L. Toniolo, Characterization of fresh and aged natural ingredients used in historical ointments by molecular spectroscopic techniques: IR, Raman and fluorescence, Anal Bioanal Chem. 2011, 401(6), pp: 1827-37.

[14] A. Mounier, G. Le Bourdon, C. Aupetit, C. Belin, L. Servant, S. Lazare, Y. Lefrais, F, Daniel, Hyperspectral imaging, spectrofluorimetry, FORS and XRF for the non-invasive study of medieval miniatures materials, Heritage Science 2014, 2(24), pp 1-12.

[15] A. Lluveras, I. Bonaduce, A. Andreotti, M.P. Colombini, GC/MS analytical procedure for the characterization of glycerolipids, natural waxes, terpenoid resins, proteinaceous and polysaccharide materials in the same paint microsample avoiding interferences from inorganic media, Anal. Chem. 2010, 82 (1), pp 376-386.

General conclusions

My PhD work was aimed at developing new analytical approaches based on the combination of traditional spectroscopic techniques with multivariate analysis tools to enhance the information referred to traditional binding media used in paintings. Improving their characterization and identification, thus their differentiation within the same organic class, represented the main purpose aimed at understanding both the relative ageing process and interaction with pigments.

A new methodology, based on the application of Principal Component Analysis (PCA) to combined first derivative FT-NIR and Raman spectra, was developed, thus its potentialities were investigated in order to exhaustively characterize traditional neat binding media and complex systems, such as oil-paint models. It was demonstrated that the combination of FT-NIR and Raman spectra, after a correct data pre-processing procedure, together with the exploitation of multivariate analysis (e.g. PCA), avoids loss of information and enables the increase of sensitivity, maximizing the extracted information. A more complete analysis and characterization with respect to separate datasets was indeed achieved. This aspect was particularly highlighted in the study of drying oils and oil-paint models.

The proposed analytical approach revealed to be a valuable and meaningful tool, able to distinguish and to differentiate traditional binders belonging to each considered class. Indeed, it immediately highlighted their main spectral features in both the investigated regions. Nevertheless, no differentiation within drying oils or glues groups was observed. This result indicated and suggested the need for further PCA modelling of each sub-group in order to fine-tune the analysis in the case of compounds belonging to the same organic class.

In the study focused on drying oils the proposed methodology provided the increasing of the sensitivity for the characterization of the different evaluated typologies of oils, and at the same time it highlighted slight differences present in their chemical composition, up to the tracing of the manufacturers.

Consequently, to addition of a pigment, the analysed models became more complex. A model set of samples with a mixture of different pigments and linseed/poppy-seed oil was prepared. The analysis of these oil-paint models led to exhaustively characterize these more complex systems, up to a possible identification of the oil used to prepare them. An important perspective, arose from this study, regarded the chemical information provided by the third principal components (PC3s), obtained from the analysis of all the different

data groups; they could be ascribable to the drying oil's spectral contributions, and helped to differentiate the oils utilized.
Finally, the application of PCA to combined first derivative FT-NIR and Raman spectra was successfully exploited in the study of two aged white oil-paint models, prepared with lead and zinc white pigments. This methodology individuated and defined some probable ageing trends, enhancing the understanding of their ageing processes. This analytical approach allowed a more complete and rapid description of the main chemical changes involved in the curing process, detectable by means of the two considered vibrational spectroscopic techniques.

Additionally, in order to better understand the chemical composition of different binding media (e.g. proteinaceous binders) and their modifications with ageing, a preliminary study focused on 2D-fluorescence spectroscopy was performed. Fluorescence spectroscopy was found to be able to differentiate the various classes of neat binding media, even without a complete characterization of the multiple fluorophores present, also proving information about their ageing.
Furthermore, egg-based, drying oils, polysaccharides and proteinaceous binders were properly differentiated thanks to the application of PCA to Excitation-Emission (EE) maps, highlighting good potentialities regarding a future joined application of 2D-fluorescence spectroscopy with vibrational techniques, based on the exploitation of further multivariate analytical tools (e.g. Partial Least Squares regression - PLS). A good sensitivity for proteinaceous binders was revealed, thus overstepping the difficulty of their differentiation/characterization, often encountered with common analytical approaches.

Acknowledgments

I want to acknowledge first of all my Ph.D. tutors, Dr. Maurizio Becucci, for his constant help and ideas for the progress of the project, Dr. Marilena Ricci, for her dedication and her remarkable support and Dr. Marcello Picollo, for his important advices and suggestions.
I want specially to thank Dr. Costanza Cucci for her important help, supervision and useful advices for the processing of the data and the application of the multivariate analysis during all these three years. I am also grateful to Dr. Cristiana Lofrumento for her remarkable support.
Dr. Jacopo La Nasa is also acknowledged for his cooperation and contribution to this work.
I also wish to take the opportunity to thank Prof. Anglos Demetrios, Dr. Aggelos Filippidis and Dr. Zoe Eirini Papliaka, for all their support and dedication during the six months spent in Heraklion. Thank you to all the group of "Photonics for Cultural Heritage" at IESL-FORTH for their special welcome and useful advices.
Finally, I want to acknowledge my family and all my friends for sharing with me every moment of this experience and for their support and friendship.

This research has been founded by the Italian Ministry of Instruction, University and Research (MIUR) through the PRIN 2010-11 project (Project No. 2010329WPF).

APPENDICES

APPENDIX A: RAW and FIRST DERIVATIVE spectra referred to each binder

In the following appendix, raw and corresponding first derivative FT-NIR and micro-Raman spectra referred to each binder are reported along with the assignments for main bands.

FT-NIR spectra are reported as first, whereas micro-Raman spectra as second.

Furthermore, raw FT-NIR spectra are shown without any pre-treatment, while micro-Raman spectra are shown after baseline subtraction to better highlight all Raman bands.
All first derivative spectra are shown, after application of the pre-processing described in **Part I.**

EGG WHITE (EW)

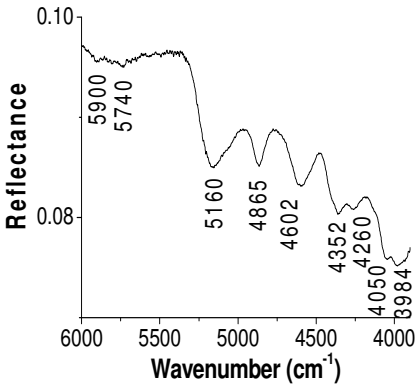
Reflectance
0.10
0.08
5900
5740
5160
4865
4602
4352
4260
4050
3984
6000
5500
5000
4500
4000
Wavenumber (cm-1)

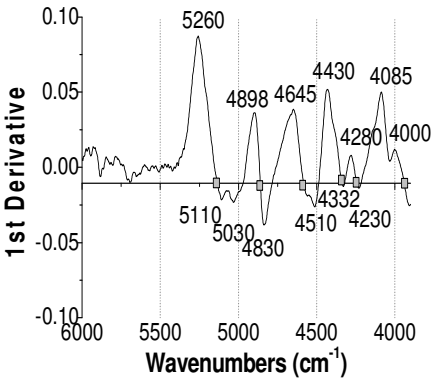
1st Derivative
0.10
0.05
0.00
-0.05
-0.10
5260
4898
4645
4430
4085
4280
4000
4332
5110
5030
4830
4510
4230
6000
5500
5000
4500
4000
Wavenumbers (cm-1)

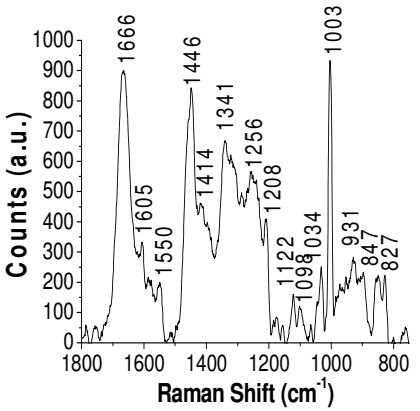
Counts (a.u.)
1000
900
800
700
600
500
400
300
200
100
0
1666
1605
1550
1446
1414
1341
1256
1208
1122
1098
1034
1003
931
847
827
1800
1600
1400
1200
1000
800
Raman Shift (cm-1)

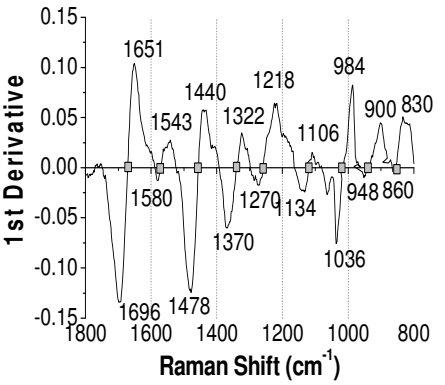
1st Derivative
0.15
0.10
0.05
0.00
-0.05
-0.10
-0.15
1651
1440
1543
1218
1322
984
900
830
1106
1580
1270
948
860
134
1370
1036
1696
1478
1800
1600
1400
1200
1000
800
Raman Shift (cm-1)

Frequency (cm^{-1})	Assignment	Ref.
5900	1st overtone $\nu_a(CH_3)$	[1-2]
5740	1st overtone $\nu_s(CH_3)$	[1-2]
5160	$\nu(OH)+\delta(OH)$	[1-2]
4865	$\nu(NH)+\delta(NH)$	[1-2]
4602	1st overtone ν(CO)amide I + amide II	[1-2]
4352	$\nu_a(CH_2)+\delta_a(CH_2)$	[1-2]
4260	$\nu_s(CH_2)+\delta_s(CH_2)$	[1-2]
4050	CH combination (CH_2)/ 3rd overtone δ(CC)	[1-2]
3984	C-H aromatic/1st overtone ν (C-N-C) amide	[1]

Frequency (cm^{-1})	Assignment	Ref.
1666	Amide I	[3-4]
1605	Phe/Tyr	[4]
1550	Trp	[4]
1446	C-H_2 scissoring	[3-4]
1414	Aspartic and glutamic acids (C=O stretching)	[4]
1341	CH_2 deformation	[3-4]
1256	Amide III	[3-4]
1208	Phe/Tyr	[4]
1122	C-CT stretching	[4]
1098	C-C,C-N stretching	[3-4]
1034	Phe	[4]
1003	Phe ring breathing	[3-4]
931	C-C stretching	[3-4]
847	Tyr	[4]
827	Tyr	[4]

EGG YOLK (EY)

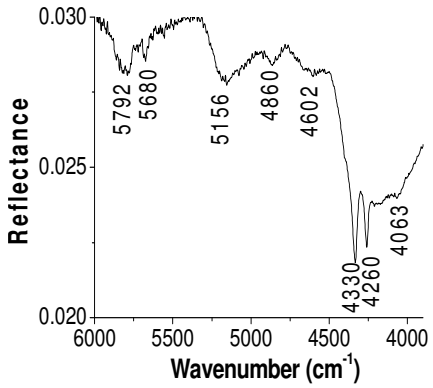
Reflectance
Wavenumber (cm-1)
5792
5680
5156
4860
4602
4330
4260
4063

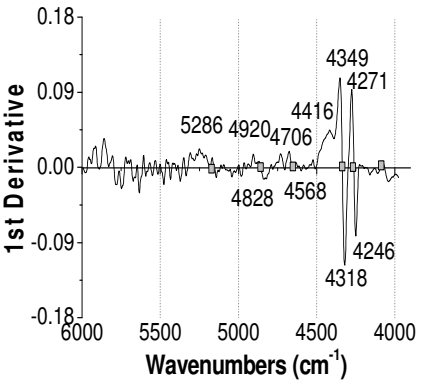
1st Derivative
Wavenumbers (cm-1)
4349
4271
4416
5286
4920
4706
4828
4568
4246
4318

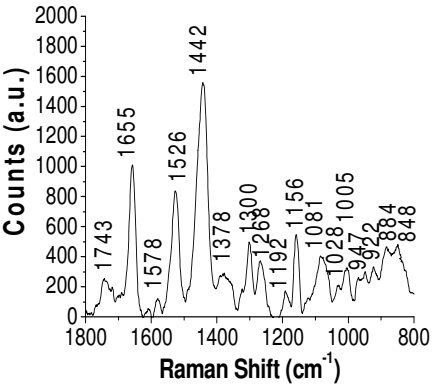
Counts (a.u.)
Raman Shift (cm-1)
1743
1655
1578
1526
1442
1378
1300
1268
1192
1156
1081
1028
1005
947
922
884
848

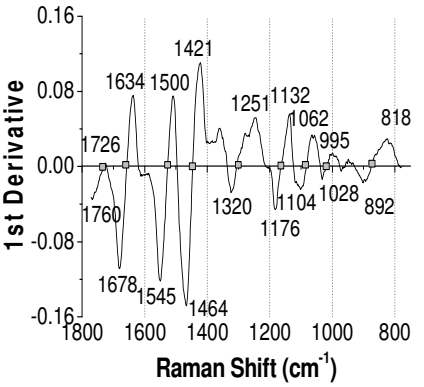
1st Derivative
Raman Shift (cm-1)
1421
1634
1500
1251
1132
1062
818
1726
995
1760
1320
1104
1028
892
1176
1678
1545
1464

Frequency (cm^{-1})	Assignment	Ref.
5792	1st overtone asymmetric stretching $\nu_a(CH)$ [CH_2]	(1-2)
5680	1st overtone symmetric stretching $\nu_s(CH)$ [CH_2]	(1-2)
5156	$\nu(OH)+\delta(OH)$	(1-2)
4860	$\nu(NH)+\delta(NH)$	(1-2)
4602	1st overtone $\nu(CO)$ amide I + amide III	(1-2)
4330	$\nu_a(CH_2)+\delta_a(CH_2)$	(1-2)
4260	$\nu_s(CH_2)+\delta_s(CH_2)$	(1-2)
4063	CH combination (CH_2)/ 3rd overtone $\delta(CC)$	(1-2)

Frequency (cm^{-1})	Assignment	Ref.
1743	C=O stretching	(4-5)
1655	Amide I/ *cis* $\nu(C=C)$	(3-5)
1578	Phe/Tyr	(4)
1522	Trp	(4)
1435	C-H_2 scissoring	(3-5)
1300	In phase methylene twisting motion $\delta(CH_2)_2$	(5)
1268	Amide III	(3-4)
1192	Phe/Tyr	(4)
1156	C-CT stretching	(4)
1081	C-C,C-N stretching	(3-4)
1028	Phe	(4)
1005	Phe ring breathing	(3-4)
947	C-C vibration, phosphate symmetric stretching	(4)
922	C-C stretching	(3-4)
884	Trp	(4)
848	Tyr	(4)

WHOLE EGG (WE)

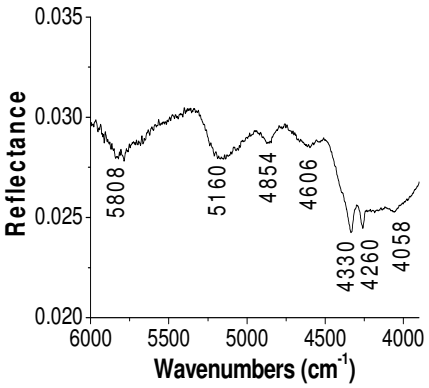
Reflectance
Wavenumbers (cm-1)
5808
5160
4854
4606
4330
4260
4058

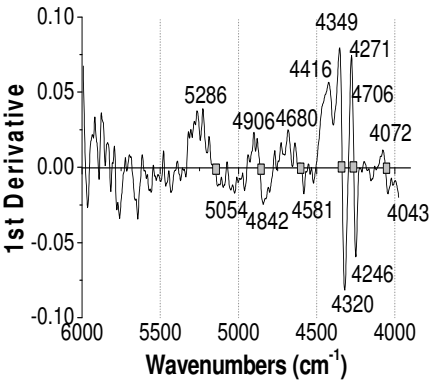
1st Derivative
Wavenumbers (cm-1)
4349
4271
4416
4706
5286
4906
4680
4072
5054
4842
4581
4043
4246
4320

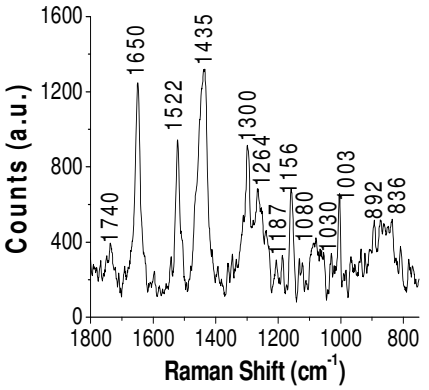
Counts (a.u.)
Raman Shift (cm-1)
1740
1650
1522
1435
1300
1264
1156
1187
1080
1030
1003
892
836

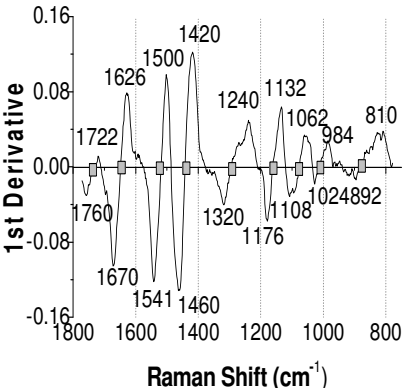
1st Derivative
Raman Shift (cm-1)
1420
1500
1626
1240
1132
1062
1722
984
810
1760
1320
1108
1024892
1176
1670
1541
1460

Frequency (cm^{-1})	Assignment	Ref.
5808	1st overtone asymmetric stretching $\nu_a(CH)$ $[CH_2]$	[1-2]
5160	$\nu(OH)+\delta(OH)$	[1-2]
4854	$\nu(NH)+\delta(NH)$	[1-2]
4606	1st overtone $\nu(CO)$amide I + amide III	[1-2]
4330	$\nu_a(CH_2)+\delta_a(CH_2)$	[1-2]
4260	$\nu_s(CH_2)+\delta_s(CH_2)$	[1-2]
4058	CH combination (CH_2)/ 3rd overtone $\delta(CC)$	[1-2]

Frequency (cm^{-1})	Assignment	Ref.
1740	C=O stretching	[4-5]
1650	Amide I/ *cis* ν(C=C)	[3-5]
1522	Trp	[4]
1435	C-H_2 scissoring	[3-5]
1300	In phase methylene twisting motion $\delta(CH_2)_2$	[5]
1264	Amide III	[3-4]
1187	Phe/Tyr	[4]
1156	C-CT stretching	[4]
1080	C-C,C-N stretching	[3-4]
1030	Phe	[4]
1003	Phe ring breathing	[3-4]
892	Trp	[4]
836	Tyr	[4]

CASEIN (C)

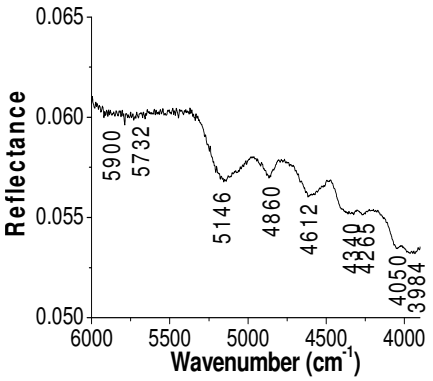
Reflectance
Wavenumber (cm-1)
5900
5732
5146
4860
4612
4340
4265
4050
3984

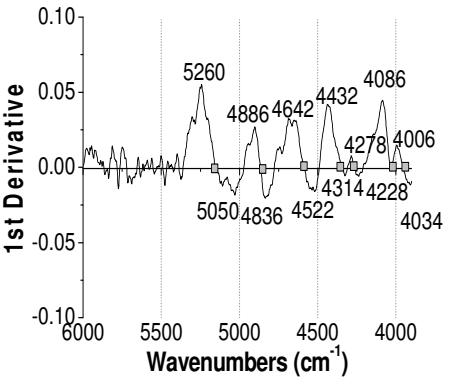
1st Derivative
Wavenumbers (cm-1)
5260
4886
4642
4432
4086
4278
4006
4314
4228
5050
4836
4522
4034

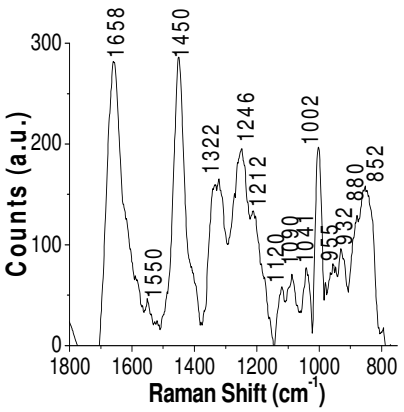
Counts (a.u.)
Raman Shift (cm-1)
1658
1450
1322
1246
1212
1120
1090
1041
1002
955
932
880
852
1550

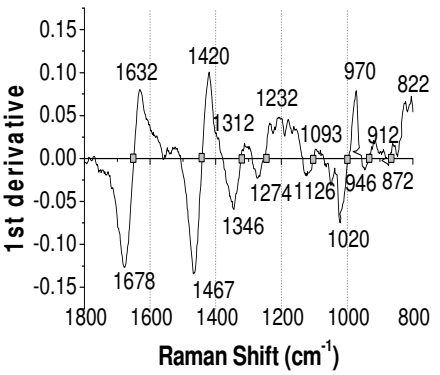
1st derivative
Raman Shift (cm-1)
1632
1420
970
822
1232
1312
1093
912
1274
1126
946
872
1346
1020
1678
1467

Frequency (cm^{-1})	Assignment	Ref.
5900	1st overtone $\nu_a(CH_2)$	[1-2]
5732	1st overtone $\nu_S(CH_2)$ [aromatic associated]	[1-2]
5146	$\nu(OH)+\delta(OH)$	[1-2]
4860	$\nu(NH)+\delta(NH)$	[1-2]
4612	1st overtone $\nu(CO)$amide I + amide III	[1-2]
4340	$\nu_a(CH_2)+\delta_a(CH_2)$	[1-2]
4265	$\nu_s(CH_2)+\delta_s(CH_2)$/ovoalbumin	[1-2]
4050	CH combination (CH_2)/ 3rd overtone $\delta(CC)$	[1-2]
3984	1st overtone ν (C-N-C) amide	[1]

Frequency (cm^{-1})	Assignment	Ref.
1658	Amide I	[3-4]
1550	Trp	[4]
1450	C-H_2 scissoring	[3-4]
1322	CH_2 deformation	[4]
1246	Amide III	[3-4]
1212	Phe/Tyr	[4]
1120	C-CT stretching	[4]
1090	$\nu(CC)$ (aliphatic)/C-N stretching	[3-4]
1041	Phe	[4]
1002	Phe ring breathing	[3-4]
955	C-C vibration, phosphate symmetric stretching	[4]
932	C-C stretching	[3-4]
880	Trp	[4]
852	Tyr	[4]

RABBIT SKIN GLUE (RG)

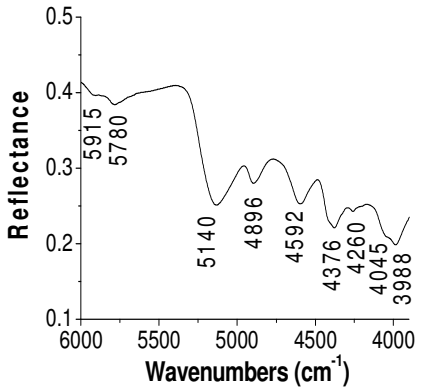

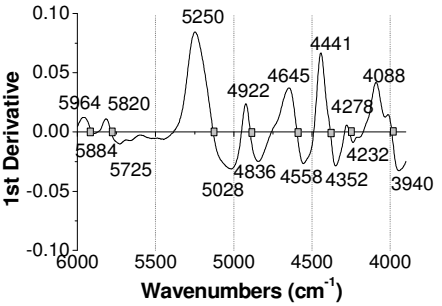

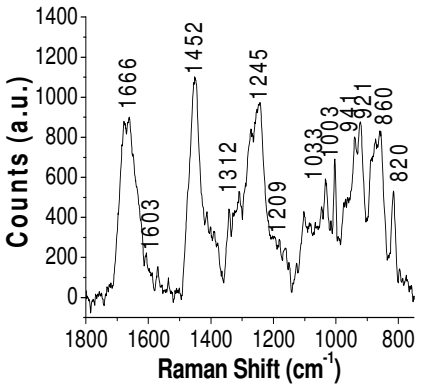

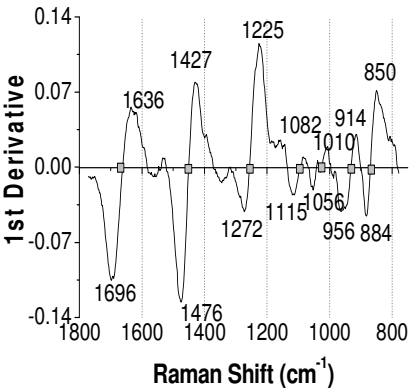

Frequency (cm^{-1})	Assignment	Ref.
5915	C-H aromatic/1st overtone $\nu_a(CH_2)$	[1]
5780	1st overtone $\nu_s(CH_2)$	[1-2]
5140	ν(OH)+ δ (OH)	[1-2]
4896	ν_s(NH)+ δ (NH) [νN-H symmetric and Amide II deformation (N-H in plane bending) combination]	[1-2]
4592	1st overtone ν(CO) amide I+amide III deformation (C-N stretching/N-H in plane bending)	[1-2]
4376	$\nu_a(CH_2)$+ δ (CH_2)	[1-2]
4260	$\nu_s(CH_2)$+ δ (CH_2)	[1-2]
4045	CH combination (CH_2)/ 3rd overtone δ(CC)	[1-2]
3988	1st overtone ν (C-N-C) amide	[1]

Frequency (cm^{-1})	Assignment	Ref.
1666	Amide I	[3-4]
1603	Phe/Tyr	[4]
1452	C-H_2 scissoring	[3-4]
1312	CH_2 deformation	[4]
1245	Amide III	[3-4]
1209	Phe/Tyr	[4]
1033	Phe	[4]
1003	Phe ring breathing	[3-4]
941	C-C stretching	[3-4]
921	C-C vibration δ (CH_3)	[3-4]
860	Tyr	[4]
819	C-C stretching	[3-4]

STRONG GLUE (SG)

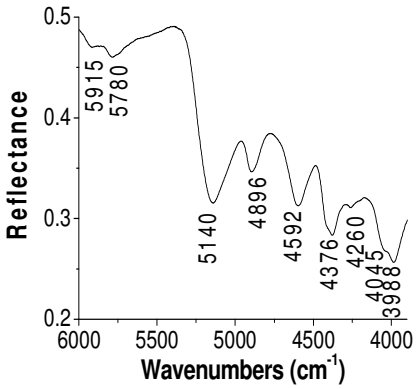

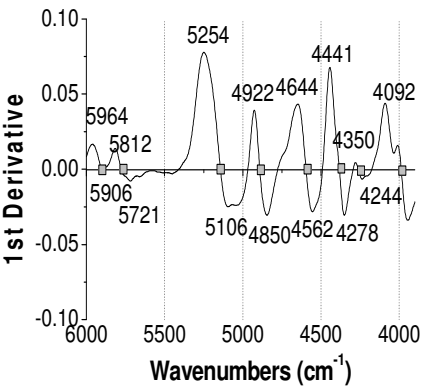

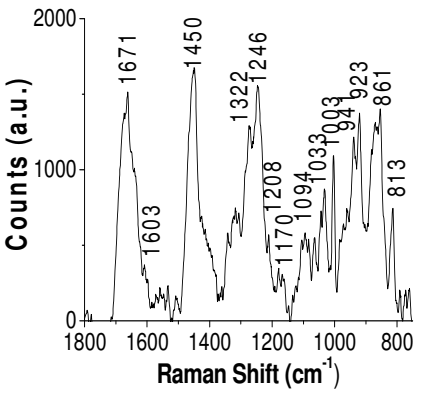

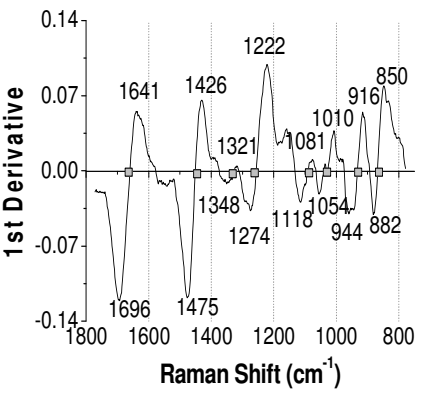

Frequency (cm^{-1})	Assignment	Ref.
5915	C-H aromatic/1st overtone $\nu_a(CH_2)$	[1]
5780	1st overtone $\nu_s(CH_2)$	[1-2]
5140	ν(OH)+ δ (OH)	[1-2]
4896	ν_s(NH)+ δ (NH) [νN-H symmetric and Amide II deformation (N-H in plane bending) combination]	[1-2]
4592	1st overtone ν(CO) amide I+amide III deformation (C-N stretching/N-H in plane bending)	[1-2]
4376	$\nu_a(CH_2)$+ δ (CH_2)	[1-2]
4260	$\nu_s(CH_2)$+ δ (CH_2)	[1-2]
4045	CH combination (CH_2)/ 3rd overtone δ(CC)	[1-2]
3988	1st overtone ν (C-N-C) amide	[1]

Frequency (cm^{-1})	Assignment	Ref.
1671	Amide I	[3-4]
1603	Phe/Tyr	[4]
1450	C-H_2 scissoring	[3-4]
1322	CH_2 deformation	[4]
1246	Amide III	[3-4]
1208	Phe/Tyr	[4]
1170	Aliphatic CH_3 anti symmetric; aromatic CH_2 rock	[4]
1094	C-C, C-N stretching	[3-4]
1033	Phe	[4]
1003	Phe ring breathing	[3-4]
941	C-C stretching	[3-4]
923	C-C vibration δ (CH_3)	[3-4]
861	Tyr	[4]
813	C-C stretching	[4]

FISH GLUE (FG)

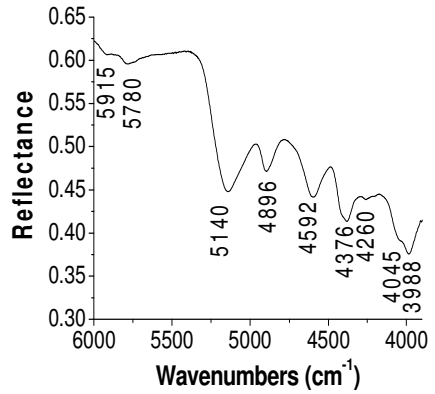
Reflectance
Wavenumbers (cm-1)
5915
5780
5140
4896
4592
4376
4260
4045
3988

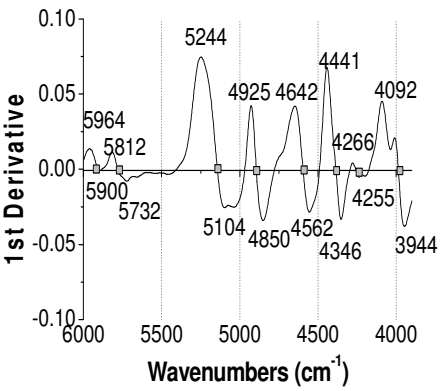
1st Derivative
Wavenumbers (cm-1)
5964
5812
5900
5732
5244
5104
4925
4850
4642
4562
4441
4346
4266
4092
4255
3944

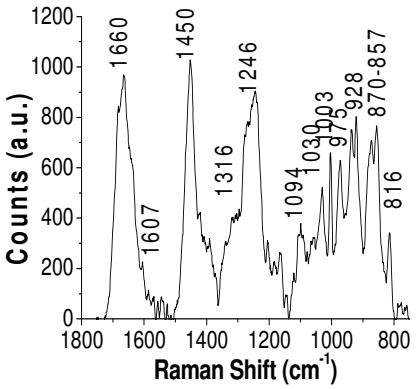
Counts (a.u.)
Raman Shift (cm-1)
1660
1607
1450
1316
1246
1094
1030
1003
975
928
870-857
816

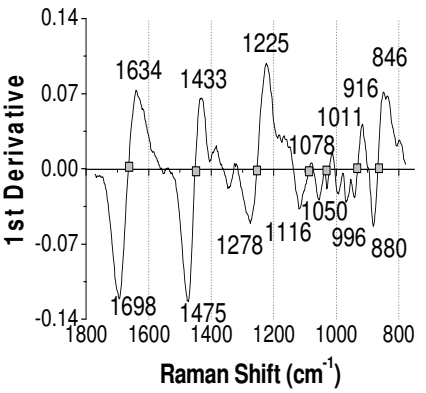
1st Derivative
Raman Shift (cm-1)
1634
1698
1433
1475
1225
1278
1116
1078
1050
1011
996
916
880
846

Frequency (cm^{-1})	Assignment	Ref.
5915	C-H aromatic/1st overtone $\nu_a(CH_2)$	[1]
5780	1st overtone $\nu_s(CH_2)$	[1-2]
5140	ν(OH)+ δ (OH)	[1-2]
4896	ν_s(NH)+ δ (NH) [νN-H symmetric and Amide II deformation (N-H in plane bending) combination]	[1-2]
4592	1st overtone ν(CO) amide I+amide III deformation (C-N stretching/N-H in plane bending)	[1-2]
4376	$\nu_a(CH_2)$+ δ (CH_2)	[1-2]
4260	$\nu_s(CH_2)$+ δ (CH_2)	[1-2]
4045	CH combination (CH_2)/ 3rd overtone δ(CC)	[1-2]
3988	1st overtone ν (C-N-C) amide	[1]

Frequency (cm^{-1})	Assignment	Ref.
1665	Amide I	[3-4]
1607	Phe/Tyr	[4]
1450	C-H_2 scissoring	[3-4]
1406	Aspartic and glutamic acids (C=O stretching)	[4]
1316	CH_2 deformation	[4]
1246	Amide III	[3-4]
1094	C-C, C-N stretching	[3-4]
1030	Phe	[4]
1003	Phe ring breathing	[3-4]
975	C-C vibration δ (CH_2)	[3-4]
928	C-C vibration δ (CH_3)	[3-4]
870-856	Tyr	[4]
816	C-C stretching	[4]

ARABIC GUM (AG)

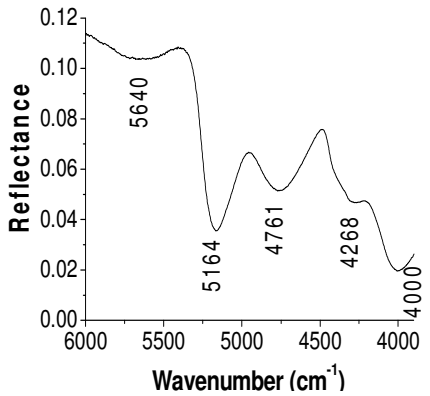

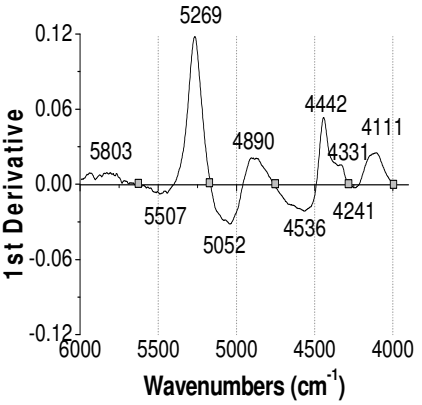

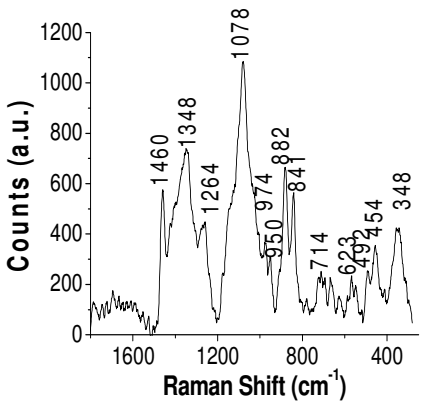

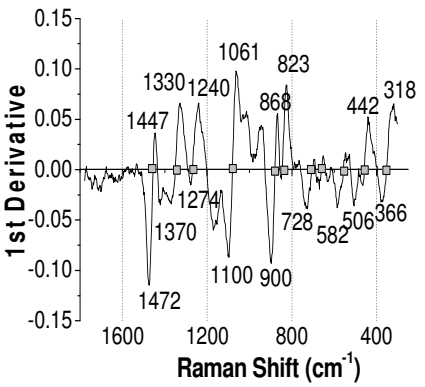

Frequency (cm^{-1})	Assignment	Ref.
5640	C-H methylene (2 νC-H)	[1]
5164	O-H stretching and HOH bending combination (.O-H and HOH)	[1]
4761	O-H bending and C-O stretching combination. O-H/C-O polymeric (.O-H and .C-O)/ 4ν C=O-C polymeric (C=O and C-O stretching)	[1]
4268	C-H combination (2 νCH_2 symmetric stretching and δCH_2)	[1]
4000	C-H stretching and C-C and C-O-C stretching combination	[1]

Frequency (cm^{-1})	Assignment	Ref.
1460	$\delta(CH_2)$ scissoring	[6]
1348	$\delta(CH_2)$ wagging	[6]
1264	$\tau(CH_2)$	[6]
1078	ν(COC) ether group (ring)	[6]
974	$\delta(CH_3)$	[6]
950	CC symmetrical stretching	[6]
882	ν(COC)	[6]
841	ν(COC)	[6]
714	ν(CC)	[6]
623	δ(CCC)	[6]
492	δ(CCC)	[6]
454	δ(CCC)	[6]
348	τ (CCC)	[6]

TRAGACANTH GUM (TG)

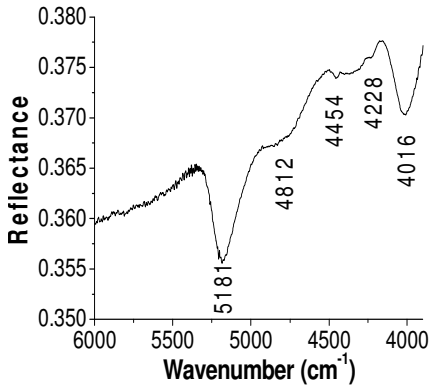

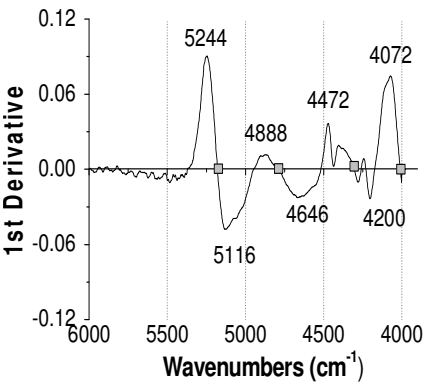

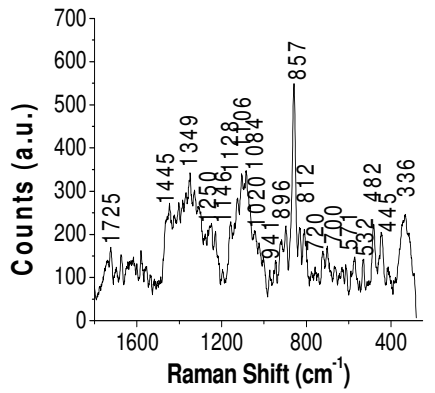

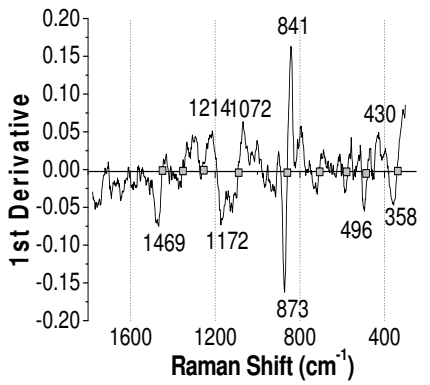

Frequency (cm^{-1})	Assignment	Ref.
5181	O-H stretching and HOH bending combination (.O-H and HOH)	[1]
4812	O-H bending and C-O stretching combination. O-H/C-O polymeric (.O-H and .C-O)	[1]
4454-4228	C-H stretching and CH_2 deformation combination	[1]
4016	C-H stretching and C-C (and C-O-C) stretching combination [+simile a cellulose]	[1]

Frequency (cm^{-1})	Assignment	Ref.
1725	ν(C=O)	[6]
1445	δ(CH_2) scissoring	[6]
1349	δ(CH_2) wagging	[6]
1250	τ(CH_2)	[6]
1146	ν(CC)	[6]
1128	ν(CC)	[6]
1106	ν(CC) uronic acid	[6]
1084	ν(COC) ether group (ring)	[6]
1020	ν(CC) uronic acid	[6]
941	ν(COC)	[6]
896	ν(COC)	[6]
857	ν(COC)	[6]
812	ν(COC)	[6]
720-700	ν(CC)	[6]
571	δ(CCO)	[6]
532	δ(CCO)	[6]
482	δ(CCC)	[6]
445	δ(CCC)	[6]
336	τ (CCC)	[6]

DRYING OILS

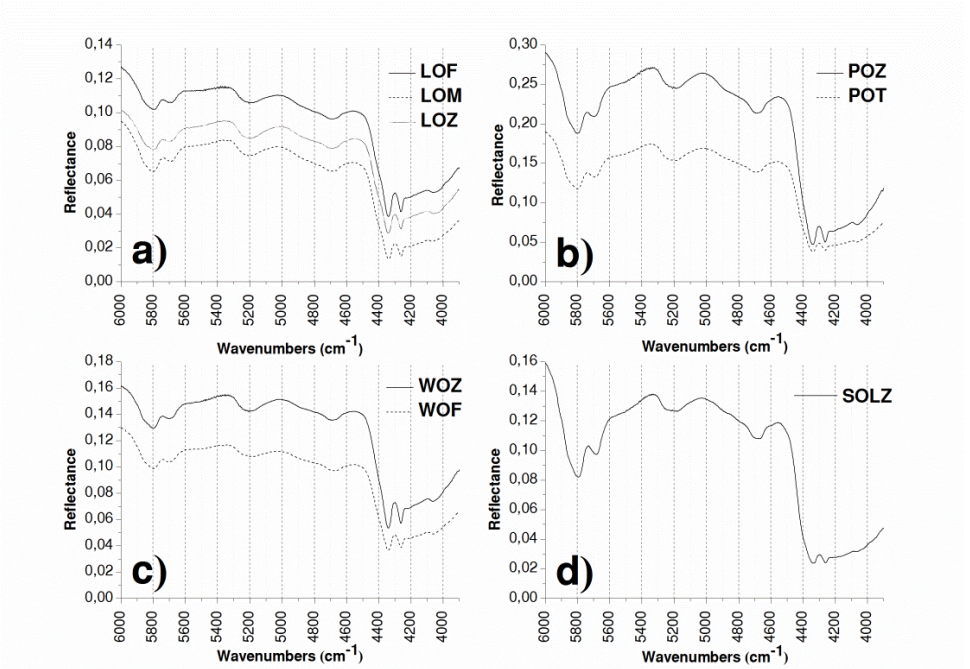
a)
LOF
LOM
LOZ
b)
POZ
POT
c)
WOZ
WOF
d)
SOLZ
Reflectance
Wavenumbers (cm-1)

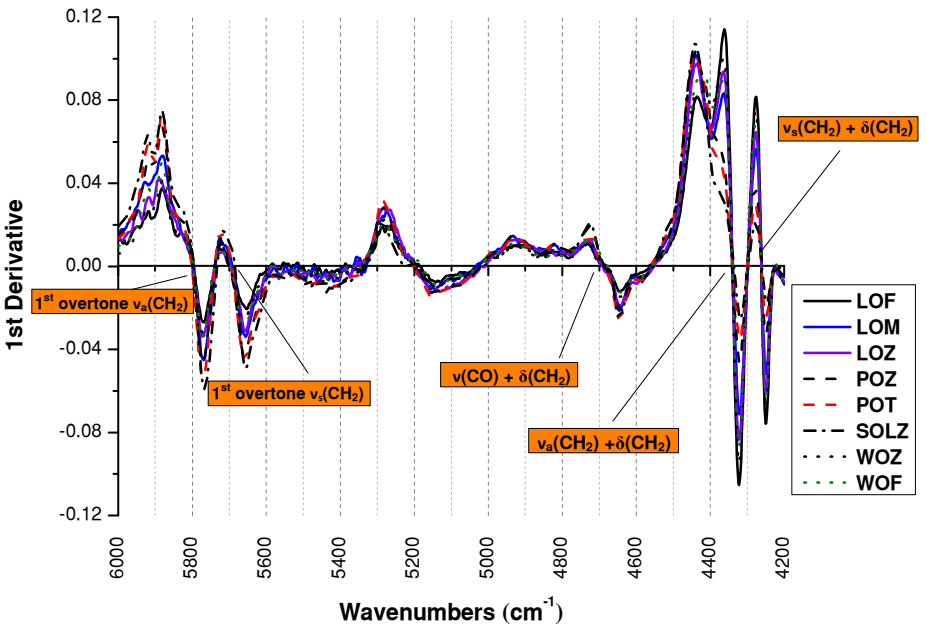
1st Derivative
Wavenumbers (cm-1)
1st overtone νa(CH2)
1st overtone νs(CH2)
ν(CO) + δ(CH2)
νa(CH2) +δ(CH2)
νs(CH2) + δ(CH2)
LOF
LOM
LOZ
POZ
POT
SOLZ
WOZ
WOF

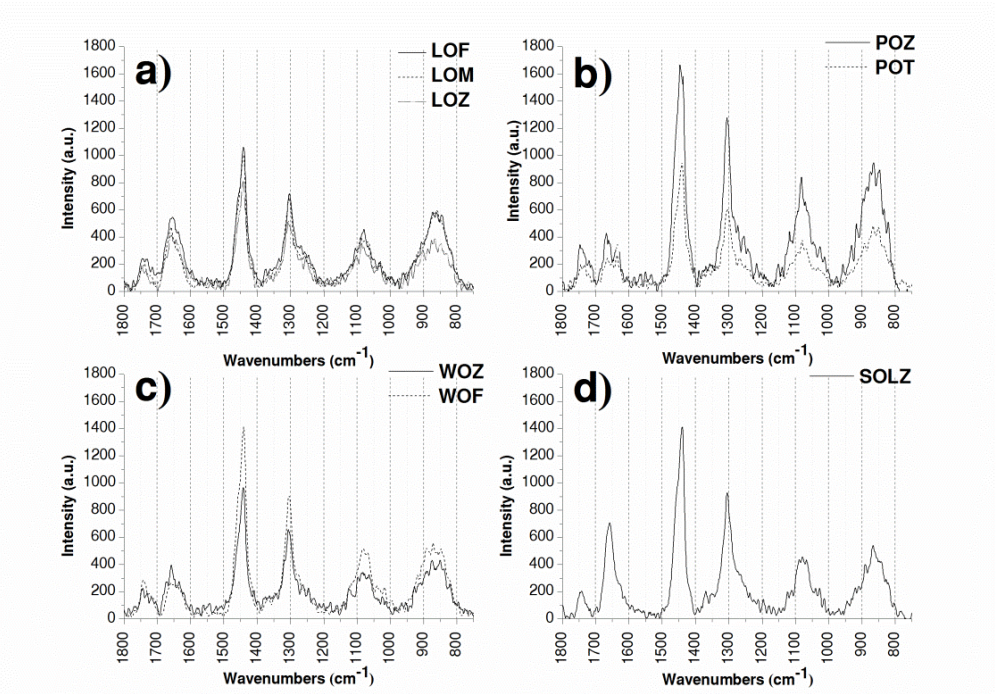
a)
LOF
LOM
LOZ
b)
POZ
POT
c)
WOZ
WOF
d)
SOLZ
Intensity (a.u.)
Wavenumbers (cm-1)

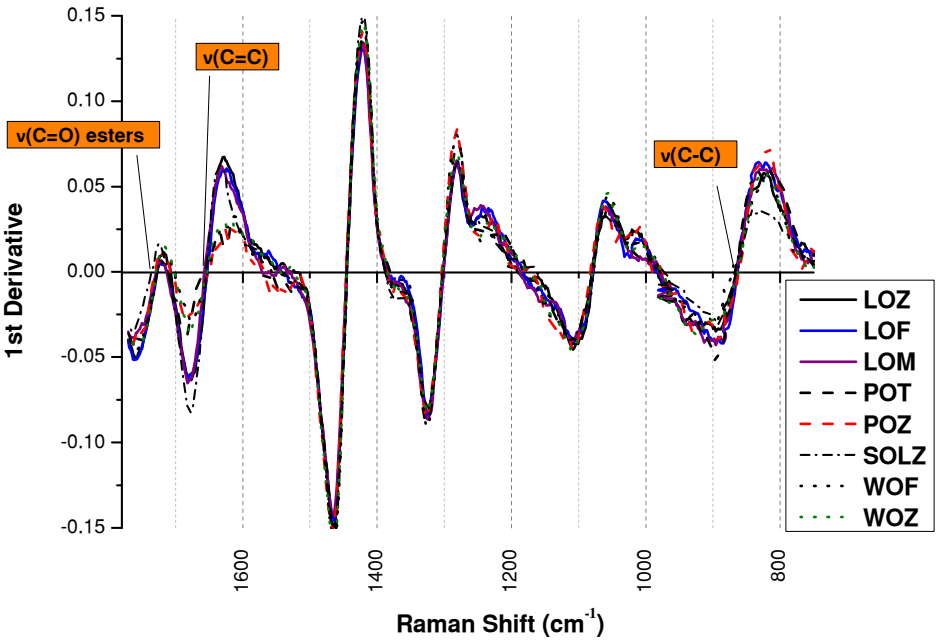
ν(C=O) esters
ν(C=C)
ν(C-C)
1st Derivative
Raman Shift (cm-1)
LOZ
LOF
LOM
POT
POZ
SOLZ
WOF
WOZ

LOZ	LOF	LOM	WOZ	WOF	POZ	POT	SOLZ	cm-1	Functional group[b]	Assignment	Ref.[b]
5792 (s-sh)	5796 (s-sh)	5798 (s-sh)	5800 (s-sh)	5800 (s-sh)	5800 (s-sh)	5802 (s-sh)	5796 (s-sh)	5794	-CH_2-	1st overtone asymmetric stretching ν_a(CH)	[1-2]
5698 (s-sh)	5694 (s-sh)	5688 (s-sh)	5704 (s-sh)	5700 (s-sh)	5698 (s-sh)	5694 (s-sh)	5685 (s-sh)	5698	-CH_2-	1st overtone symmetric stretching ν_s(CH)	[1-2]
							5258 (m-br)	5260	.C=OOH	2nd overtone stretching ν(C=O) Acids, carboxylic	[1]
5202 (m-br)	5200 (m-br)	5205 (m-br)	5202 (m-br)	5190 (m-br)	5181 (m-br)	5205 (m-br)	5181 (m-br)	5179	.C=OOR	2nd overtone stretching ν(C=O) Acids and esthers	[1-2]
4707 (m-br)	4707 (m-br)	4707 (m-br)			4707 (m-br)	4707 (m-br)	4707 (m-br)	4707	-COOR	stretching ν(CH) + stretching ν(C=O)	[1-2]
			4690 (m-br)	4680 (m-br)				4690		stretching ν(CH) + stretching ν(C=O)	[7]
4595 (vw)	4597 (vw)	4597 (vw)	4597 (vw)	4600 (vw)	4610 (vw)	4597 (vw)	4604 (w)	4595	-HC=CH-	symmetric stretching ν_s(CH) + stretching ν(C=C)	[8]
4340 (s-sh)	4340 (s-sh)	4340 (s-sh)	4340 (s-sh)	4340 (s-sh)	4340 (s-sh)	4340 (s-sh)	4335 (s-sh)	4340	-CH_2-	asymmetric stretching ν_a(CH) + bending δ(CH)	[1-2]
4261 (s-sh)	4261 (s-sh)	4261 (s-sh)	4261 (s-sh)	4261 (s-sh)	4261 (s-sh)	4261 (s-sh)	4261 (s-sh)	4261	-CH_2-	symmetric stretching ν_s(CH) + bending δ(CH)	[1-2]
4060 (w-sh)	4060 (w-sh)	4062 (w-sh)	4063 (w-sh)	4063 (w-sh)	4063 (w-sh)	4067 (w-sh)	4063 (w-sh)	4060	-CH_2-	Combination bending	[1]

[a]sh (sharp); br (broad); m (medium); s (strong); w (weak); sd (shoulder)/[b]Refs 1-3. Bands which have not been identified are not assigned but are listed for completeness

LOZ	LOM	LOF	WOZ	WOF	POZ	POT	SOLZ	cm^{-1}	Assignment[b]	Ref.[b]
1728 (m-br)	1728 (m-br)	1728 (m-br)	1729 (m-br)	1728 (m-br)	1731 (m-br)	1728 (m-br)	1735 (m-br)	1740 1730	Stretching ν(C=O) saturated esters Stretching ν(C=O) unsaturated esters	[9-10]
1654 (s)	1658 (s)	1654 (s)	1652 (m)	1652 (m)	1654 (m)	1660 (m)	1654 (s)	1655	Stretching ν(C=C) [*cis* dialkyl C=C double bond]	[5]
1441 (s-sh)	1441 (s-sh)	1441 (s-sh)	1441 (s-sh)	1441 (s-sh)	1441 (s-sh)	1441 (s-sh)	1441 (s-sh)	1440	Bending $\delta(CH_2)$	[5]
1306 (s-sh)	1303 (s-sh)	1303 (s-sh)	1303 (s-sh)	1303 (s-sh)	1303 (s-sh)	1303 (s-sh)	1303 (s-sh)	1300	In phase methylene twisting motion $\delta(CH_2)_2$	[5]
(1265) (w)	(1265) (w)	(1260) (w)	(1262) (w)	(1258) (w)	(1258) (w)	(1258) (w)	(1262) (w)	1265	Rocking deformation of *cis* dialkylethylenes r(CH=CH)	[5]
1072 (s-br)	1078 (s-br)	1078 (s-br)	1078 (s-br)	1078 (s-br)	1078 (s-br)	1078 (s-br)	1075 (s-br)	1085	Stretching ν(C-C)	[11]
865 (s-br)	865 (s-br)	862 (s-br)	862 (s-br)	870 (s-br)	862 (s-br)	867 (s-br)	865 (s-br)	864	Stretching ν(C-C)	[11]

[a]s (strong); m (medium); w (weak); sh (sharp); br (broad)/[b]Refs 17, 22-24. Bands which have not been identified are not assigned but are listed for completeness

References

[1] J. Workman, L. Weyer Practical Guide to Interpretative Near-Infrared Spectroscopy, CRC Press- Taylor and Francis, Boca Raton, 2007.

[2] M. Vagnini, C. Miliani, L. Cartechini, P. Rocchi, B.G. Brunetti, A. Sgamellotti, FT-NIR spectroscopy for non-invasive identification of natural polymers and resins in easel paintings, Anal. Bioanal. Chem. 2009, 395, pp 2107-2118.

[3] P. Vandenabeele, B. Wehling, L. Moens, H. Edwards, M. De Reu, G. Van Hooydonk, Analysis with Micro-Raman Spectroscopy of Natural Organic Binding Media and Varnishes Used in Art, Anal. Chim. Acta. 2000, 407(1-2), pp 261-274.

[4] A. Nevin, I. Osticioli, D. Anglos, A. Burnostck, S. Cather, E. Castellucci, Raman spectra of proteinaceous materials used in paintings: A multivariate analytical approach for classification and identification, Anal. Chem. 2007, 79, pp 6143-6151.

[5] E. Manzano, J. García-Atero, A. Dominguez-Vidal, M.J. Ayora-Cañada, L. Fermín Capitán-Vallvey, N. Navas, Discrimination of aged mixtures of lipidic paint binders by Raman spectroscopy and chemometrics, J. Raman Spectrosc. 2011, 43, pp 781-786.

[6] L. Brambilla , C. Riedo, C. Baraldi, A. Nevin, M. C. Gamberini, C. D'Andrea, O. Chiantore, S. Goidanich, L. Toniolo, Characterization of fresh and aged natural ingredients used in historical ointments by molecular spectroscopic techniques: IR, Raman and fluorescence, Anal. Bioanal. Chem. 2011**,** 401, pp 1827-1837

[7] J.B. Lambert, H.F. Shurvell, R.G. Cooks, Introduction to Organic Spectroscopy, Macmillan Publ., New York, 1987.

[8] J.S. Shenk, J.J. Workman, M.O. Westrhaus, "Application of NIR spectroscopy to agricultural products" in D.A. Burns and Ciurczak E.W. (eds), Handbook of Near-Infrared Spectroscopy Marcel Dekker Inc., New York,2001, pp 419-474

[9] D. Lin-Vien, N.B. Colthup, W.G. Fately, J.G. Grasselli, The handbook of infrared and raman characteristic frequencies of organic molecules, Academic Press, San Diego, 1991.

[10] H. Yang, J. Irudayaraj, Characterization of semi-solid fats and oils by fourier transform infrared photoacoustic spectroscopy, J. Am. Oil Chem. Soc. 2001, 78, pp 889-895.

[11] O. Zovi, L. Lecamp, C. Loutelier-Bourhis, C. M. Lange, C. Bunel, Stand reaction of linseed oil, J. Lipid Sci. Technol. 2011, 113, pp 616-626.

APPENDIX B: RAW and FIRST DERIVATIVE spectra referred to each pigment

In the following appendix, raw and corresponding first derivative FT-NIR and micro-Raman spectra referred to each pigment are reported along with the assignments for all main bands.

FT-NIR spectra are reported as first, whereas micro-Raman spectra as second.

Furthermore, raw FT-NIR spectra are shown without any pre-treatment, while micro-Raman spectra are shown after baseline subtraction. By contrast, all first derivative spectra are shown, after application of the pre-processing described in **Part I**.

AZURITE (A)

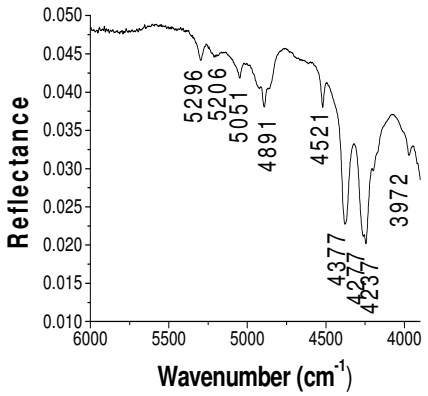
Reflectance
Wavenumber (cm-1)
5296
5206
5051
4891
4521
4377
4277
4237
3972

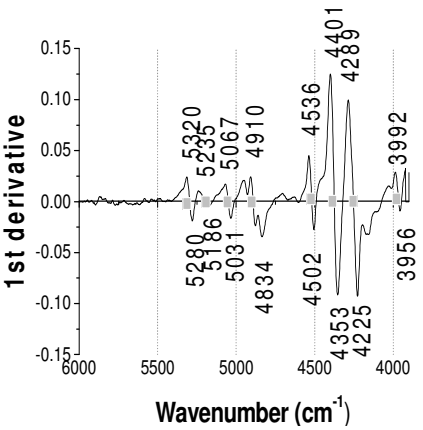
1st derivative
Wavenumber (cm-1)
5320
5235
5067
4910
4536
4401
4289
3992
5280
5186
5031
4834
4502
4353
4225
3956

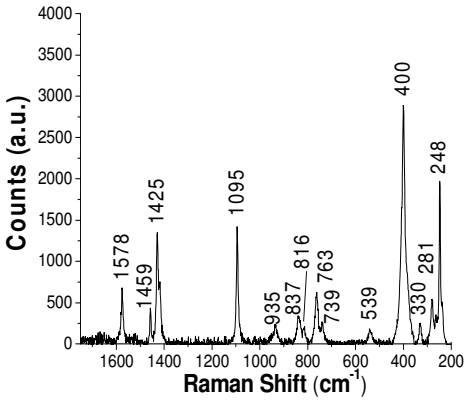
Counts (a.u.)
Raman Shift (cm-1)
1578
1459
1425
1095
935
837
816
763
739
539
400
330
281
248

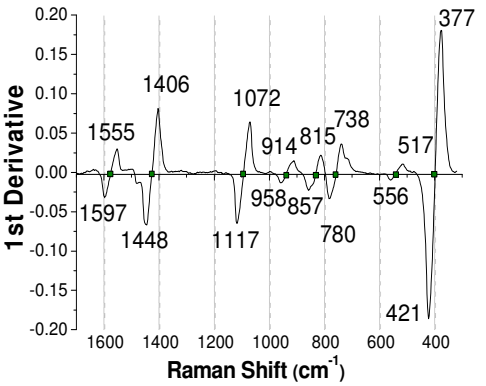
1st Derivative
Raman Shift (cm-1)
1555
1406
1597
1448
1117
1072
914
958
857
815
780
738
556
517
421
377

Frequency (cm^{-1})	Assignment	Ref.
5296	-	
5206	$\nu_1+3\nu_3$	[1]
5051	$2\nu_1+2\nu_3$	[1]
4891	-	
4521	$\nu_1+2\nu_3+\nu_4$ or $3\nu_1+2\nu_4$	[1]
4377	$\nu + \delta(OH)$	[3]
4237	$3\nu_3$	[1-3]
3972	$\nu_1+2\nu_3$	[2]

Frequency (cm^{-1})	Assignment	Ref.
1578	Antisymmetric stretching of carbonate ion	[4]
1469	Antisymmetric stretching of carbonate ion	[5]
1425	Antisymmetric stretching of carbonate ion	[5]
1095	Symmetric stretching of C-O bond in carbonate ion	[4-5]
935	-	
837	Bending *out of phase* of carbonate ion**	[4]
816	Bending *in phase* of carbonate ion	[4]
763	Bending out of plane carbonate ion	[5]
739	Bending out of plane of carbonate ion	[5]
539	-	
400	Vibration of Azurite lattice	[4]
330	-	
281	Vibration of Azurite lattice	[4]
248	Bending (O-Cu-OH)	[4]

AFGHANISTAN LAZURITE (AU)

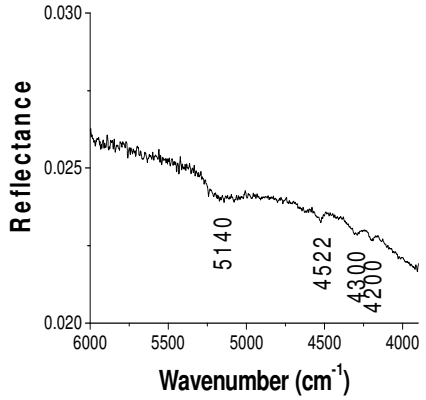

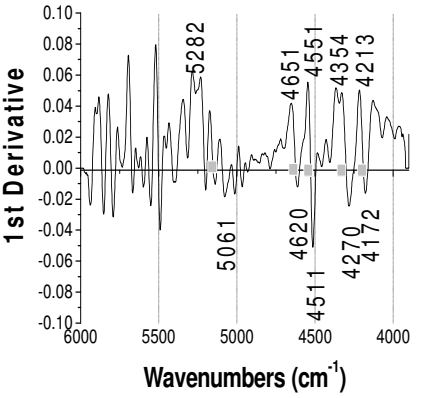

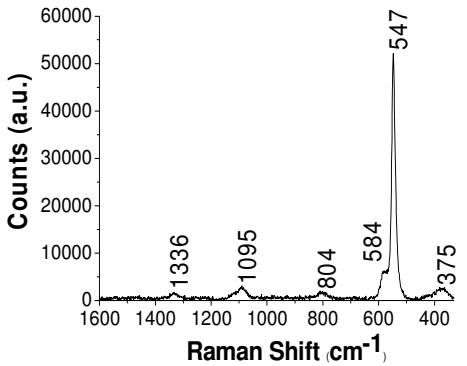

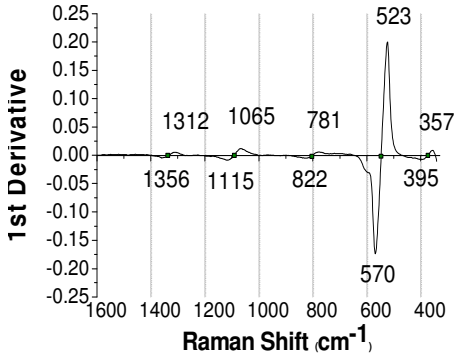

Frequency (cm^{-1})	Assignment	Ref.
5140	ν(OH)+δ(OH)	[2]
4522	1st overtone of ν(S-H), 2 ν(S-H), where ν(S-H) is 2344 cm^{-1}	[6]
4300	This doublet could correspond to the band at 4527 cm^{-1} observed in synthetic ultramarine. In fact, looking at the mid-infrared spectrum, this latter displays a ν(Si-O) absorption band at a higher frequency in comparison to Afghanistan lapis lazuli > Combination of ν(OH)+ν(Si-O)	[6]
4200		[6]

Frequency (cm^{-1})	Assignment	Ref.
1336	$\delta(S_3^-)+2\nu_a(S_3^-)$	[11]
1095	1st overtone symmetric stretching, $2\nu_s$ (S_3^-)	[8]
804	$\nu_s+\delta$ (δ is bending of ion S_3^-, ~262cm^{-1})	[9]
584	ν_a (S_3^-)	[10]
547	ν_s (S_3^-)	[8-9]
375	Pyrite (mineral often associated with lazurite)	[7]

SHYNTHETIC ULTRAMARINE (SU)

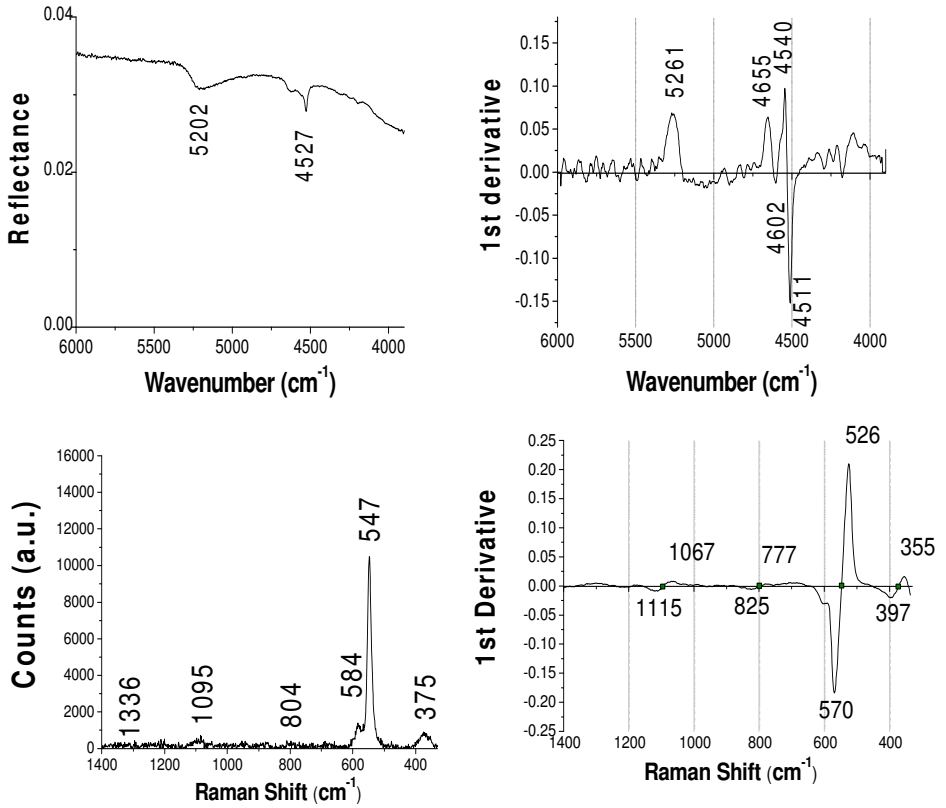

Frequency (cm^{-1})	Assignment	Ref.
5202	Combination of stretching and bending modes of absorbed water, ν(OH)+δ(OH)	[6, 12]
4527	Combination of ν(OH) and ν(Si-O)	[6]

Frequency (cm^{-1})	Assignment	Ref.
1336	$\delta(S_3^-)+2\nu_a(S_3^-)$	[11]
1095	1st overtone symmetric stretching, $2\nu_s$ (S_3^-)	[8]
804	$\nu_s+\delta$ (δ is bending of ion S_3^-, ~262cm^{-1})	[9]
584	ν_a (S_3^-)	[10]
547	ν_s (S_3^-)	[7-9]
375	Pyrite (mineral often associated with lazurite)	[7]

PHTHALOCYANINE BLUE (PB)

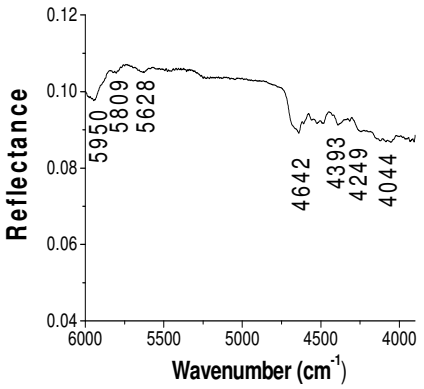

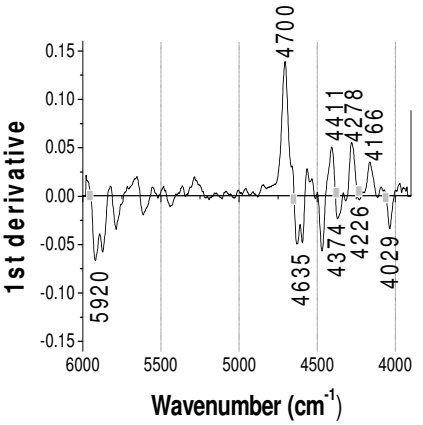

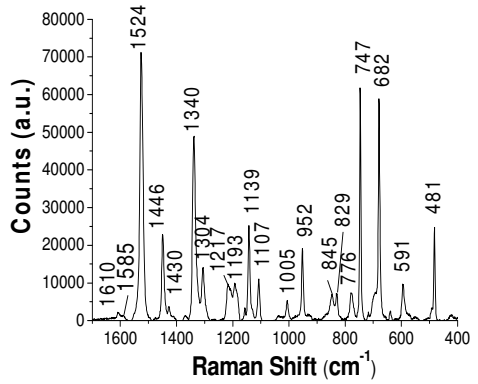

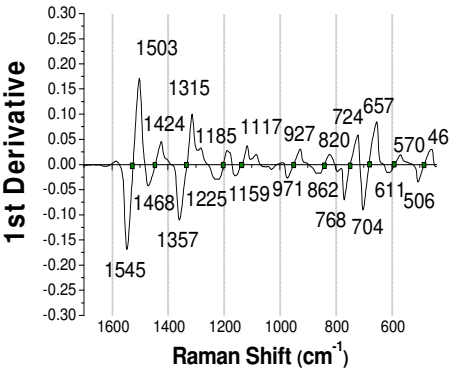

Frequency (cm^{-1})	Assignment	Ref.
5950	1st overtone ν(C-H) – aromatic CH	[2]
5809	ν(C-H) CH methyl	[2]
5628	ν(C-H) CH methyl	[2]
4642	ν(C-H) + ν(CC) aromatic CH/ 3ν(C=C)	[2]
4393	ν(C-H) +$\delta(CH_2)$	[2]
4249	ν(C-H) +δ(CH) aromatic CH	[2]
4044	3δ(CH) aromatic CH/ 2 ν(C-N-C)	[2]

Atomic numbering and fractional definition (ring a, a', b, b', c, c', d, d', e, e' , f, f') in CuPc:

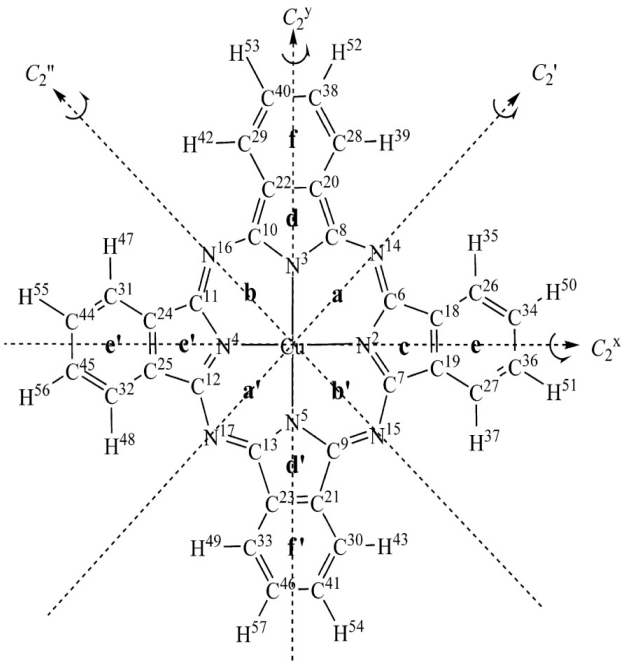

Frequency (cm^{-1})	Assignment	Ref.
1610	[[ρ_r (C^{18}–C^{19}, C^{34}–C^{36})$_S$, ρ_r (C^{24}–C^{25}, C^{44}–C^{45})$_S$]$_S$, [ρ_r (C^{20}–C^{22}, C^{38}–C^{40})$_S$, ρ_r (C^{21}–C^{23}, C^{41}–C^{46})$_S$]$_S$]$_{AS}$	[13]
1585	[ν_s (C^{18}–C^{19}, C^{34}–C^{36}, C^{24}–C^{25}, C^{44}–C^{45}), ν_s (C^{20}–C^{22}, C^{38}–C^{40}, C^{21}–C^{23}, C^{41}–C^{46})]$_S$	[13]
1524	[ν_s (C^6–N^{14}, C^7–N^{15}, C^{11}–N^{16}, C^{12}–N^{17}), ν_s (C^8–N^{14}, C^9–N^{15}, C^{10}–N^{16}, C^{13}–N^{17})]$_{AS}$, [δ_s ($C^6N^2C^7$, $C^{11}N^4C^{12}$), δ_s ($C^8N^3C^{10}$, $C^9N^5C^{13}$)]$_{AS}$	[13]
1446	[ν_s (C^6–N^{14}, C^8–N^{14}, C^{12}–N^{17}, C^{13}–N^{17}), ν_s (C^7–N^{15}, C^9–N^{15}, C^{10}–N^{16}, C^{11}–N^{16})]$_{AS}$, ρ_r [($C^6N^2C^7$, $C^{11}N^4C^{12}$)$_s$, ρ_r ($C^8N^3C^{10}$, $C^9N^5C^{13}$)$_s$]$_{AS}$, δs (N^2CuN^3, N^4CuN^5)	[13]
1430	[ν_s(C^{18}–C^{19}, C^{24}–C^{25}), ν_s (C^{20}–C^{22}, C^{21}–C^{23})]$_{AS}$, [[δ(C^{26}–H^{35}, C^{27}–H^{37}), δ(C^{31}–H^{47}, C^{32}–H^{48})]$_s$, [δ(C^{28}–H^{39}, C^{29}–H^{42}), δ(C^{30}–H^{43}, C^{33}–H^{49})]$_S$]$_{AS}$	[13]
1340	[ν_s (C^{18}–C^{19}, C^{24}–C^{25}, C^{38}–C^{40}, C^{41}–C^{46}), ν_s (C^{20}–C^{22}, C^{21}–C^{23}, C^{34}–C^{36}, C^{44}–C^{45})]$_{AS}$, η_{as} (C^{26}…C^{27}, C^{31}…C^{32}) su $C^x{}_2$, η_{as}(C^{28}…C^{29}, C^{30}…C^{31}) su $C^y{}_2$	[13]
1304	[ν_s (Cu–N^2, Cu–N^4), ν_s (Cu–N^3, Cu–N^5)]$_{AS}$, [ρ_r ($C^6N^{14}C^8$, $C^{10}N^{16}C^{11}$)s, ρ_r ($C^7N^{15}C^9$, $C^{12}N^{17}C^{13}$)s]$_S$, [ν_s (C^{18}–C^{19}, C^{24}–C^{25}), ν_s (C^{20}–C^{22}, C^{21}–C^{23})]$_{AS}$	[13]
1217	[[ρ_r (C^{26}–H^{35}, C^{27}–H^{37})s, ρ_r (C^{31}–H^{47}, C^{32}–H^{48})s]$_S$, [ρ_r (C^{28}–H^{39}, C^{29}–H^{42})s, ρ_r (C^{30}–H^{43}, C^{33}–H^{49}) s]$_S$]$_{AS}$, δs(N^2CuN^3, N^4CuN^5)	[13]
1193	-	-
1139	[[δ (C^{34}–H^{50}, C^{36}–H^{51}), δ (C^{44}–H^{55}, C^{45}–H^{56})]$_S$, [δ (C^{38}–H^{52}, C^{40}–H^{53}), δ (C^{41}–H^{54}, C^{46}–H^{57})]$_S$]$_{AS}$, [[δ (C^{26}–H^{35}, C^{27}–H^{37}), δ (C^{31}–H^{47}, C^{32}–H^{48})]$_S$, [δ (C^{28}–H^{39}, C^{29}–H^{42}), δ (C^{30}–H^{43}, C^{33}–H^{49})]$_S$]$_{AS}$	[13]
1107	[[ρ_r (C^{34}–H^{50}, C^{36}–H^{51})s, ρ_r (C^{45}–H^{56}, C^{44}–H^{55})s]$_S$, [ρ_r (C^{26}–H^{35}, C^{27}–H^{37})s, ρ_r (C^{32}–H^{48}, C^{31}–H^{47})s]$_S$]$_{AS}$, [[ρ_r (C^{38}–H^{52}, C^{40}–H^{53})s, ρ_r (C^{46}–H^{57}, C^{41}–H^{54})s]$_S$, [ρ_r (C^{28}–H^{39}, C^{29}–H^{42})s, ρ_r (C^{33}–H^{49}, C30–H43)s]$_S$]$_{AS}$, δs (N^2CuN^3, N^4CuN^5)	[13]
1005	-	-
952	δS (N^2CuN^3, N^4CuN^5), η_{as} (N^{14}, N^{17}) su C'_2, η_{as} (N^{15}, N^{16}) su C'_2, [ρ_r (c, c')s, ρ_r (d, d')s]$_{AS}$	[13]
845	-	-
829	ν_s (Cu–Ni), η_{as} (N^{14}, N^{17}) su C'_2 , η_{as} (N^{15}, N^{16}) su C''_2, [νs (c, c', d, d'), ν_s (e, e' , f, f')]$_S$	[13]
776	[ν_s (Cu–N^2, Cu–N^4), ν_s (Cu–N^3, Cu–N^5)]$_{AS}$, [ν_s (c, c', e, e'), ν_s (d, d', f, f')]$_{AS}$	[13]
747	[ν_s (Cu–N^2, Cu–N^4), ν_s(Cu–N^3, Cu–N^5)]$_{AS}$, [δ_s ($C^6N^2C^7$, $C^{11}N^4C^{12}$), δ_s ($C^8N^3C^{10}$, $C^9N^5C^{13}$)]$_{AS}$	[13]
682	η_{as}(N^{14}, N^{17}) su C'_2 , η_{as}(N^{15}, N^{16}) su C''_2 , η_{as}(C^{18}–C^{19}, C^{24}–C^{25}) su $C^x{}_2$, η_{as}(C^{20}–C^{22}, C^{21}–C^{23}) su $C^y{}_2$	[13]
591	ρ_r ($C^6N^2C^7$, $C^{11}N^4C^{12}$, $C^8N^3C^{10}$, $C^9N^5C^{13}$)s, [ρ_r [(C^{18}–C^{19}, C^{34}–C^{36})s, ρ_r (C^{24}–C^{25}, C^{44}–C^{45})s]$_S$, [ρ_r (C^{20}–C^{22}, C^{38}–C^{40})s, ρ_r (C^{21}–C^{23}, C^{41}–C^{46})s]$_S$]$_S$	[13]
481	[ρ_r (e, e')s, ρ_r (f, f')s]$_{AS}$, δs (N^2CuN^3, N^4CuN^5)	[13]

LEAD WHITE (LW)

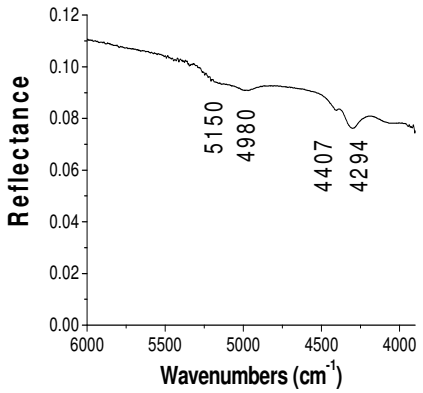

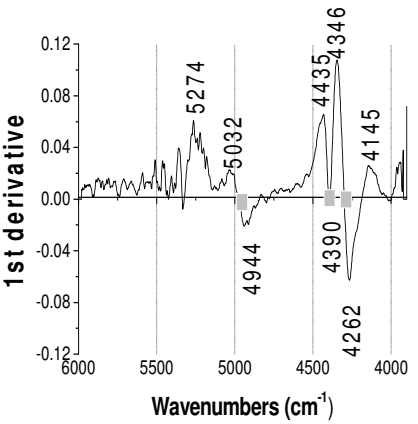

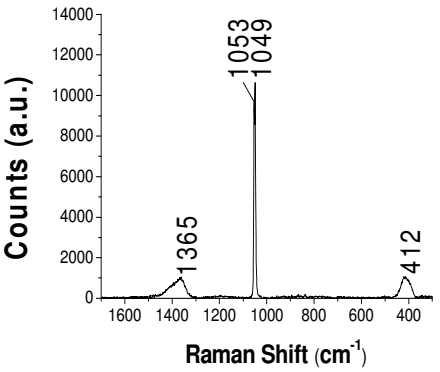

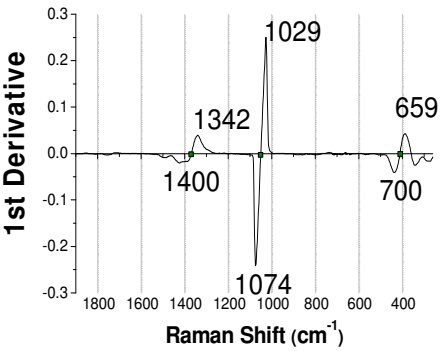

Frequency (cm^{-1})	Assignment	Ref.
5150	Combination bands of water (OH^-)	[2, 14]
4980	ν(OH)+ν(CO)	[15]
4407	Probably due to higher overtones of stretching or combinations of stretching/bending of the carbonate ion	[14]
4294	ν(OH)+deformation modes (Pb-OH)/$3\nu_3$ (CO_3^{2-}) and ν + δ(OH)	[15]

Frequency (cm^{-1})	Assignment	Ref.
1365	Stretching carbonate ion (Hydrocerussite)	[16]
1053	Symmetric stretching Carbonate ion (Hydrocerussite)	[16]
1049	Symmetric stretching Carbonate ion (Hydrocerussite)	[16]
412	Vibrations of PbO (Hydrocerussite)	[16]

ZINC WHITE (ZW)

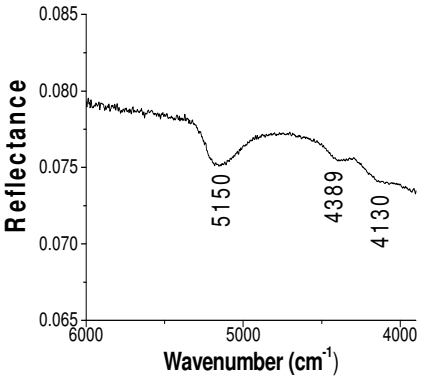

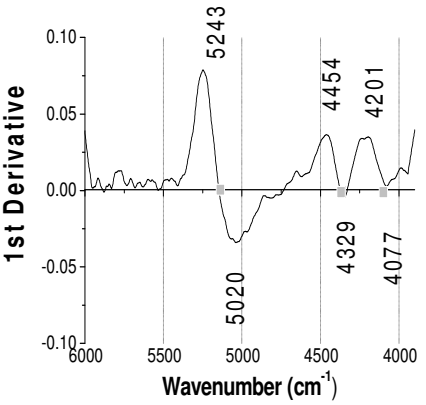

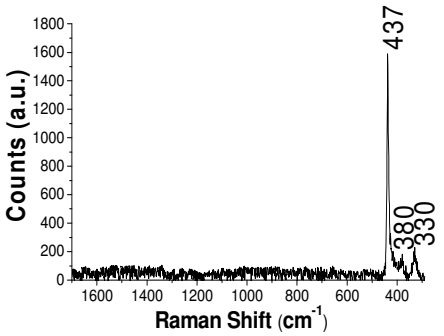

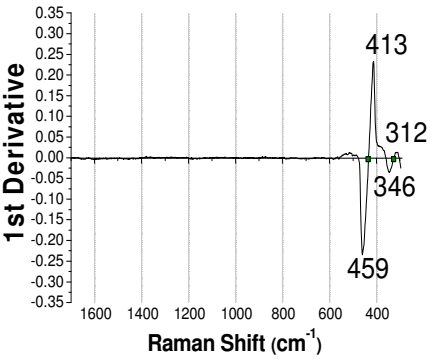

Frequency (cm^{-1})	Assignment	Ref.
5150	ν(OH)+δ(OH)	[2]
4389	Impurities/ ν(OH) with ν(Si-O)	[17]
4130	Impurities/ ν(OH) with ν(Si-O)	[17]

Frequency (cm^{-1})	Assignment	Ref.
437	Vibration mode of phonon in the ZnO crystal (wurtzite) with symmetry E_2	[18-19]
383	E1 transverse optical phonon	[18-19]
330	Symmetric stretching Zn-O	[18-19]

References

[1] S.J. Gaffey, Spectral reflectance of carbonate minerals in the visible and near infrared (0.35–2.55 microns): calcite, aragonite, and dolomite, Am. Mineral. 1986, 71, pp 151-162.

[2] J. Workman, L. Weyer Practical Guide to Interpretative Near-Infrared Spectroscopy, CRC Press- Taylor and Francis, Boca Raton, 2007.

[3] C. Miliani, F. Rosi, A. Doveri, B.G. Brunetti, Reflection infrared spectroscopy for the non-invasive in situ study of artists' pigments, Appl. Phys. A 2012, 106, pp 295-307.

[4] R.L Frost., W.N. Martens, L. Rintoul, E. Mahmutagic, J.T. Kloprogge, Raman spectroscopic study of azurite and malachite at 298 and 77 K, J. Raman. Spectrosc. 2002, 33, pp 252-259.

[5] M.J. Genge, A.P. Jones, G.D. Price, An infrared and Raman study of carbonate glasses: implications for the structure of carbonatite magmas, Geochim. Cosmochim. Ac. 1995, 59, pp 927-937.

[6] M. Bacci, C. Cucci, E. Del Federico, A. Ienco, A. Jerschow, J.M. Newman, M. Picollo, An integrated spectroscopic approach for the identification of what distinguishes Afghan lapis lazuli from others, Vib. Spectrosc. 2009, 49, pp 80-83.

[7] M. Bicchieri, M. Nardone, P.A. Russo, A. Sodo, M. Corsi, G. Cristoforetti, V. Palleschi, A. Salvetti, E. Tognoni, Characterization of azurite and lazurite based pigments by laser induced breakdown spectroscopy and micro-Raman spectroscopy, Spectrochim. Acta B 2001, 56, pp 915-922.

[8] I. Osticioli, N.F.C. Mendesa, A. Nevin, F.P. Gil, M. Becucci, E. Castellucci, Analysis of natural and artificial ultramarine blue pigments using laser induced breakdown and pulsed Raman spectroscopy, statistical analysis and light microscopy, Spectrochim. Acta A 2009, 73, pp 523-531.

[9] R.J.H. Clark, M.L. Curri, C.L. Laganara, The Identification of Lapis Lazuli on Medieval Pottery Fragments from the South of Italy, Spectrochim. Acta A 1997, 53, pp 597-603.

[10] B. Ledé, A. Demortier, N. Gobeltz-Hautecœur, J.-P. Lelieur, E. Picquenard, C. Duhayon, Observation of the ν3 Raman band of S_3^- inserted into sodalite cages, J. Raman Spectrosc. 2007, 38, pp 1461-1468

[11] P. Colomban, Lapis lazuli as unexpected blue pigment in Iranian Lâjvardina ceramics, J. Raman Spectrosc. 2003, 34, pp 420-423.

[12] J. Madejova, P. Komadel, Baseline studies of The Clay Minerals Society Source Clays: Infrared methods, Clay Clay miner. 2001, 49, pp 410-422.

[13] Li Daocong, P. Zhenghe, D. Lizhi, S. Yufang, Z. Yunhong, Theoretical studies on molecular structure and vibrational spectra of copper phthalocyanine, Vib. Spectrosc. 2005, 39, pp 191-199.

[14] M. Bacci, D. Magrini, M. Picollo, M. Vervat, A study of the blue colors used by Telemaco Signorini, 1835–1901, J. Cult. Herit. 2009, 10, pp 275-280.

[15] M. Vagnini, C. Miliani, L. Cartechini, P. Rocchi, B.G. Brunetti, A. Sgamellotti, FT-NIR spectroscopy for non-invasive identification of natural polymers and resins in easel paintings, Anal. Bioanal. Chem. 2009, 395, pp 2107-2118.

[16] R.J. Gettens, H. Kühn, W.T. Chase, Lead White, in: A. Roy (Ed.), Artists pigments: a handbook of their history and characteristics, vol. 2, Oxford University Press, New York, 1993, pp. 67-81.

[17] F. Casadio, V. Rose, High-resolution fluorescence mapping of impurities in historical zinc oxide pigments: hard x-ray nanoprobe applications to the paints of Pablo Picasso, Appl. Phys. A 2013, 111, pp 1-8.

[18] I.M. Bell, R.J.H. Clark, P.J. Gibbs, Raman spectroscopic library of natural and synthetic pigments (pre- ≈ 1850 A.D.), Spectrochim. Acta A, 1997, 53, pp 2159-2179.

[19] M.F. Cerqueira, A.G., Rolo T. Viseu, J. Ayres de Campos, T. De Lacerda-Arôso, F. Oliveira, M.I. Vasilevskiy, E.Alves, Raman study of doped-ZnO thin films grown by rf sputtering, Phys. Status Solidi C 2010, 7(9), pp 2290-2293.

APPENDIX C: Combined first derivative FT-NIR and micro-Raman spectra referred to each oil-paint model

In the following appendix, the combined first derivative FT-NIR and micro-Raman spectra referred to each oil-paint model are reported. The main contributions related to pigments and binders are highlighted by means of different colours/patterns.

Linseed oil-paint models combined first derivative FT-NIR and micro-Raman spectra.

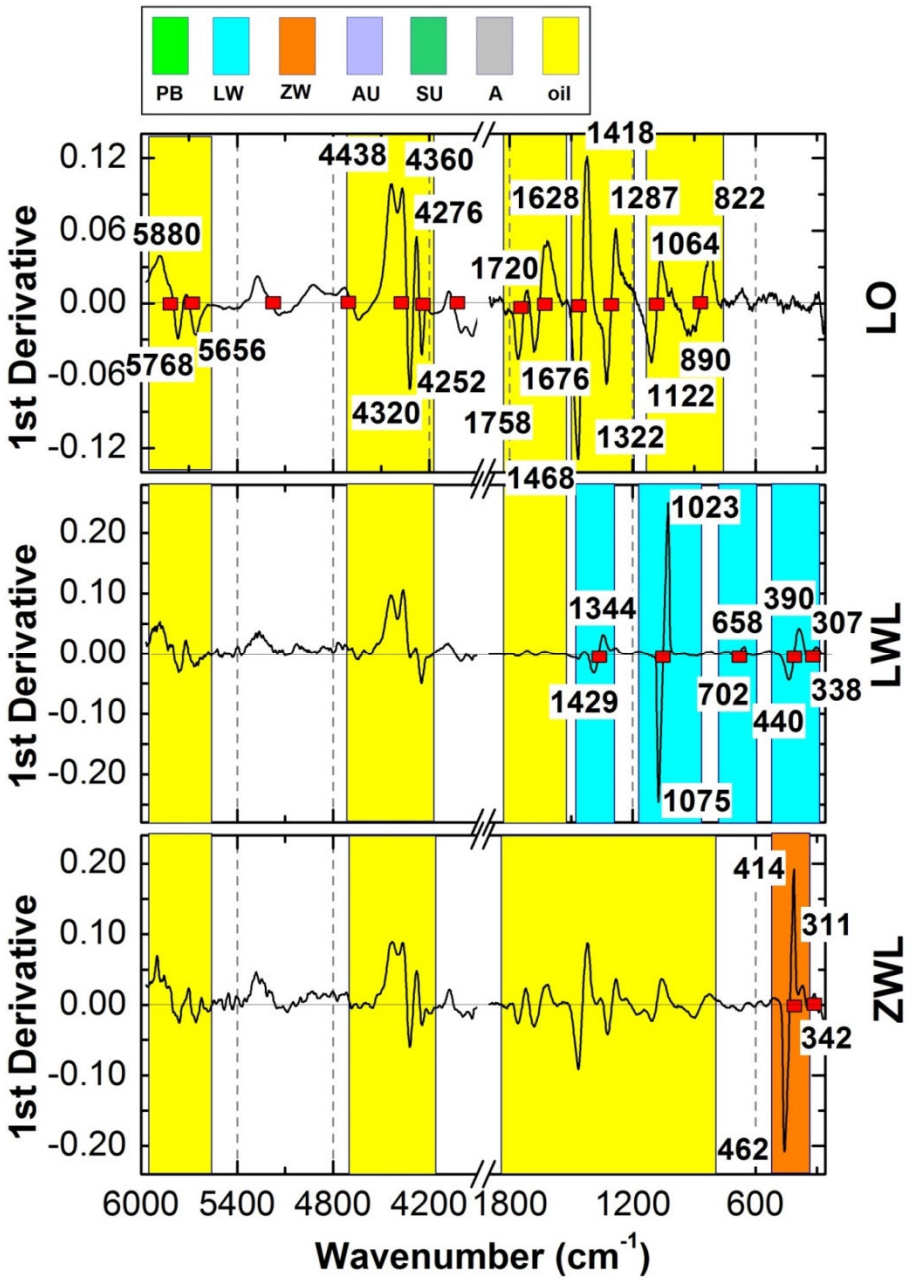

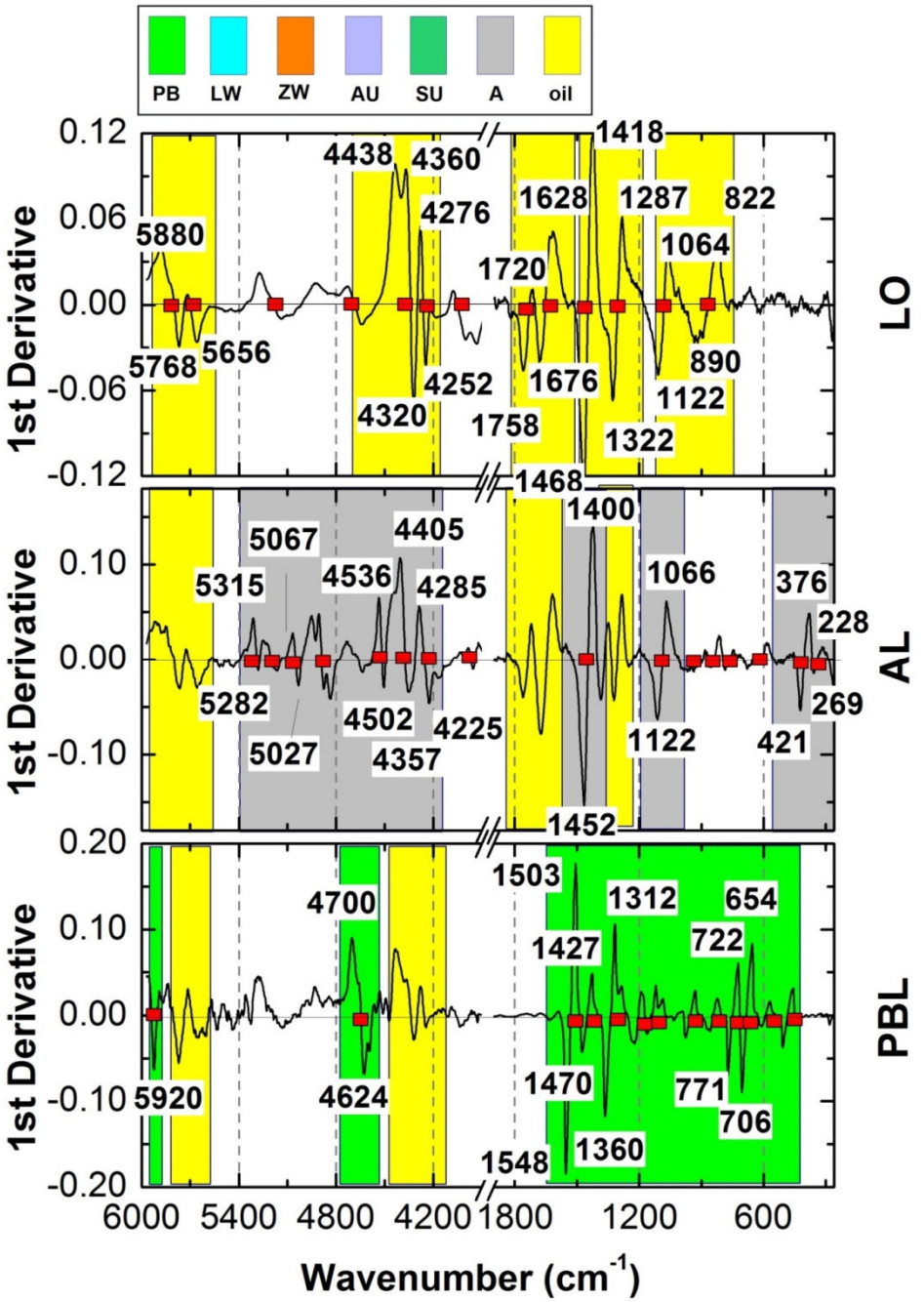
PB
LW
ZW
AU
SU
A
oil
1st Derivative
0.12
0.06
0.00
-0.06
-0.12
5880
5768
5656
4438
4360
4276
4320
4252
1758
1418
1628
1287
822
1064
1720
1676
1322
890
1122
LO
1468
1400
5067
4405
5315
4536
4285
1066
376
228
5282
4502
4225
5027
4357
269
1122
421
1452
AL
0.20
0.10
0.00
-0.10
-0.20
1503
4700
1312
654
1427
722
5920
4624
1470
771
706
1360
1548
PBL
6000
5400
4800
4200
1800
1200
600
Wavenumber (cm-1)

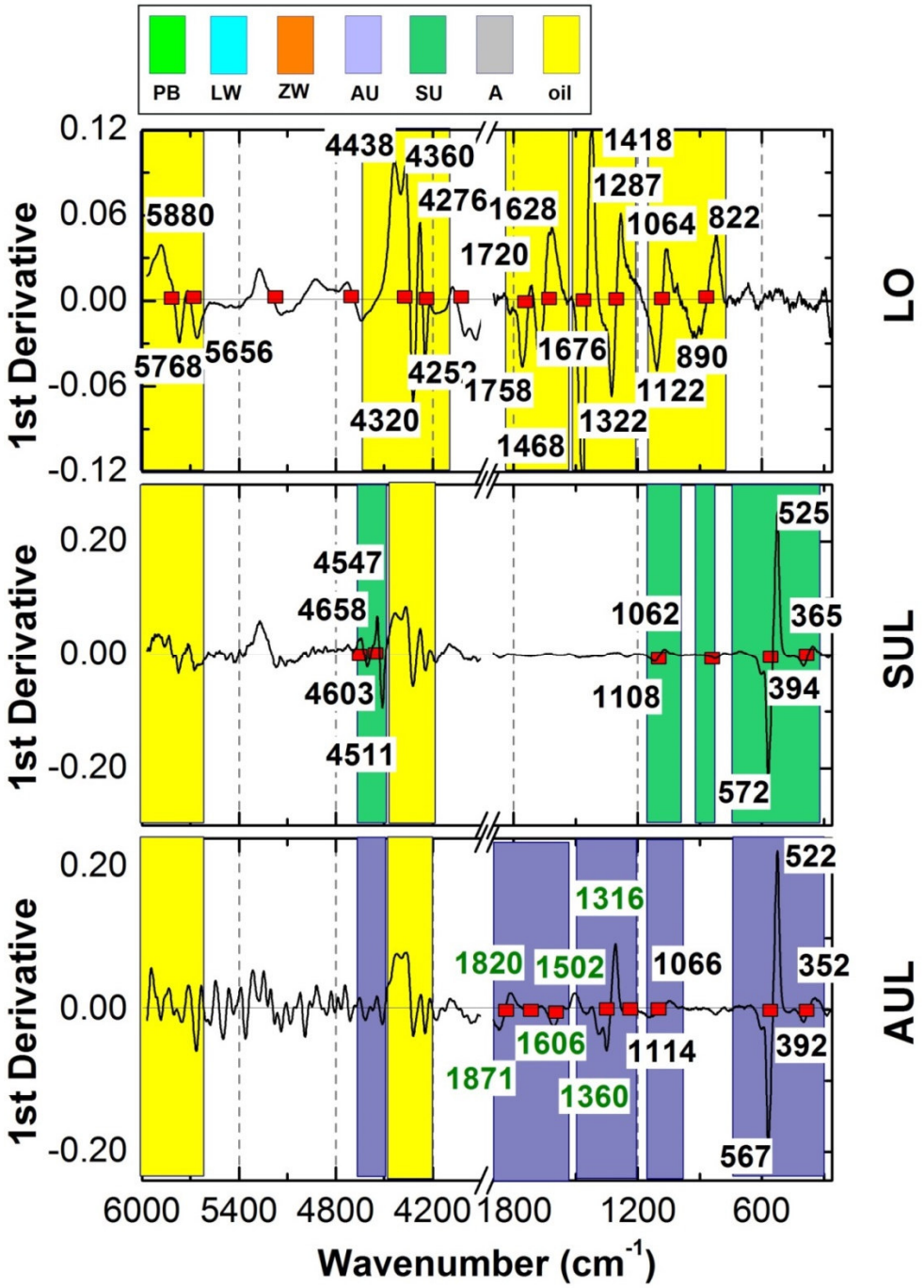
PB
LW
ZW
AU
SU
A
oil
1st Derivative
0.12
0.06
0.00
-0.06
-0.12
5880
5768
5656
4438
4360
4276
4320
4252
1628
1720
1758
1468
1418
1287
1064
822
1676
1322
1122
890
LO
0.20
0.00
-0.20
4547
4658
4603
4511
1062
1108
525
365
394
572
SUL
0.20
0.00
-0.20
1316
1820
1502
1606
1871
1360
1066
1114
522
352
392
567
AUL
6000
5400
4800
4200
1800
1200
600
Wavenumber (cm-1)

Poppy-seed oil-paint models combined first derivative FT-NIR and micro-Raman spectra.

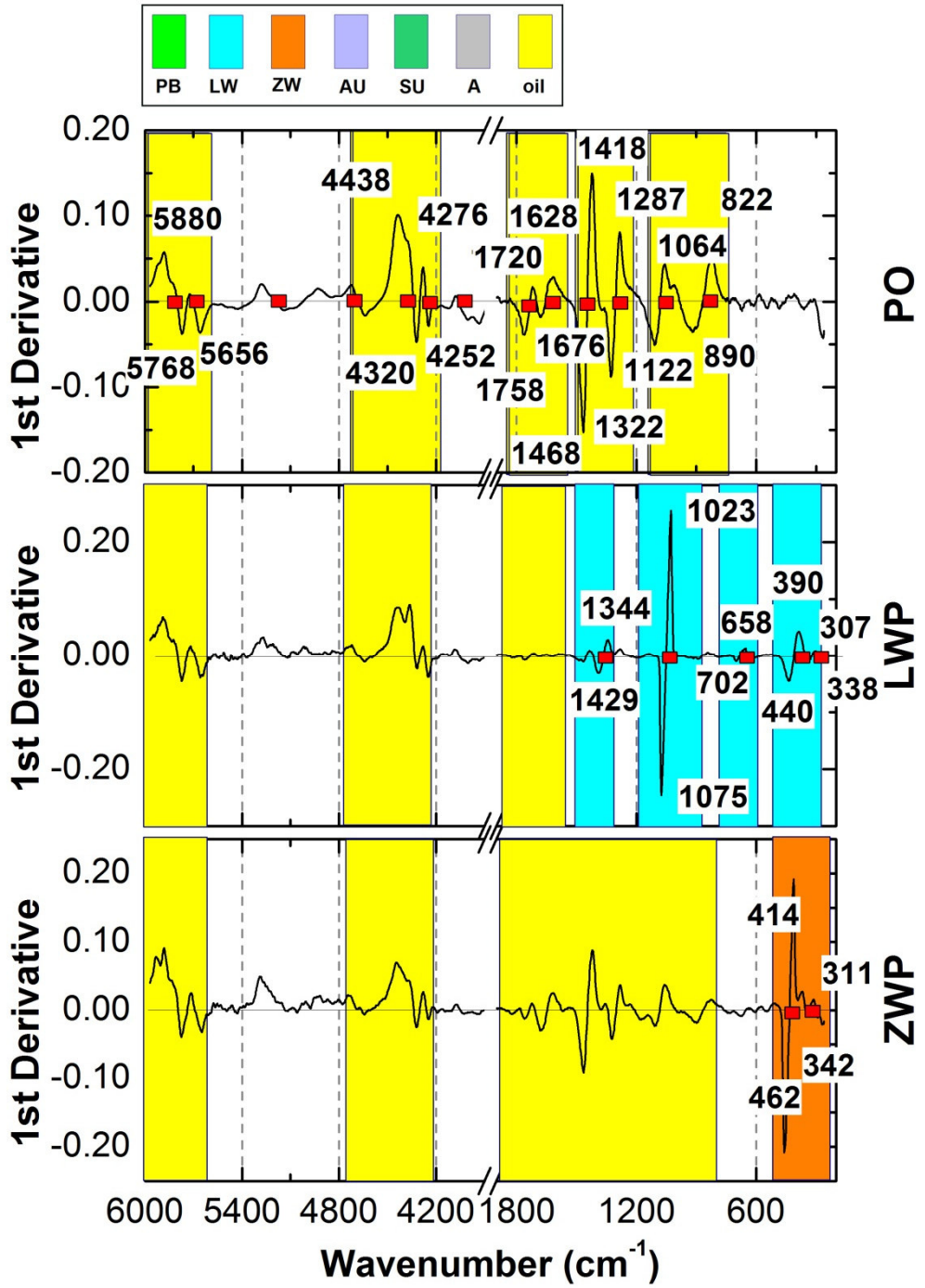

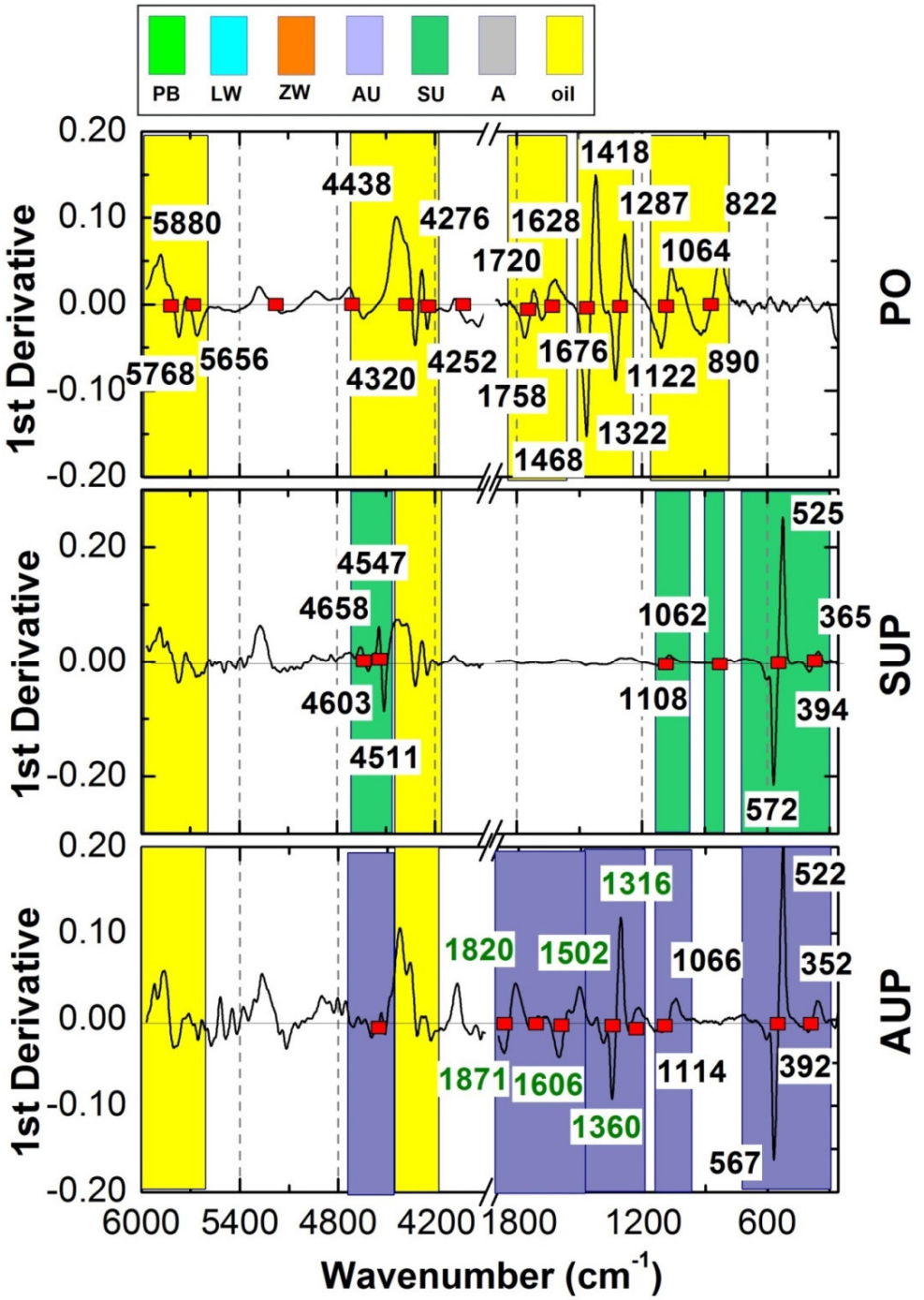
PB
LW
ZW
AU
SU
A
oil
1st Derivative
0.20
0.10
0.00
-0.10
-0.20
5880
4438
4276
1628
1418
1287
822
1064
1720
5768
5656
4320
4252
1758
1676
1122
890
1322
1468
PO
4547
4658
4603
4511
1062
525
365
1108
394
572
SUP
1316
522
1820
1502
1066
352
1871
1606
1360
1114
392
567
AUP
6000
5400
4800
4200
1800
1200
600
Wavenumber (cm-1)

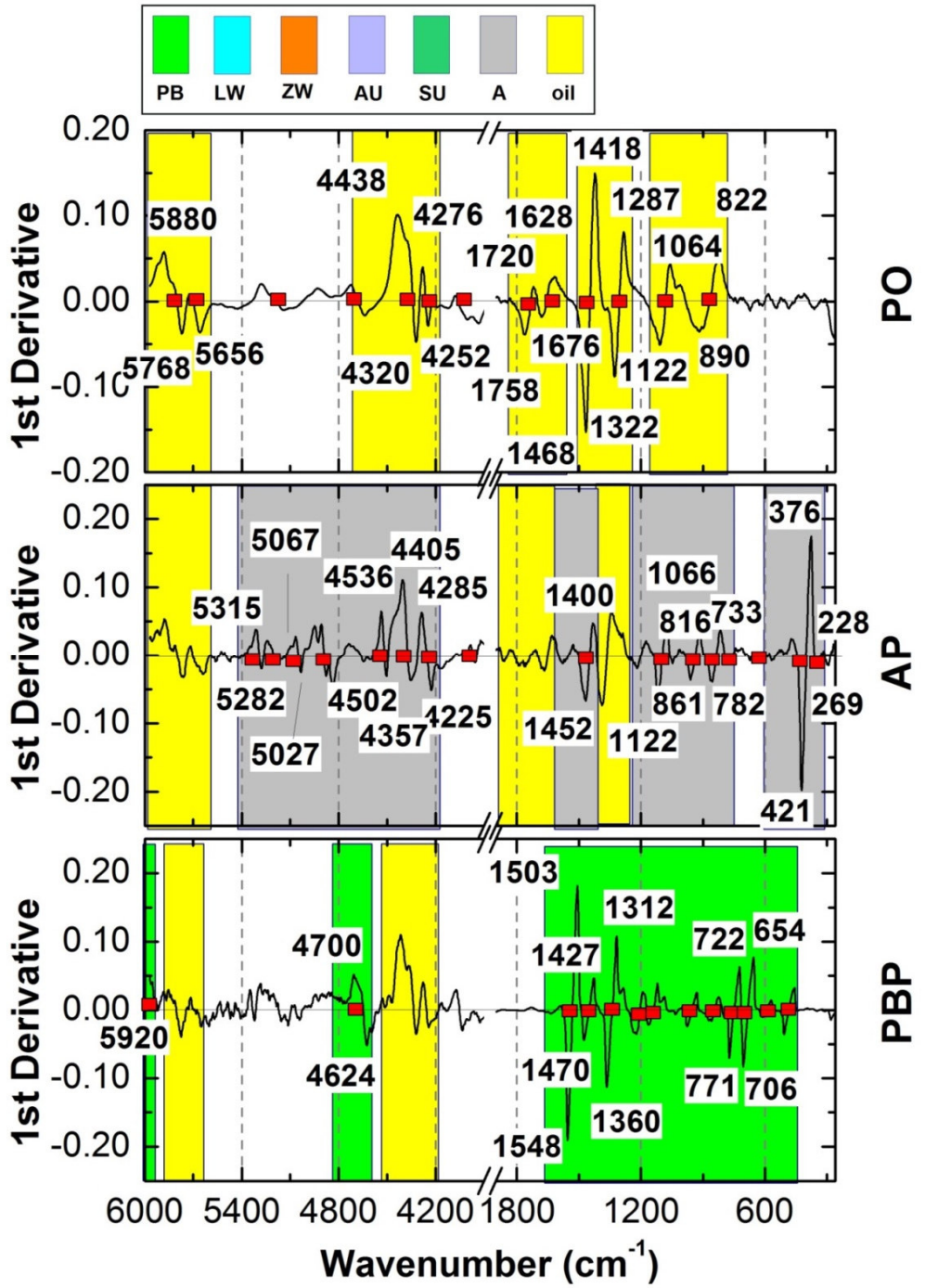
PB
LW
ZW
AU
SU
A
oil
1st Derivative
0.20
0.10
0.00
-0.10
-0.20
5880
4438
4276
1628
1418
1287
822
1720
1064
5768
5656
4320
4252
1758
1676
1122
890
1322
1468
PO
5067
4405
4536
4285
5315
1400
1066
376
816
733
228
5282
4502
4225
4357
5027
1452
1122
861
782
269
421
AP
1503
1312
4700
1427
722
654
5920
4624
1470
771
706
1360
1548
PBP
6000
5400
4800
4200
1800
1200
600
Wavenumber (cm-1)

APPENDIX D: RAW and FIRST DERIVATIVE spectra referred to the aged neat linseed oil and white-oil mixtures

In the following appendix, raw and corresponding first derivative FT-NIR and micro-Raman spectra referred to neat linseed oil and two white-oil mixtures prepared with lead and zinc white pigments are reported.

FT-NIR spectra are reported as first, whereas micro-Raman spectra as second.

Furthermore, raw FT-NIR spectra are shown without any pre-treatment, while micro-Raman spectra are shown after baseline subtraction. By contrast, all first derivative spectra are shown, after application of the pre-processing described in **Part I.**

Neat linseed oil has been analysed after 3, 9 and 24 months of natural ageing, whereas the lead white- and zinc white-oil based models after 9 and 24 months.

The FT-NIR and Raman spectra of two 10-year old mock-ups prepared with lead and zinc white pigments mixed with linseed oil are also reported. For these last samples, the ground has been prepared with gypsum, calcite, rutile and linseed oil.

NEAT LINSEED OIL

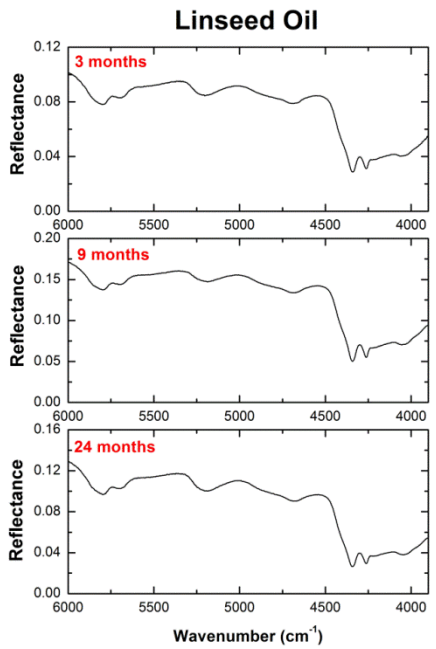

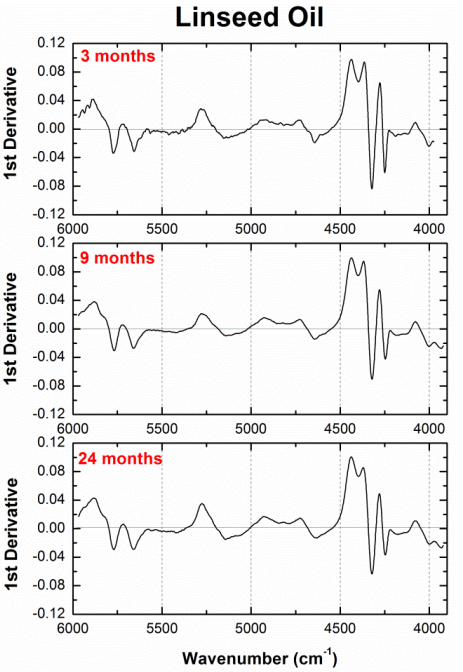

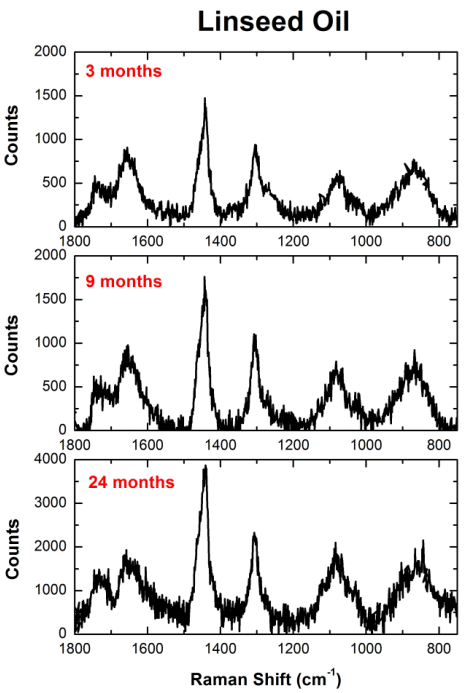

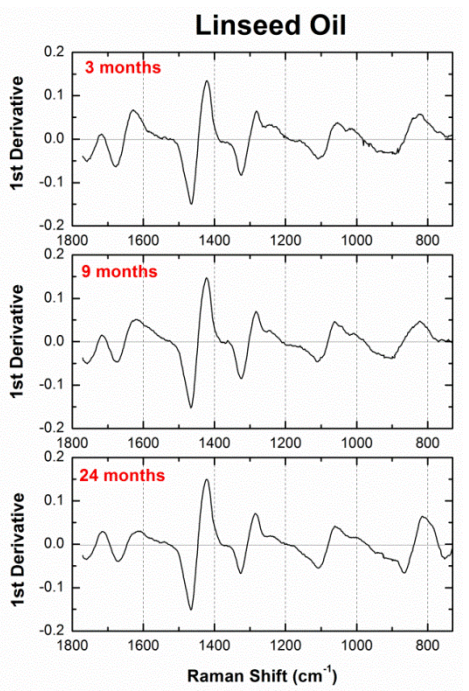

LEAD WHITE WITH LINSEED OIL (LWL)

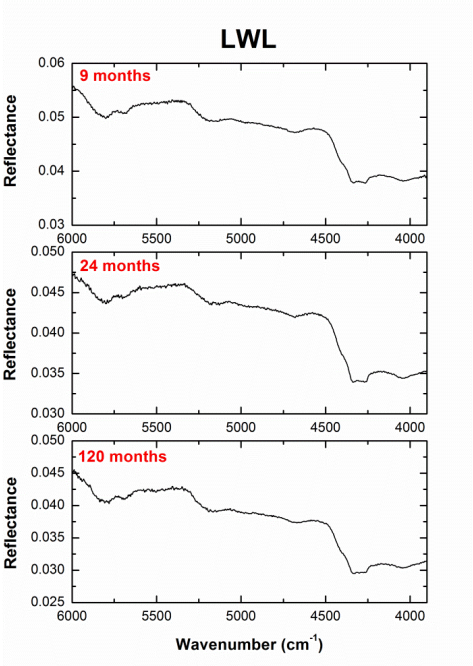

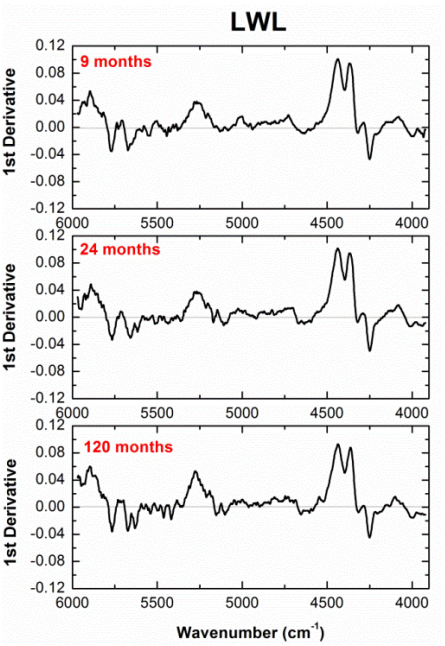

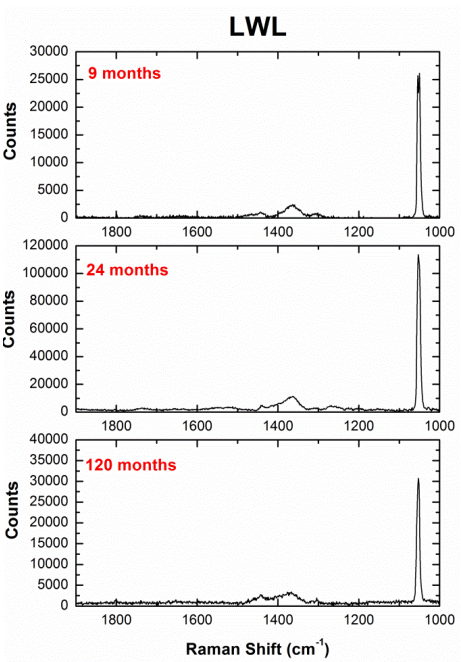

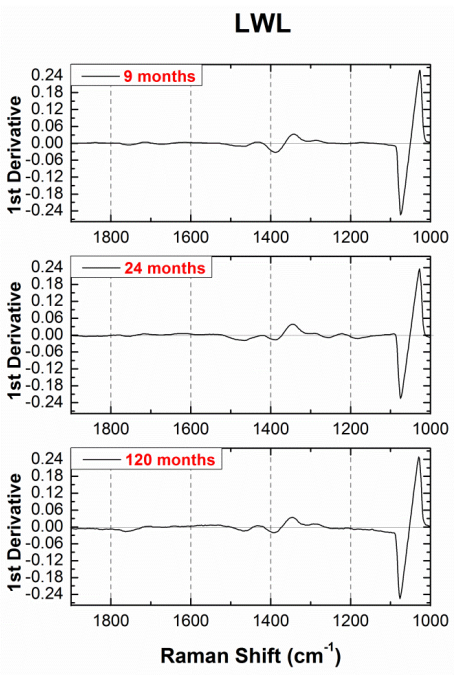

ZINC WHITE WITH LINSEED OIL (ZWL)

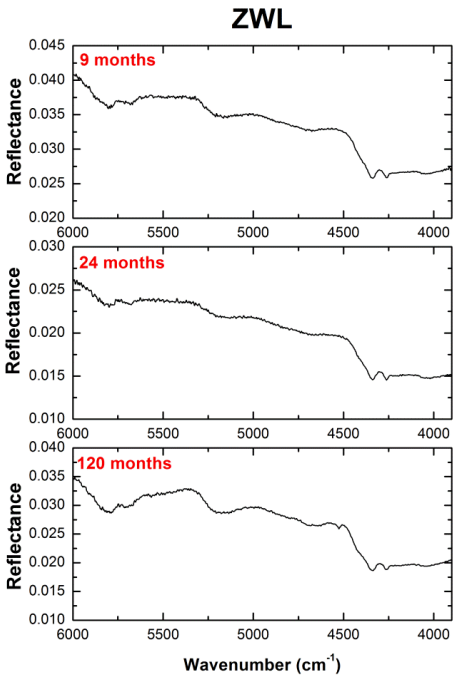

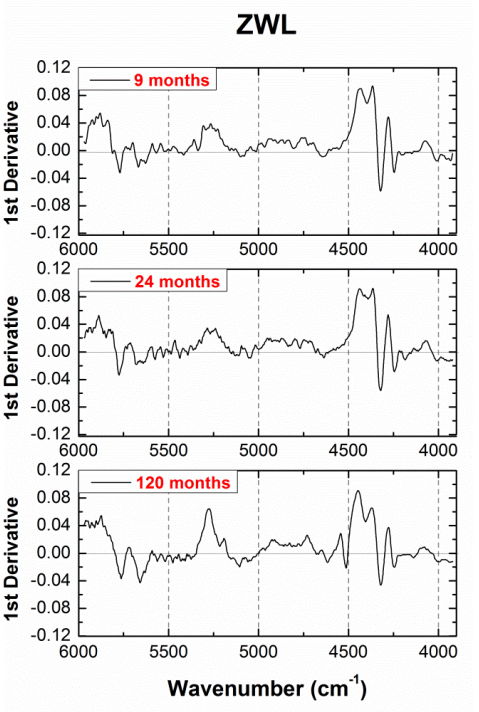

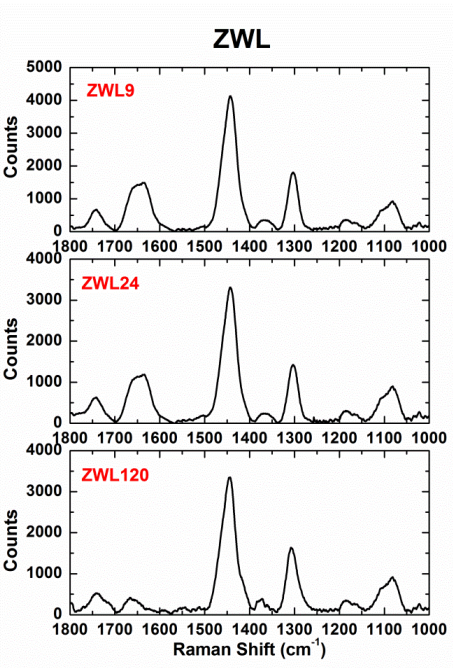

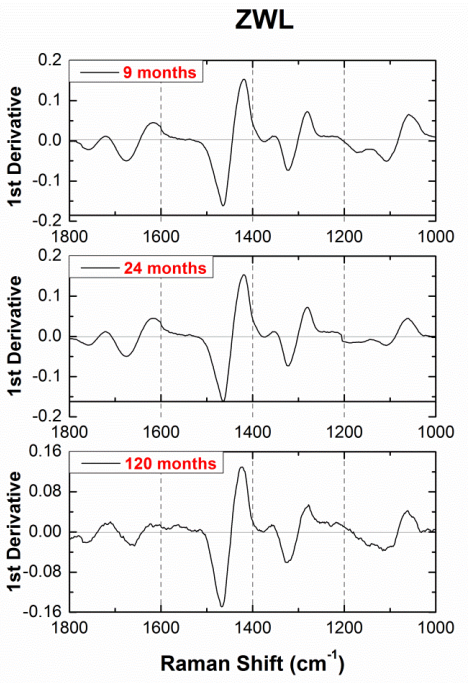

APPENDIX E: 2D-Fluorescence (EE) maps of neat binders

In this appendix, EE maps (Excitation-Emission maps) acquired on each neat binder are reported along with the corresponding emission spectra extracted from each of them. Moreover, **tentative assignments** for the main emission maxima/bands are reported, according to literature references (only if it is possible).

Scans were recorded with the following excitation-emission spectral ranges:

- Proteinaceous binders (Ex: 250-530 nm; Em: 290-800 nm)
- Lipidic binders (Ex: 250-550 nm; Em: 290-750 nm)
- Polysaccharide binders (Ex: 250-550 nm; Em: 290-750 nm)

Regarding proteinaceous binders, for the extraction of the single emission spectra, the following excitation wavelengths were selected: 270, 290, 310, 350 and 390 nm (EW and C); 270, 310, 350 (RG, SG and FG) and of 310, 390, 430 and 470 nm (EY and WE). As regards drying oils, for the extraction of the single emission spectra, the following excitation wavelengths were selected: 350, 390, 430 and 470 nm. Regarding polysaccharides binders, for the extraction of the single emission spectra, the following excitation wavelengths were selected: 270, 310, 350 and 430 nm.

For each EE map, all the emission bands/ranges with corresponding excitation intervals, are also reported. For those binding media that show more emission bands, the strongest one is reported as first and successively the less intense.

All these binding media were analysed after an ageing of 18 months. So, their ageing process is already started.

PROTEINACEOUS BINDING MEDIA

CASEIN (C) [1-2]

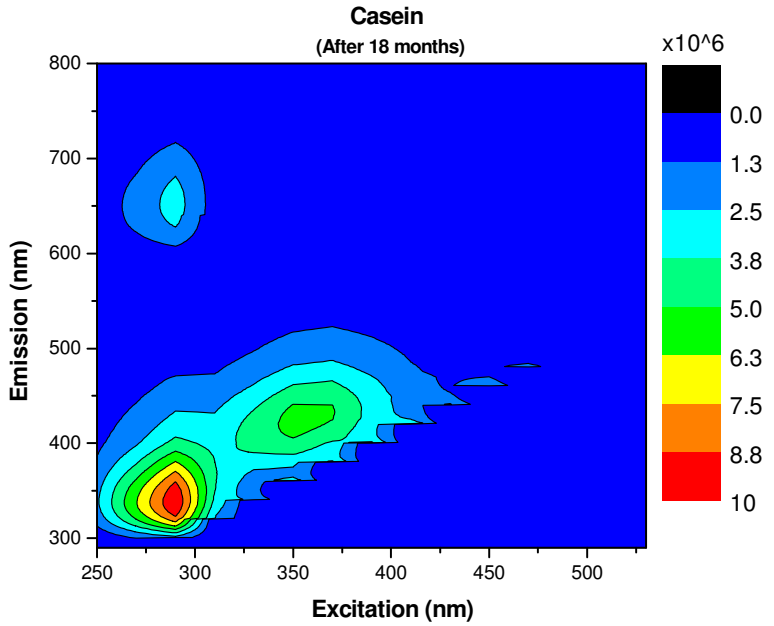

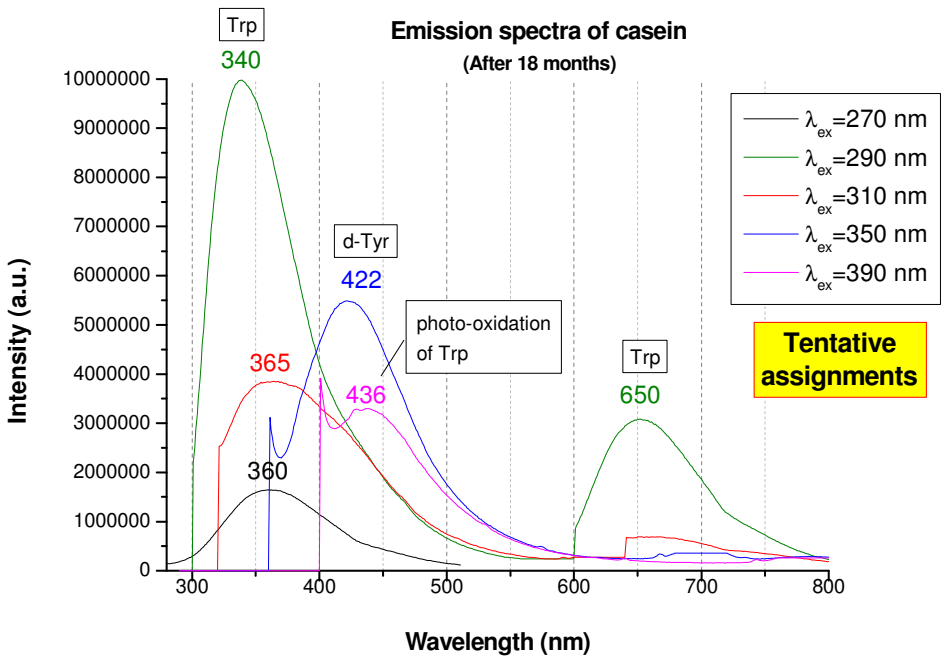

Excitation (nm)	Emission (nm)
284-292 (288)	325-355 (340)
343-370 (355)	406-440 (425)
282-295 (288)	630-677 (652)

RABBIT SKIN GLUE (RG) [1-2]

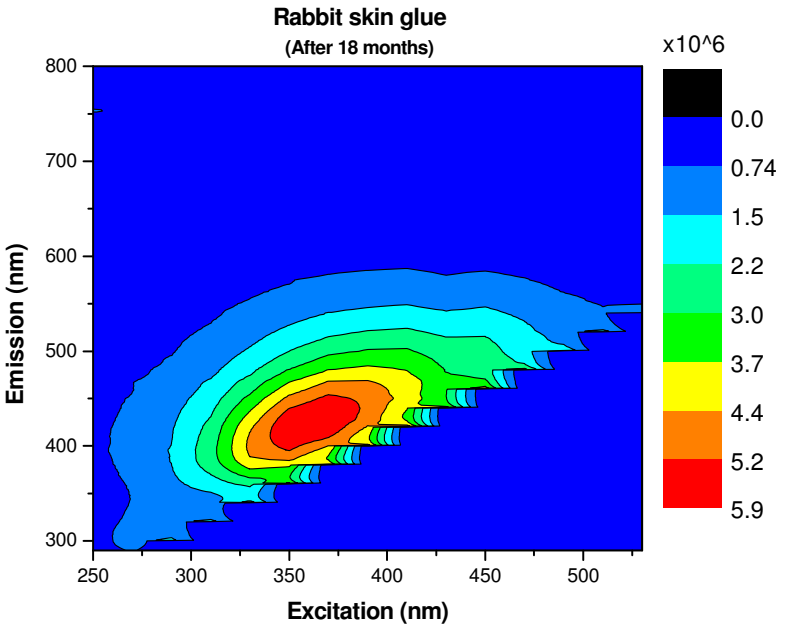

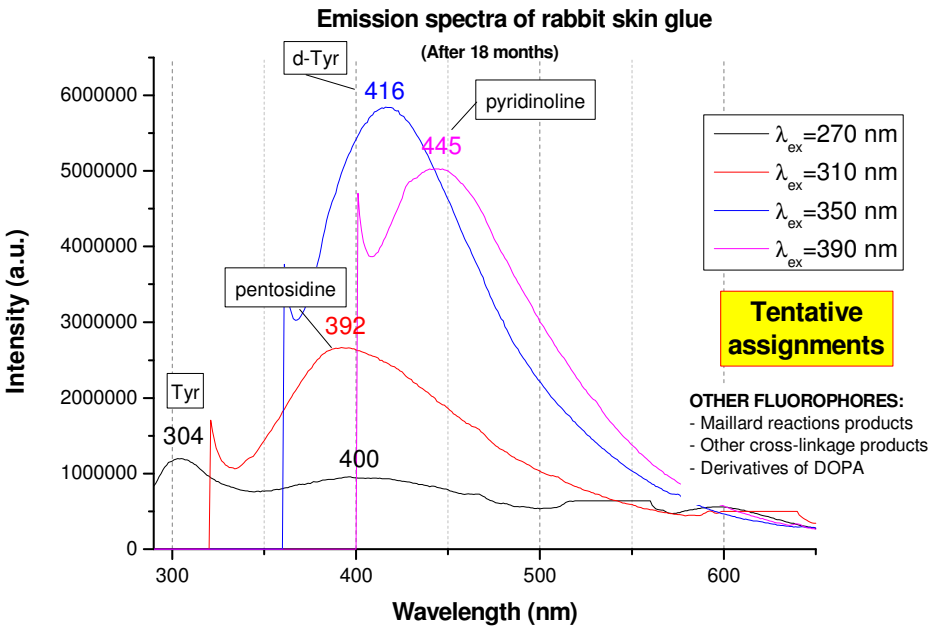

Excitation (nm)	Emission (nm)
340-385	394-455
~268	~307

STRONG GLUE (SG) [1-2]

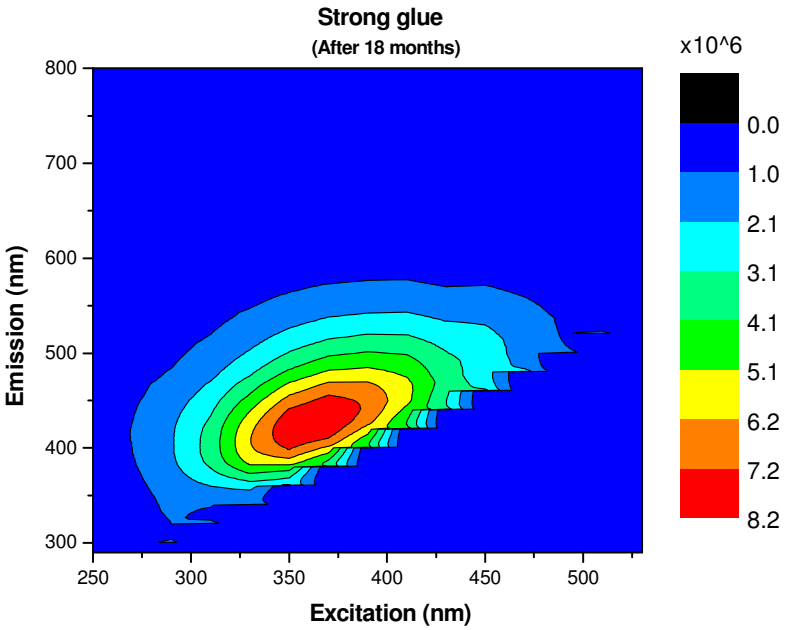

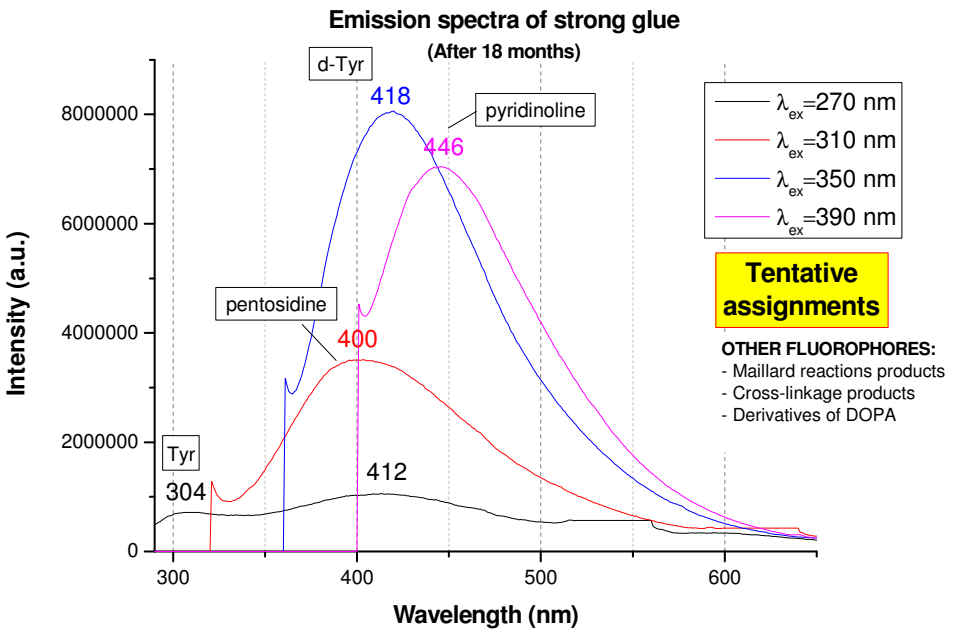

Excitation (nm)	Emission (nm)
341-442	400-457

FISH GLUE (FG) [1-2]

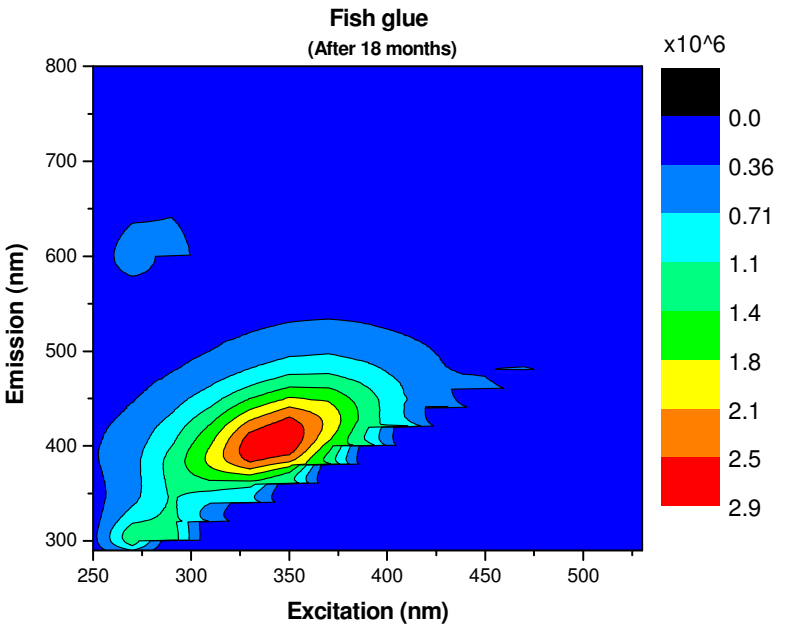

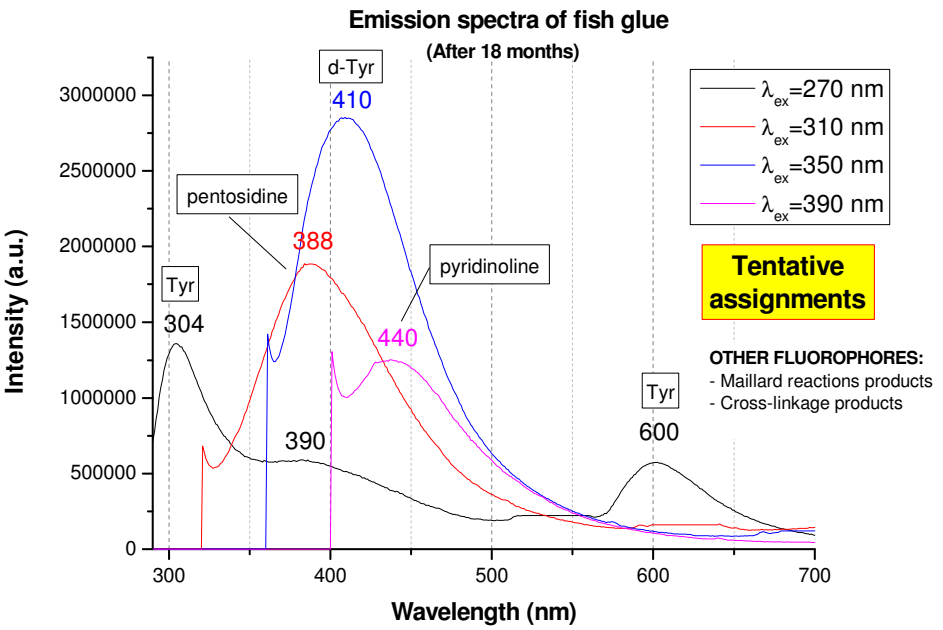

Excitation (nm)	Emission (nm)
324-356 (340)	385-431 (407)
270	307
~270	~602

EGG WHITE (EW) [1-2]

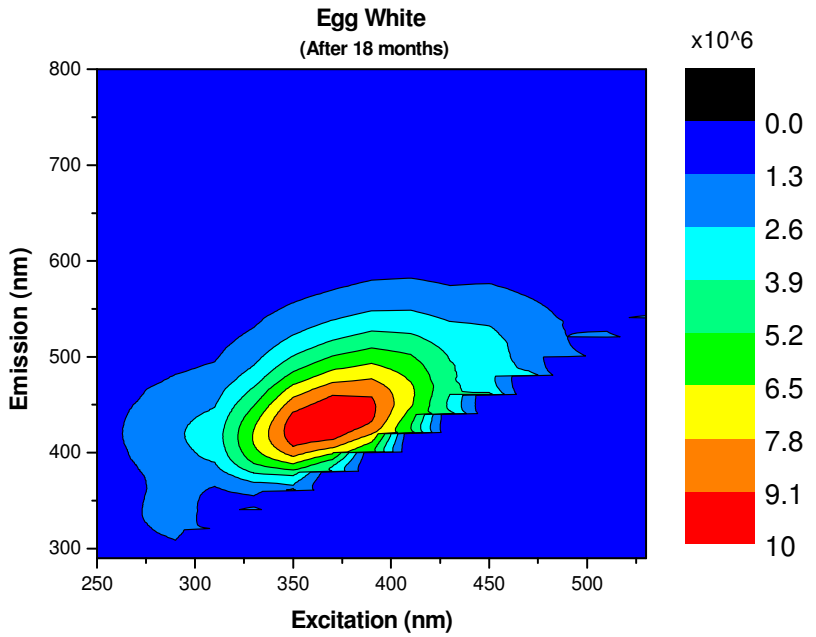

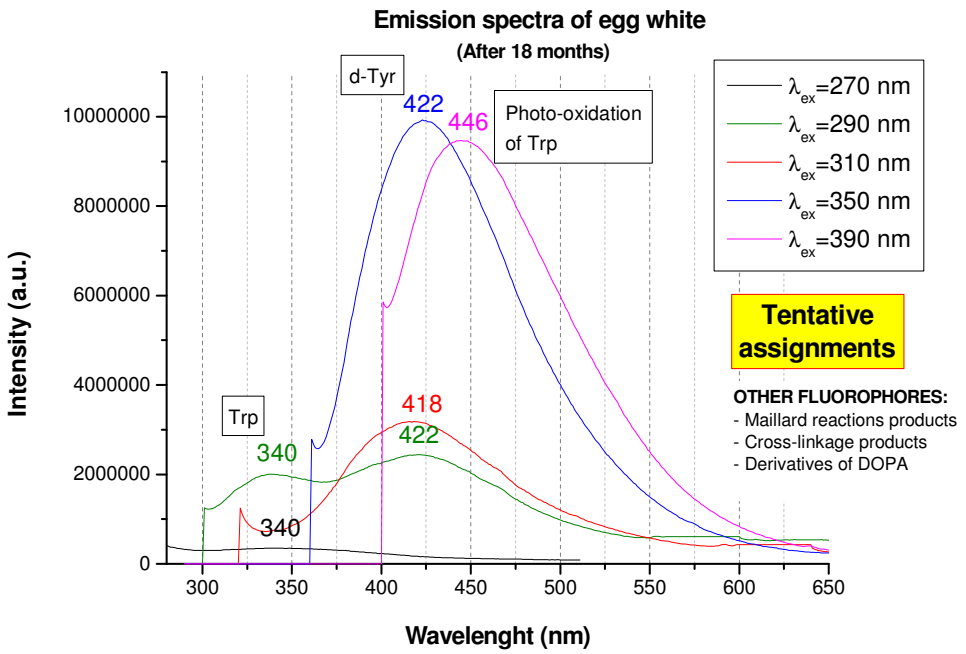

Excitation (nm)	Emission (nm)
345-390	405-460
~290	~330

EGG YOLK (EY) [1-2]

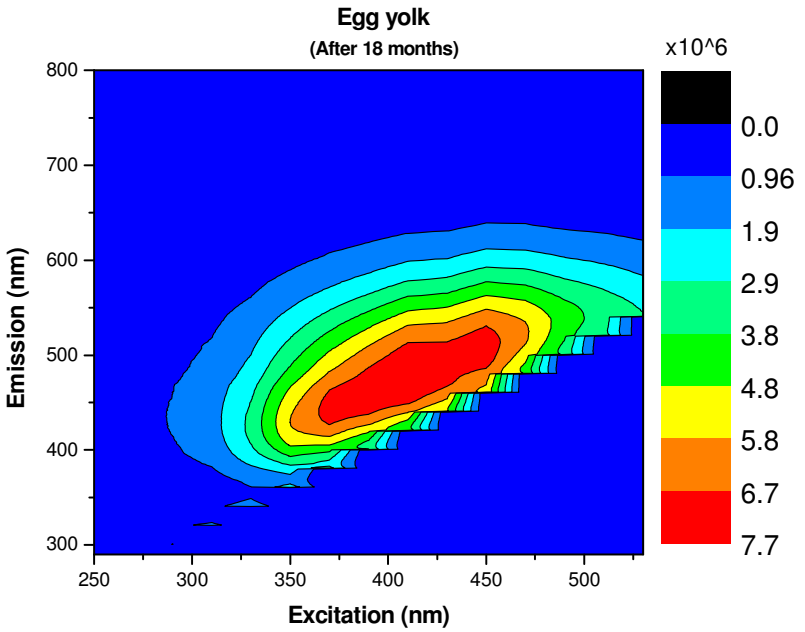

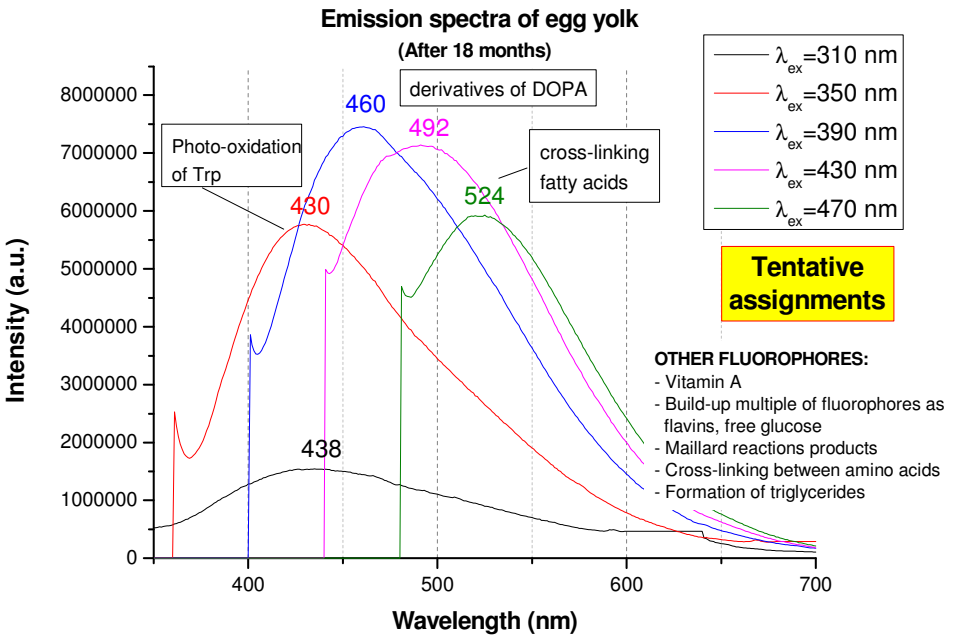

Excitation (nm)	Emission (nm)
365-455	425-515

WHOLE EGG (WE) [1-2]

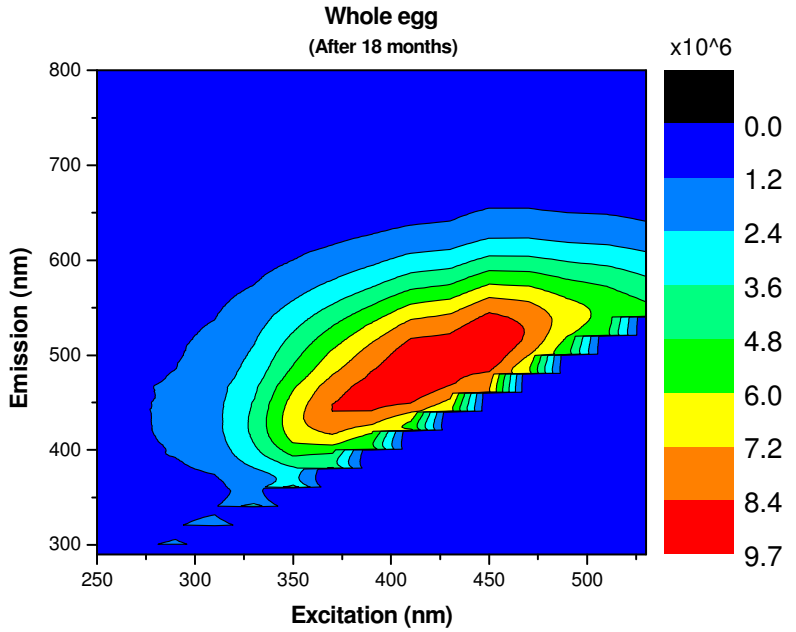

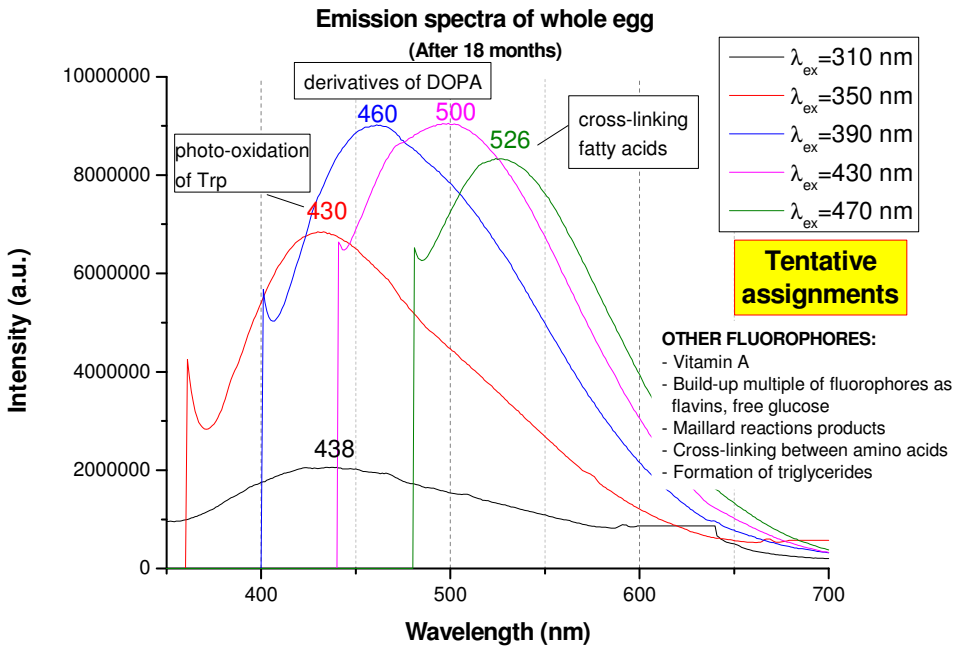

Excitation (nm)	Emission (nm)
370-465	440-545

LIPIDIC BINDING MEDIA

LINSEED OIL ZECCHI (LOZ) [4-5]

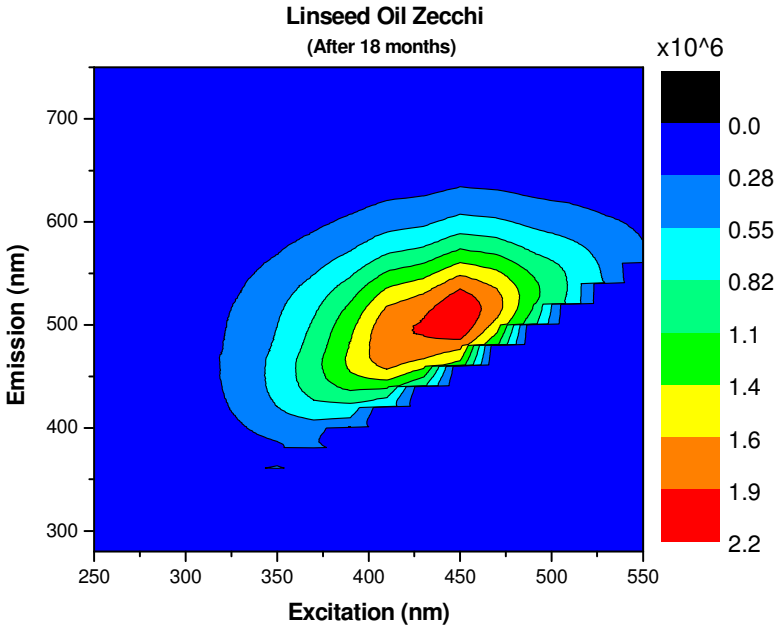

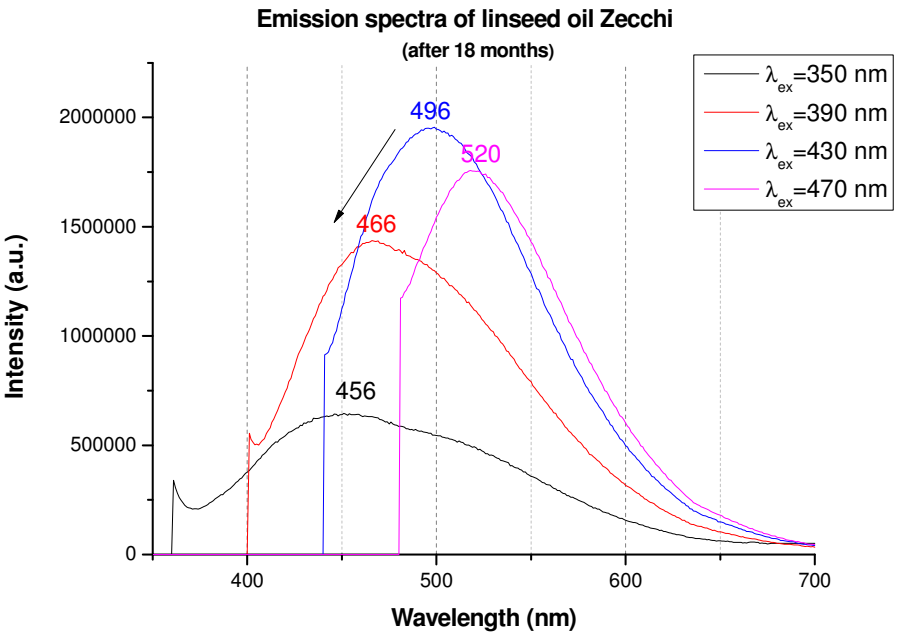

Excitation (nm)	Emission (nm)
424-460	485-536

LINSEED OIL FERRARIO (LOF) [4-5]

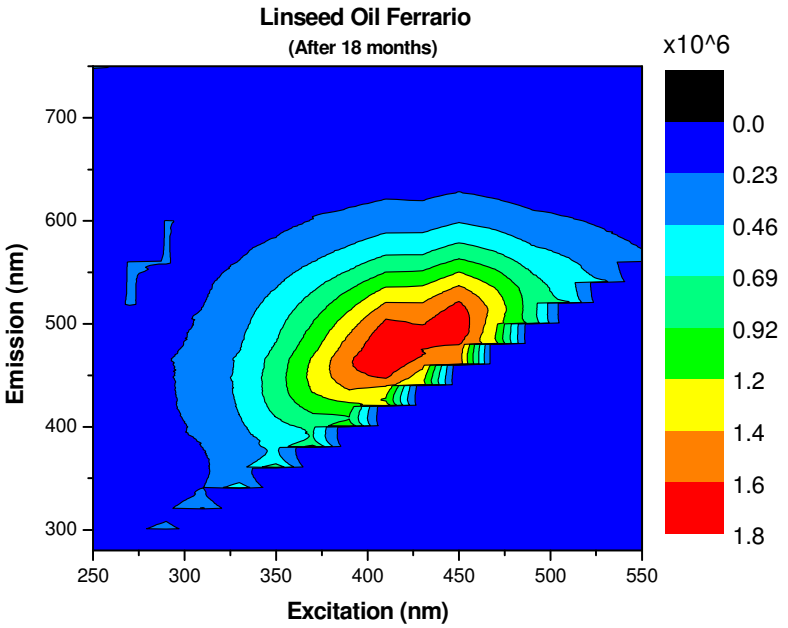

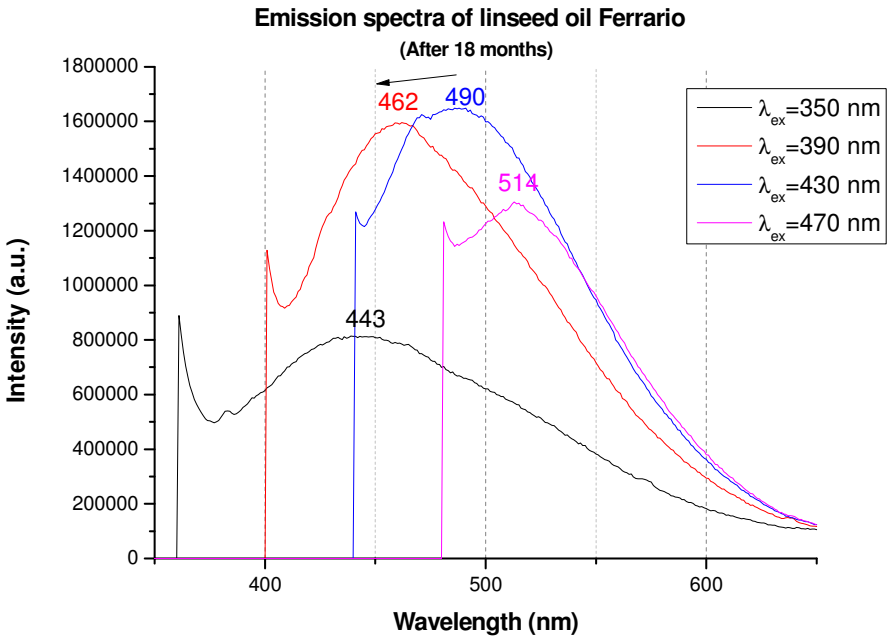

Excitation (nm)	Emission (nm)
390-456	448-520

LINSEED OIL MAIMERI (LOM) [4-5]

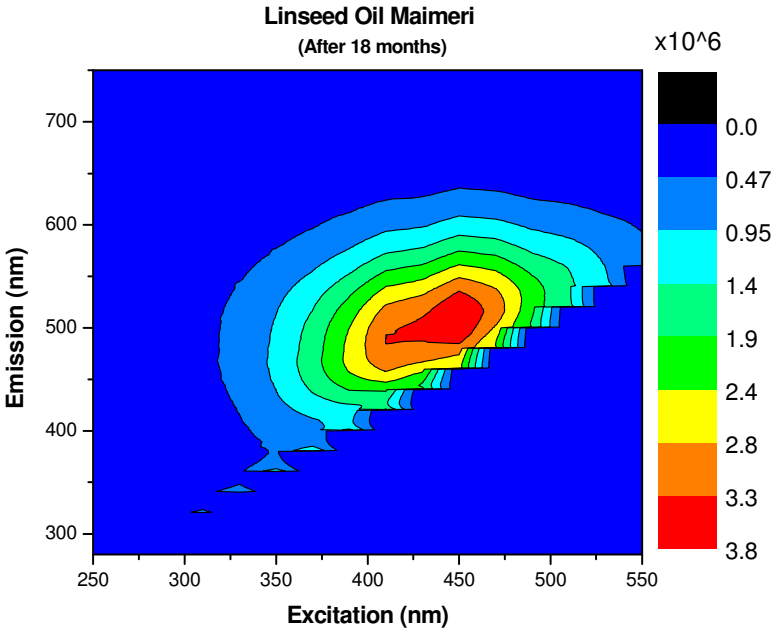

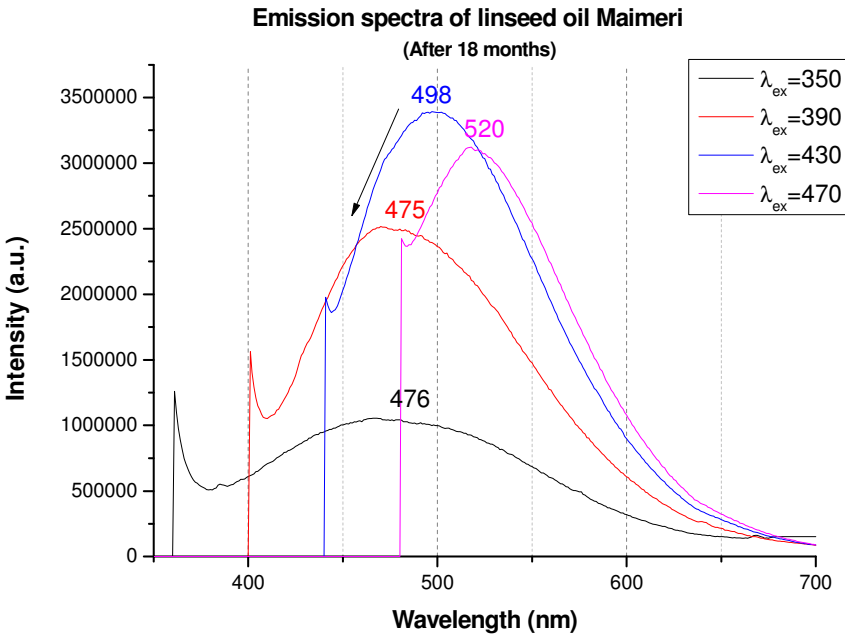

Excitation (nm)	Emission (nm)
410-460	486-536

POPPY-SEED OIL TALENS (POT) [4-5]

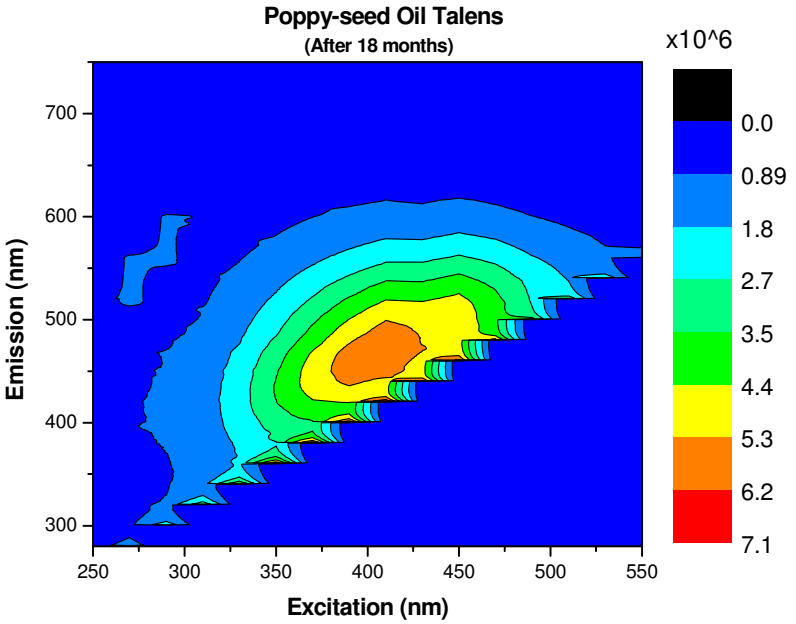

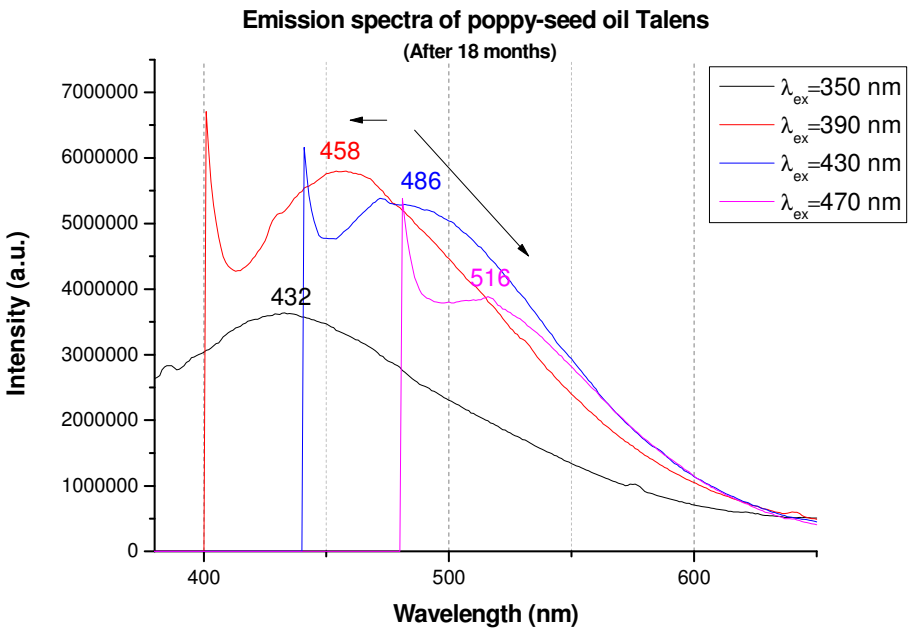

Excitation (nm)	Emission (nm)
380-430	436-500

POPPY-SEED OIL ZECCHI (POZ) [4-5]

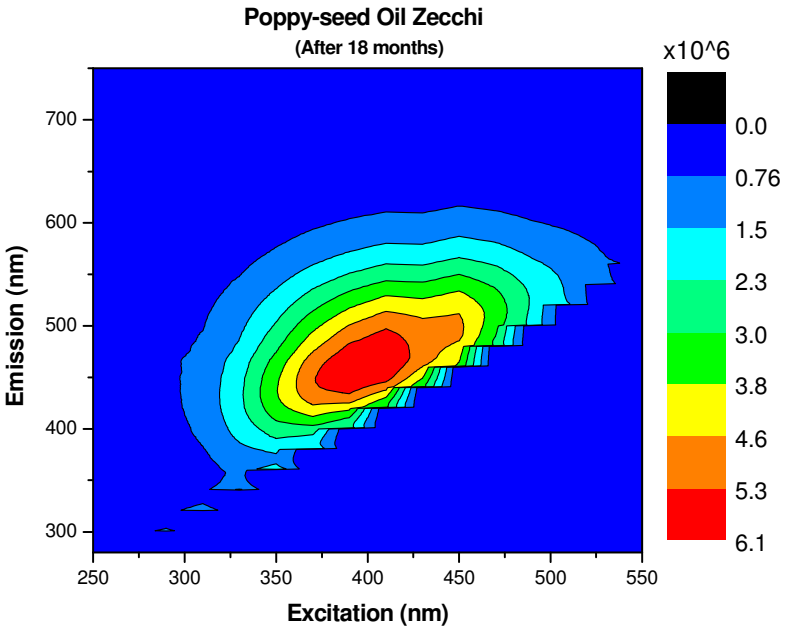

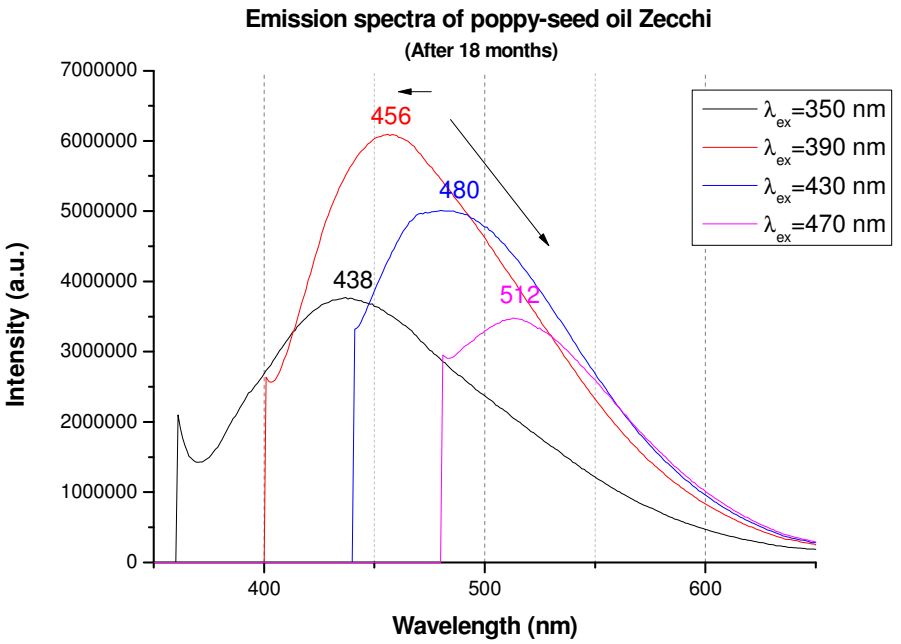

Excitation (nm)	Emission (nm)
370-422	434-500

WALNUT OIL ZECCHI (WOZ) [4-5]

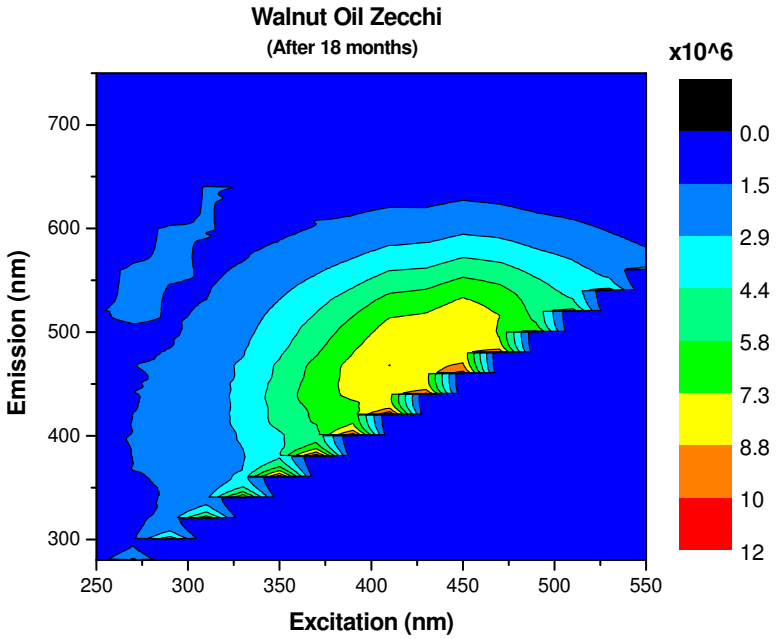

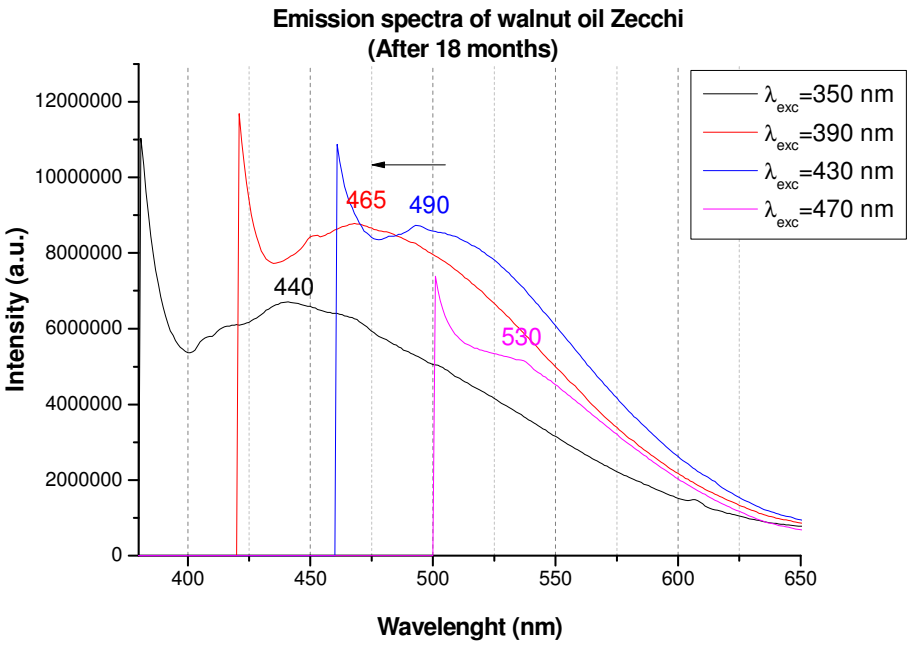

Excitation (nm)	Emission (nm)
382-470	400-530

WALNUT OIL FERRARIO (WOF) [4-5]

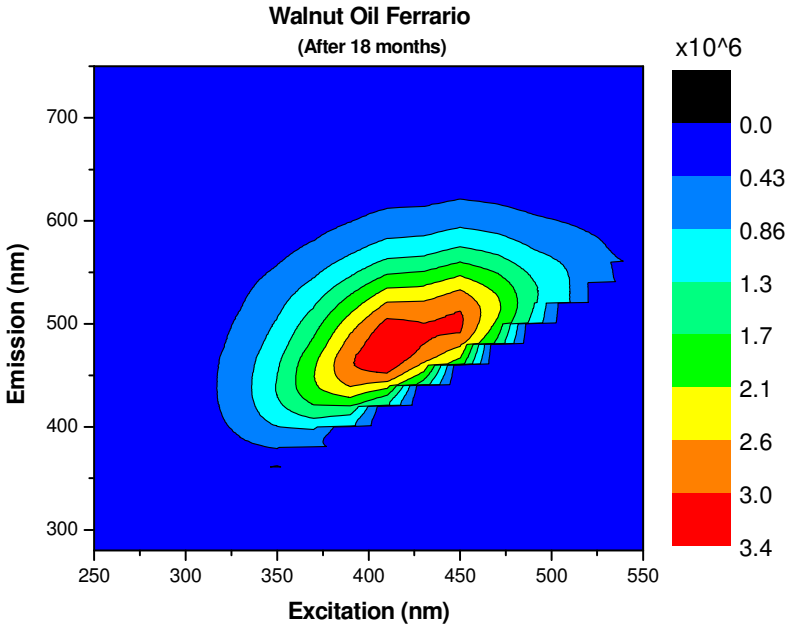

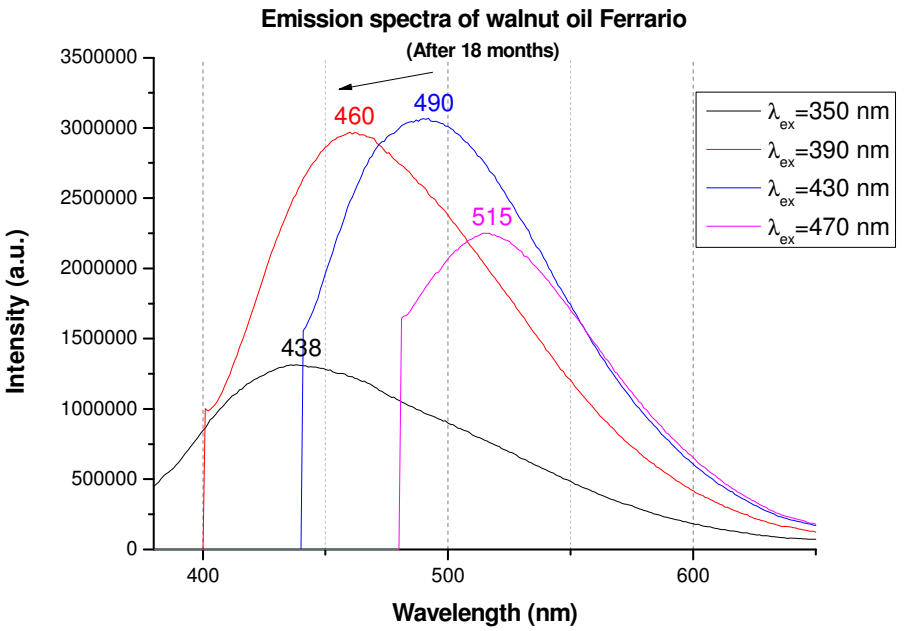

Excitation (nm)	Emission (nm)
390-450	450-505

STAND-OIL ZECCHI (SOLZ) [4-5]

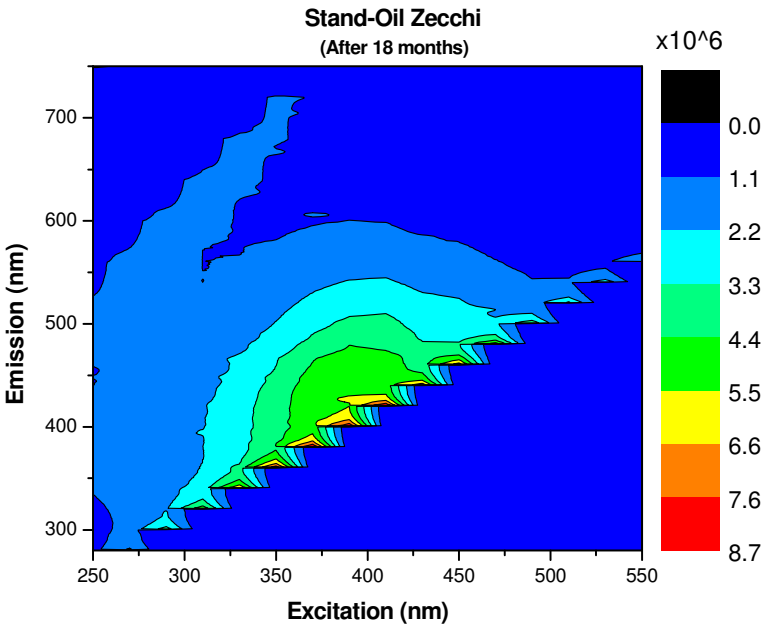

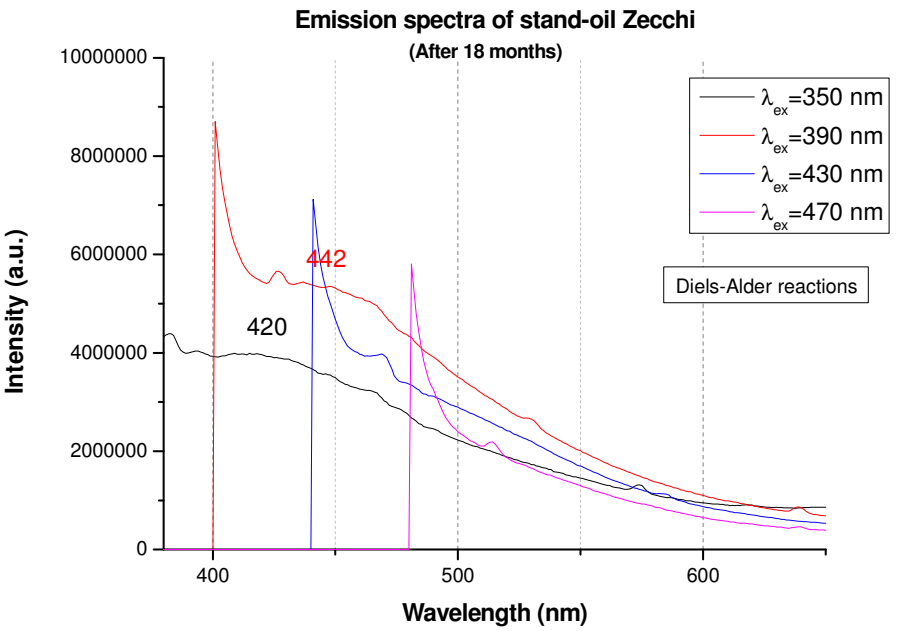

Excitation (nm)	Emission (nm)
~386	~436

POLYSACCHARIDES BINDING MEDIA

ARABIC GUM (AG) [6-8]

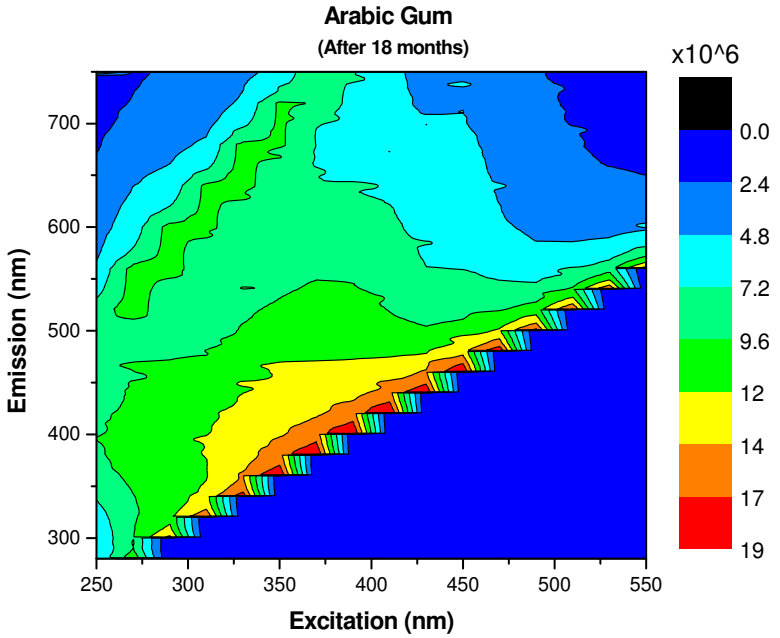

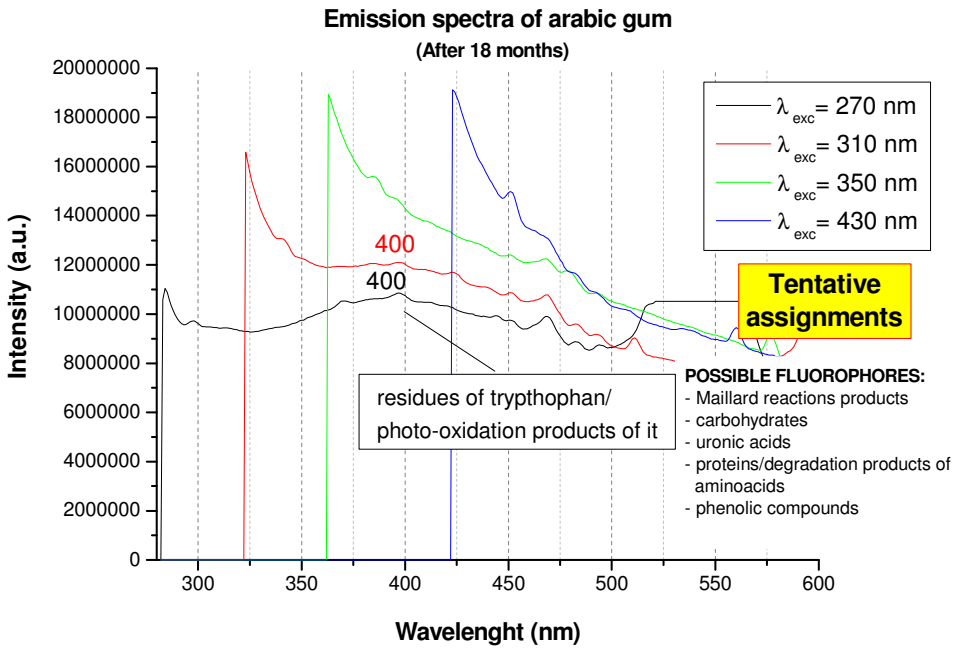

Excitation (nm)	Emission (nm)	Maximum
~(333-415)	~(378-476)	~(353/412)

TRAGACANTH GUM (TG) [6-8]

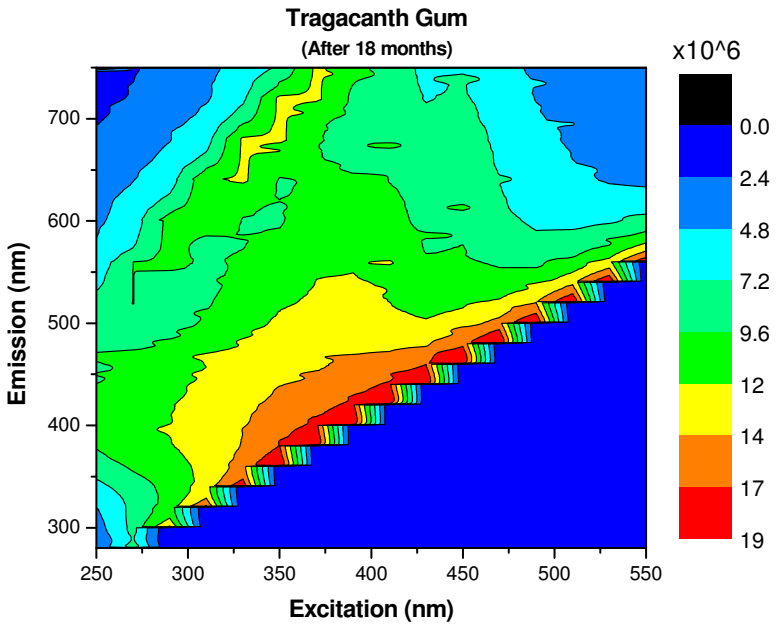

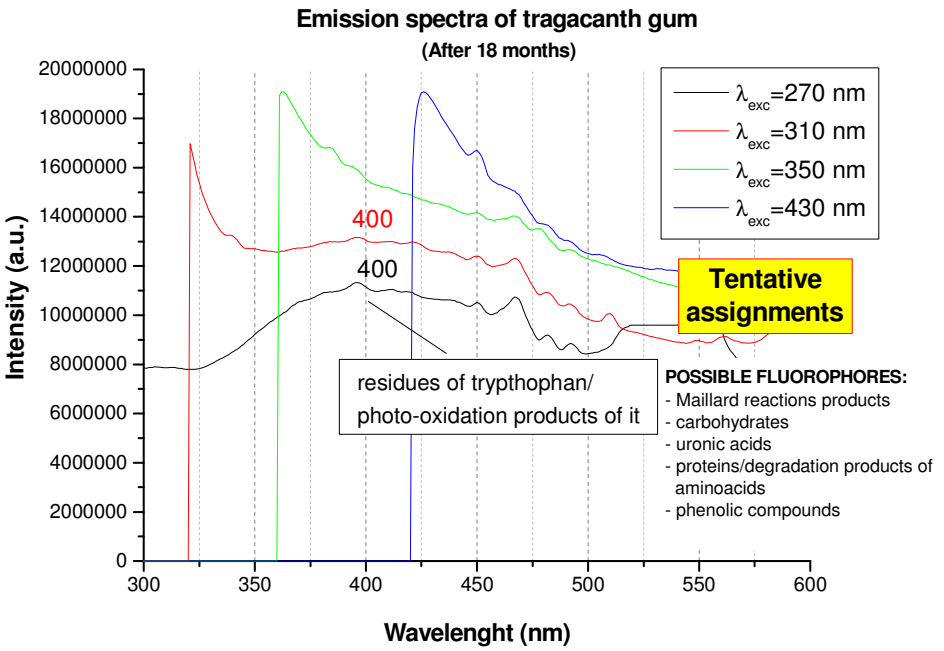

Excitation (nm)	Emission (nm)	Maximum
~(332-420)	~(373-470)	~(366/404)

References

[1] A. Nevin, D. Anglos, S. Cather, A. Burnstock, The influence of visible light and inorganic pigments on fluorescence excitation emission spectra of egg-, casein and collagen-based painting media, Appl. Phys. 2008**,** A92, pp 69-76.

[2] A. Nevin, S. Cather, D. Anglos, C. Fotakis, LIF of protein-based media, Anal. Chim. Acta 2006, 573-574, pp 341-346.

[3] A. Nevin, D. Comelli, G. Valentini, R. Cubeddu, Total Synchronous Fluorescence Spectroscopy Combined with Multivariate Analysis: Method for the classification of Selected Resins, Oils, and Protein-Based Media Used in Paintings, Anal. Chem. 2009, 81, pp 1784-1791.

[4] E. R. De la Rie, Fluorescence of paint and varnish layers (part II), Stud. Conserv. 1982, 27, pp.-65-68.

[5] T. Miyoshi, Fluorescence from Oil Colours, Linseed Oil and Poppy Oil under N2 Laser Excitation, Jpn. J. Appl. Phys. 1985, 24(3), pp 371-372.

[6] A. Mounier, G. Le Bourdon, C. Aupetit, C. Belin, L. Servant, S. Lazare, Y. Lefrais, F, Daniel, Hyperspectral imaging, spectrofluorimetry, FORS and XRF for the non-invasive study of medieval miniatures materials, Heritage Science 2014, 2(24), pp 1-12.

[7] J. L. Larson, K.S. Kim Shin, J. I. Zink, Photoluminescence spectroscopy of natural resins and organic binding media of paintings, JAIC 1991, Vol. 30, No. 1 (7), pp 89-104.

[8] L. Brambilla,, C. Riedo, C. Baraldi, A. Nevin, M. C. Gamberini, C. D'Andrea, O. Chiantore, S. Goidanich, L. Toniolo, Characterization of fresh and aged natural ingredients used in historical ointments by molecular spectroscopic techniques: IR, Raman and fluorescence, Anal Bioanal Chem. 2011, 401(6), pp: 1827-37.